frontiers | Research Topics

Advances in magnetotelluric imaging

Edited by
Bo Yang, Ying Liu, Graham Heinson and Andreas Junge

Published in
Frontiers in Earth Science

ISSN 1664-8714
ISBN 978-2-8325-6817-0
DOI 10.3389/978-2-8325-6817-0

Generative AI statement
Any alternative text (Alt text) provided alongside figures in the articles in this ebook has been generated by Frontiers with the support of artificial intelligence and reasonable efforts have been made to ensure accuracy, including review by the authors wherever possible. If you identify any issues, please contact us.

About Frontiers

Frontiers is more than just an open access publisher of scholarly articles: it is a pioneering approach to the world of academia, radically improving the way scholarly research is managed. The grand vision of Frontiers is a world where all people have an equal opportunity to seek, share and generate knowledge. Frontiers provides immediate and permanent online open access to all its publications, but this alone is not enough to realize our grand goals.

Frontiers journal series

The Frontiers journal series is a multi-tier and interdisciplinary set of open-access, online journals, promising a paradigm shift from the current review, selection and dissemination processes in academic publishing. All Frontiers journals are driven by researchers for researchers; therefore, they constitute a service to the scholarly community. At the same time, the *Frontiers journal series* operates on a revolutionary invention, the tiered publishing system, initially addressing specific communities of scholars, and gradually climbing up to broader public understanding, thus serving the interests of the lay society, too.

Dedication to quality

Each Frontiers article is a landmark of the highest quality, thanks to genuinely collaborative interactions between authors and review editors, who include some of the world's best academicians. Research must be certified by peers before entering a stream of knowledge that may eventually reach the public - and shape society; therefore, Frontiers only applies the most rigorous and unbiased reviews. Frontiers revolutionizes research publishing by freely delivering the most outstanding research, evaluated with no bias from both the academic and social point of view. By applying the most advanced information technologies, Frontiers is catapulting scholarly publishing into a new generation.

What are Frontiers Research Topics?

Frontiers Research Topics are very popular trademarks of the *Frontiers journals series*: they are collections of at least ten articles, all centered on a particular subject. With their unique mix of varied contributions from Original Research to Review Articles, Frontiers Research Topics unify the most influential researchers, the latest key findings and historical advances in a hot research area.

Find out more on how to host your own Frontiers Research Topic or contribute to one as an author by contacting the Frontiers editorial office: frontiersin.org/about/contact

Advances in magnetotelluric imaging

Topic editors

Bo Yang — Zhejiang University, China

Ying Liu — China University of Geosciences Wuhan, China

Graham Heinson — University of Adelaide, Australia

Andreas Junge — Goethe University Frankfurt, Germany

Citation

Yang, B., Liu, Y., Heinson, G., Junge, A., eds. (2025). *Advances in magnetotelluric imaging*. Lausanne: Frontiers Media SA. doi: 10.3389/978-2-8325-6817-0

Table of contents

frontiers | Frontiers in Earth Science

TYPE Editorial
PUBLISHED 21 August 2025
DOI 10.3389/feart.2025.1677791

OPEN ACCESS

EDITED AND REVIEWED BY
Kenneth Philip Kodama,
Lehigh University, United States

*CORRESPONDENCE
Bo Yang,
bo.yang@zju.edu.cn

RECEIVED 01 August 2025
ACCEPTED 11 August 2025
PUBLISHED 21 August 2025

CITATION
Yang B and Liu Y (2025) Editorial: Advances in magnetotelluric imaging.
Front. Earth Sci. 13:1677791.
doi: 10.3389/feart.2025.1677791

Editorial: Advances in magnetotelluric imaging

Bo Yang[1]* and Ying Liu[2]

[1]School of Earth Sciences, Zhejiang University, Hangzhou, China, [2]School of Geophysics and Geomatics, China University of Geosciences, Wuhan, China

KEYWORDS

geo-electromagnetism, magnetotelluric, inversion, anisotropy, modeling, electrical structure

Editorial on the Research Topic
Advances in magnetotelluric imaging

Introduction

Geo-electromagnetic methods, especially the magnetotelluric (MT) sounding technique, are irreplaceable geophysical methods used for imaging the Earth's subsurface electrical structure. The establishment of several continent-scale MT arrays, such as EarthScope, SinoProbe, and AusLamp, has underscored the need for advancements in data processing and modeling techniques. Benefiting from rapid developments in three-dimensional inversion algorithms and the release of open-source codes, a substantial volume of continent-scale imaging results has been published in the last few decades. These contributions have offered new, solid evidence that enhances our understanding of geodynamic processes. They also foster a range of novel insights into how the electrical structure can reveal aspects of tectonic evolution and the distribution of mineral resources. Given these developments, we advocate for this Research Topic dedicated to the latest advances in MT imaging, which has published 11 contributions on the new methodologies and findings.

Advances in magnetotelluric imaging

The articles published in this Research Topic presented the latest advances regarding geo-electromagnetic methods, covering numerical modeling, anisotropy, imaging and practical corrections.

Long presents a meshfree numerical approach for forward modelling of geophysical electromagnetic responses, offering a flexible alternative to traditional mesh-based methods like finite element or finite differenceBy using unconnected points and radial basis functions, the method efficiently handles complex geological geometries and irregular topography without the need for structured meshes. The approach is validated through tests on both synthetic and realistic models, including the challenging Dublin Test Model two and the irregular Voisey's Bay deposit, showing strong agreement with analytical and independent numerical solutions. The results demonstrate the meshfree

method's accuracy and potential for improving geophysical interpretation in mineral exploration.

Zhang et al. develop a 3D finite element forward modeling algorithm for cross-well induced polarization (IP) in anisotropic media, accounting for directional variations in both conductivity and polarizability. The method is validated using complex isotropic and anisotropic models, confirming its accuracy and effectiveness. Numerical experiments on horizontal and inclined plate models reveal that anisotropy significantly affects the amplitude and shape of apparent polarizability responses, with the most pronounced effects observed in the x-direction for horizontal layers, while y-direction anisotropy shows minimal deviation from isotropic behavior. These findings enhance the understanding of anisotropic influences on cross-well IP data and provide a crucial theoretical basis for more accurate interpretation in practical mineral and resource exploration.

Liu and Sun present a 3D staggered finite difference method for MT forward modeling in axis-anisotropic media, solving the electric field governing equations using the quasi-minimum residual method with validated accuracy against 2D quasi-analytic solutions. Their study demonstrates that MT data can effectively identify horizontal electrical anisotropy, offering valuable insight for characterizing anisotropic geological structures in exploration applications.

Huang et al. propose a new coupling method, minimum cross-gradient support (MCGS), for geophysical inversion that improves the integration of prior information by enhancing constraint strength in regions with weak model gradients. By applying a minimum support function to the cross-gradient, MCGS balances gradient magnitude and direction, allowing for flexible control via focusing factors and reducing reliance on highly accurate prior models. Synthetic tests on a double-blocks and a nappe structure model show that MCGS outperforms traditional cross-gradient and joint minimum gradient support methods in model recovery and constraint effectiveness. Applied to real MT data from the Junggar Basin, MCGS inversion successfully imaged key resistivity structures, including potential Carboniferous remnants and basement distribution, providing new insights into the region's tectonic evolution.

Liu et al. present a physics-informed auto-encoder approach for MT inversion, in which the decoder is replaced with the MT forward operator to ensure physically consistent results and improve data fitting. By embedding the governing physical laws into the network architecture, the method enhances the reliability and interpretability of neural network-based inversions. Scaling laws are introduced to adapt real-world observation systems to the trained model, improving its applicability across diverse survey configurations. Demonstrated on both synthetic and field data, the approach achieves inversion accuracy comparable to classic Occam's inversion with significantly higher computational efficiency, offering a promising path toward fast, robust, and physically grounded MT imaging.

Yu and Han introduce an improved 3D MT forward modeling framework that incorporates a divergence correction procedure for arbitrary anisotropic media, enhancing the convergence of iterative solvers. Originally developed for isotropic conditions, the divergence correction is successfully adapted to anisotropic cases, significantly reducing the number of solver iterations and improving computational efficiency and stability. The method is validated across four numerical examples, including 1D, 2D, and complex 3D anisotropic models, demonstrating robust performance even at long periods and in highly heterogeneous settings. The results highlight the method's effectiveness in accelerating simulations while maintaining accuracy, making it a valuable tool for practical anisotropic MT modeling.

Yang et al. present a high-resolution 3D resistivity model of the Baogutu porphyry copper belt in NW China, derived from a dense natural-source audio-frequency MT (AMT) array of 176 sites. A parallel 3D inversion scheme was applied, and the resulting model was validated through lab-measured rock resistivity and borehole data, revealing prominent east-west conductive zones extending to 600 m depth. The inverted resistivity structure shows strong correlation with shear wave velocity, and their positive relationship helps identify potential mineralized zones. The study demonstrates that dense AMT surveys combined with 3D inversion can reliably image deep mineralized structures and guide future exploration drilling.

Li et al. summarize recent advances in MT studies of the Central Asian Orogenic Belt (CAOB), a complex tectonic zone formed by the closure of the Paleo-Asian Ocean and subsequent crustal collisions and extensions. The authors highlight two recent MT surveys conducted in the Beishan and Bainaimiao segments, revealing detailed crustal and upper mantle electrical structures that shed light on deep deformation mechanisms and continental dynamics. These studies identify key low-resistivity zones, likely associated with fluids, melts, or shear zones, and discuss their implications for lithospheric evolution. The review concludes with an overview of the region's lithospheric electrical characteristics and outlines future directions for MT research to further unravel the geodynamic history of the CAOB.

Ji et al. address the challenge of electrical anisotropy in MT imaging, which can severely distort subsurface models when ignored in standard isotropic inversions. By analyzing phase tensors and induction vectors, the authors identify anisotropic features and estimate anisotropic parameters in 2D models, then apply an equivalence-based approach to convert anisotropic structures into equivalent isotropic anomalies. These equivalent structures are incorporated as prior information in 2D isotropic inversion, significantly improving the recovery of true isotropic features. The proposed method offers a practical and novel strategy for detecting and accounting for electrical anisotropy in MT data interpretation, bridging the gap toward more reliable subsurface imaging in complex geological settings.

Zeng et al. present a robust MT inversion strategy that circumvents the challenges of static shift correction by excluding affected apparent resistivity data and relying solely on phase data during inversion. Leveraging the fact that static shift impacts only amplitude-related measurements, the method preserves inversion accuracy while avoiding error-prone correction procedures. Tests on both synthetic and field data show that the phase-only approach effectively recovers deep subsurface structures with high fidelity. The results demonstrate that accurate MT imaging can be achieved without static shift correction, offering a practical and reliable alternative for data interpretation in geologically complex areas.

Zhang et al. present a MT investigation along a profile from Chazha to Luomai, crossing the northwestern margin of the

Sichuan-Yunnan diamond block—a key region for understanding material escape from the Tibetan Plateau. Using nonlinear conjugate gradient 3D inversion, the research reveals a segmented deep electrical structure. A prominent high-resistivity zone associated with the Dedeng-Batang-Riyu fault acts as a sharp electrical boundary, effectively isolating the Qiangtang block to the southwest from the Sichuan-Yunnan block to the northeast. This finding redefines the northwest boundary of the Sichuan-Yunnan block from a diffuse transitional zone to a distinct, resistive tectonic barrier. Within the block, two major crustal conductive layers at 5–20 km and 10–30 km depths suggest complex internal deformation, challenging the prevailing lower crustal flow model by indicating significant upper-middle crustal weakening and potential localized fluid or partial melt presence. These results provide new insights into the geodynamic evolution and rheological structure of eastern Tibet.

Summary and outlook

MT methods are crucial for probing deep geological structures, particularly in tectonically complex regions like the Central Asian Orogenic Belt and the Sichuan-Yunnan diamond block, where they reveal detailed crustal and mantle electrical structures linked to tectonic evolution and material flow. Electrical anisotropy significantly impacts MT data, and recent advances in forward modeling, inversion techniques, and anisotropy-aware processing—such as divergence correction, minimum cross-gradient support, and physics-informed neural networks—have improved the accuracy and reliability of subsurface imaging. Innovative strategies, including phase-only inversion to avoid static shift and equivalence-based anisotropy compensation, offer practical solutions to long-standing interpretation challenges. Studies integrating MT with seismic and petrophysical data demonstrate strong correlations that enhance the identification of mineralized zones and lithospheric features. Together, these advancements underscore the importance of accounting for anisotropy, static effects, and multi-physics constraints to achieve high-resolution, geologically meaningful models. Overall, modern MT research is moving toward more robust, physically consistent, and integrative approaches that deepen our understanding of Earth's geodynamic processes.

Reference

Junke, L., Xinyu, X., and Yurong, L. (2024). Study of response characteristics of cross-well induced polarization method in anisotropic media. *Front. Earth Sci.* doi:10.3389/feart.2024.1443764

Author contributions

BY: Writing – review and editing, Writing – original draft. YL: Writing – review and editing.

Funding

The author(s) declare that no financial support was received for the research and/or publication of this article.

Conflict of interest

The authors declare that the research was conducted in the absence of any commercial or financial relationships that could be construed as a potential conflict of interest.

Generative AI statement

The author(s) declare that no Generative AI was used in the creation of this manuscript.

Any alternative text (alt text) provided alongside figures in this article has been generated by Frontiers with the support of artificial intelligence and reasonable efforts have been made to ensure accuracy, including review by the authors wherever possible. If you identify any issues, please contact us.

Publisher's note

frontiers | Frontiers in Earth Science

TYPE Original Research
PUBLISHED 11 July 2024
DOI 10.3389/feart.2024.1432992

OPEN ACCESS

EDITED BY
Nannan Zhou,
Chinese Academy of Sciences (CAS), China

REVIEWED BY
Hualiang Zhao,
Shandong University, China
Jianhui Li,
China University of Geosciences
Wuhan, China

*CORRESPONDENCE
Jianbo Long,
jl7037@mun.ca

†PRESENT ADDRESS
Jianbo Long,
Department of Earth Sciences, Memorial University of Newfoundland,
St. John's, NL, Canada

RECEIVED 15 May 2024
ACCEPTED 13 June 2024
PUBLISHED 11 July 2024

CITATION
Long J (2024), Meshfree modelling of magnetotelluric and controlled-source electromagnetic data for conductive earth models with complex geometries.
Front. Earth Sci. 12:1432992.
doi: 10.3389/feart.2024.1432992

Meshfree modelling of magnetotelluric and controlled-source electromagnetic data for conductive earth models with complex geometries

Jianbo Long*†

Department of Electronic System, Norwegian University of Science and Technology, Trondheim, Norway

Geophysical electromagnetic survey methods are particularly effective in locating conductive mineral deposits or mineralization zones in a mineral resource exploration. The forward modelling of the electromagnetic responses over such targets is a fundamental task in quantitatively interpreting the geophysical data into a geological model. Due to the ubiquitous irregular and complex geometries associated with the mineral rock units, it is critical that the numerical modelling approach being used is able to adequately and efficiently incorporate any necessary geometries of the Earth model. To circumvent the difficulties in representing complex but necessary geometry features in an Earth model for the existing mesh-based numerical modelling approaches (e.g., finite element and finite difference methods), I present a meshfree modelling approach that does not require a mesh to solve the Maxwell's equations. The meshfree approach utilizes a set of unconnected points to represent any geometries in the Earth model, allowing for the maximal flexibility to account for irregular surface geometries and topography. In each meshfree subdomain, radial basis functions are used to construct meshfree function approximation in transforming the differential equations in the modelling problem into linear systems of equations. The method solves the potential function equations of the Maxwell's equations in the modelling. The modelling accuracy using the meshfree method is examined and verified using one magnetotelluric model and two frequency-domain controlled-source models. The magnetotelluric model is the well-known Dublin Test Model 2 in which the spherical geometry of the conductor in the shallow subsurface may pose as a challenge for many numerical modelling methods. The first controlled-source model is a simple half-space model with the electric dipole source for which analytical solutions exist for the modelling responses. The second controlled-source model is the volcanic massive sulphide mineral deposit from Voisey's Bay, Labrador, Canada in which the deposit's surface is highly irregular. For all modellings, the calculated electromagnetic responses are found to agree with other independent numerical solutions and the analytical solutions. The advantages

of the meshfree method in discretizing the Earth models with complex geometries in the forward modelling of geophysical electromagnetic data is clearly demonstrated.

KEYWORDS

mineral exploration, electromagnetic, resistivity, magnetotelluric, controlled-source, meshfree, numerical modelling

1 Introduction

Geophysical electromagnetic (EM) survey methods continue to be important in the exploration of mineral resources, particularly those with a high conductivity contrast from their host rocks (e.g., copper, zinc, iron, nickle) (Strangway et al., 1973; Dyck and West, 1984; Farquharson and Craven, 2009; Smith, 2014; Gehrmann et al., 2019). In recent years, due to the increasing acknowledgement of the important role of mineral resources in energy transition, various "critical mineral resource" initiatives have been proposed (e.g., Schulz et al., 2017) and how we as a society can meet the demands has sparkled much discussion (Jones, 2023).

A geophysical EM survey directly produces a map of the distribution of electrical conductivity of the subsurface. Naturally, the interpretation of any EM data collected over a region of interest becomes vital in determining the parameters of potential mineral deposits that may host economic resources. At the centre of a quantitative interpretation of EM data is the numerical modelling of EM responses (including controlled-source EM, magnetotelluric, transient EM data) which plays a critical role in the development of theories and methods of various EM survey techniques. Of the various advancements made over the last few decades (e.g., Nabighian, 1988; Zhdanov, 2010; Smith, 2014), the numerical modelling of EM data has steadily evolved from closed-form, analytical computations of EM responses over relatively simple conductivity models that started around 1960s (Wait, 1960; Nabighian, 1988) to fully numerical simulations of Maxwell's equations over Earth models with complex geometries and nonlinear, anisotropic conductivity distributions nowadays (e.g., Newman, 2014; Han et al., 2018).

The importance of representing realistically complex geometries of conductive mineral deposits or mineralization zones in the EM data modelling becomes obvious since mineral deposits or mineralization zones are naturally of irregular shapes of geometry, with some presenting quite extreme geometries (e.g., uranium deposits associated with thin graphite Zeng et al., 2019; Lu et al., 2021). Despite the ubiquitous existence and importance of such realistic geometries, there are still significant challenges faced by numerical modelling techniques in terms of efficiently incorporating the geometries. These challenges are precisely what this study is trying to solve and in order to do so, a new type of modelling techniques called *meshfree methods* is used which I will present in detail in the following sections.

Numerical methods of forward modelling EM responses over a general three-dimensional (3-D) conductivity Earth model are often focused on mesh-based modelling methods in the applied geophysics which include finite difference (e.g., Yee, 1966; Taflove and Umashankar, 1990; Mackie et al., 1993; Wang and Hohmann, 1993; Newman and Alumbaugh, 1995; Streich, 2009), finite volume (e.g., Jahandari and Farquharson, 2014; Jahandari et al., 2017), integral equation (e.g., Jones and Pascoe, 1972; Hohmann, 1975; Newman et al., 1986; Farquharson and Oldenburg, 2002; Chen et al., 2021) and finite element methods (e.g., Coggon, 1971; Pridmore et al., 1981; Badea et al., 2001; Nam et al., 2007; Puzyrev et al., 2013; Li J. et al., 2017; Rochlitz et al., 2019). They are termed *mesh-based modelling methods* in this study because they have the common feature of relying on a mesh-based discretization (e.g., rectilinear, triangular and tetrahedral meshes; see Figure 1A,B) of the conductivity model. Among these mesh-based methods, finite difference approaches may face more challenges than others in accurately representing complex topography surfaces and irregular surface geometries of a conductor since they require tensor-grid function approximation of differential equations. In contrast, finite volume, integral equation and finite element methods do not face such limitation. It may be argued that finite element modelling techniques, if combined with unstructured meshes whose automatic generations are facilitated by modern mesh generation software (Fabri et al., 2000; Si, 2015), are the most flexible mesh-based approaches in the modelling of EM data over complex Earth models (Coggon, 1971; Günther et al., 2006; Nam et al., 2007; Miensopust et al., 2013).

For real-life geometries of exploration targets, unstructured meshes (e.g., triangular and tetrahedral meshes) possess a unique advantage in efficiently and accurately representing complex geometries that are important characteristics of potential exploration targets (Lelièvre et al., 2012; Lu et al., 2021). However, accurate numerical solution of EM responses using mesh-based modelling techniques, including finite element and finite volume methods, also require a certain degree of regularity of the mesh cells. In the finite element case, for example, the effect of the mesh quality (e.g., the ratio of the largest to smallest cell sizes, elongation, dihedral angles and radius-edge ratio of cells for tetrahedral meshes) on the computational accuracy is demonstrated to be significant (Du et al., 2009). Poor mesh quality can lead to very slow convergence or divergence in iteratively solving the resulting linear system of equations in modelling controlled-source EM data using a vector finite element implementation (Ansari and Farquharson, 2014). On the other hand, ensuring the quality of the mesh can lead to overwhelmingly excessive number of elements in the generated mesh, therefore intractable computational resources, in order to sufficiently conform to the real geometries in the model (Schwarzbach et al., 2011; Nalepa et al., 2016).

The dilemma in balancing the quality of unstructured meshes and the number of mesh cells is often addressed using adaptive mesh refinement techniques (Oden and Prudhomme, 2001; Key and Ovall, 2011; Schwarzbach et al., 2011; Ren et al., 2013; Zhang et al., 2018; Spitzer, 2024). In an adaptive mesh refinement approach, the current mesh used for the modelling of EM responses can be further

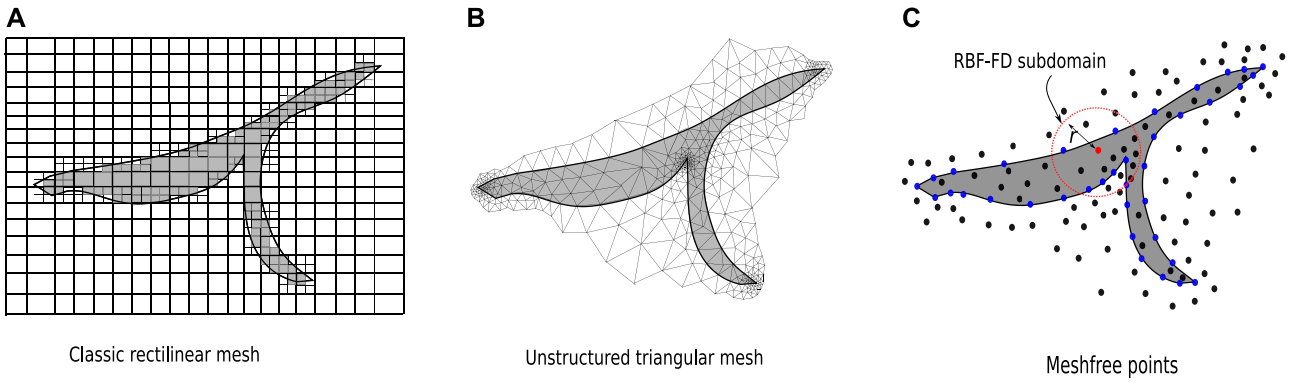

FIGURE 1
Schematic illustration of model discretizations for 2-D irregular geometries using **(A)** rectilinear mesh with local quadtree refinements, **(B)** unstructured triangular mesh and **(C)** meshfree points. Adapted from Long and Farquharson (2019c).

refined or coarsened based on an estimate of the current numerical modelling error. The ideal result is that only the part of the mesh with the largest numerical errors is refined. In the unstructured mesh scenario, the adaptive refining process is often carried out by locally modifying the mesh, rather than re-meshing the whole Earth model, due to the concern of efficiency and robustness of the process (Zhang et al., 2018; Liu et al., 2023). However, complications may arise during the adaptive mesh refining. First, as the topology of the mesh changes at each refining step the mapping between the old mesh and the new mesh needs to be calculated in order to update the degrees of freedom, which can be an expensive and rather complicated process. Second, further dividing the cells in the current mesh may produce "hanging nodes" due to the non-conforming new cells within the parent cells (Jahandari et al., 2021). The nonconformity of the new mesh may be eliminated at the cost of further refining neighbouring cells, often with a lower quality of the generated new cells.

Alternatively, the Earth model can be discretized using *meshfree points* (see Figure 1C) and the corresponding numerical modelling techniques are called *meshfree methods* (Nguyen et al., 2008; Chen et al., 2017). A set of unconnected points, or meshfree points, serve for the same purpose as that of a quality mesh in obtaining an accurate numerical solution in forward modelling the EM data. Because of the lack of connectivity among the points, the physical property distribution (i.e., the conductivity distribution for EM data modelling) will be *sampled* on the points when discretizing the partial differential equations. With a meshfree point discretization, the density and regularity of the point distribution are still important for accurate numerical modellings; however, the advantages of manipulating points over mesh generations are:

- With comparable regularity of a quality mesh, the generation of points requires much less effort in computer programming and is more straightforward. Also, the development of dedicated point generation software is also significantly easier (Fornberg and Flyer, 2015).
- Since there is no topology requirement, the generation of quality, unstructured meshfree points can be more robust than generating a quality unstructured mesh (Du et al., 2002; Slak and Kosec, 2019).
- Adaptive point refining and/or coarsening is more computationally efficient than the same process when using meshes, since any addition or deletion of local points does not need to affect the rest of the points. The nonconformity issue and its complications in a mesh-based adaptive refining are completely removed (Rabczuk and Belytschko, 2005).

Based on a distribution of points, many meshfree methods for solving partial differential equations have been proposed (Chen et al., 2017). For geophysical data modelling, however, only a few different meshfree methods have been proposed for seismic wave field modelling (e.g., Jia and Hu, 2006; Takekawa et al., 2015; Li B. et al., 2017), gravity data modelling (e.g., Long and Farquharson, 2019c) and EM data modelling (e.g., Wittke and Tezkan, 2014; Long and Farquharson, 2017; Long and Farquharson, 2019a; Long and Farquharson, 2019b). In general, different meshfree methods differ in the choice of basis functions, the types of meshfree points (i.e., uniform or unstructured) and in that whether numerical integration is required in transforming the partial differential equations into the linear system of equations. The meshfree method demonstrated here, mostly known as *radial-basis-function based finite difference* (RBF-FD), does not need the potentially expensive step of numerical integration. It also naturally supports unstructured point distributions allowing for an efficient discretization of complex-geometry conductivity models. Meshfree modelling of EM data is considered to be more challenging than those of seismic and gravity data since the EM fields are discontinuous across conductivity discontinuities (Long and Farquharson, 2019b).

The rest of the study is organized as follows. The details of the meshfree modelling method in the context of numerically solving Maxwell's equations will be first presented, which is followed by the demonstration of the numerical accuracy of the method using a magnetotelluric example and two controlled-source EM examples. Further discussions for the applicability for other types of geophysical data of the modelling method are also presented before I conclude the study.

2 Methods

2.1 Maxwell's equations for meshfree modelling

The frequency-domain Maxwell's equations for the electromagnetic field in the quasi-static limit are expressed as (Stratton, 2007)

$$\nabla \times \mathbf{E} = -i\omega \mathbf{B}, \tag{1}$$

$$\nabla \times \mathbf{H} = \sigma \mathbf{E} + \mathbf{J}_{exe}, \tag{2}$$

for Faraday's law and Ampère's law, respectively. Here, $\mathbf{E}$ and $\mathbf{B}$ are the electric field and magnetic induction vector, respectively. $\mathbf{B} = \mu\mathbf{H}$ with $\mathbf{H}$ as the magnetic field and μ the magnetic permeability. σ is the conductivity distribution of the Earth model. $\omega = 2\pi f$ with f as the ordinary frequency in Hz, i is the imaginary unit, and the convention of the time dependence $e^{i\omega t}$ is used here. $\mathbf{J}_{exe}$ represents any external EM sources as a current density vector; for example, the current density of an induction loop or of an electric dipole grounded into the Earth.

Eliminating $\mathbf{H}$ in Eqs 1, 2 through simple substitutions leads to the second-order Helmholtz equation for $\mathbf{E}$:

$$\nabla \times \mu^{-1} \nabla \times \mathbf{E} + i\omega\sigma \mathbf{E} = -i\omega \mathbf{J}_{exe}. \tag{3}$$

Here, the Earth materials are assumed to be non-ferromagnetic so that the magnetic permeability μ is just that of free space (μ_0). As a result, Eq. 3 is further simplified as:

$$\nabla \times \nabla \times \mathbf{E} + i\omega\mu\sigma \mathbf{E} = -i\omega\mu \mathbf{J}_{exe}. \tag{4}$$

A naive solving of Eq. 4 using numerical methods may lead to spurious or incorrect numerical solutions of EM responses if the discontinuous nature of $\mathbf{E}$ at conductivity jumps is not considered. The ability of handling such discontinuities is one of the reasons behind the popularity of Yee-scheme finite difference methods (Yee, 1966) and vector finite element methods (Jin, 2014) when numerically solving Eq. 4.

In the meshfree modelling of EM responses, the degrees of freedom of the unknown function (e.g., $\mathbf{E}$ in Eq. 4) are coincident with the point locations in a point discretization of the Earth model, a scenario similar to scalar finite element methods (Jin, 2014). As demonstrated in detail by Long and Farquharson (2019b), the RBF-FD meshfree method using scalar *meshfree basis functions*, like scalar finite element methods, will force the numerical solution of the unknown function to be continuous everywhere. In this scenario, EM potential function equations can be used instead of the Helmholtz equation for the electric field. Using the vector magnetic potential $\mathbf{A}$ and electric scalar potential ϕ defined via the relations (Stratton, 2007):

$$\mathbf{E} \coloneqq -i\omega \mathbf{A} - \nabla\phi, \tag{5}$$

$$\mathbf{H} \coloneqq \mu^{-1} \nabla \times \mathbf{A}, \tag{6}$$

we have the Helmholtz equation for the potential functions:

$$\nabla \times \nabla \times \mathbf{A} + i\omega\mu\sigma \mathbf{A} + \sigma\mu\nabla\phi = \mu \mathbf{J}_{exe}, \tag{7}$$

which is obtained by substituting Eq. 5 into Eq. 4. Also, taking the divergence of Eq. 7 gives us the conservation of charge equation for the potential functions:

$$\nabla \cdot (i\omega\sigma \mathbf{A} + \sigma\nabla\phi) = \nabla \cdot \mathbf{J}_{exe}. \tag{8}$$

In Eq. 8, the distribution of electric charges resulting from EM sources such as grounded electric dipoles is represented by the term $\nabla \cdot \mathbf{J}_{exe}$. It is well known that the ungauged potential equations, Eqs 7, 8, does not provide a unique solution of the pair $(\mathbf{A}, \phi)$, despite that the electric and magnetic fields, which are calculated using Eqs 5 and 6, from solving the potential equations may still be unique (Badea et al., 2001). Here, the Coulomb gauge condition $\nabla \cdot \mathbf{A} = 0$ is applied to Eq. 7 to stabilize the numerical solution (Badea et al., 2001; Long and Farquharson, 2019b). Taking advantage of the vector identity $\nabla \times \nabla \times \mathbf{A} = \nabla(\nabla \cdot \mathbf{A}) - \nabla^2 \mathbf{A}$, the Coulomb-gauged Helmholtz equation for the potential functions becomes

$$-\nabla^2 \mathbf{A} + i\omega\mu\sigma \mathbf{A} + \sigma\mu\nabla\phi = \mu \mathbf{J}_{exe}. \tag{9}$$

Both potential functions, $\mathbf{A}$ and ϕ, are continuous across any conductivity jumps. In fact, the vector potential $\mathbf{A}$ is also *smooth* at conductivity jumps (Long and Farquharson, 2019b). The component-wise form of the pair of Eqs 9, 8 which are discretized here using the RBF-FD meshfree method is

$$-\nabla^2 A_x + i\omega\mu\sigma A_x + \sigma\mu \frac{\partial \phi}{\partial x} = \mu J_x, \tag{10}$$

$$-\nabla^2 A_y + i\omega\mu\sigma A_y + \sigma\mu \frac{\partial \phi}{\partial y} = \mu J_y, \tag{11}$$

$$-\nabla^2 A_z + i\omega\mu\sigma A_z + \sigma\mu \frac{\partial \phi}{\partial z} = \mu J_z, \tag{12}$$

$$i\omega \nabla \cdot (\sigma \mathbf{A}) + \nabla \cdot (\sigma\nabla\phi) = \nabla \cdot \mathbf{J}, \tag{13}$$

for EM data modelling with a general source where $\mathbf{J} = J_x\hat{\mathbf{x}} + J_y\hat{\mathbf{y}} + J_z\hat{\mathbf{z}}$ represents $\mathbf{J}_{exe}$ in previous equations.

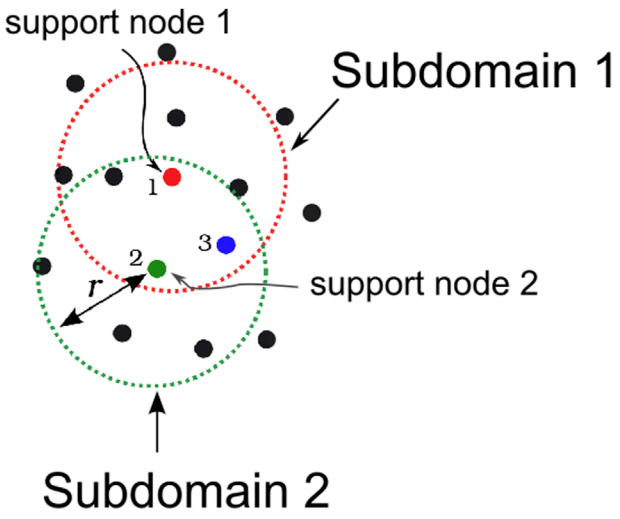

FIGURE 2
Illustration of meshfree subdomains. A subdomain for a point ("node") contains a certain number of points within the chosen distance r from the point. Here, subdomain 1 contains 7 meshfree points (with the support node 1 as the center), and subdomain 2 also contains 7 meshfree points.

2.2 RBF-FD

The description of the RBF-FD meshfree numerical method here follows Long and Farquharson (2017, 2019a,b, 2020, 2024) and references therein. Like mesh-based numerical methods, the first step of the RBF-FD is to locally approximate an unknown function, f, as some simple, rationale functions. In mesh-based finite difference methods, this is often done using Taylor expansions at a point using linear or quadratic functions depending on the finite difference scheme and order (e.g., first-order backward). In mesh-based finite element methods, this is typically done by using low-order polynomial basis functions within an element (i.e., a cell in the mesh). In the meshfree RBF-FD, the unknown function at any point (called *support node*, see Figure 2) is locally approximated as a linear combination of translations of a single *radial basis function* (RBF) using the neighbouring n points in the *subdomain* of that point (Figure 2). Such interpolant $s(\mathbf{r})$ can be written as

$$s(\mathbf{r}) = \sum_{k=1}^{n} R(\|\mathbf{r} - \mathbf{r}_k\|) \cdot c_k, \tag{14}$$

where $\mathbf{r} = (x, y, z)$, $\|\cdot\|$ is the l_2 norm, c_k are the interpolation coefficients, and $\mathbf{r}_k = (x_k, y_k, z_k)$ is the position of the kth point which is also the center of the corresponding RBF $R(\|\mathbf{r} - \mathbf{r}_k\|)$. Note that unlike polynomial functions, a RBF is always radially symmetric around its center (Buhmann, 2003). To determine the interpolation coefficients in Eq. 14, a local linear system of equations resulting from the Lagrange interpolation conditions ($s(\mathbf{r}_i) = f_i$, $i = 1, \ldots, n$, with f_i as the sampled function values at the n points), which can be written as

$$\begin{pmatrix} R(\|\mathbf{r}_1 - \mathbf{r}_1\|) & R(\|\mathbf{r}_1 - \mathbf{r}_2\|) & \cdots & R(\|\mathbf{r}_1 - \mathbf{r}_n\|) \\ R(\|\mathbf{r}_2 - \mathbf{r}_1\|) & R(\|\mathbf{r}_2 - \mathbf{r}_2\|) & \cdots & R(\|\mathbf{r}_2 - \mathbf{r}_n\|) \\ \vdots & \vdots & \ddots & \vdots \\ R(\|\mathbf{r}_n - \mathbf{r}_1\|) & R(\|\mathbf{r}_n - \mathbf{r}_2\|) & \cdots & R(\|\mathbf{r}_n - \mathbf{r}_n\|) \end{pmatrix} \begin{pmatrix} c_1 \\ c_2 \\ \vdots \\ c_n \end{pmatrix} = \begin{pmatrix} f_1 \\ f_2 \\ \vdots \\ f_n \end{pmatrix}, \tag{15}$$

or in a compact matrix form

$$\mathbf{K}\mathbf{c} = \mathbf{f}, \tag{16}$$

needs to be solved. The 3-D RBFs $R(\mathbf{r}, \mathbf{r}_0) = r^5$, $r = \sqrt{(x - x_0)^2 + (y - y_0)^2 + (z - z_0)^2}$ are used in the RBF-FD method for its computational efficiency and robustness in solving the local linear system in Eq. 16 (see detailed discussions in Long and Farquharson, 2019c). It can be proved that using the RBF, the symmetric matrix $\mathbf{K}$ is always invertible as long as the local points are distinct (Fasshauer, 2007). This flexibility of point locations allows for arbitrary point distributions to be used which will be important in representing complex geometries in an Earth model. In practice, Eq. 15 is enriched with additional low-order polynomials to avoid numerical singularity in case the positions of meshfree points in a subdomain become too extreme (e.g., colinear, see Long and Farquharson, 2019c).

Using the above meshfree interpolant, any differential operator $\mathbf{D}$ (e.g., ∇^2 in Eq. 10) can be discretized over the meshfree subdomains in the form of a linear combination of n local function values, a process that is similar to the traditional mesh-based finite difference approximation but in a more general treatment: $\mathbf{D}f|_{\mathbf{r}_i} \approx \sum_{k=1}^{n} b_k f_k$. In RBF-FDs, the discretization of the operator $\mathbf{D}$ is multi-dimensional, while in the classical mesh-based finite differences the discretization of $\mathbf{D}$ is restricted to be directional approximation (i.e., only 1-D). The weights, b_k, are then obtained by solving the following $n \times n$ local linear system

$$\begin{pmatrix} R(\|\mathbf{r}_1 - \mathbf{r}_1\|) & R(\|\mathbf{r}_1 - \mathbf{r}_2\|) & \cdots & R(\|\mathbf{r}_1 - \mathbf{r}_n\|) \\ R(\|\mathbf{r}_2 - \mathbf{r}_1\|) & R(\|\mathbf{r}_2 - \mathbf{r}_2\|) & \cdots & R(\|\mathbf{r}_2 - \mathbf{r}_n\|) \\ \vdots & \vdots & \ddots & \vdots \\ R(\|\mathbf{r}_n - \mathbf{r}_1\|) & R(\|\mathbf{r}_n - \mathbf{r}_2\|) & \cdots & R(\|\mathbf{r}_n - \mathbf{r}_n\|) \end{pmatrix} \begin{pmatrix} b_1 \\ b_2 \\ \vdots \\ b_n \end{pmatrix} = \begin{pmatrix} \mathbf{D}R_1(\mathbf{r})|_{\mathbf{r}_i} \\ \mathbf{D}R_2(\mathbf{r})|_{\mathbf{r}_i} \\ \vdots \\ \mathbf{D}R_n(\mathbf{r})|_{\mathbf{r}_i} \end{pmatrix}, \tag{17}$$

and form as the nonzeros in the corresponding rows of the coefficient matrix $\mathbf{A}$ in the resultant $N \times N$ global linear system $\mathbf{A}\mathbf{x} = \mathbf{h}$ (N is the total number of points). Here, $\mathbf{D}R_1(\mathbf{r})|_{\mathbf{r}_i}$ denotes the value of $\mathbf{D}R_1(\mathbf{r})$ at the location $\mathbf{r}_i$ and can be readily calculated using the chain rules of the derivatives for the chosen RBF. $\mathbf{x}$ is the vector of the unknown function values at the degrees of freedom (i.e., meshfree

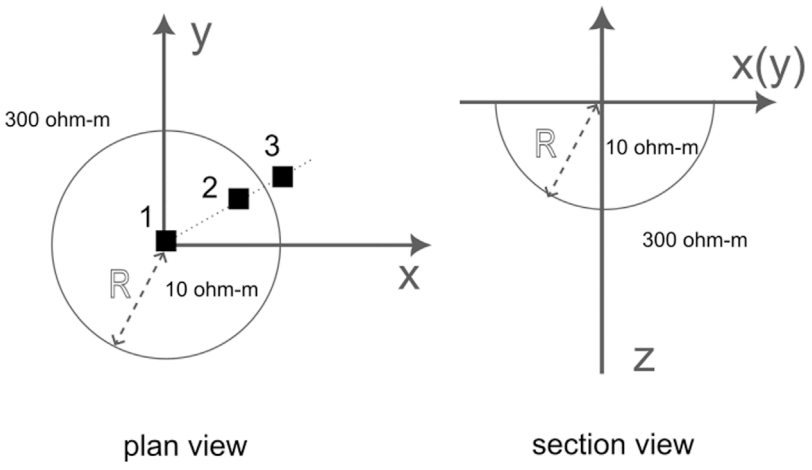

FIGURE 3
Schematic illustration of the Dublin Test Model 2 (DTM2). Three MT sites at the surface are marked with black squares (at R = 0, 4,500 m, 5,100 m from the origin, respectively) in the plan view (left). The radius of the hemisphere conductor is R = 5000 m.

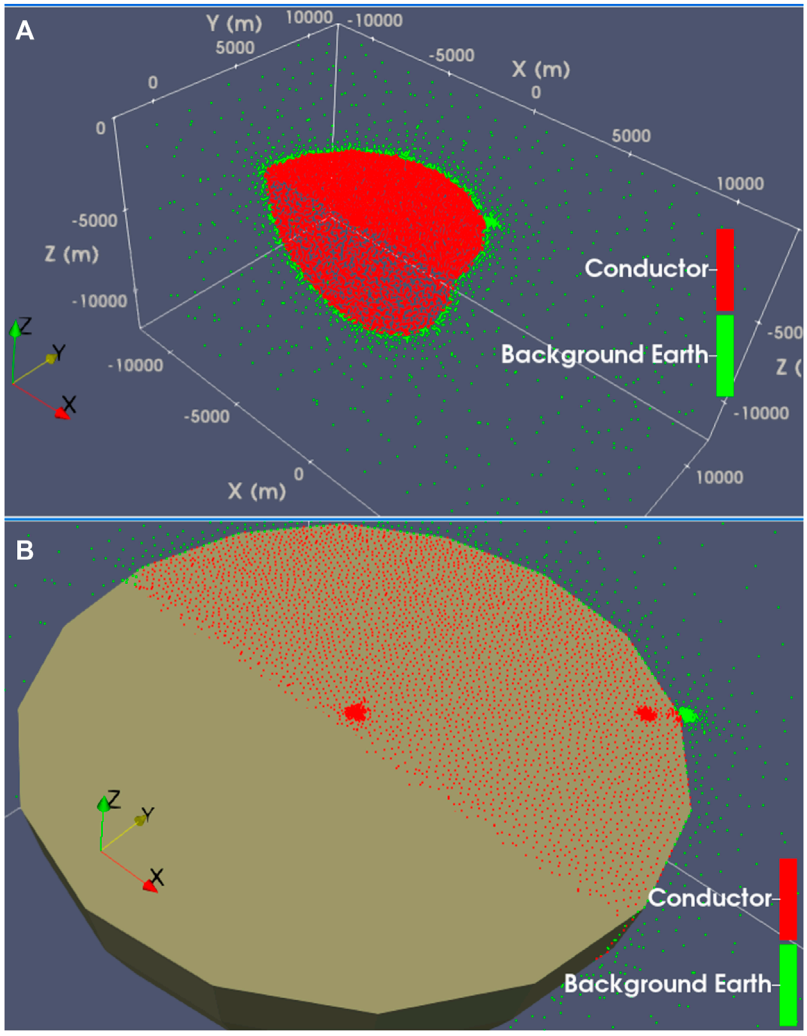

FIGURE 4
Perspective 3-D views of the meshfree point discretization of the Dublin Test Model 2 (DTM2). In Panel **(A)**: unstructured points inside the conductor. In Panel **(B)**: 3 MT sites at the surface (at $R =$ 0, 4,500 m, 5,100 m from the origin, respectively) are shown with dense points due to local refinements, and the 3-D hemisphere conductor in the original model is represented by a multi-facet polyhedron.

points in the RBF-FD). The proof of Eq. 17 is thoroughly presented in Long and Farquharson (2019b). The right-hand-side vector $\mathbf{h}$ is formed from proper boundary conditions and the discretizations of EM source terms. Note that only Eq. 17 needs to be solved in transforming the differential equations (Eq. 10 to Eq. 13) into linear systems of equations. The well-known numerical analysis package LAPACK subroutines were used to numerically solve Eq. 17. In this study, all meshfree points are unstrutured and the size of meshfree subdomains is fixed as $n = 30$ (the number of points in a meshfree subdomain) and the selection of the closest $n = 30$ points for each subdomain is carried out using a kd-tree point selection method which is the same as in Long and Farquharson (2019b). The fixed number of points in subdomains means that the relative distances among the n points in a meshfree subdomain can be smaller (e.g., near CSEM sources) when high numerical accuracies are needed.

3 Numerical results

In this section, the modellings of different EM data using the meshfree method are demonstrated. The global linear system from discretizing the $\mathbf{A}$-ϕ potential function equations is asymmetric, complex-valued and can be solved using either iterative solvers or direct solvers. In this study, all global linear systems are solved using the MUMPS direct solver (Amestoy et al., 2001, version 5.3.3).

3.1 Magnetotelluric data

The magnetotelluric (MT) conductivity model for the demonstration of the meshfree modelling is the Dublin Test Model 2 (DTM2, Miensopust et al., 2013) in which a hemispherical conductor is buried at the top of the subsurface (Figure 3).

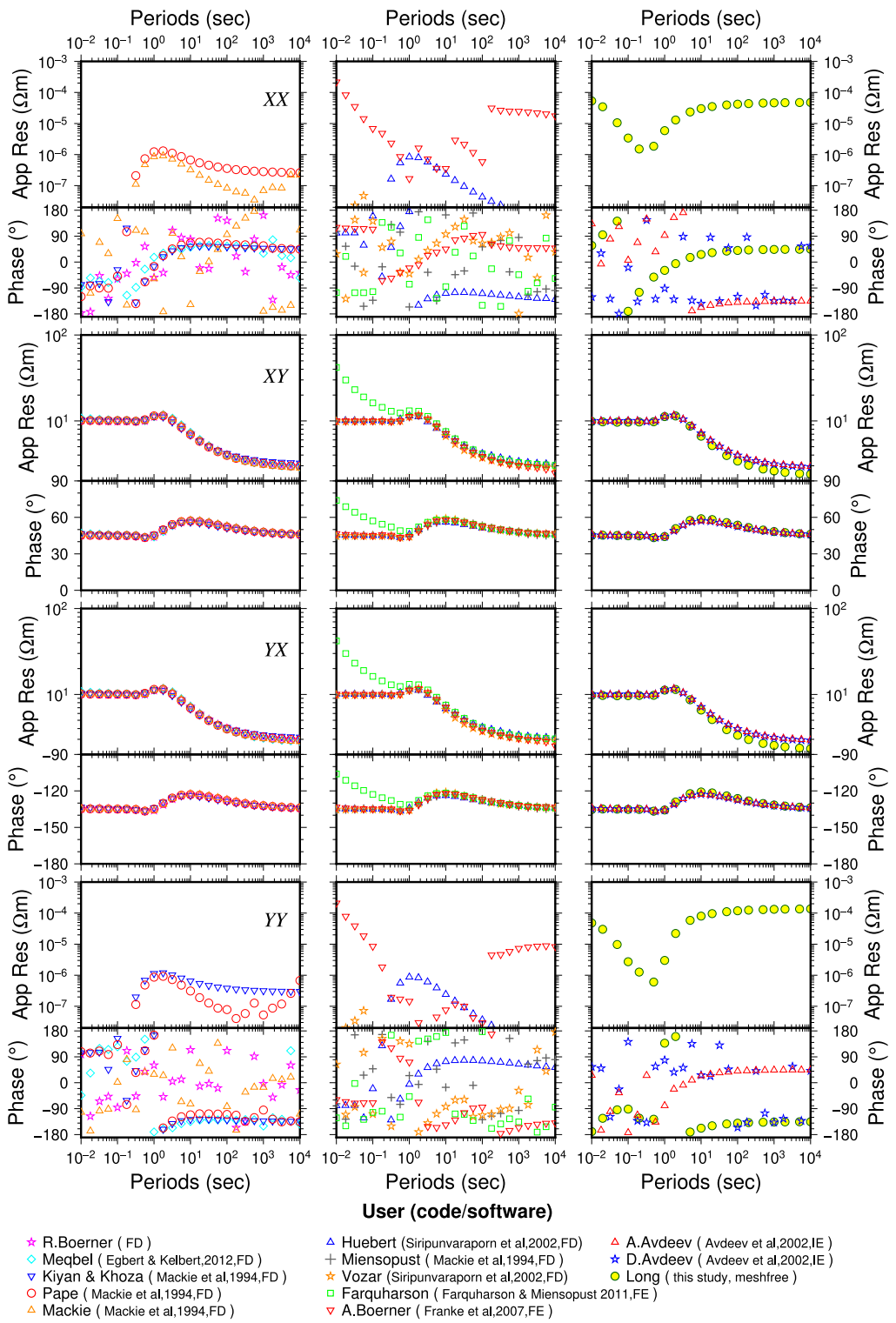

FIGURE 5
Comparison of the meshfree solution and other solutions for the Site-1 (origin) MT responses for DTM2. From top to bottom are XX, XY, YX, and YY components of the impedance tensor. Different users or runners of the used modelling codes are shown in the legend with algorithm acronyms as FD (finite difference), FE (finite element) and, IE (integral equation).

The hemispherical conductor has the resistivity of 10 Ωm and the background earth's resistivity is 300 Ωm. The radius of the hemisphere is $R = 5$ km. Because of the perfect symmetry of the conductivity structure, there exists analytical solutions of MT responses at the galvanic limit (i.e., zero-frequency limit). For the same reason, the observed MT responses will be symmetric. These

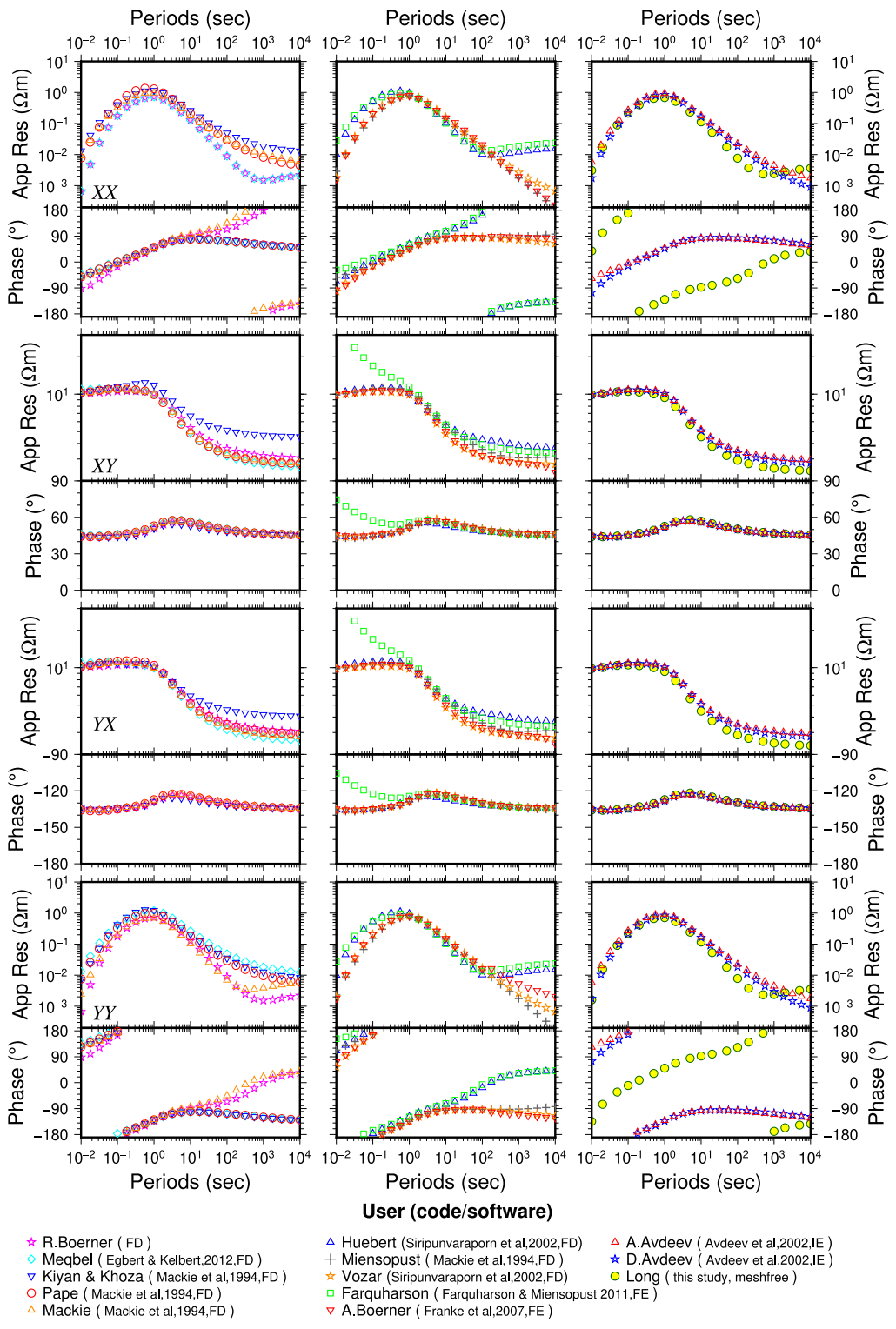

FIGURE 6
Comparison of the meshfree solution and other solutions for the Site-2 ($R = 4500$ m) MT responses for DTM2. From top to bottom are XX, XY, YX, and YY components of the impedance tensor. Different users or runners of the used modelling codes are shown in the legend with algorithm acronyms as FD (finite difference), FE (finite element) and, IE (integral equation).

features of this model make it a good example for the comparison of different numerical modelling algorithms (Miensopust et al., 2013). However, also due to the spherical surface geometry of the conductor, mesh-based modelling techniques, particularly those relying on tensor-grid or rectilinear meshes, will face challenges in accurately representing the geometry, and therefore in

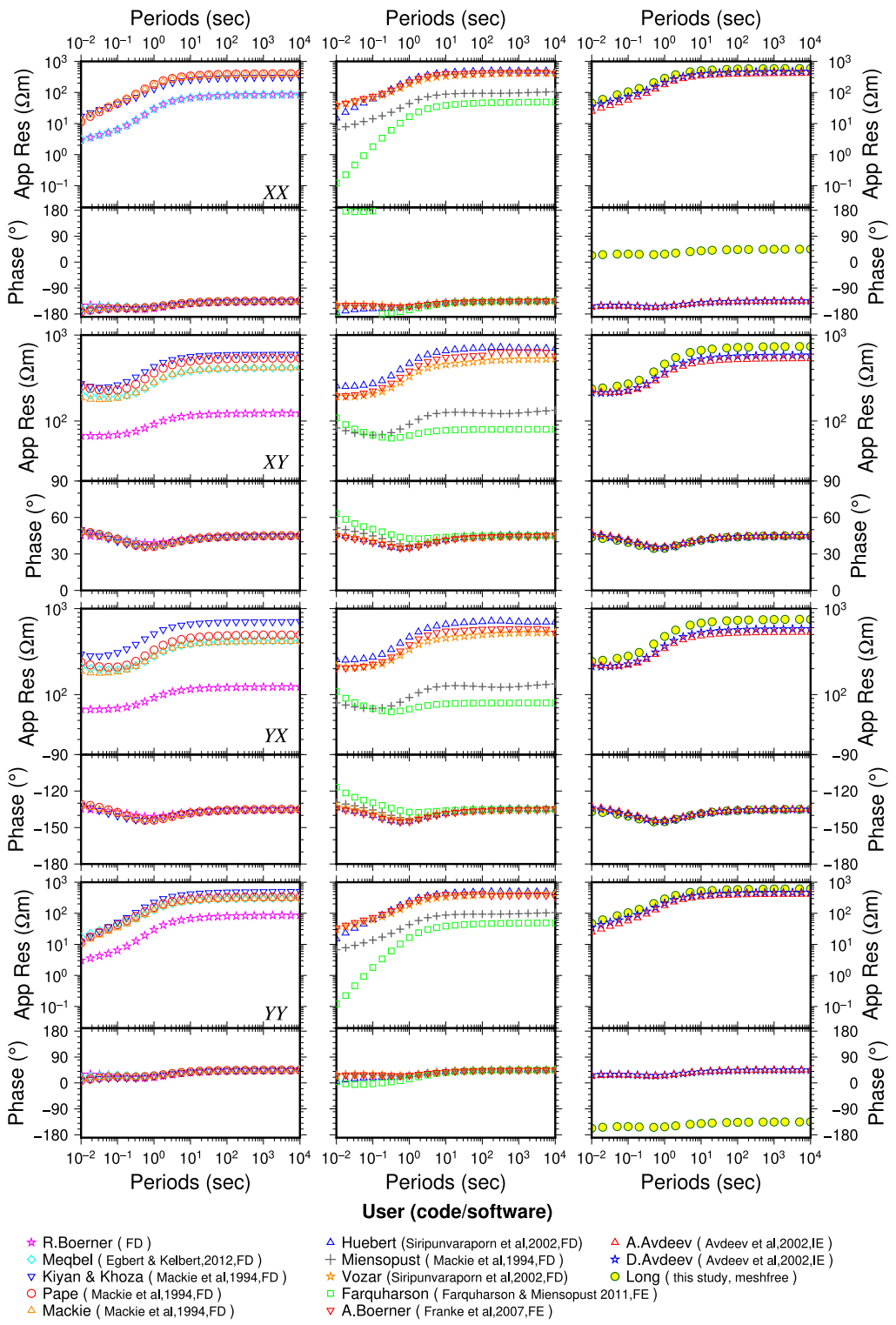

FIGURE 7
Comparison of the meshfree solution and other solutions for the Site-3 ($R = 5100$ m) MT responses for DTM2. From top to bottom are XX, XY, YX, and YY components of the impedance tensor. Different users or runners of the used modelling codes are shown in the legend with algorithm acronyms as FD (finite difference), FE (finite element) and, IE (integral equation).

studying the effects of shallow inhomogeneities of the conductivity distribution on the MT data at sites near the edge of the conductor.

In MT data modellings, the EM source terms in Eqs 10–13, i.e., $\mathbf{J}$ and its divergence, vanish as the actual EM sources are far away from the surface of the Earth (Long and Farquharson, 2019b). In this

model, the boundary conductivity distribution is that of the uniform subsurface and 1-D boundary conditions were used to compute boundary values (see details in Long and Farquharson, 2019b). The EM responses in the MT scenario are typically represented using apparent resistivity and phase data which are calculated from the electric and magnetic fields at the measurement locations. Although the previous study using the RBF-FD method (Long and Farquharson, 2019b) has demonstrated the effectiveness of the modelling capability, particularly how the discontinuous electric field can be correctly modelled using the developed RBF-FD method here, it does not demonstrate the flexible meshfree discretization of highly irregular surface geometries as we see in the DTM2 here. The unstructured point discretization with local refinements for this model is shown in Figure 4. The total number of points in the discretization is $N = 165,940$ for a computational domain of $\{(x,y,z)| -30\text{km} \le x,y \le 30\text{km}, -50\text{km} \le z \le 10\text{km}\}$.

Three MT sites (Figure 3) are designed here to examine the modelling accuracy of the meshfree method. Site 1 is at the origin of the coordinate system and at the center of the hemisphere conductor. Site 2 ($R = 4500$ m; $x = y = 3182$ m) is 500 m away from the edge of the hemisphere and is inside the hemisphere (same as Site 10 in Miensopust et al. (2013)). Site 3 ($R = 5100$ m; $x = y = 3606$ m) is 100 m away from the edge of and outside the hemisphere (same as Site 18 in Miensopust et al. (2013)). MT responses at Site 2 and 3 are expected to be significantly affected by the irregular shape of the hemisphere for long periods. Same as Miensopust et al. (2013), the frequency range of 10^{-4} Hz to 100 Hz (periods from 0.01 s to 10,000 s) were used for the examination. The calculated MT responses at the three sites using the meshfree RBF-FD method were compared with other independent solutions (all using mesh-based modelling methods) that are documented from Miensopust et al. (2013) and are shown in Figures 5–7 for the three sites. At each site, the apparent resistivity and phase data for the four components of the impedance tensor (i.e., Z_{XX}, Z_{XY}, Z_{YX} and Z_{YY}) are plotted from top to bottom.

At Site 1 (Figure 5), which is at the origin of the model, the theoretical apparent resistivity of the MT responses for Z_{XX} and Z_{YY} are zero, which explains the extremely small and random numerical values of the apparent resistivity and phase data observed for all numerical solutions. For the off-diagonal components Z_{XY} and Z_{YX}, almost all numerical solutions agree with each other. At Site 2 (Figure 6) and Site 3 (Figure 7), all four components of the impedance tensor will be non-zero due to the edge effect of the conductor. For the phase data in the Z_{XX} and Z_{YY} components at these two sites, the meshfree solution appears to deviate from other solutions; this is because of the difference in the Coordinate systems being used and the phase angle calculation methods.[1] The meshfree numerical solutions are validated by the following two observations: the symmetry in the solution (MT responses for Z_{XX} and Z_{YY} are the same, so are the Z_{XY} and Z_{YX}) and the good agreement with the majority of other independent solutions. Note that among those independent solutions, a few solutions (e.g., Kiyan and Khoza) have a clear deviation from the main MT response curves in long periods (after 10 s for Site 2) due to insufficient mesh discretizations around the edge of the hemisphere conductor.

3.2 Frequency-domain controlled-source EM data

To compute the controlled-source EM (CSEM) responses, the external source terms in Eqs 10–13 (**J** and its divergence) will be non-zero at the locations of the source. Here, in the context of the

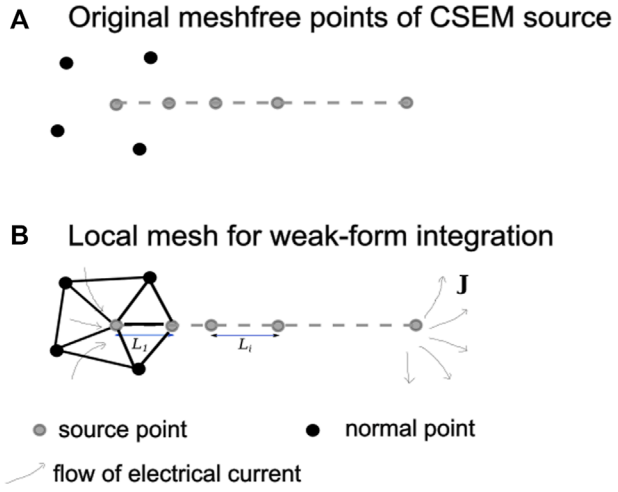

FIGURE 8
Schematic illustration of meshfree point representation of CSEM source wires. Panel **(A)**: the grounded wire is represented by 5 special points designated as source points. Panel **(B)**: for each source point, a local unstructured mesh is formed using the point (left-most source point here) and its neighbouring points.

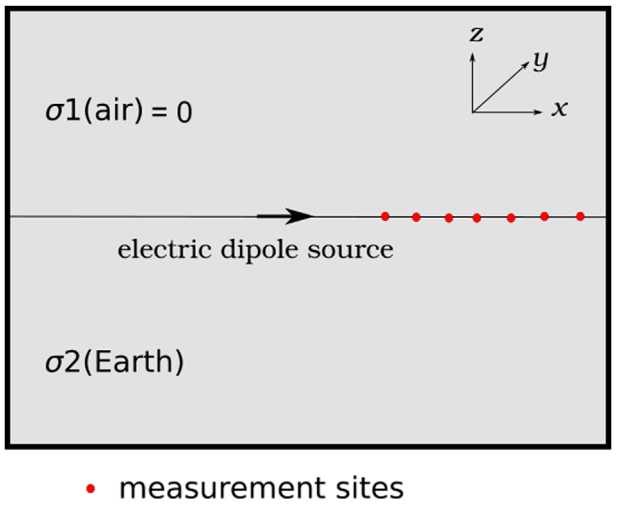

FIGURE 9
A half-space conductivity model with the horizontal electric dipole source (black arrow) at the top of the subsurface. Adapted from Long and Farquharson (2019a).

1 The solutions provided from Miensopust et al. (2013) only have the computed phase angles, rather than the impedance values themselves

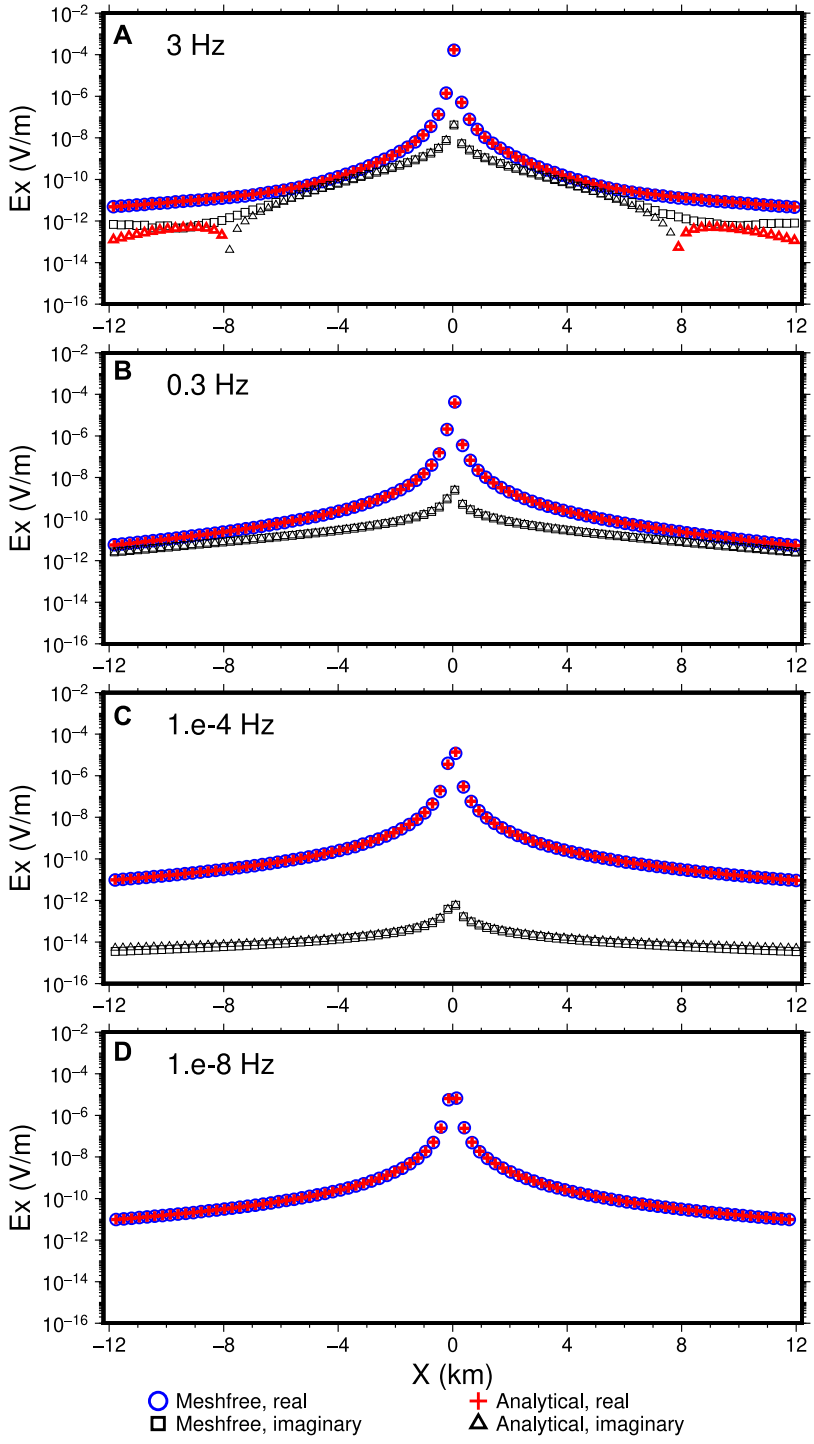

FIGURE 10
Comparison between the meshfree and the analytical solutions. From **(A–D)**, each panel shows the real and imaginary parts of E_x of the two solutions at a different frequency. All real part values are positive. The imaginary part values are all negative values except for bold, colored symbols (as the imaginary analytical solution at $f = 3$ Hz shows). In panel **(D)**, the imaginary E_x values are outside the range and are not shown.

meshfree RBF-FD method, the source handling method of Long and Farquharson (2019a) is used. As shown in Figure 8, any CSEM source wire is initially represented by meshfree points in space with proper distances and regularity of distribution among them. For each point representing the source wire, a local unstructured mesh is contructed by connecting the points found in the subdomain of the point. Then a finite element-like weak-form treatment (e.g., Badea et al., 2001; Jin, 2014) is used to discretize the equations

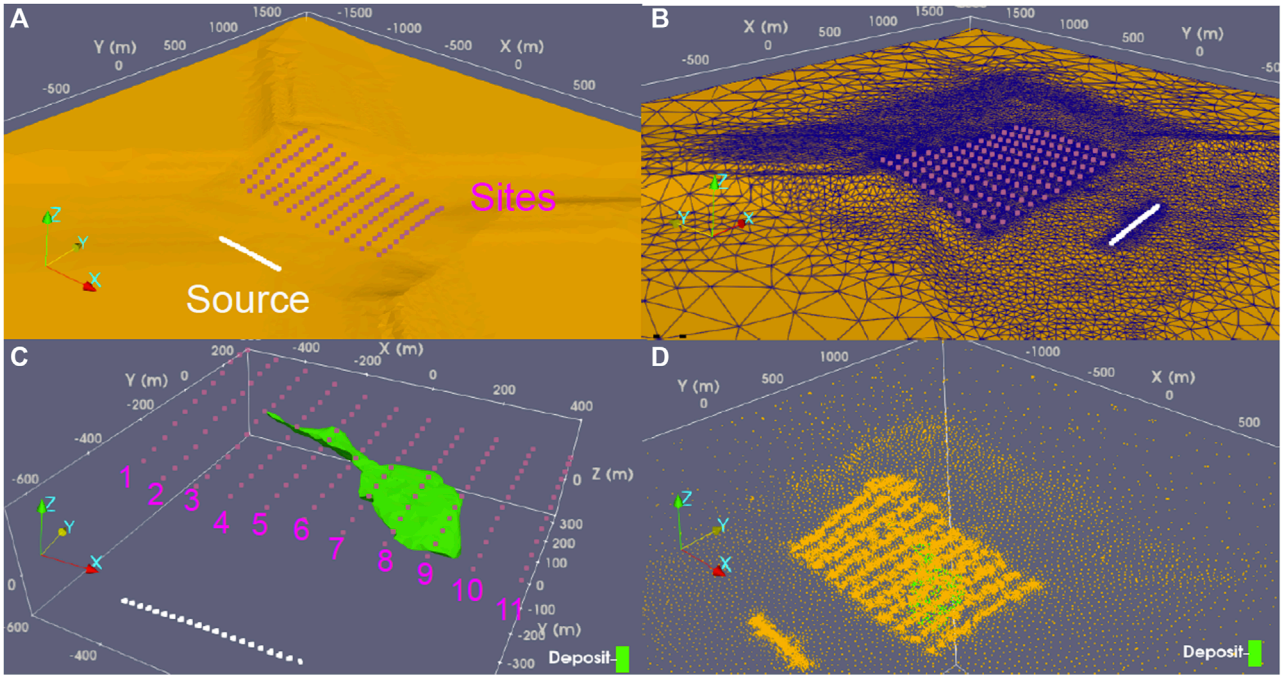

FIGURE 11
3-D views of the CSEM configuration of the Ovoid deposit model. Panels **(A)** and **(B)**: two different views of the grounded wire source (white dots) and the CSEM measurement sites (purple dots) overlaying the Earth's surface with topography. Panel **(C)**: the geometry of the Ovoid mineral deposit in the subsurface and the 11 profiles of measurement sites numbered from 1 ($x = -600$ m) to 11 ($x = 400$ m) from west to east. Panel **(D)**: meshfree point discretization of the subsurface when viewed from the air, with the CSEM source and site locations locally refined.

at the source point in which the electrical current of the wire will be coincident with the edges of the local mesh which is of tetrahedral type in this study. The number of nodes in this local mesh is very small ($\leq = n = 30$) and the mesh connectivity is generated automatically using common mesh generation software (e.g., Tetgen and Gmsh). For grounded wires, the divergence of the current density is only non-zero at the beginning and the ending source points.

The above method is capable of treating an arbitrarily shaped controlled source (grounded wires or current loops) in the point discretization of an Earth model. Because of this capability, the total-field approach of modelling the EM data, as described in Eqs 10–13 in the case of potential functions, is being used here and will provide more flexibility in handling complex topography and surface geometries. Under the total-field approach, the boundary values of the EM field on the computational domain is zero.

3.2.1 Half-space model

The first CSEM test model is that of a uniform subsurface with an electric dipole source at the Earth's surface (Figure 9). Although the model is relatively ideal, analytical solutions exist for the EM fields at the surface which allows for a first-step examination of the accuracy of the developed RBF-FD meshfree method for CSEM data modellings. An x-directed electric dipole, for example, will have the current density $\mathbf{J}_s$ as (Ward and Hohmann, 1988)

$$\mathbf{J}_s = I_0 \left[\mathcal{H}(x_1) - \mathcal{H}(x_2)\right] \delta(y - y_0)\, \delta(z - z_0)\, \hat{\mathbf{x}}, \tag{18}$$

where I_0 is the current intensity, $\mathcal{H}(x)$ is Heaviside function, (x_1, y_0, z_0) and (x_2, y_0, z_0) are the two ends of the grounded wire, and δ is the Dirac delta function. The closed-form, analytical formula (eq. 4.159 in Ward and Hohmann, 1988) for computing the inline electric field due to the above CSEM transmitter (Eq. 18) for any measurement locations at the surface of the subsurface (i.e., at $z = 0$) is:

$$E_x(x, y) = \frac{I_0 \mathrm{d}s}{2\pi\sigma\rho^3}\left[1 + (ik\rho + 1)\, e^{-ik\rho} - \frac{3y^2}{\rho^2}\right], \tag{19}$$

where $\rho = \sqrt{x^2 + y^2}$, $k = -i\omega\mu\sigma$ is the wavenumber with σ as the conductivity of the subsurface. In the case of dipole sources where the length of the grounded wire approaches infinitesimally small in relative to the distance from the dipole to measurement locations, $ds = 1$in Eq. 19.

The current density of the electric dipole source is set to be 1 A. For the meshfree solution, a set of unstructured points with local refinements around the dipole source was used. The actual CSEM source in the meshfree modelling is 1 m in length along the x direction and is represented by six points with the equal spacing of 0.2 m from $x = -0.5$ m to $x = 0.5$ m. Four frequencies at $f = 3, 0.3, 10^{-4}$ and 10^{-8} Hz were used for the accuracy examination. The uniform Earth's subsurface has the conductivity of 0.02 S/m. With this conductivity value, the very low frequency of 10^{-8} Hz will approach the direct current limit and the electric field responses will approach those of a direct current resistivity survey. The total number of the points for the

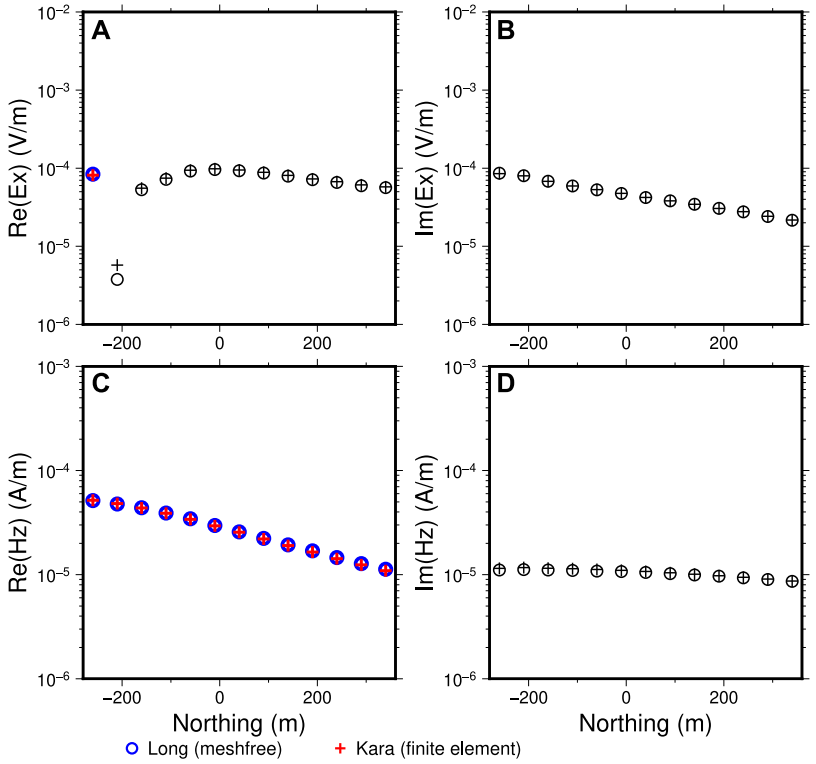

FIGURE 12
Computed E_x and H_z components of the CSEM responses at $f = 500$ Hz over the Ovoid model at the site profile $x = 400$ m (Profile 11 in Figure 11 (c)). Panels **(A)** and **(B)**: real and imaginary parts of E_x, respectively. Panels **(C)** and **(D)**: real and imaginary parts of H_z, respectively. Bold, colored symbols indicate positive values; thin, black symbols represent negative values.

model discretization is 81,951 which are distributed within the computational domain $\{(x,y,z)| -40\text{km} \le x,y,z \le 40\text{km}\}$ where the dipole is located at the center. The computed E_x responses at the surface $(y = z = 0)$ are shown in Figure 10. As evident from the comparison, the two solutions have an excellent agreement with each other, demonstrating the computational accuracy of the meshfree method. At the highest frequency $f = 3$ Hz (Figure 10A), the imaginary E_x from the meshfree numerical solution starts to deviate from the theoretical solution when $\|x\| \ge 7$ km. This deviation is due to the decreased point density after the distance. At lower frequencies, such deviation vanishes due to less rapid changes of the EM field at the same locations. In addition, when the frequency approaches the direct current limit (Figure 10C,D), the frequency-domain E_x response has the real part almost unchanged but the imaginary part continuously decreased until zero; that is, E_x response is approaching the direct current resistivity response, which is another evidence of the correct modelling of the CSEM responses.

3.2.2 Ovoid mineral deposit model

The second CSEM test example is from the volcanic massive sulphide mineral deposit (termed as Ovoid deposit here) from Voisey's Bay, Labrador, Canada, which has been under extensive studies for both geology and geophysical data modelling studies (e.g., Jahandari and Farquharson, 2014; Li J. et al., 2017; Long and Farquharson, 2019c; Kara and Farquharson, 2023). The Ovoid deposit is a highly conductive iron-dominant deposit with complex surface geometry which serves as a perfect testing example for geophysical data modelling software. To test the meshfree modelling method developed here, the real topography of the Earth's surface (also see Jahandari and Farquharson, 2014; Kara and Farquharson, 2023) has been used here. The nearest point of the deposit to the surface is about 70 m below the uneven surface (see Figure 11). Following Kara and Farquharson (2023), a grounded wire of 400 m long with a current density of 1 A along the easting direction (Figure 11A,B) is used as the source for a ground EM survey. The offset of the wire source is roughly 600 m away from the central part of the deposit. There are 143 measurement sites at the surface designed as receiver locations which are distributed evenly along 11 South-to-North profiles (Figure 11C). The profile spacing is 100 m. The site spacing along each profile is approximately 50 m. The highly conductive deposit is assumed to have a uniform conductivity of 1 S/m here and the relatively resistive background earth is assigned the conductivity of 0.001 S/m. Both conductivity values are taken from the previous test model of Kara and Farquharson (2023) for facilitating a direct comparison of the meshfree modelling results with theirs.

For the model discretization, the meshfree points used here are also directly taken from the point distribution from the tetrahedral mesh used by Kara and Farquharson (2023) which are visualized

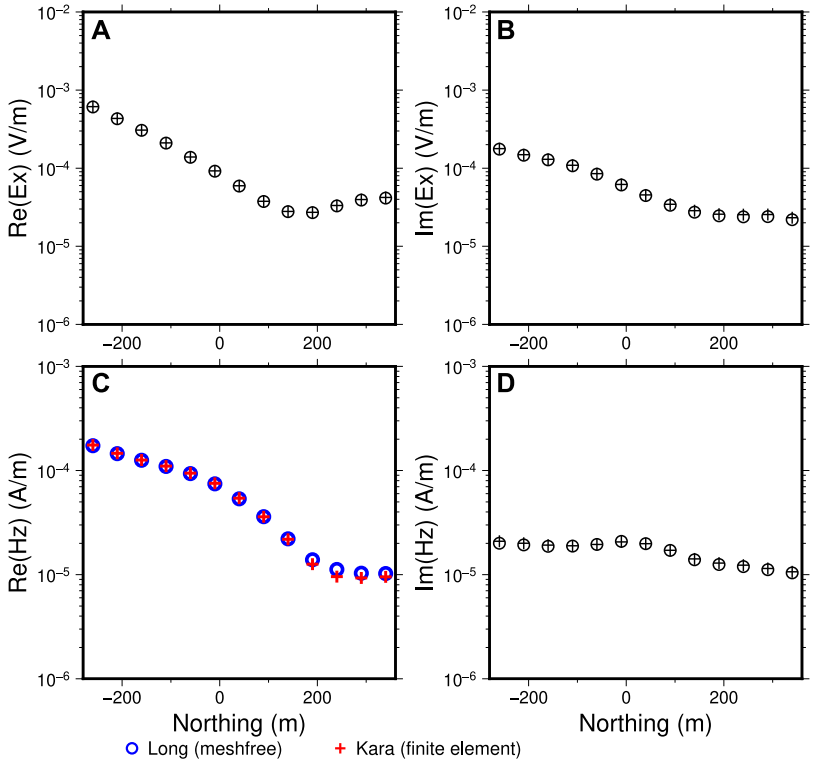

FIGURE 13
Computed E_x and H_z components of the CSEM responses at $f = 500$ Hz over the Ovoid model at the site profile $x = 0$ m (Profile 7 in Figure 11C). Panels **(A)** and **(B)**: real and imaginary parts of E_x, respectively. Panels **(C)** and **(D)**: real and imaginary parts of H_z, respectively. Bold, colored symbols indicate positive values; thin, black symbols represent negative values.

in Figure 11D. In their modelling, they have used a vector finite element method for computing the CSEM responses. For both finite element methods and meshfree methods, the local refinements around the transmitter and the receiver locations are necessary to improve the numerical modelling accuracy. The 400-m long grounded wire is represented in the meshfree method using 80 points located at the topographic surface with in average 5 m of distance apart from each other (see Figure 8). The total number of points for this discretization is 44,230 within the computational domain of $\{(x,y,z)|-20\text{km} \le x,y,z \le 20\text{km}\}$. For long grounded wire sources, the inline electric field and vertical magnetic field components are often the main measurements. The computed E_x and H_z responses using the meshfree method are compared with the finite element results of Kara and Farquharson (2023) which are shown in Figures 12–14 at the measurement site profiles $x = 400, 0, -200$ m (also see Figure 11C), respectively, for the frequency of 500 Hz. It is seen that the two independent solutions, calculated using the same model discretization (i.e., meshfree points and tetrahedral mesh), have a very good agreement with each other for all sites (see supplemental materials for the comparison for the remaining profiles). The strong EM induction caused by the deposit is well reflected at the sites that are more closely above the deposit (see the profiles $x = -200$ m and $x = 0$ m). The higher frequency (i.e., $f = 1500$ Hz) responses for the profile $x = -200$ (Profile 5) is also shown in Figure 15. Comparing Figure 15 with Figure 14, it is seen that at the higher frequency, the EM responses, particularly H_z responses, attenuate faster in space.

4 Discussions

Direct current resistivity (DCR) survey methods are also frequently used for mineral resource exploration. Although I have not directly shown the modelling capability of the meshfree method for DCR data modelling, the first CSEM modelling example (in the case of $freq \to 0$) is essentially a simple demonstration of how the developed meshfree modelling approach can be directly applied to compute DCR data for a general conductivity model. When the frequency is zero, the potential function equations described in Eqs 10–13 will be reduced to the exact potential function equation (i.e., Poisson's equation for ϕ) used for DCR data computation.

For model discretization, the unstructured meshfree points were generated using a combination of existing open-source software tools (including Tetgen and Paraview). The geophysical community is likely to continue to benefit from research in other fields. In the situation of dedicated software development for meshfree point generation, there have been significant research and development in the past decade (Fornberg and Flyer, 2015). It is anticipated that, like the history of the classical finite element methods, more open-source

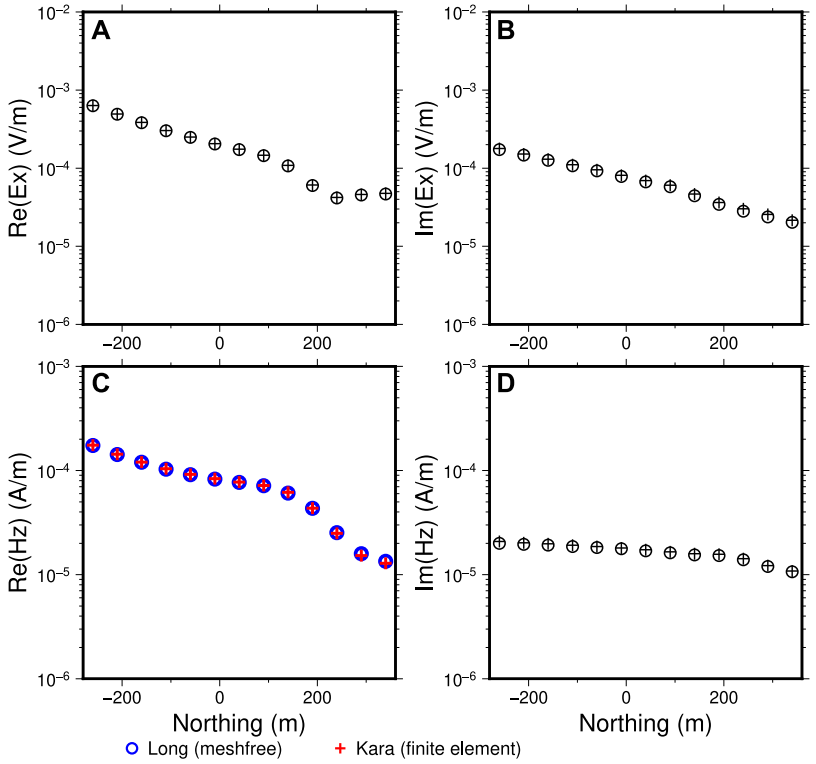

FIGURE 14
Computed E_x and H_z components of the CSEM responses at $f = 500$ Hz over the Ovoid model at the site profile $x = -200$ m (Profile 5 in Figure 11C). Panels **(A)** and **(B)**: real and imaginary parts of E_x, respectively. Panels **(C)** and **(D)**: real and imaginary parts of H_z, respectively. Bold, colored symbols indicate positive values; thin, black symbols represent negative values.

point generation tools will be available once the meshfree methods along with their capability of incorporating complex geometries become more widely known.

5 Conclusion

Earth models in the context of mineral resource exploration using geophysical survey methods often have rather complex surface geometries. It is important that the numerical forward modelling of geophysical EM data for such models is capable of efficiently handling these geometries. A meshfree modelling method that uses only unconnected points, instead of the traditional pixel cell-based meshes, to represent geometries has been developed and presented here. The $\mathbf{A}$-ϕ potential equations instead of the Helmholtz equation for the electric field are used for the continuity property of the potential functions. The meshfree method supports both uniform and non-uniform, unstructured point distributions with the latter being of particularly advantageous in discretizing Earth models with complex geometries with a minimal amount of points.

The modelling accuracy and the capability of handling highly irregular surface geometries of the method are demonstrated using three EM modelling examples. The first example is a magnetotelluric model in which the magnetotelluric impedance responses of a hemisphere-shaped near-surface conductor were modelled. The second example is an idealized half-space conductivity model excited with a grounded electric dipole source for which closed-form analytical solutions exist. The third example, which is also a controlled-source example, is the real-life highly conductive Ovoid mineral deposit model in which the realistic surface geometry of the deposit and the topography were used. The EM transmitter for this example is a 400 m long grounded wire. Through these examples, the feasibility of easily representing irregular surface geometries of the Earth models is clearly demonstrated. The point discretizations are considered to be more advantageous over traditional mesh discretizations for complex Earth models as they are easier to generate and manipulate. For all examples, the modelling accuracies of the meshfree method are verified using other independent numerical solutions or analytical solutions.

The demonstrated meshfree modelling method is also applicable to other geophysical data modellings in which numerical solutions and complex geometries of the model are important. The developed meshfree method for geophysical EM data modellings is shown to be effective for both natural-source magnetotelluric surveys and controlled-source EM surveys. For the magnetotelluric example, the meshing of the spherical surface geometry is a non-trivial task, especially for numerical methods that are restricted to the use of rectilinear meshes, as evident from the large differences

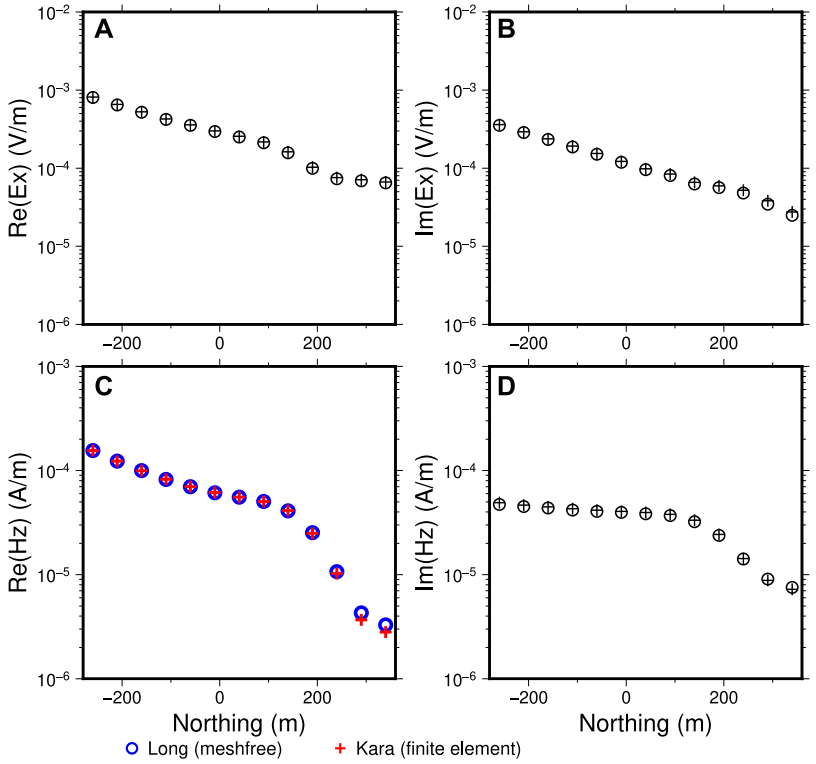

FIGURE 15
Same CSEM responses as in Figure 14 but at $f = 1500$ Hz. Panels **(A,B)**: real and imaginary parts of Ex, respectively. Panels **(C,D)**: real and imaginary parts of Hz, respectively. Bold, colored symbols indicate positive values; thin, black symbols represent negative values.

of modelled magnetotelluric responses among some independent solutions (Miensopust et al., 2013). The representation of such geometry is however quite straightforward and easy in the meshfree point discretization.

Data availability statement

The raw data supporting the conclusions of this article will be made available by the authors, without undue reservation.

Author contributions

JL: Conceptualization, Data curation, Investigation, Methodology, Software, Writing–original draft, Writing–review and editing.

Funding

The author(s) declare that no financial support was received for the research, authorship, and/or publication of this article.

Acknowledgments

Kara and Farquharson are thanked for graciously providing the mesh data to build the Ovoid deposit model discretization and for sharing their finite element solutions to compare with in this study.

Conflict of interest

The author declares that the research was conducted in the absence of any commercial or financial relationships that could be construed as a potential conflict of interest.

Publisher's note

References

Amestoy, P., Duff, I. S., Koster, J., and L'Excellent, J.-Y. (2001). A fully asynchronous multifrontal solver using distributed dynamic scheduling. *SIAM J. Matrix Analysis Appl.* 23, 15–41. doi:10.1137/s0895479899358194

Ansari, S., and Farquharson, C. G. (2014). 3D finite-element forward modeling of electromagnetic data using vector and scalar potentials and unstructured grids. *Geophysics* 79, E149–E165. doi:10.1190/geo2013-0172.1

Badea, E. a., Everett, M. E., Newman, G. a., and Biro, O. (2001). Finite-element analysis of controlled-source electromagnetic induction using Coulomb-gauged potentials. *Geophysics* 66, 786–799. doi:10.1190/1.1444968

Buhmann, M. D. (2003). *Radial basis functions*. Cambridge: Cambridge University Press. doi:10.1017/CBO9780511543241

Chen, C., Kruglyakov, M., and Kuvshinov, A. (2021). Advanced three-dimensional electromagnetic modelling using a nested integral equation approach. *Geophys. J. Int.* 226, 114–130. doi:10.1093/gji/ggab072

Chen, J.-S., Hillman, M., and Chi, S.-W. (2017). Meshfree methods: progress made after 20 years. *J. Eng. Mech.* 143, 04017001. doi:10.1061/(asce)em.1943-7889.0001176

Coggon, J. H. (1971). Electromagnetic and electrical modeling by the finite element method. *Geophysics* 36, 132–155. doi:10.1190/1.1440151

Du, Q., Gunzburger, M., and Ju, L. (2002). Meshfree, probabilistic determination of point sets and support regions for meshless computing. *Comput. methods Appl. Mech. Eng.* 191, 1349–1366. doi:10.1016/s0045-7825(01)00327-9

Du, Q., Wang, D., and Zhu, L. (2009). On mesh geometry and stiffness matrix conditioning for general finite element spaces. *SIAM J. Numer. Analysis* 47, 1421–1444. doi:10.1137/080718486

Dyck, A. V., and West, G. F. (1984). The role of simple computer models in interpretations of wide-band, drill-hole electromagnetic surveys in mineral exploration. *Geophysics* 49, 957–980. doi:10.1190/1.1441741

Fabri, A., Giezeman, G.-J., Kettner, L., Schirra, S., and Schönherr, S. (2000). On the design of CGAL a computational geometry algorithms library. *Softw. Pract. Exp.* 30, 1167–1202. doi:10.1002/1097-024x(200009)30:11<1167::aid-spe337>3.0.co;2-b

Farquharson, C. G., and Craven, J. A. (2009). Three-dimensional inversion of magnetotelluric data for mineral exploration: an example from the McArthur River uranium deposit, Saskatchewan, Canada. *J. Appl. Geophys.* 68, 450–458. doi:10.1016/j.jappgeo.2008.02.002

Farquharson, C. G., and Oldenburg, D. W. (2002). An integral equation solution to the geophysical electromagnetic forward-modelling problem. *Methods Geochem. Geophys. (Elsevier)* 35, 3–19. doi:10.1016/S0076-6895(02)80083-X

Fasshauer, G. E. (2007). Meshfree approximation methods with matlab, vol. 6 of *Interdiscip. Math. Sci. World Sci*. doi:10.1142/6437

Fornberg, B., and Flyer, N. (2015). Fast generation of 2-D node distributions for mesh-free PDE discretizations. *Comput. Math. Appl.* 69, 531–544. doi:10.1016/j.camwa.2015.01.009

Gehrmann, R., North, L. J., Graber, S., Szitkar, F., Petersen, S., Minshull, T., et al. (2019). Marine mineral exploration with controlled source electromagnetics at the TAG hydrothermal field, 26°N mid-atlantic ridge. *Geophys. Res. Lett.* 46, 5808–5816. doi:10.1029/2019gl082928

Günther, T., Rücker, C., and Spitzer, K. (2006). Three-dimensional modelling and inversion of DC resistivity data incorporating topography-II. Inversion. *Geophys. J. Int.* 166, 506–517. doi:10.1111/j.1365-246x.2006.03011.x

Han, B., Li, Y., and Li, G. (2018). 3D forward modeling of magnetotelluric fields in general anisotropic media and its numerical implementation in Julia. *Geophysics* 83, F29–F40. doi:10.1190/geo2017-0515.1

Hohmann, G. W. (1975). Three-dimensional induced polarization and electromagnetic modeling. *Geophysics* 40, 309–324. doi:10.1190/1.1440527

Jahandari, H., Ansari, S., and Farquharson, C. G. (2017). Comparison between staggered grid finite–volume and edge–based finite–element modelling of geophysical electromagnetic data on unstructured grids. *J. Appl. Geophys.* 138, 185–197. doi:10.1016/j.jappgeo.2017.01.016

Jahandari, H., Bihlo, A., and Donzelli, F. (2021). Forward modelling of gravity data on unstructured grids using an adaptive mimetic finite-difference method. *J. Appl. Geophys.* 190, 104340. doi:10.1016/j.jappgeo.2021.104340

Jahandari, H., and Farquharson, C. G. (2014). A finite-volume solution to the geophysical electromagnetic forward problem using unstructured grids. *Geophysics* 79, E287–E302. doi:10.1190/geo2013-0312.1

Jia, X., and Hu, T. (2006). Element-free precise integration method and its applications in seismic modelling and imaging. *Geophys. J. Int.* 166, 349–372. doi:10.1111/j.1365-246X.2006.03024.x

Jin, J.-M. (2014). *The finite element method in electromagnetics*. 3 edn. USA: John Wiley & Sons.

Jones, A. G. (2023). Mining for net zero: the impossible task. *Lead. Edge* 42, 266–276. doi:10.1190/tle42040266.1

Jones, F. W., and Pascoe, L. J. (1972). The perturbation of alternating geomagnetic fields by three-dimensional conductivity inhomogeneities. *Geophys. J. Int.* 27, 479–485. doi:10.1111/j.1365-246X.1972.tb06103.x

Kara, K. B., and Farquharson, C. G. (2023). 3D minimum-structure inversion of controlled-source EM data using unstructured grids. *J. Appl. Geophys.* 209, 104897. doi:10.1016/j.jappgeo.2022.104897

Key, K., and Ovall, J. (2011). A parallel goal-oriented adaptive finite element method for 2.5-D electromagnetic modelling. *Geophys. J. Int.* 186, 137–154. doi:10.1111/j.1365-246x.2011.05025.x

Lelièvre, P., Carter-McAuslan, A., Farquharson, C., and Hurich, C. (2012). Unified geophysical and geological 3D Earth models. *Lead. Edge* 31, 322–328. doi:10.1190/1.3694900

Li, B., Liu, Y., Sen, M. K., and Ren, Z. (2017a). Time-space-domain mesh-free finite difference based on least squares for 2D acoustic-wave modeling. *Geophysics* 82, T143–T157. doi:10.1190/geo2016-0464.1

Li, J., Farquharson, C. G., and Hu, X. (2017b). 3D vector finite-element electromagnetic forward modeling for large loop sources using a total-field algorithm and unstructured tetrahedral grids. *Geophysics* 82, E1–E16. doi:10.1190/geo2016-0004.1

Liu, Z., Ren, Z., Yao, H., Tang, J., Lu, X., and Farquharson, C. (2023). A parallel adaptive finite-element approach for 3-D realistic controlled-source electromagnetic problems using hierarchical tetrahedral grids. *Geophys. J. Int.* 232, 1866–1885. doi:10.1093/gji/ggac419

Long, J., and Farquharson, C. G. (2017). "Three-dimensional controlled-source EM modeling with radial basis function-generated finite differences: a meshless approach," in *SEG technical program expanded abstracts 2017* (China: Society of Exploration Geophysicists), 1209–1213.

Long, J., and Farquharson, C. G. (2019a). "Meshfree modelling of 3-D controlled-source EM data: a new method to treat the singular source terms," in *SEG technical program expanded abstracts 2019* (China: Society of Exploration Geophysicists), 1050–1054.

Long, J., and Farquharson, C. G. (2019b). On the forward modelling of three-dimensional magnetotelluric data using a radial-basis-function-based mesh-free method. *Geophys. J. Int.* 219, 394–416. doi:10.1093/gji/ggz306

Long, J., and Farquharson, C. G. (2019c). Three-dimensional forward modelling of gravity data using mesh-free methods with radial basis functions and unstructured nodes. *Geophys. J. Int.* 217, 1577–1601. doi:10.1093/gji/ggz115

Long, J., and Farquharson, C. G. (2020). "Meshfree modelling of 2D MT data with RBF-FD and unstructured points," in *SEG international exposition and annual meeting (SEG)*. China, SEG.

Long, J., and Farquharson, C. G. (2024). *Three-dimensional controlled-source electromagnetic data modelling with a hybrid meshfree-finite element approach*. Germany: preparation.

Lu, X., Farquharson, C. G., Miehé, J.-M., and Harrison, G. (2021). 3D electromagnetic modeling of graphitic faults in the Athabasca Basin using a finite-volume time-domain approach with unstructured grids. *Geophysics* 86, B349–B367. doi:10.1190/geo2020-0657.1

Mackie, R. L., Madden, T. R., and Wannamaker, P. E. (1993). Three-dimensional magnetotelluric modeling using difference equations—theory and comparisons to integral equation solutions. *Geophysics* 58, 215–226. doi:10.1190/1.1443407

Miensopust, M. P., Queralt, P., Jones, A. G., and modellers, D. M. (2013). Magnetotelluric 3-D inversion—a review of two successful workshops on forward and inversion code testing and comparison. *Geophys. J. Int.* 193, 1216–1238. doi:10.1093/gji/ggt066

Nabighian, M. N. (1988). *Electromagnetic methods in applied geophysics: voume 1, theory*. Germany: Society of Exploration Geophysicists.

Nalepa, M., Ansari, S., and Farquharson, C. (2016). "Finite-element simulation of 3D CSEM data on unstructured meshes: an example from the East Coast of Canada," in *SEG technical program expanded abstracts 2016* (Germany: Society of Exploration Geophysicists), 1048–1052.

Nam, M. J., Kim, H. J., Song, Y., Lee, T. J., Son, J.-S., and Suh, J. H. (2007). 3D magnetotelluric modelling including surface topography. *Geophys. Prospect.* 55, 277–287. doi:10.1111/j.1365-2478.2007.00614.x

Newman, G. A. (2014). A review of high-performance computational strategies for modeling and imaging of electromagnetic induction data. *Surv. Geophys.* 35, 85–100. doi:10.1007/s10712-013-9260-0

Newman, G. A., and Alumbaugh, D. L. (1995). Frequency-domain modelling of airborne electromagnetic responses using staggered finite differences. *Geophys. Prospect.* 43, 1021–1042. doi:10.1111/j.1365-2478.1995.tb00294.x

Newman, G. A., Hohmann, G. W., and Anderson, W. L. (1986). Transient electromagnetic response of a three-dimensional body in a layered earth. *Geophysics* 51, 1608–1627. doi:10.1190/1.1442212

Nguyen, V. P., Rabczuk, T., Bordas, S., and Duflot, M. (2008). Meshless methods: a review and computer implementation aspects. *Math. Comput. Simul.* 79, 763–813. doi:10.1016/j.matcom.2008.01.003

Oden, J. T., and Prudhomme, S. (2001). Goal-oriented error estimation and adaptivity for the finite element method. *Comput. Math. Appl.* 41, 735–756. doi:10.1016/s0898-1221(00)00317-5

Pridmore, D., Hohmann, G., Ward, S., and Sill, W. (1981). An investigation of finite-element modeling for electrical and electromagnetic data in three dimensions. *Geophysics* 46, 1009–1024. doi:10.1190/1.1441239

Puzyrev, V., Koldan, J., de la Puente, J., Houzeaux, G., Vazquez, M., and Cela, J. M. (2013). A parallel finite-element method for three-dimensional controlled-source electromagnetic forward modelling. *Geophys. J. Int.* 193, 678–693. doi:10.1093/gji/ggt027

Rabczuk, T., and Belytschko, T. (2005). Adaptivity for structured meshfree particle methods in 2D and 3D. *Int. J. Numer. Methods Eng.* 63, 1559–1582. doi:10.1002/nme.1326

Ren, Z., Kalscheuer, T., Greenhalgh, S., and Maurer, H. (2013). A goal-oriented adaptive finite-element approach for plane wave 3-D electromagnetic modelling. *Geophys. J. Int.* 194, 700–718. doi:10.1093/gji/ggt154

Rochlitz, R., Skibbe, N., and Günther, T. (2019). custEM: customizable finite-element simulation of complex controlled-source electromagnetic data. *Geophysics* 84, F17–F33. doi:10.1190/geo2018-0208.1

Schulz, K. J., DeYoung Jr, J. H., Seal II, R. R., and Bradley, D. C. (2017). Critical mineral resources of the United States—an introduction. *Tech. Rep. U. S. Geol. Surv*. doi:10.3133/pp1802A

Schwarzbach, C., Börner, R.-U., and Spitzer, K. (2011). Three-dimensional adaptive higher order finite element simulation for geo-electromagnetics-a marine CSEM example. *Geophys. J. Int.* 187, 63–74. doi:10.1111/j.1365-246X.2011.05127.x

Si, H. (2015). TetGen, a delaunay-based quality tetrahedral mesh generator. *ACM Trans. Math. Softw.* 41, 1–36. doi:10.1145/2629697

Slak, J., and Kosec, G. (2019). On generation of node distributions for meshless PDE discretizations. *SIAM J. Sci. Comput.* 41, A3202–A3229. doi:10.1137/18m1231456

Smith, R. (2014). Electromagnetic induction methods in mining geophysics from 2008 to 2012. *Surv. Geophys.* 35, 123–156. doi:10.1007/s10712-013-9227-1

Spitzer, K. (2024). Electromagnetic modeling using adaptive grids–Error estimation and geometry representation. *Surv. Geophys.* 45, 277–314. doi:10.1007/s10712-023-09794-9

Strangway, D., Swift Jr, C., and Holmer, R. (1973). The application of audio-frequency magnetotellurics (AMT) to mineral exploration. *Geophysics* 38, 1159–1175. doi:10.1190/1.1440402

Stratton, J. A. (2007). *Electromagnetic theory*. USA: John Wiley & Sons.

Streich, R. (2009). 3D finite-difference frequency-domain modeling of controlled-source electromagnetic data: direct solution and optimization for high accuracy. *Geophysics* 74, F95–F105. doi:10.1190/1.3196241

Taflove, A., and Umashankar, K. R. (1990). The finite-difference time-domain method for numerical modeling of electromagnetic wave interactions. *Electromagnetics* 10, 105–126. doi:10.1080/02726349008908231

Takekawa, J., Mikada, H., and Imamura, N. (2015). A mesh-free method with arbitrary-order accuracy for acoustic wave propagation. *Comput. Geosciences* 78, 15–25. doi:10.1016/j.cageo.2015.02.006

Wait, J. R. (1960). Propagation of electromagnetic pulses in a homogeneous conducting earth. *Appl. Sci. Res. Sect. B* 8, 213–253. doi:10.1007/bf02920058

Wang, T., and Hohmann, G. W. (1993). A finite-difference, time-domain solution for three-dimensional electromagnetic modeling. *Geophysics* 58, 797–809. doi:10.1190/1.1443465

Ward, S. H., and Hohmann, G. W. (1988). 4. Electromagnetic theory for geophysical applications. *Electromagn. Methods Appl. Geophys.* 1 (4), 130–311. doi:10.1190/1.9781560802631.ch4

Wittke, J., and Tezkan, B. (2014). Meshfree magnetotelluric modelling. *Geophys. J. Int.* 198, 1255–1268. doi:10.1093/gji/ggu207

Yee, K. S. (1966). Numerical solution of initial boundary value problems involving Maxwell's equations in isotropic media. *IEEE Trans. Antennas Propag.* 14, 302–307. doi:10.1109/TAP.1966.1138693

Zeng, S., Hu, X., Li, J., Farquharson, C. G., Wood, P. C., Lu, X., et al. (2019). Effects of full transmitting-current waveforms on transient electromagnetics: insights from modeling the Albany graphite deposit. *Geophysics* 84, E255–E268. doi:10.1190/geo2018-0573.1

Zhang, B., Yin, C., Ren, X., Liu, Y., and Qi, Y. (2018). Adaptive finite element for 3d time-domain airborne electromagnetic modeling based on hybrid posterior error estimation. *Geophysics* 83, WB71–WB79. doi:10.1190/geo2017-0544.1

Zhdanov, M. S. (2010). Electromagnetic geophysics: notes from the past and the road ahead. *Geophysics* 75, 75A49–75A66. doi:10.1190/1.3483901

frontiers | Frontiers in Earth Science

TYPE Original Research
PUBLISHED 21 August 2024
DOI 10.3389/feart.2024.1443764

OPEN ACCESS

EDITED BY
Bo Yang,
Zhejiang University, China

REVIEWED BY
Jinghe Li,
Guilin University of Technology, China
Zeqiu Guo,
Sichuan University, China

*CORRESPONDENCE
Zhou Lei,
501161@yangtzeu.edu.cn

RECEIVED 04 June 2024
ACCEPTED 08 August 2024
PUBLISHED 21 August 2024

CITATION
Junke Z, Lei Z, Xinyu W, Xingbing X, Yurong M and Liangjun Y (2024) Study of response characteristics of cross-well induced polarization method in anisotropic media. *Front. Earth Sci.* 12:1443764. doi: 10.3389/feart.2024.1443764

Study of response characteristics of cross-well induced polarization method in anisotropic media

Zhang Junke[1,2], Zhou Lei[1,2]*, Wang Xinyu[3], Xie Xingbing[1,2], Mao Yurong[1,2] and Yan Liangjun[1,2]

[1]College of Geophysics and Petroleum Resources, Yangtze University, Wuhan, Hubei, China, [2]Key Laboratory of Exploration Technologies for Oil and Gas Resources, Ministry of Education, Yangtze University, Wuhan, Hubei, China, [3]School of Geophysics and Geomatics, China University of Geosciences (Wuhan), Wuhan, Hubei, China

The borehole induced polarization method has been widely used in deep mineral exploration, oil and gas resource exploration, and water resource exploration because of its high efficiency and good exploration effect. At present, the related research on the cross-well induced polarization method assumes that the underground medium is isotropic, but the electrical characteristics of the actual earth medium are anisotropic. To analyze the influence of the anisotropic characteristics on the cross-well induced polarization method, in this paper, the anisotropic forward algorithm of conductivity and polarizability in different principal axis directions based on the finite element method is studied. A three-dimensional forward simulation of the cross-well induced polarization method in anisotropic media is realized. The effectiveness and correctness of the algorithm are verified by testing and comparing complex 3-D isotropic and anisotropic models. Anisotropic geological models of the horizontal plate and inclined plate are constructed to analyze the anisotropic influences of conductivity and polarizability in different principal axis directions on the cross-well induced polarization response. The results show that the emitter sources with different depths in the well have different influences on the electrical response of the plates. Anisotropic conductivity and polarizability in horizontal plates exhibit most pronounced characteristics in the x-direction, significantly influencing the apparent polarizability curves. However, when the resistivity and polarizability are both anisotropic, the change in the z-direction is the most complicated. When the plate is inclined, the amplitude of the electrical response curve decreases to a certain extent, and the position where the amplitude appears shifts to different degrees. Notably, the response curves of the y-direction anisotropy are basically consistent with the response curves of the isotropy, regardless of the anisotropy of the conductivity and polarizability or anomalous body tilts. The results of this study improve our understanding of the influence of anisotropy on cross-well induced polarization and provide theoretical support for the interpretation of cross-well induced polarization data considering anisotropy.

KEYWORDS

cross-well induced polarization method, anisotropy, finite element method, conductivity and polarizability, three-dimensional forward

1 Introduction

With the development and advancement of science and technology, the demand for mineral resources such as oil and metal deposits is continuously increasing in China. Along with the progressive exploration of surface and near-surface metal deposits, the possibility of finding large or super-large metal deposits in the near surface is getting smaller, thus deep mineral exploration techniques emerged (Mi, 2019). Geophysical prospecting methods have been applied in mineral exploration for more than one hundred years and have played a vital role. Underground geophysical prospecting as an important geophysical prospecting method. It is characterized by a high signal-to-noise ratio, anti-interference and large exploration depth. And it plays an important role in metal mining exploration (Zhou et al., 2009). In recent decades, underground geophysical prospecting methods have grown into characteristic geophysical prospecting techniques in China and have been expanded and applied in oil exploration, hydrological engineering geological surveying and other fields. Correspondingly, higher requirements need to be met to enable the advancement and diversity of underground geophysical prospecting methods and techniques.

From the middle of the last century to the present, the borehole geophysical prospecting method has provided new technologies and means for the exploration of underground metal deposits in China because its detection device is placed in the drill holes, which places it closer to the deep underground ore body and produces a strong exploration signal. It is not easily disturbed by the topography and human activities on the surface (Cao, 2004; Feng et al., 2010; Xiong, 2004). In particular, the borehole induced polarization method (borehole induced polarization, IP) can not only be used to explore massive sulfide deposits with clear resistivity differences from the surrounding rocks but also can effectively explore disseminated (porphyry) metal deposits with less resistivity difference (Wang et al., 2004). Cross-well IP is mainly used to discover cross-well blind ore and to determine the continuity between the ore beds exposed by drilling (Yuan et al., 2011). Scholars at home and abroad have paid more and more attention to research on cross-well electrical exploration and have made many achievements in both forward and inversion (Mcmonnies, 2007; Lamontagne, 2024; Stolz, 2000; Yu et al., 2006; Deng and Li, 2014). Shima (1987) proposed the technology of resistivity tomography for the first time and constructed a low-resistivity inclined structure to verify the feasibility of this technology. Zhdanov and Yoshioka. (2003) developed a new technology for cross-well 3-D imaging and verified the ability of this method to reflect the electrical properties of underground conductive formations and to fully display the position and shape distribution of conductive formations in an application to synthetic data.Arato and Godio. (2014) applied the staggered grid method to the inversion process of cross-well resistivity data, which greatly improved the imaging effect of the two-dimensional cross-well resistivity. The algorithms developed by Dong and Zhu (1999); Dong (1997); Liu et al. (2001) algorithms based on the Jacobi matrix have investigated the problem of cross-well resistivity tomography using the finite element method. The travel time curve tracking technology in analogical seismology, such as that developed by Di and Wang (1997), uses the method of tracking the potential using a current line to attain the resistivity tomography, and the actual effect is greatly improved compared with the finite element method. Lv et al. (2003) determined the parameters of the direct imaging of cross-well resistivity, which can reflect the properties and positions of cross-well electrical inhomogeneity without relying on inversion methods. Xiong et al. (2016) used the finite element method to better solve the well-well 2.5-dimensional forward modeling problem, and based on this, they conducted approximate resistivity imaging of a cross-well profile. This method was demonstrated to have a high efficiency and good imaging effect. All of the above studies were based on the hypothesis that the underground geological bodies are electrically isotropic. In actual exploration and research, it has been found that the electrical anisotropic characteristics of underground geological bodies are difficult to ignore and have a great influence on the actual forward and inversion (Wang, 2002; Linde and Pedersen, 2004; Hou et al., 2006; Yan et al., 2014; Zhu et al., 2021). Kenkel et al. (2012) investigated the effect of anisotropic complex conductivities in the frequency domain, with a particular emphasis on the polarization properties (i.e., phase angles). Hu et al. (2023) developed a 3D IP forward modelling considering arbitrary anisotropy and topography using the finite element method (FEM). And investigated the effects of anisotropy and topography on the interpretation of IP data. Previous studies on electrical anisotropy have focused on direct current and transient electromagnetic methods, and deeper studies are needed to characterize the anisotropic dielectric response to excitation in wells (Schmutz et al., 2000; Hou et al., 2006; Hu et al., 2021). Therefore, in this paper, considering the electrical anisotropy of a cross-well anomaly bodies, the finite element method is used to discuss and analyze the electrical response characteristics of a cross-well anisotropic anomaly bodies. The results of this study provide valuable theoretical support for data processing and interpretation of actual cross-well IP exploration.

2 Basic theory

2.1 Anisotropic medium theory

In isotropic media, the resistivity and conductivity are scalar quantities. In anisotropic media, the resistivity, conductivity and polarizability can be expressed in tensor form (Equation 1).

$$\rho = \sigma^{-1}, \sigma = \begin{pmatrix} \sigma_{xx} & \sigma_{xy} & \sigma_{xz} \\ \sigma_{yx} & \sigma_{yy} & \sigma_{yz} \\ \sigma_{zx} & \sigma_{zy} & \sigma_{zz} \end{pmatrix}, \eta = \begin{pmatrix} \eta_{xx} & \eta_{xy} & \eta_{xz} \\ \eta_{yx} & \eta_{yy} & \eta_{yz} \\ \eta_{zx} & \eta_{zy} & \eta_{zz} \end{pmatrix} \quad (1)$$

For the convenience of calculation, any conductivity tensor σ can be obtained from the principal axis anisotropic conductivity tensor σ_0 through three Euler rotations (Yin, 2010), where the sum of σ_x, σ_y and σ_z is defined as the principal conductivity. Similarly, an arbitrary polarizability tensor can be obtained (Equation 2).

$$\sigma_0 = \begin{pmatrix} \sigma_x & 0 & 0 \\ 0 & \sigma_y & 0 \\ 0 & 0 & \sigma_z \end{pmatrix} \quad (2)$$

In Cartesian coordinates, the conductivity tensor can be expressed as follows (Wang, 2015; Liu et al., 2018) (Equation 3):

$$\sigma = D\sigma_0 D^{-T} \tag{3}$$

where $D = D_1 D_2 D_3$, and the rotation matrices for three times counterclockwise rotations respectively (Equations 4–6).

$$D_1 = \begin{pmatrix} \cos\alpha & -\sin\alpha & 0 \\ \sin\alpha & \cos\alpha & 0 \\ 0 & 0 & 1 \end{pmatrix} \tag{4}$$

$$D_2 = \begin{pmatrix} 1 & 0 & 0 \\ 0 & \cos\beta & -\sin\beta \\ 0 & \sin\beta & \cos\beta \end{pmatrix} \tag{5}$$

$$D_3 = \begin{pmatrix} \cos\gamma & -\sin\gamma & 0 \\ \sin\gamma & \cos\gamma & 0 \\ 0 & 0 & 1 \end{pmatrix} \tag{6}$$

α, β, γ are the anisotropic strike angle, anisotropic dip angle and anisotropic deflection angle respectively (Pek and Santos, 2006).

2.2 Total potential method

The partial differential equation satisfied by the potential in a rectangular coordinate system is as follows (Equation 7):

$$\frac{\partial}{\partial x}\left(\sigma\frac{\partial U}{\partial x}\right) + \frac{\partial}{\partial y}\left(\sigma\frac{\partial U}{\partial y}\right) + \frac{\partial}{\partial z}\left(\sigma\frac{\partial U}{\partial z}\right) = -\frac{4\pi}{\omega_A} I\delta(x_A)\delta(y_A)\delta(z_A) \tag{7}$$

The boundary value problem of the total potential in the point source field is (Xu, 1994) (Equation 8)

$$\begin{cases} \nabla\cdot(\sigma\nabla U) = -\dfrac{4\pi}{\omega_A} I\delta(A) & \in \Omega \\ U_1 = U_2 & \in \Gamma \\ \sigma_1\dfrac{\partial U_1}{\partial n} = -\sigma_2\dfrac{\partial U_2}{\partial n} & \in \Gamma \\ \sigma\dfrac{\partial U}{\partial n} = 0 & \in \Gamma_s \\ \dfrac{\partial U}{\partial n} + \dfrac{\cos(r,n)}{r}U = 0 & \in \Gamma_\infty \end{cases} \tag{8}$$

According to the variational principle, the boundary value problem of the point source field is transformed into the following variational problems (Equation 9):

$$\begin{cases} F(U) = \int_\Omega \left[1/2\sigma\nabla U^2 - \left(\dfrac{4\pi}{\omega_A}\right) I\delta(A)U\right] d\Omega + 1/2\int_{\Gamma\infty}\sigma U^2\cos(r,n)/r d\Gamma \\ \sigma F(U=0) \end{cases} \tag{9}$$

I is the current; U is the total potential value; σ is the electrical conductivity; r is the distance from the power supply point source to the boundary; n is the outer normal vector of the infinite boundary; Ω is the target region; and Γ_∞ is the infinite boundary of the region Ω.

2.3 Abnormal potential method

In the numerical calculation in the resistivity method, the total potential U is usually taken as the research object, and the total potential U consists of two parts (Equation 10):

$$U = u_0 + u \tag{10}$$

The normal potential u_0 is the potential generated by the point source in the uniform half space or the entire space, and the normal potential is calculated by an analytical solution. u is an abnormal potential, which is produced by an inhomogeneous body. Because the potential function U is singular at the point of the power supply point, the calculation error is very large due to the influence of the vicinity of the power supply point. The difference between the total potential method and the abnormal potential method is the source, the functional in the finite element of the total potential method has a source term. However, the point source term is not included in the abnormal potential method u, so the singularity at the point source is eliminated by the abnormal potential method, and the calculation accuracy is greatly improved (Xu, 1994).

It is assumed that there is an electrical inhomogeneity in the dielectric σ_1 (Figure 1). The conductivity of the anomaly is σ_2, and the conductivity of the dielectric where the point power supply is located is σ_0. And $\sigma_1 = \sigma_0$; Ω_1, Ω_2, u_1, u_2 denote σ_1, σ_2 occupied area and the abnormal potential. The differential equation and boundary condition of the abnormal potential u are as follows (Equation 11):

$$\begin{cases} \dfrac{\partial u}{\partial n} = 0 & \in \Gamma_s \\ u_1 = u_2 & \in \Gamma \\ \sigma_1\dfrac{\partial u_1}{\partial n_1} + \sigma_2\dfrac{\partial u_2}{\partial n_2} = -\left(\sigma_2\dfrac{\partial u_0}{\partial n_1} + \sigma_2\dfrac{\partial u_0}{\partial n_2}\right) & \in \Gamma \\ \dfrac{\partial u}{\partial n} + \dfrac{\cos(r,n)}{r}u = 0 & \in \Gamma_\infty \\ \nabla\cdot(\sigma u) = -\nabla\cdot(\sigma' u_0) \end{cases} \tag{11}$$

where σ is the dielectric conductivity, and σ' is the residual conductivity.

The boundary value problem satisfied by the abnormal potential of the three-dimensional point source field is transformed into a variational problem (Equation 12):

$$\begin{cases} F(u) = \int_\Omega \left[1/2\sigma(\nabla u)^2 + \sigma'\nabla u_0\cdot\nabla u\right] d\Omega + \int_{\Gamma\infty}\dfrac{\sigma u^2\cos(r,n)}{2r} + \dfrac{\sigma' u_0 u\cos(r,n)}{r} d\Gamma \\ \sigma F(u) = 0 \end{cases} \tag{12}$$

2.4 Equivalent resistivity method

The forward calculation of the polarizability is found by the equivalent resistivity. When induced polarization effects are not considered, the value of the primary field potential ΔU_1 is obtained from the forward calculation; when induced polarization effects in the subsurface medium are considered, the forward show gets the total field potential ΔU. The anomalous potential method was used for both forward potentials. According to the theory of Seigel (Harold, 1959), the primary field potential ΔU_1 is solved by forward modeling, and the

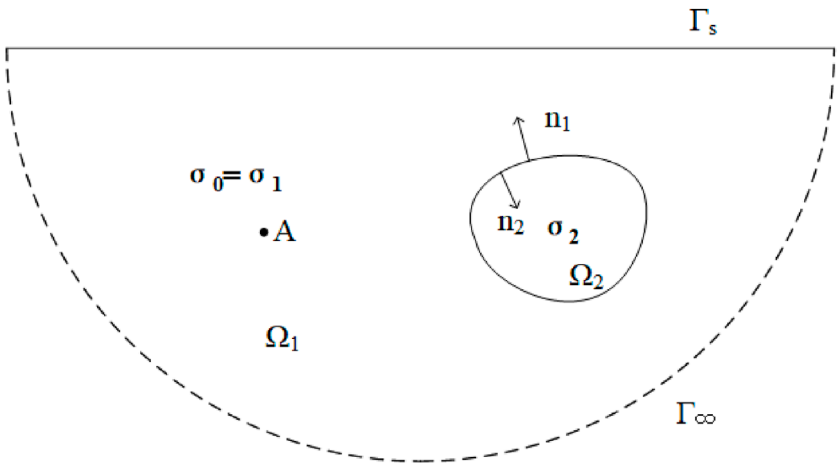

FIGURE 1
Geoelectric section of an inhomogeneous body (Xu, 1994). A is the point power supply, Ω_2 is the electrical inhomogeneity with conductivity σ_2, and n1 and n2 are the internal and external normal directions of the inhomogeneity boundary.

total field potential ΔU (polarization field potential) is obtained using the equivalent resistivity ρ^* instead of the original model resistivity ρ. The secondary field potential ΔU_2 is obtained by subtracting the primary field potential from the total field potential. The following relationships can be obtained by expressing the equivalent apparent resistivity ρ_s^*, apparent resistivity ρ_s, apparent polarizability η_s, polarizability η, and device coefficient K as follows (Equations 13–17):

$$\Delta U = \Delta U_1 + \Delta U_2 \tag{13}$$

$$\rho^* = \frac{\rho}{1-\eta} \tag{14}$$

$$\rho_s = K\frac{\Delta U_1}{I} \tag{15}$$

$$\rho_s^* = K\frac{\Delta U}{I} \tag{16}$$

$$\eta_S = \frac{\Delta U_2}{\Delta U} \times 100\% = \frac{\Delta U - \Delta U_1}{\Delta U} \times 100\% = \frac{\rho_s^* - \rho_s}{\rho_s^*} \times 100\% \tag{17}$$

2.5 Three-dimensional forward theory of the cross-well induced polarization method based on the finite element method

As shown in Figure 2, $u_i(i = 1,2,3,4)$ for the potential on the vertex, and the potential u of any point P in the cell can be obtained by linear interpolation as follows (Xu, 1994) (Equation 18):

$$u = \sum_{i-1}^{4} N_i u_i \tag{18}$$

N_i is the shape function, which is the volume ratio of two tetrahedrons (Equation 19).

$$N_1 = \frac{V_{P234}}{V_{1234}}, N_2 = \frac{V_{P143}}{V_{1234}}, N_3 = \frac{V_{P124}}{V_{1234}}, N_4 = \frac{V_{P132}}{V_{1234}} \tag{19}$$

The shape function and its coefficients can be expressed as follows (Equations 20, 21):

$$N_i = \frac{1}{6V}(a_i x + b_i y + c_i z + d_i) \tag{20}$$

$$a_1 = \begin{vmatrix} y_2 & z_2 & 1 \\ y_3 & z_3 & 1 \\ y_4 & z_4 & 1 \end{vmatrix}, b_1 = -\begin{vmatrix} x_2 & z_2 & 1 \\ x_3 & z_3 & 1 \\ x_4 & z_4 & 1 \end{vmatrix}, c_1 = \begin{vmatrix} x_2 & y_2 & 1 \\ x_3 & y_3 & 1 \\ x_4 & y_4 & 1 \end{vmatrix}, d_1 = -\begin{vmatrix} x_2 & y_2 & z_2 \\ x_3 & y_3 & z_3 \\ x_4 & y_4 & z_4 \end{vmatrix}$$

$$a_2 = -\begin{vmatrix} y_1 & z_1 & 1 \\ y_3 & z_3 & 1 \\ y_4 & z_4 & 1 \end{vmatrix}, b_2 = \begin{vmatrix} x_1 & z_1 & 1 \\ x_3 & z_3 & 1 \\ x_4 & z_4 & 1 \end{vmatrix}, c_2 = -\begin{vmatrix} x_1 & y_1 & 1 \\ x_3 & y_3 & 1 \\ x_4 & y_4 & 1 \end{vmatrix}, d_2 = \begin{vmatrix} x_1 & y_1 & z_1 \\ x_3 & y_3 & z_3 \\ x_4 & y_4 & z_4 \end{vmatrix}$$

$$a_3 = \begin{vmatrix} y_1 & z_1 & 1 \\ y_2 & z_2 & 1 \\ y_4 & z_4 & 1 \end{vmatrix}, b_3 = -\begin{vmatrix} x_1 & z_1 & 1 \\ x_2 & z_2 & 1 \\ x_4 & z_4 & 1 \end{vmatrix}, c_3 = \begin{vmatrix} x_1 & y_1 & 1 \\ x_2 & y_2 & 1 \\ x_4 & y_4 & 1 \end{vmatrix}, d_3 = -\begin{vmatrix} x_1 & y_1 & z_1 \\ x_2 & y_2 & z_2 \\ x_4 & y_4 & z_4 \end{vmatrix}$$

$$a_4 = -\begin{vmatrix} y_1 & z_1 & 1 \\ y_2 & z_2 & 1 \\ y_3 & z_3 & 1 \end{vmatrix}, b_4 = \begin{vmatrix} x_1 & z_1 & 1 \\ x_2 & z_2 & 1 \\ x_3 & z_3 & 1 \end{vmatrix}, c_4 = -\begin{vmatrix} x_1 & y_1 & 1 \\ x_2 & y_2 & 1 \\ x_3 & y_3 & 1 \end{vmatrix}, d_4 = \begin{vmatrix} x_1 & y_1 & z_1 \\ x_2 & y_2 & z_2 \\ x_3 & y_3 & z_3 \end{vmatrix} \tag{21}$$

When performing anisotropic forward, conductivity is the tensor form. Tetrahedral mesh to discrete equations. By integrating the four terms in the variational problem using the abnormal potential method in Equation 12, we can obtain the following equation (Equation 22).

$$\begin{aligned} F(U) &= \sum\left(\frac{\sigma}{2}u^T K_{1e} u + \sigma' u^T K_{1e} u_0 + \frac{\sigma}{2}u^T K_{2e} u + \sigma' u^T K_{2e} u_0\right) \\ &= \frac{1}{2}u^T K u + u^T K' u_0 \end{aligned} \tag{22}$$

If Equation 22 is changed to zero, we can obtain the following equation (Equation 23):

$$Ku = K' u_0 \tag{23}$$

Likewise, polarizability anisotropy is based on the principle of the equivalent resistivity method. Its partial differential equation discretization is consistent with the resistivity method.

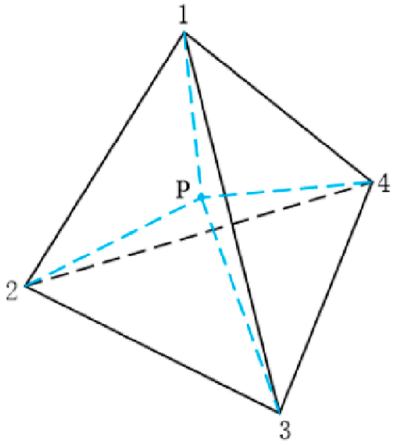

FIGURE 2
Tetrahedral element. P is the center of the tetrahedron, and 1, 2, 3, and 4 are vertex numbers respectively.

In this paper, an improved symmetric step-by-step over-relaxation preconditioned conjugate gradient iterative algorithm (SSOR-PCG) (Lin, 1998) is used. The matrix of coefficient A of the linear equations Ax=b is an n-order symmetric positive definite matrix, and the splitting matrix of the symmetric step-by-step over-relaxation iteration (SSOR method) is used as the pretreatment matrix M (Equation 24):

$$M = (2-\omega)^{-1}\left(\frac{D}{\omega}+L\right)\left(\frac{D}{\omega}\right)^{-1}\left(\frac{D}{\omega}+L\right)^{T} \tag{24}$$

where D is the diagonal matrix of A, which is a strictly lower triangular matrix with L as A. $0 < \omega < 2$ is the relaxation factor.

In Figure 1, when the point power is underground and the underground $\sigma = \sigma_0$ is a homogeneous conductive medium, the potential at this time is the normal potential u_0, and thus (Equation 25),

$$\nabla\cdot(\sigma_0\nabla u_0) = -I\delta(A) \tag{25}$$

u_0 can be obtained from the analytical solution (Equation 26). Then, the abnormal potential u at each node of the grid can be obtained by solving Equation 23, and the total potential can be calculated using Equation 10.

$$U_0 = \frac{\rho I}{4\pi}\left(\frac{1}{R}+\frac{1}{R'}\right) \tag{26}$$

R is the distance from the measuring point to the point current source A, and R' is the distance from the measuring point to the imaginary point current source A'.

3 Algorithm validation

3.1 Three-dimensional complex isotropic cross-well sphere model

To verify the accuracy of the code written in this study, the cross-well sphere model in a homogeneous isotropic medium is used for verification (Xiong et al., 2016). The model shown in Figure 3 is established. The well spacing is 30 m, and the underground body is a low-resistivity sphere. Source point A supplies power at a depth of 20 m in well 1. There are 50 measuring points within every 1 m from 1 to 50 m in well 2. The resistivity of the sphere is 1 Ω·m, the radius of the sphere is 1 m, the burial depth of the center of the sphere is 20 m, the distance between the two wells is 15 m, and the resistivity of the surrounding rock is 100 Ω·m. The results calculated in this paper are compared with the analytical solutions calculated by Xiong et al. (2016).

As shown in Figure 4, the results calculated using the proposed algorithm are in good agreement with those calculated by Xiong et al. (2016), with a maximum relative error of 0.096% and an average relative error of 0.079%. The correctness and validity of the algorithm are verified, which also demonstrates the accuracy of the subsequent analysis of the results presented in this paper.

3.2 Three-dimensional anisotropic model

To further validate the correctness of the proposed algorithm, a 3-D anisotropic model was created (Figure 5) (Xiong et al., 2023). In the model, the anomaly is a 100 m × 100 m × 100 m cube, the burial depth of the center of the anomaly is 55 m, and the size of the surrounding rock is 6,000 m × 6,000 m × 3,000 m. The conductivity of the surrounding rock is $\sigma = \begin{pmatrix} 0.01 & 0 & 0 \\ 0 & 0.0025 & 0 \\ 0 & 0 & 0.01 \end{pmatrix} S\cdot m^{-1}$, and the conductivity of the anomaly is $\sigma = \begin{pmatrix} 0.04 & 0 & 0 \\ 0 & 0.01 & 0 \\ 0 & 0 & 0.04 \end{pmatrix} S\cdot m^{-1}$. A secondary device is used to study the response characteristics of the apparent resistivity at a pole distance of 40 m. The excitation point is located at the origin of the coordinates of point A (0, 0, 0), and the measurement point M is rotated 10° clockwise around the excitation point to complete the observation of the 36 measurement points around the circle. We compare the results calculated in this paper with those calculated by Xiong et al. (2023).

As shown by the curve in Figure 6, this algorithm matches the results calculated by Xiong et al. (2023) well, with a maximum relative error of −1.1%. This verifies the correctness and validity of this algorithm and also indicates the accuracy of the subsequent analysis of the results presented in this paper.

4 Study of IP response between wells in electrically anisotropic media

To study the response of the induced polarization method for different cross-well geological models with conductivity and polarizability are anisotropic in different principal axis directions for abnormal bodies, a cross-well model (Figure 7) is designed. The abnormal bodies are divided into horizontal plate bodies and inclined plate bodies, and the inclined plate bodies are formed by rotating the horizontal plate bodies counterclockwise by 45°. The distance between the wells is 400 m, and three emitter sources A1,

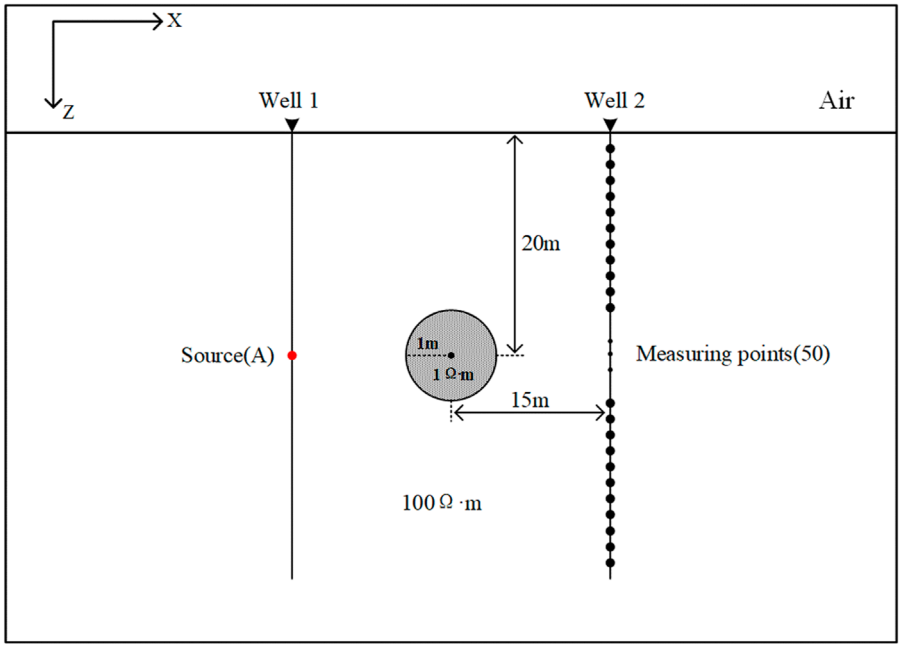

FIGURE 3
Schematic diagram of the three-dimensional complex isotropic cross-well sphere model. The emission source is located 20 m in Well 1. There are 50 measuring points in Well 2. The distance between the center of low-resistance sphere (1 Ω·m) and Well 2 is 15 m, and the surrounding rock resistivity is 100 Ω m.

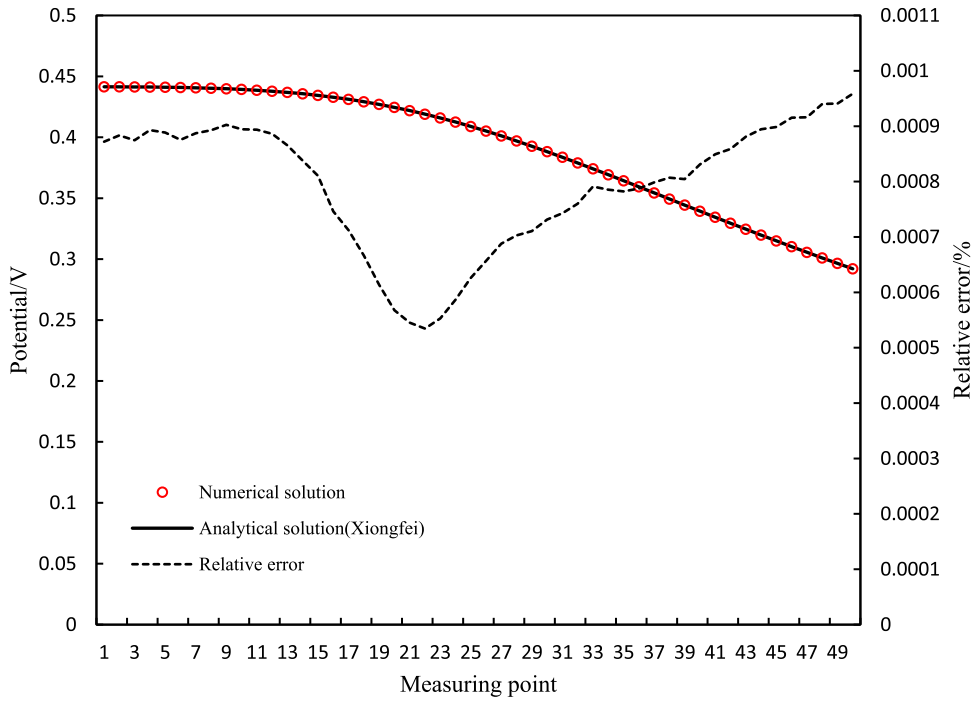

FIGURE 4
Comparison of the numerical solution and analytical solution. The red circle is the numerical solution curve, the black solid line is the analytical solution curve, and the black dotted line is the error curve.

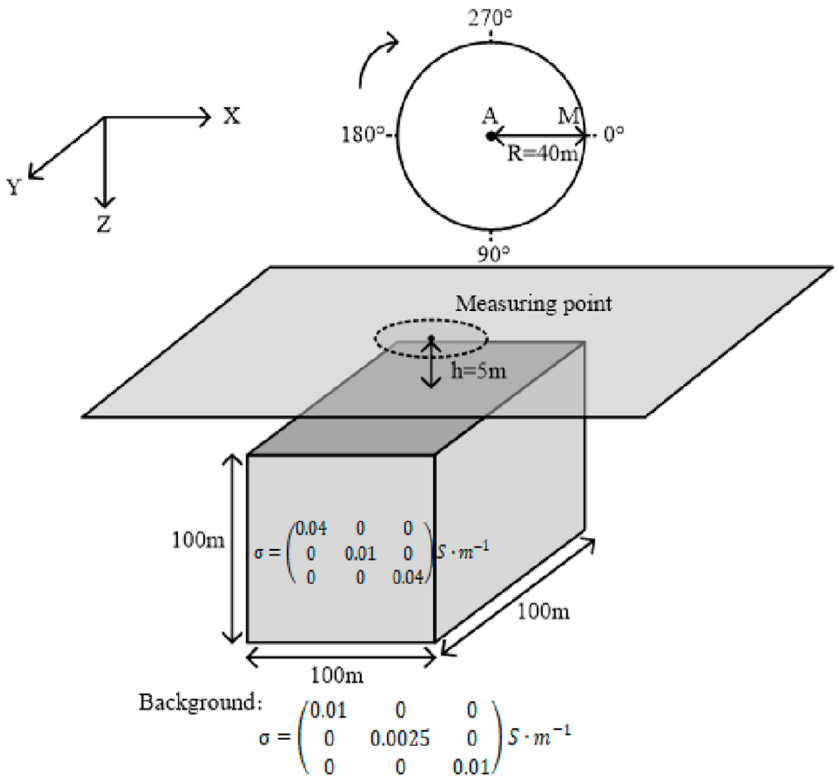

FIGURE 5
3-D anisotropic model. The survey line is a circle with a radius of 40 m on the ground, and the abnormal body is a cube with a side length of 100 m and a depth of 5 m underground.

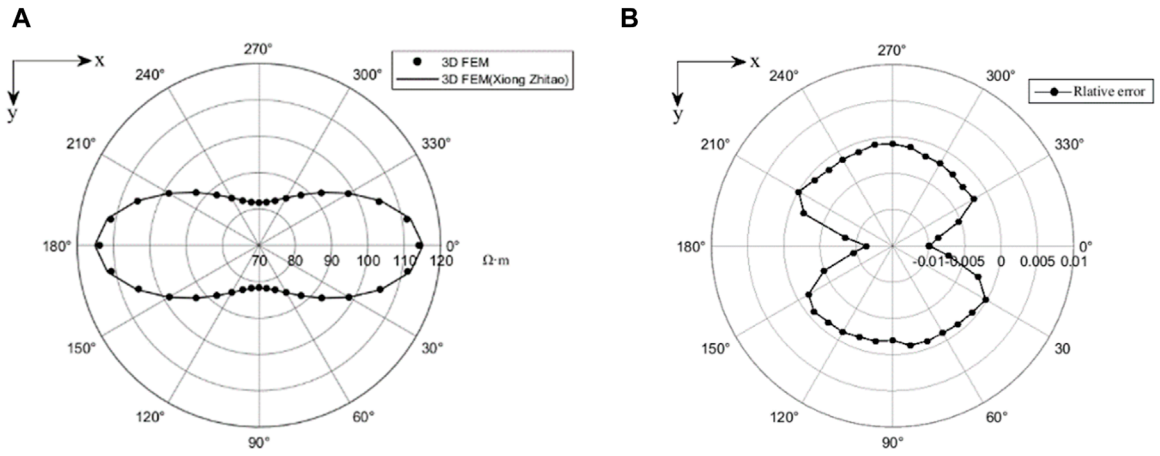

FIGURE 6
Curve plots of the apparent resistivity **(A)** and relative error **(B)** for the different algorithms of three-dimensional anisotropy. The point is the apparent resistivity of 3D FEM algorithm, and the line is the apparent resistivity curve of 3D FEM (Xiong Zhitao) algorithm.

A2, and A3 are located at depths of 400, 600, and 800 m, respectively, in the wells. The center of the anomaly body is 600 m deep; the center is 200 m away from the measuring well, and the scale is 100 m × 100 m × 50 m (in the X, Y, and Z directions). The survey lines in well 2 are vertically arranged in a straight line. The first measurement point is located at the wellhead, and the last measurement point is located 1,200 m below the wellhead, with a total of 601 measurement points. The observed electrode system is a bipolar device.

Regarding the mesh dissection, to better fit the complex cross-well model, a free tetrahedral mesh is used. To improve the accuracy, the mesh size is reduced, and the numbers of the meshes at the emission source, survey line and abnormal body are increased.

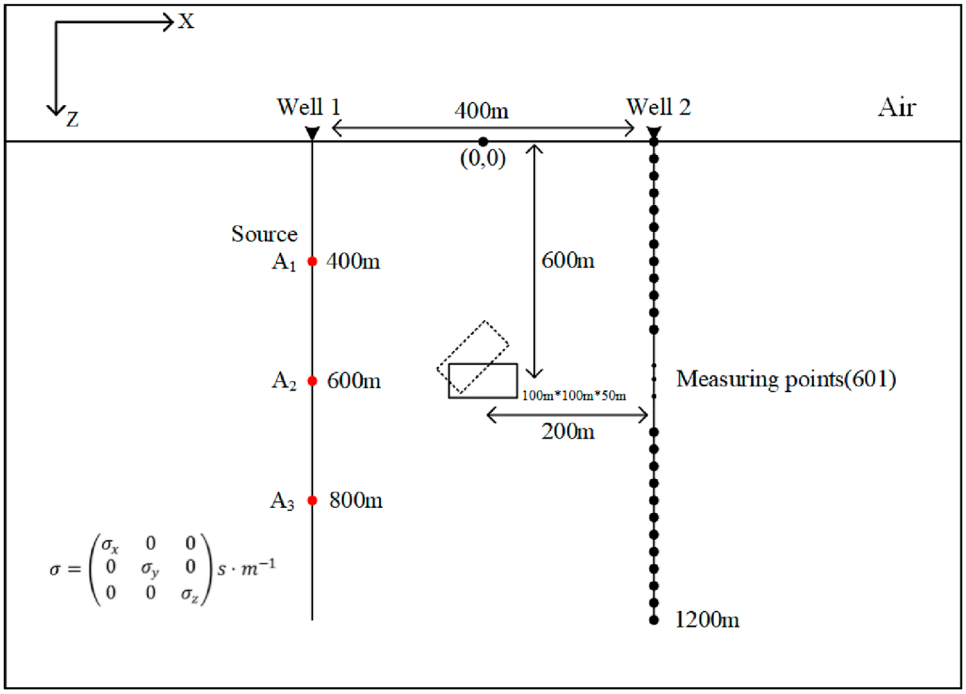

FIGURE 7
Schematic diagram of the cross-well induced polarization logging model. The emission sources are located at 400 m, 600 m, and 800 m in Well 1. There are 601 measuring points in Well 2, and the distance between adjacent measuring points is 2 m. The depth of 600 m between the two wells is a horizontal plate-like body (dotted line is inclined plate-like body) of 100 m * 100 m * 50 m.

TABLE 1 Mesh generation results for the different abnormal bodies. The results are horizontal plate and inclined plate respectively.

Mesh generation result		
Model type	Total number of complete grid cells	Total number of nodes
Horizontal plate-like body	1,728,741	174,034
Inclined plate-like body	1,027,928	173,910

To achieve a better mesh dissection effect and to obtain more accurate calculation results, mesh processing is also carried out at the boundary. The results of different anomalies after the completion of mesh dissection are presented in Table 1. A diagram of the specific mesh generation is presented in Figure 8.

4.1 The surrounding rock and the abnormal body are isotropic

To more effectively study and analyze the influence of the anisotropy, the response of the isotropy of the surrounding rock and anomalous body in different principal axis directions is analyzed in the research process, and the isotropic conductivity tensor of the surrounding rock and anomaly of the two cross-well geological models are set to be respectively: $\sigma_{surrounding\ rock} = \begin{pmatrix} 0.01 & 0 & 0 \\ 0 & 0.01 & 0 \\ 0 & 0 & 0.01 \end{pmatrix} S \cdot m^{-1}$ and $\sigma_{anomalous\ body} = \begin{pmatrix} 1 & 0 & 0 \\ 0 & 1 & 0 \\ 0 & 0 & 1 \end{pmatrix} S \cdot m^{-1}$. The polarizability isotropic tensor of the anomalous body is $\eta = \begin{pmatrix} 0.5 & 0 & 0 \\ 0 & 0.5 & 0 \\ 0 & 0 & 0.5 \end{pmatrix}$. When the polarizability of the surrounding rock is not considered, and the excitation current is 50 A.

Figures 9, 10 respectively show the anomaly curves of the isotropic apparent resistivity and apparent polarizability obtained from the forward calculation of the horizontal plates and inclined plates. Analyzing the cross-well IP response helps to understand the characteristics of the observed abnormal curves. The anomaly field caused by the horizontal plate-like body can be regarded as the combined effect of multiple electric dipole fields (Lv et al., 2012). The curves for the anomaly show the excitation characteristics of different depth emission sources in comparison to the anomaly

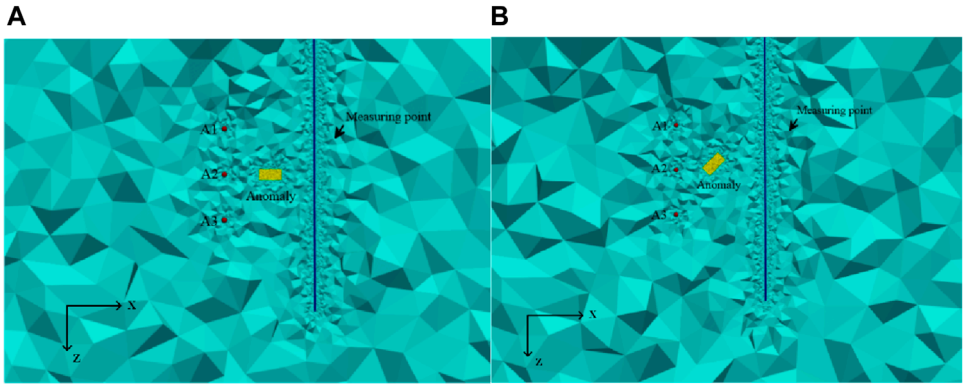

FIGURE 8
Diagram of the cross-well model mesh generation: **(A)** Horizontal plate-like body; and **(B)** inclined plate-like body. A1, A2, and A3 are excitation sources, yellow rectangular box is abnormal body, and blue line is borehole survey line.

and the excitation characteristics of the emitter sources for plate-like bodies with different inclinations. It can be seen that the curves of the apparent resistivity and apparent polarizability of the horizontal plate-like body are axisymmetric. In Figure 9, the emitter is close to the anomalous body at 600 m, the curve is most curved, and the values of the apparent resistivity and apparent polarizability reach the maximum at the center of the anomalous body. The maximum apparent resistivity and minimum apparent polarizability can be observed, and the curves exhibit a reverse stretching shape, which is caused by the emitter being close to the center of the anomalous body, the underground low resistivity body has obvious attraction to the current, and the current density is high; whereas the shallow and deep parts are far away from the emitter and anomalous body, and the current density is small. The extreme values of the apparent resistivity and apparent polarizability produced by the emitters at 400 and 800 m are near the bottom boundary and the top boundary, respectively, which are related to the position of the emitter. The emitter is located at the center of the anomalous body (at 600 m), so the extreme values are located at the center of the anomalous body. Similarly, because the abnormal body is rotated by 45°, the abnormal curves of the inclined plate-like body is roughly the same as that of the horizontal plate-like body, and the reason for this is the same as in the case of the horizontal plate-like body. Different from the horizontal plate-like body, the inclined plate-like body causes the absolute values of the apparent resistivity and apparent polarizability of the emitters at different positions to decrease to a certain extent and has the greatest influence on the emitters at a shallow depth of 400 m. Because of the inclination of the plate-like body, the positions of all of the extreme values of the response curves are shifted upward and the variations in the amplitude of the curves become wider to a certain extent.

Therefore, the response of the isotropic surrounding rock and abnormal body has been analyzed. A good foundation for analyzing the anisotropy of the conductivity and polarizability of the abnormal body.

4.2 Polarizability is isotropic and conductivity is anisotropic of abnormal body

To better analyze the influence of the anisotropy of the anomalous bodies conductivity on the apparent resistivity and apparent polarizability, it is assumed that the anomalous bodies polarizability is isotropic and the anomalous bodies conductivity is anisotropic in different principal axis directions. In addition, the anisotropic conductivity tensors of the two modeled anomalous bodies are set as $\sigma = \begin{pmatrix} 0.02 & 0 & 0 \\ 0 & 1 & 0 \\ 0 & 0 & 1 \end{pmatrix} S \cdot m^{-1}$, $\sigma = \begin{pmatrix} 1 & 0 & 0 \\ 0 & 0.02 & 0 \\ 0 & 0 & 1 \end{pmatrix} S \cdot m^{-1}$ and $\sigma = \begin{pmatrix} 1 & 0 & 0 \\ 0 & 1 & 0 \\ 0 & 0 & 0.02 \end{pmatrix} S \cdot m^{-1}$, and the isotropic polarizability tensors of the two modeled anomalous bodies are set as $\eta = \begin{pmatrix} 0.5 & 0 & 0 \\ 0 & 0.5 & 0 \\ 0 & 0 & 0.5 \end{pmatrix}$. We set up an isotropic medium with a surrounding rock conductivity of $0.01 S \cdot m^{-1}$, the polarizability is set to 0, and the excitation current is 50 A. The effects of the conductivity on the anisotropy of the apparent resistivity and apparent polarizability of three emitters in the two models were compared.

Figure 11 shows the response curves of the apparent resistivity and apparent polarizability produced by the emission sources at different positions under the condition of anisotropic conductivity for the horizontal plate-like body. As can be seen from Figure 11, the effect of x-direction anisotropic conductivity is maximized regardless of the location of the emission source for the apparent resistivity response curves, and the conductivity of the x-direction anisotropy greatly reduces the apparent resistivity compared to the isotropic condition. The extreme positions of the apparent resistivity curves for the emission sources at 400 and 800 m shift downward and upward, respectively, compared with that for the emission source at 600 m. Compared to the apparent resistivity curve, the

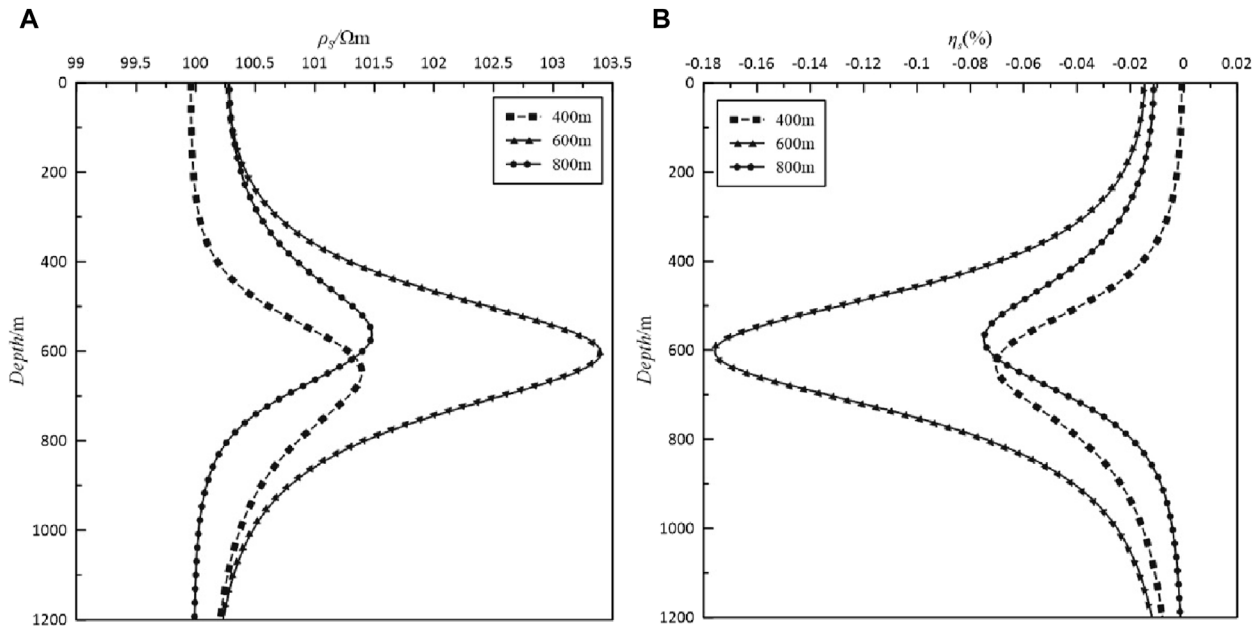

FIGURE 9
Graphs of the **(A)** apparent resistivity and **(B)** apparent polarizability of the isotropic horizontal plate-like body. The response curves with squares are the results for 400 m excitation sources, the response curves with triangles are the results for 600 m excitation sources, and the response curves with dots are the results for 800 m excitation sources.

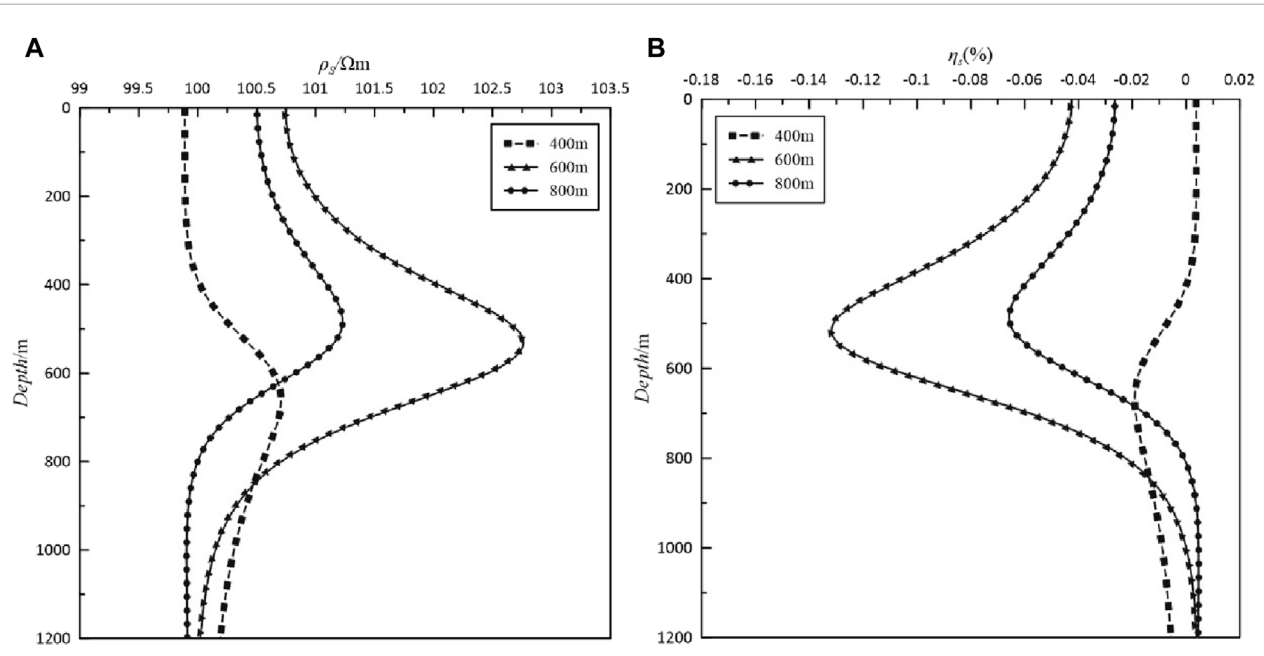

FIGURE 10
Graphs of the **(A)** apparent resistivity and **(B)** apparent polarizability of the isotropic inclined plate-like body. The response curves with squares are the results for 400 m excitation sources, the response curves with triangles are the results for 600 m excitation sources, and the response curves with dots are the results for 800 m excitation sources.

apparent polarizability curve has more obvious changes. The x-direction anisotropic conductivity causes the extreme absolute value of the apparent polarizability to greatly increase compared with the isotropy. It should be noted that the extreme position of the apparent polarizability is near 600 m regardless of the position of the emitter. The apparent polarizability curve of the y-direction anisotropic conductivity is basically consistent with the response curve for the isotropic condition and is independent of the position

of the emission source. The apparent polarizability curve of the z-direction anisotropic conductivity exhibits obvious characteristics and is related to the position of the emitter. When the emitter and plate are located at the same depth, the absolute value of the apparent polarizability only slightly increases. When the emitter is located at 400 and 800 m, the absolute value of the extreme value of the apparent polarizability increases, and the position shifts downward for the emitter located at 400 m and upward for the emitter located at 800 m.

Figure 12 presents the response curves of the apparent resistivity and apparent polarizability produced by the emission sources at different locations under the anisotropic conductivity condition for the inclined plate-like body. The curves of the apparent resistivity and apparent polarizability at y-direction anisotropy are consistent with the isotropic characteristics, but the extreme value decreases and the position shifts upward compared with the horizontal plate-like body. The anisotropic response characteristic in the z-direction is more distinct. The inclination of the plate-like body causes the extreme value of the z-direction anisotropic apparent resistivity to be less than the isotropy at the 600 and 800 m emitters, and the extreme value shifts downward. However, the extreme value of the apparent resistivity at the location of the 400 m emitter is greater than the isotropy, and its position shifts upward. The apparent polarizability also changes obviously at the locations of the 600 and 800 m emitters. Compared to the horizontal plate-like body, the absolute value of the extreme value of the apparent polarizability increases and its position shifts upward.

4.3 Polarizability is anisotropic and conductivity is isotropic of abnormal body

To better analyze the effects of the anisotropy of the anomaly's polarizability on the apparent resistivity and apparent polarizability, it is assumed that the conductivity of the anomalous body is isotropic and the polarizability of the anomalous body is anisotropic in different principal axis directions. The anisotropy polarizability tensors of the two models are $\eta = \begin{pmatrix} 0.2 & 0 & 0 \\ 0 & 0.5 & 0 \\ 0 & 0 & 0.5 \end{pmatrix}$, $\eta = \begin{pmatrix} 0.5 & 0 & 0 \\ 0 & 0.2 & 0 \\ 0 & 0 & 0.5 \end{pmatrix}$ and $\eta = \begin{pmatrix} 0.5 & 0 & 0 \\ 0 & 0.5 & 0 \\ 0 & 0 & 0.2 \end{pmatrix}$, and the isotropy tensor of the conductivity of the anomalous body is set $\sigma = \begin{pmatrix} 1 & 0 & 0 \\ 0 & 1 & 0 \\ 0 & 0 & 1 \end{pmatrix} S \cdot m^{-1}$. An isotropic medium with a surrounding rock conductivity of $0.01 S \cdot m^{-1}$, the polarizability is set to 0, and an excitation current is 50 A. Because the anisotropy of the anomalous polarizability for each different emitter model does not affect the apparent resistivity and corresponds to the apparent resistivity when the principal axis is isotropic, we only need to compare the influence of the anisotropic apparent polarizability of each different emitter model in the different principal axis directions.

Figure 13 presents the apparent polarizability response curves for the horizontal plate-like body when the polarizability is anisotropic in different principal axis directions. It can be seen from the diagrams for the three different emission source models that the x-direction anisotropic polarizability has the greatest influence on the apparent polarizability, which leads to a significant decrease in the extreme absolute value of the apparent polarizability at the center of the abnormal body, and the absolute values of the apparent polarizability in the upper and lower parts of the abnormal body are reduced to a certain extent. The responses of the apparent polarizability for anisotropy and isotropy of polarizability in the y-direction are almost the same, and it only increases slightly at the minimum position. When the polarizability is anisotropic in the z-direction, the apparent polarizability of the emitter model at 600 m is similar to that in the isotropic case, and it increases slightly at the minimum position. The apparent polarizability only changes at 400 and 800 m. When the emitter is located at 400 m, the minimum value of the apparent polarizability at the center of the anomalous body increases slightly and the extreme center shifts upward. The apparent polarizability above the anomaly body is larger than that for the isotropic case, while the apparent polarizability below the anomaly body is smaller than that for the isotropic case. When the source is located at 800 m, the change in the apparent polarizability is the opposite to that when the source is located at 400 m.

Figure 14 presents the apparent polarizability response curves when the polarizability is anisotropic in different principal axis directions for the inclined plate. Compared with that for the horizontal plate, the apparent polarizability curves change greatly when the abnormal body is tilted. In particular, the anisotropy characteristics of the abnormal body are most obvious when excited at the upper and lower positions of the abnormal body is located at 400 and 800 m, respectively, and the response curves fluctuate strongly. Compared to the horizontal plate, the extreme position of the apparent polarizability curves of the x-direction anisotropic polarizability shifts downward and upward. The apparent polarizability curves of the *y*-axis anisotropic polarizability are basically the same as for the case in which the polarizability is isotropic, but the position of the extreme value is different from that for the horizontal plate-like body. When the polarizability is anisotropic in the z-direction, the extreme apparent polarizability of the emitter at 400 m is almost the same as that for the isotropic case, and the absolute values of the extreme apparent polarizability for the other two emitters decrease. Consistent with the anisotropic conductivity of the anomalous body, the inclination of the plate-like body causes the absolute value of the extreme apparent polarizability of the emitter to decrease greatly when the emitter is located at 400 m. For both the horizontal and inclined plate-like bodies, it was found that the absolute value of the apparent polarizability is the largest when the emitter is located at 600 m, that is, the response characteristics of the emitter located closest to the anomalous body are the most obvious when the emitter is located at 600 m.

4.4 Conductivity and polarizability of abnormal body are anisotropic

To analyze the influences of the anisotropy of the conductivity and polarizability of the anomalous bodies on the apparent resistivity and apparent polarizability in the cross-well induced polarization method, the anisotropy tensors of the conductivity of the anomalous bodies in the two models

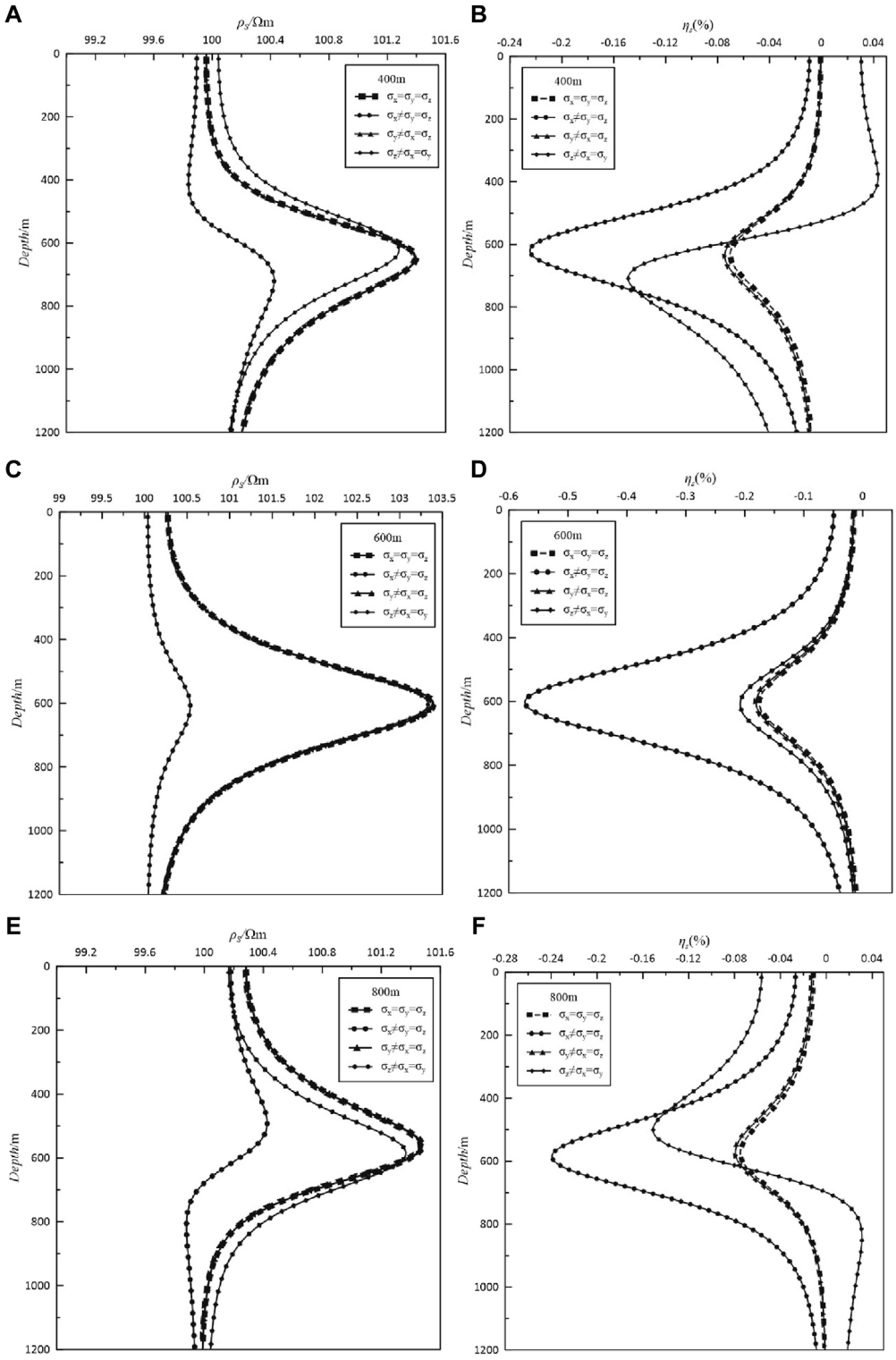

FIGURE 11
Curves of the anisotropy of the conductivity of the horizontal plate-like body (left **(A,C,E)**: apparent resistivity, and right **(B,D,F)**: apparent polarizability). The response curves with squares are the results of isotropic anomalies, the response curves with dots are the results of anisotropic anomalies of conductivity in the x-direction, the response curves with triangles are the results of anisotropic anomalies of conductivity in the y-direction, and the response curves with rhombuses are the ones of anisotropic anomalies of conductivity in the z-direction.

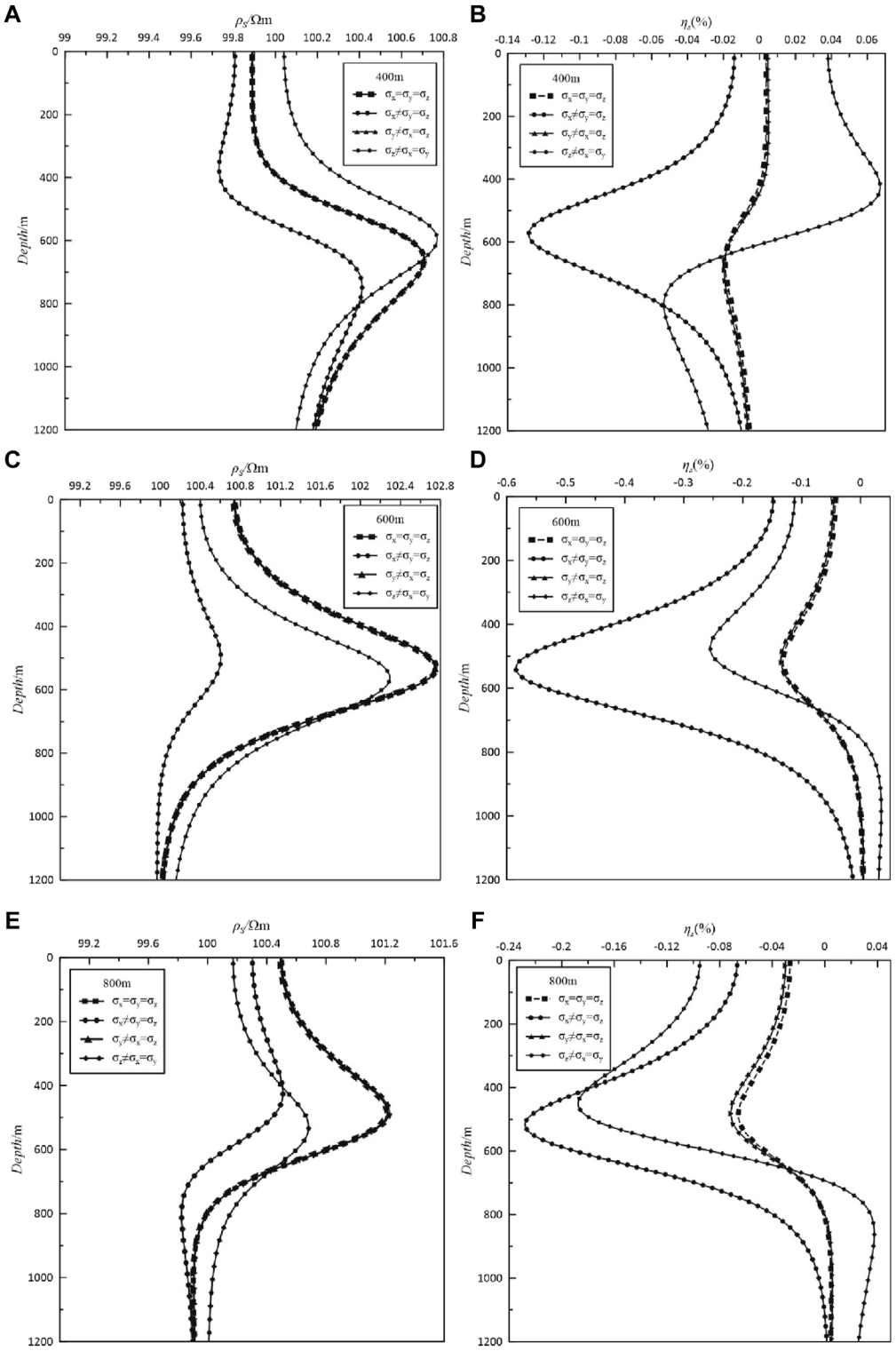

FIGURE 12
Curves of the anisotropy of the conductivity of the inclined plate-like body (left: **(A,C,E)** apparent resistivity, and right: **(B,D,F)** apparent polarizability). The response curves with squares are the results of isotropic anomalies, the response curves with dots are the results of anisotropic anomalies of conductivity in the x-direction, the response curves with triangles are the results of anisotropic anomalies of conductivity in the y-direction, and the response curves with rhombuses are the results of anisotropic anomalies of conductivity in the z-direction.

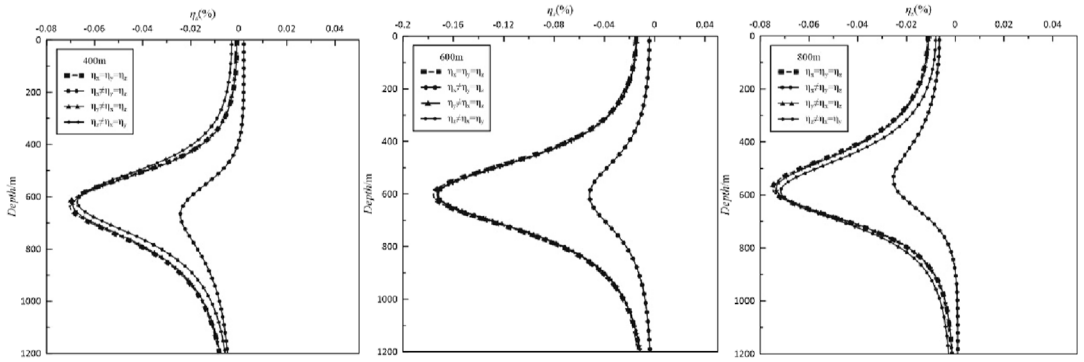

FIGURE 13
Curves of the anisotropic apparent polarizability for the horizontal plate-like body. The response curves with squares are the results of isotropic anomalies, the response curves with dots are the results of anisotropic anomalies of polarizability in the x-direction, the response curves with triangles are the results of anisotropic anomalies of polarizability in the y-direction, and the response curves with rhombuses are the results of anisotropic anomalies of polarizability in the z-direction.

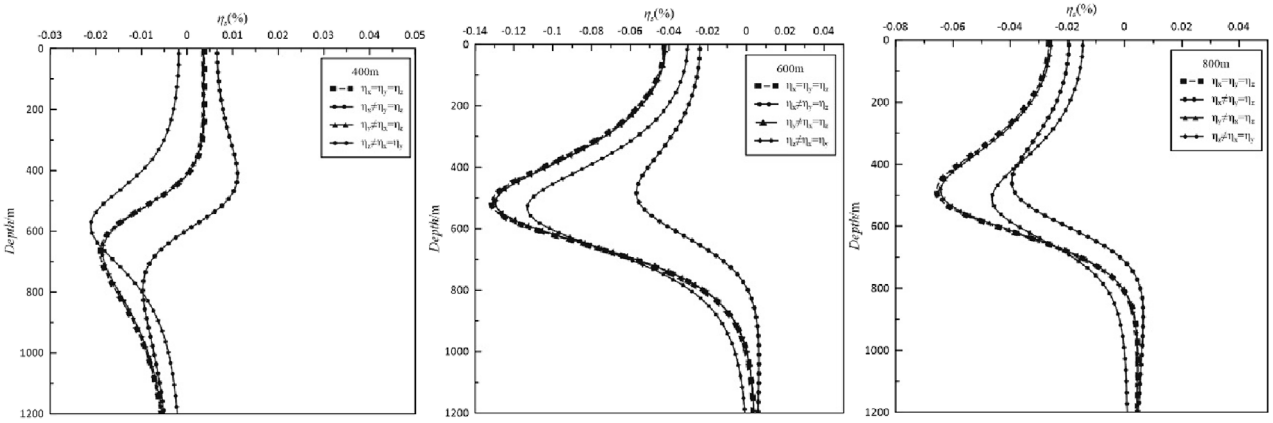

FIGURE 14
Curves of the anisotropic apparent polarizability anomaly for the inclined plate-like body. The response curves with squares are the results of isotropic anomalies, the response curves with dots are the results of anisotropic anomalies of polarizability in the x-direction, the response curves with triangles are the results of anisotropic anomalies of polarizability in the y-direction, and the response curves with rhombuses are the results of anisotropic anomalies of polarizability in the z-direction.

are set as $\sigma = \begin{pmatrix} 0.02 & 0 & 0 \\ 0 & 1 & 0 \\ 0 & 0 & 1 \end{pmatrix} S \cdot m^{-1}$, $\sigma = \begin{pmatrix} 1 & 0 & 0 \\ 0 & 0.02 & 0 \\ 0 & 0 & 1 \end{pmatrix} S \cdot m^{-1}$ and $\sigma = \begin{pmatrix} 1 & 0 & 0 \\ 0 & 1 & 0 \\ 0 & 0 & 0.02 \end{pmatrix} S \cdot m^{-1}$. When the anisotropic tensors of the polarizability of the anomalous bodies are set as $\eta = \begin{pmatrix} 0.2 & 0 & 0 \\ 0 & 0.5 & 0 \\ 0 & 0 & 0.5 \end{pmatrix}$, $\eta = \begin{pmatrix} 0.5 & 0 & 0 \\ 0 & 0.2 & 0 \\ 0 & 0 & 0.5 \end{pmatrix}$ and $\eta = \begin{pmatrix} 0.5 & 0 & 0 \\ 0 & 0.5 & 0 \\ 0 & 0 & 0.2 \end{pmatrix}$, the conductivity of the surrounding rock is set to $0.01 S \cdot m^{-1}$, and the polarizability is set to 0, the excitation current is 50 A. Similarly, because the anisotropy of the polarizability of the anomalous body does not affect the apparent resistivity, the response of the apparent resistivity of the anomalous body of each different emitter source in the model corresponds to the apparent resistivity of the anisotropy of the conductivity of the anomalous body one by one. Here, we only need to compare the influence of the apparent polarizability of the anisotropic anomalous body of the three emitters in different directions of the principal axis.

Figure 15 presents the apparent polarizability response curves produced by the emitters located at different depths when the conductivity and polarizability of the horizontal plate-like body are anisotropic. Compared with the isotropic case, the responses of the apparent polarizability produced by the three different emitters for the x-direction and y-direction anisotropy exhibit similar change characteristics, and the absolute value of the apparent polarizability extremum increases, but the extreme value changes more when the x-direction anisotropy is greater than the y-direction anisotropy.

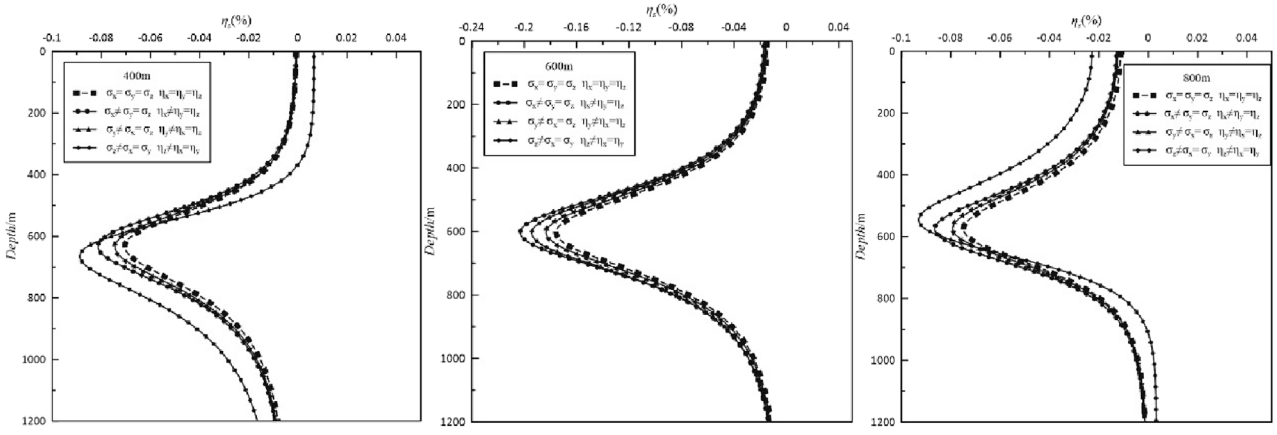

FIGURE 15
Curves of the anisotropic apparent conductivity and polarizability for the horizontal plate-like body. The response curves with squares are the results of isotropic anomalies, the response curves with dots are the results of anisotropic anomalies of conductivity and polarizability in the x-direction, the response curves with triangles are the results of anisotropic anomalies of conductivity and polarizability in the y-direction, the response curves with rhombuses are the results of anisotropic anomalies of conductivity and polarizability in the z-direction.

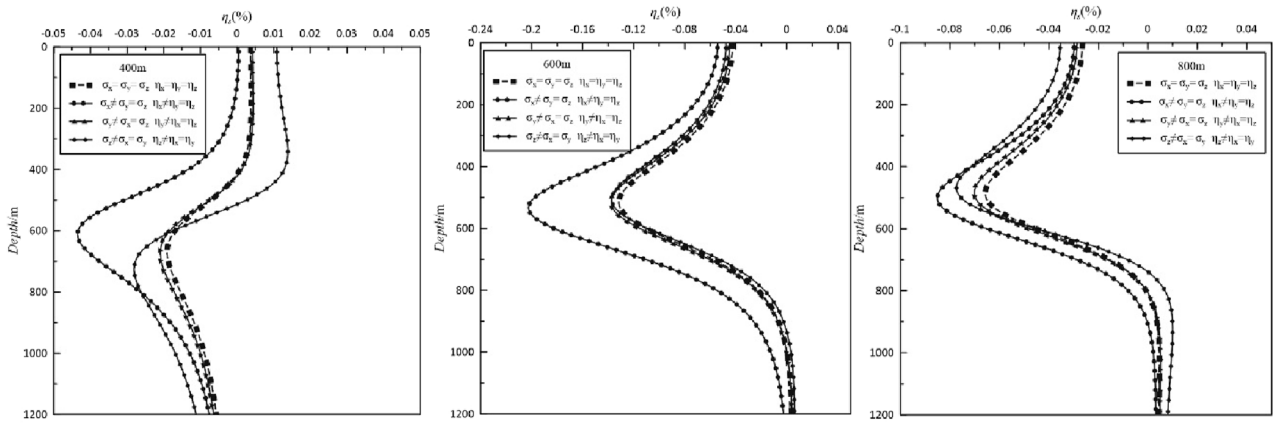

FIGURE 16
Curves of the anisotropic apparent conductivity and polarizability for the inclined plate-like body. The response curves with squares are the results of isotropic anomalies, the response curves with dots are the results of anisotropic anomalies of conductivity and polarizability in the x-direction, the response curves with triangles are the results of anisotropic anomalies of conductivity and polarizability in the y-direction, the response curves with rhombuses are the results of anisotropic anomalies of conductivity and polarizability in the z-direction.

When z-direction anisotropy is maintained at 600 m emission, the apparent polarizability extreme position is maintained near 600 m. Compared to the isotropic case, only the absolute value of the extreme value increases, and the variation characteristics are different at 400 and 800 m. Although both positions lead to an increase in the absolute value of the extreme value, the position of the extreme value shifts in the opposite directions. It shifts downward for the 400 m case and upward for the 800 m case. Figure 16 shows the curves of the response of the apparent polarizability produced by emitters located at different depths when the conductivity and polarizability of the inclined plate-like body are anisotropic. Compared to the horizontal plate-like body, the absolute value of the extreme value of apparent polarizability for the x-direction anisotropy increases more than that for the isotropic case, and the position of the extreme value shifts upward. For the *y*-axis and *z*-axis anisotropy, on the response curves of the emitter located at 800 m, the position of the extreme value shifts upward. When the emitter is located at 600 m, the position of the extreme value shifts upward and the absolute value of the extreme value decreases. When the emitter is located at 400 m, the change is greater. The inclination of the plate-like body controls the overall trend of change of the apparent polarizability curves. It should be noted that the electrical response curves for the *y*-axis anisotropy are basically consistent with the typical response curves for the isotropic case when the of the conductivity and polarizability is anisotropic in different principal axis directions or when the anomalous body is inclined.

5 Conclusion

(1) Through forward response calculations and analysis of the electrical anisotropic models of horizontal and inclined plate-like bodies, it was found that for the cross-well induced polarization method, when the electrical properties of plate-like bodies are isotropic in different principal axis directions, the extreme values of absolute values of the apparent resistivity and apparent polarizability of the emission source at 600 m are the maximum due to the attraction of the underground low resistivity to the current. There are many differences in the positions where the extreme values of the electrical curves appear due to the different positions of the emitters. When the plate-like body is inclined, the amplitudes of all of the curves decrease and shift upward.

(2) When the conductivity is anisotropic in different principal axis directions, for the horizontal plate-like body, the x-direction anisotropic conductivity has the greatest influence on the electrical characteristics and the apparent polarizability is more obvious than the apparent resistivity. In addition, the position of the emitter has an obvious influence on the apparent polarizability when the conductivity is anisotropic in z-direction. The inclination of the plate-like body causes the apparent resistivity and apparent polarizability curves to have different effects, but the extreme values of the absolute values of the apparent resistivity and apparent polarizability will decrease.

(3) When the polarizability is anisotropic in different principal axis directions, for the horizontal plate-like body, only the x-direction anisotropy has an obvious effect on the apparent polarizability curve. The y-direction and z-direction anisotropy has the same apparent polarizability curve as that for the isotropic case. The inclination of the plate-like body causes the apparent polarizability curve to change greatly. In particular, when excited at 400 m and 800 m, the anisotropy characteristics of the anomalous body are most obvious, and the response curves fluctuate strongly.

(4) When the conductivity and polarizability of the plate-like body are anisotropic, the responses of the apparent polarizability of the horizontal plate-like body when the x-direction and y-direction anisotropy are similar to those for the isotropic case, while z-direction anisotropy has a more complex influence. The inclination of the plate-like body causes the extreme position of the x-direction anisotropic apparent polarizability to shift upward. For y-direction and z-direction anisotropy, when the emitter is located above the inclined plate-like body, the overall change trend of the apparent polarizability curves decreases. It was found that for the induced polarization method, the response in a borehole is complex and changeable, and the inclination of the abnormal body also affects the response. The results of this study provide theoretical support for the study of the anisotropy of induced polarization in boreholes. In this paper, inversion is conducted to further verify and expand the forward work, so subsequent inversion work was very necessary for this study.

Data availability statement

The original contributions presented in the study are included in the article/supplementary material, further inquiries can be directed to the corresponding author.

Author contributions

ZJ: Writing–original draft. ZL: Writing–review and editing. WX: Writing–review and editing. XX: Writing–review and editing. MY: Writing–review and editing. YL: Writing–review and editing.

Funding

The author(s) declare that financial support was received for the research, authorship, and/or publication of this article. This study was funded by the National Natural Science Foundation of China (42030805 and 42274103).

Conflict of interest

The authors declare that the research was conducted in the absence of any commercial or financial relationships that could be construed as a potential conflict of interest.

Publisher's note

All claims expressed in this article are solely those of the authors and do not necessarily represent those of their affiliated organizations, or those of the publisher, the editors and the reviewers. Any product that may be evaluated in this article, or claim that may be made by its manufacturer, is not guaranteed or endorsed by the publisher.

References

Arato, A., and Godio, A. (2014). Staggered grid inversion of cross hole 2-D resistivity tomography. *J. Appl. Geophys.* 107, 60–70. doi:10.1016/j.jappgeo.2014.05.004

Cao, H. (2004). Summary of borehole geophysical technology. *Adv. Explor. Geophys.* (04), 235–240.

Deng, B., and Li, J. Z. (2014). Application effect of borehole geophysical prospecting method in metal ore exploration. *Sichuan J. Geol.* 34 (02), 276–280.

Di, Q. Y., and Wang, M. Y. (1997). Preliminary study on current line tracing potential resistivity tomography. *Adv. Geophys.* (04), 27–35.

Dong, Q. H. (1997). Some advances in cross-well resistivity tomography. *Adv. Geophys.* (03), 77–89.

Dong, Q. H., and Zhu, J. S. (1999). Cross-well resistivity tomography and its application. *Comput. Phys.* (05), 474–480. doi:10.19596/j.cnki.1001-246x.1999.05.004

Feng, J., Liu, T. Y., Yang, Y. S., and Gao, W. L. (2010). Combined inversion technology of 3D borehole geomagnetic survey and its application. *J. Adv. Geophys.* 25 (05), 1685–1691.

Harold, O. S. (1959). Mathematical formulation and type curves for induced polarization. *Geophysics* 24 (3), 547–565. doi:10.1190/1.1438625

Hou, J., Mallan, R. K., and Torres-Verdi, N. (2006). Finite-difference simulation of borehole EM measurements in 3D anisotropic media using coupled scalar-vector potentials. *Geophysics* 71 (5), G225–G233. doi:10.1190/1.2245467

Hu, D., Yang, X., Yue, M., Li, Y., and Wu, X. (2021). Prediction model for advanced detection of water-rich faults using 3D anisotropic resistivity modeling and Monte Carlo methods. *IEEE Access* 9, 18251–18261. doi:10.1109/access.2021.3053861

Hu, D. M., Tezkan, B., Niu, H., Yue, M., Yang, X., and Wu, X. (2023). 3D time-domain induced polarization modelling considering anisotropy and topography. *J. Appl. Geophys.* 208, 104871. doi:10.1016/j.jappgeo.2022.104871

Kenkel, J., Hördt, A., and Kemna, A. (2012). 2D modelling of induced polarization data with anisotropic complex conductivities. *Near Surf. Geophys.* 10 (6), 533–544. doi:10.3997/1873-0604.2012050

Lamontagne, Y. (2024). *Deep exploration with EM in boreholes*.

Lin, S. Z. (1998). Solving finite element equations by preconditioned conjugate gradient method and programming. *J. Hohai Univ.* (03), 114–117.

Linde, N., and Pedersen, L. B. (2004). Evidence of electrical anisotropy in limestone formations using the RMT technique. *Geophysics* 69 (4), 909–916. doi:10.1190/1.1778234

Liu, G. Q., Tao, G., Ke, S. Z., Yang, H. Z., and Jiang, J. Y. (2001). A perturbation method for resistivity tomography of Frechet derivative. *Seismol. Geol.* (02), 314–320.

Liu, Y. Z., Yin, C. C., Cai, J., et al. (2018). Present situation and prospect of anisotropy research in electromagnetic exploration. *J. Geophys.* 61 (08), 3468–3487.

Lv, Y. Z., Ruan, B. Y., and Huang, J. G. (2003). The 3-D immediate Cross hole tomography with direct current. *Geophys. Geochem. Comput. Tech.* (01), 60–64.

Lv, Y. Z., Ruan, B. Y., and Peng, S. P. (2012). Study on anomaly characteristics of ground-well azimuth IP observation. *Adv. Geophys.* 27 (01), 201–216. doi:10.6038/j.Issn.1004-2903.2011.06.023

Mcmonnies, B. (2007). "Ground geophysics and borehole logging-A decade of implements," in Exploration in the New Millennium: Proceedings of the Fifth Decennial International Conference on Mineral Exploration, pp. 39–49.

Mi, H. Z. (2019). Research status and development of underground geophysical exploration technology for metal deposits. *Mineral. Explor.* 10 (03), 601–605.

Pek, J., and Santos, A. M. (2006). Magnetotelluric inversion for anisotropic conductivities in layered media. *Phys. Earth and Planet. Interiors* 158 (2-4), 139–158. doi:10.1016/j.pepi.2006.03.023

Schmutz, M., Albouy, Y., Guérin, R., Maquaire, O., Vassal, J., Schott, J. J., et al. (2000). Joint electrical and time domain electromagnetism (TDEM) data inversion applied to the Super Sauze earthflow (France). *Surv. Geophys.* 21, 371–390. doi:10.1023/a:1006741024983

Shima, H. (1987). Resistivity tomography: an approach to 2-Dreistivity inverse problems. *Ann.internat.mtg.soc.expl.geophys.expanded Abstr.* (1), 59–61. doi:10.1190/1.1892038

Stolz, E. M. (2000). Electromagnetic methods applied to exploration for deep nickel sulphides in the Leinster area, Western Australia. *Explor. Geophys.* 31 (2), 222–228. doi:10.1071/eg00222

Wang, Q. Y., and Hu, Y. P. (2004). Thoughts on the shortage of metal resources and prospecting for concealed deposits. *J. Geol. Explor.* 2004 (06), 75–79.

Wang, T. (2002). The electromagnetic smoke ring in a transversely isotropic medium. *Geophysics* 67, 1779–1789. doi:10.1190/1.1527078

Wang, Z. (2015). *Forward and inversion of IP in borehole and its application*. Wuhan, China: China University of Geosciences.

Xiong, F., Lv, Y. Z., and Li, Y. (2016). Study on 2.5-dimensional approximate imaging of well-well resistivity. *Geophys. Geochem. Calc. Technol.* 38 (03), 308–313.

Xiong, P. (2004). Progress and prospect of geophysical prospecting technology in China. *Pet. Geophys. Explor.* (03), 354–358.

Xiong, Z. T., Tang, X. G., and Li, D. D. (2023). Arbitrarily anisotropic forward modeling of the 3D borehole-to-surface resistivity method based on unstructured grid finite element. *Chin. J. Geophys.* 66 (05), 2201–2218. doi:10.6038/cjg2022Q0830

Xu, S. Z. (1994). *Finite element method in geophysics*. Beijing: Science Press.

Yan, Y. J., Zhou, L., Xie, X. B., and Wang, Z. G. (2014). Transient electromagnetic response of reservoir electrical anisotropy model. *J. Eng. Geophys.* 11 (03), 346–350. doi:10.3969/j.issn.1672-7940.2014.03.013

Yin, C. C. (2010). Geoelectrical inversion for a one-dimensional anisotropic model and inherent non-uniqueness. *Geophys. J. Int.* 140 (1), 11–23. doi:10.1046/j.1365-246x.2000.00974.x2000.00974.X

Yu, A. J., Huang, H., Xu, D. L., Fan, Z. J., and Chen, X. Q. (2006). Application of comprehensive electrical method in searching for concealed deposits in Haxi gold mining area, Xinjiang. *Geol. Explor.* (06), 57–61.

Yuan, G. Q., Xiong, S. Q., Meng, Q. M., et al. (2011). Research on geophysical exploration technology and application. *J. Geol.* 85 (11), 1744–1805.

Zhdanov, M. S., and Yoshioka, K. (2003). Cross-well electromagnetic imaging in three dimensions. *Explor. Geophys.* 34 (2), 34–40. doi:10.1071/eg03034

Zhou, P., Chen, S. L., and Zhu, L. L. (2009). Review of several underground geophysical prospecting methods for metal deposits. *Geol. Bull.* 28 (Z1), 224–231.

Zhu, J., Yin, C. C., Ren, X. Y., Liu, Y. H., Hui, Z. J., and Gu, Y. (2021). Forward modeling of DC resistivity in arbitrary anisotropic media by three-dimensional unstructured spectral element method. *J. Geophys.* 64 (12), 4644–4657. doi:10.6038/cjg2021p0199

frontiers | Frontiers in Earth Science

TYPE Original Research
PUBLISHED 22 August 2024
DOI 10.3389/feart.2024.1454962

OPEN ACCESS

EDITED BY
Ying Liu,
China University of Geosciences
Wuhan, China

REVIEWED BY
Ningbo Bai,
Henan Polytechnic University, China
Changhong Lin,
China University of Geosciences, China

*CORRESPONDENCE
Qi-Ji Sun,
sunqiji422@126.com

RECEIVED 26 June 2024
ACCEPTED 12 August 2024
PUBLISHED 22 August 2024

CITATION
Liu X and Sun Q-J (2024) A study of 3D axis anisotropic response of MT.
Front. Earth Sci. 12:1454962.
doi: 10.3389/feart.2024.1454962

A study of 3D axis anisotropic response of MT

Xiao Liu and Qi-Ji Sun*

School of Hydraulic and Electric-Power, Heilongjiang University, Harbin, China

Electrical anisotropy has a significant impact on the observation data of the magnetotelluric (MT) method; therefore, it is necessary to develop forward and inverse methods in electrical anisotropic media. Based on the axis anisotropic electric field control equations, forming a large linear equation through staggered finite difference approximation, adding boundary conditions, and using the quasi-minimum residual method to solve the equation, this study obtained MT forward modeling results in axis anisotropic media. The correctness of the algorithm was verified by comparing it with the 2D quasi-analytic solution. By designing several sets of axis anisotropic 3D models, the characteristics of the apparent resistivity tensor and tipper were analyzed. The results indicated that the ρ^a_{xy}, ρ^a_{yy} and T_{zy} are sensitive to changes in resistivity in the X direction of the anomalous body, whereas the ρ^a_{yx}, ρ^a_{xx} and T_{zx} are sensitive to changes in resistivity in the Y direction. The apparent resistivity tensor and tipper are insensitive to changes in resistivity in the Z direction of the anomalous body. For exploration of anisotropic media, the apparent resistivity tensor and tipper of MT can identify the changes in resistivity in two horizontal axes directions and the boundaries of the anomalous body, which has the advantages for exploration.

KEYWORDS

MT, axis anisotropy, response characteristic, finite difference method, forward-backward algorithm

1 Introduction

Anisotropy is commonly present in the crust and upper mantle. Fractures and rock bedding in certain specific directions, as well as the stacking combination of uniform thin layers with different properties, can cause electrical anisotropy in the lithospheric structure (Postma, 1955; Wannamaker, 2005). The practice and research of geophysical exploration have shown that electrical anisotropy has a significant impact on electromagnetic observation data and that directly using isotropic models to fit data containing electrical anisotropy can result in significant errors (Yin and Weidelt, 1999; Liu and Zheng, 2024). Therefore, to improve the accuracy of electromagnetic inversion results, including magnetotelluric methods, and the level of understanding of underground structures, it is necessary to develop electromagnetic data processing and inversion methods based on anisotropic models (Liu Y. H. et al., 2018).

Research on magnetotelluric anisotropy has been increasing (Qin et al., 2022). Based on 2D numerical forward modeling techniques (Pek and Verner, 1997; Li, 2002), 3D forward modeling research results, especially the finite volume method (Han et al., 2018), the finite element method (Cao et al., 2018; Xiao et al., 2018; Liu Y. et al, 2018; Guo et al., 2020; Ye et al., 2021; Zhou et al., 2021) and the finite difference method (Yu et al., 2018; Kong, 2021), continue to emerge. The finite element method has strong simulation ability for complex shapes and terrains, and it

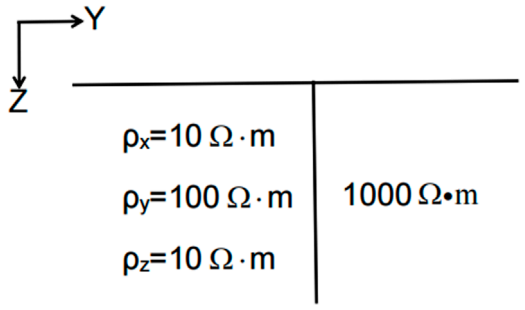

FIGURE 1
Sketch of the 2D axis anisotropic model.

establishes variational equations through the Galerkin method. A weighted posterior error estimation method was constructed using the continuity condition of current density, which has been used to calculate the magnetotelluric (MT) response of arbitrary anisotropic media (Cao et al., 2018). The finite difference method ensures that the distribution of the electromagnetic field satisfies the law of energy conservation and also simplifies the derivation of the equations.

Because of the complexity of numerical simulation for arbitrary anisotropy, this study considers the case of axis anisotropy. Axis anisotropy can be understood as the difference in conductivity in the three directions of the medium caused by factors such as mineral orientation. The conductivity tensor of arbitrary anisotropy can be obtained by three Euler rotations of the axis anisotropy. Kong (2021) used direct discretization of Maxwell's equations to achieve MT anisotropic forward modeling. In this study, the electric field control equation is solved to achieve MT axis anisotropic forward modeling. The algorithm is implemented by Fortran program. The response characteristics of the axis anisotropic target body are analyzed through three numerical examples, providing a basis for conducting MT forward and reverse modeling research with arbitrary anisotropy.

2 MT 3D forword modeling method

2.1 Finite difference method for calculating MT fields

For isotropic media, ignoring displacement current, the frequency domain control equation of the magnetotelluric method is

$$\nabla \times \mathbf{E} = i\omega\mu_0\mathbf{H} \tag{1}$$

$$\nabla \times \mathbf{H} = \sigma\mathbf{E} \tag{2}$$

where ∇ represents the Nabla operator, $\mathbf{E}$ represents the electric field, i represents an imaginary unit, ω represents the angular frequency, μ_0 represents the vacuum magnetic permeability, $\mathbf{H}$ represents the magnetic field, and σ represents the conductivity.

After organizing Equations 1, 2, the following electric field control equation is obtained:

$$\nabla \times \nabla \times \mathbf{E} = i\omega\mu_0\sigma\mathbf{E} \tag{3}$$

For 3D axis anisotropic medial, the tensor conductivity is

$$\boldsymbol{\sigma} = \begin{pmatrix} \sigma_x & 0 & 0 \\ 0 & \sigma_y & 0 \\ 0 & 0 & \sigma_z \end{pmatrix} \tag{4}$$

By substituting Equation 4 into Equation 3 and organizing, the following equations can be obtained:

$$\frac{\partial}{\partial y}\left[\frac{\partial E_y}{\partial x} - \frac{\partial E_x}{\partial y}\right] - \frac{\partial}{\partial z}\left[\frac{\partial E_x}{\partial z} - \frac{\partial E_z}{\partial x}\right] = \omega\mu_0\sigma_x E_x \tag{5}$$

$$\frac{\partial}{\partial z}\left[\frac{\partial E_z}{\partial y} - \frac{\partial E_y}{\partial z}\right] - \frac{\partial}{\partial x}\left[\frac{\partial E_y}{\partial x} - \frac{\partial E_x}{\partial y}\right] = i\omega\mu_0\sigma_y E_y \tag{6}$$

$$\frac{\partial}{\partial x}\left[\frac{\partial E_x}{\partial z} - \frac{\partial E_y}{\partial x}\right] - \frac{\partial}{\partial y}\left[\frac{\partial E_z}{\partial y} - \frac{\partial E_y}{\partial z}\right] = i\omega\mu_0\sigma_z E_z \tag{7}$$

Using the staggered finite difference approximation Equations 5–7, the following equation is obtained after sorting (Siripunvaraporna et al., 2005):

$$\mathbf{AX} = \mathbf{b} \tag{8}$$

where $\mathbf{A}$ is a symmetric large sparse coefficient matrix, $\mathbf{X}$ is a vector composed of three components of the electric field at the sampling point, and $\mathbf{b}$ is a vector composed of boundary electric field components.

When a sufficiently thick air layer is added, the influence of anomalous bodies on the top boundary of the air layer can be ignored. The four lateral boundaries can be regarded as 2D geoelectric interfaces, solved using 2D MT anisotropic finite difference codes (Kong, 2021). After introducing the boundary conditions, the three component values of the electric field in the partitioned space are obtained by solving Equation 8 using the quasi-minimum residual (QMR) method, with a preconditioner formed by an incomplete LU decomposition (Siripunvaraporna et al., 2002). To accelerate the convergence of QMR iteration, divergence correction (Smith, 1996) is also applied to the solution of the electric field. The electric and magnetic field components of each measurement point on the surface are obtained through electric field interpolation.

2.2 Calculating tensor impedance and tipper

Calculate the magnetotelluric response using TE and TM polarization simulations, denoted as E_{x1}, E_{y1}, H_{x1}, H_{y1} and H_{z1}, E_{x2}, E_{y2}, H_{x2}, H_{y2} and H_{z2}. So the expressions for the magnetotelluric impedance component and tipper component are obtained:

$$\begin{aligned} Z_{xx} &= \frac{E_{x1}H_{y2} - E_{x2}H_{y1}}{H_{x1}H_{y2} - H_{x2}H_{y1}}, Z_{xy} = \frac{E_{x2}H_{y1} - E_{x1}H_{x2}}{H_{x1}H_{y2} - H_{x2}H_{y1}} \\ Z_{yx} &= \frac{E_{y1}H_{y2} - E_{y2}H_{y1}}{H_{x1}H_{y2} - H_{x2}H_{y1}}, Z_{yy} = \frac{E_{y2}H_{x1} - E_{y1}H_{x2}}{H_{x1}H_{y2} - H_{x2}H_{y1}} \end{aligned} \tag{9}$$

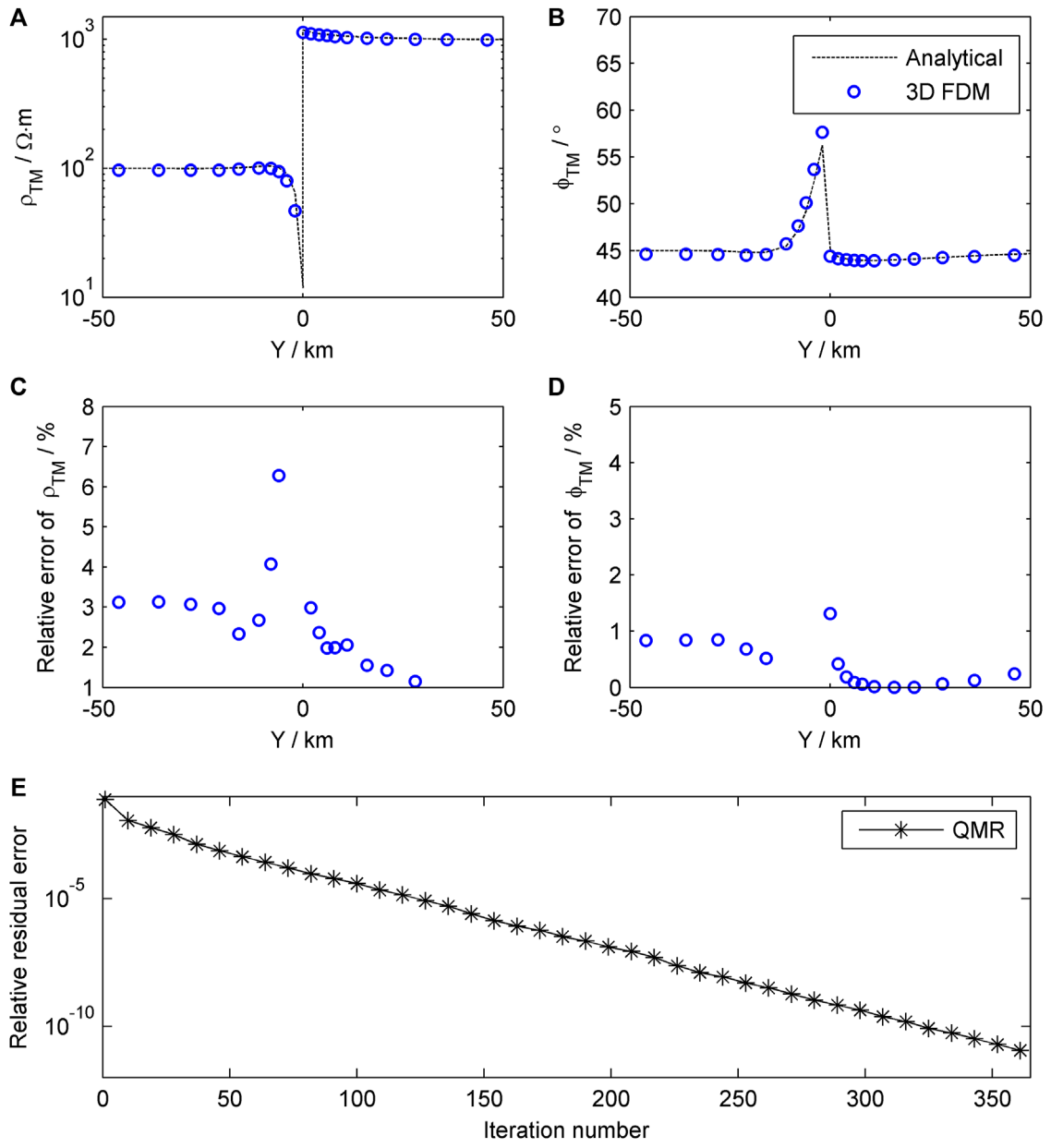

FIGURE 2
Comparison of the results of 3D forward modeling and 2D quasi-analytic solution **(A–D)** and curve of relative residual error of the QMR iteration **(E)**.

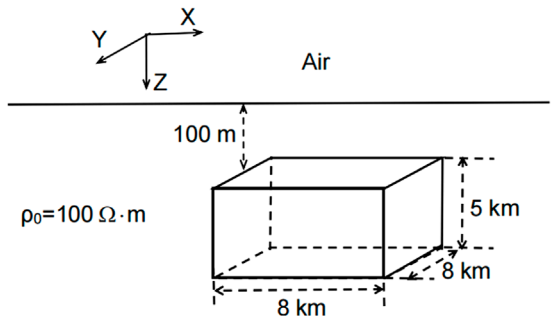

FIGURE 3
Sketch of the 3D axis anisotropic low-resistance model.

$$T_{zx} = \frac{H_{z1}H_{y2} - H_{z2}H_{y1}}{H_{x1}H_{y2} - H_{x2}H_{y1}},\ T_{zy} = \frac{H_{z2}H_{x1} - H_{z1}H_{x2}}{H_{x1}H_{y2} - H_{x2}H_{y1}} \tag{10}$$

The corresponding apparent resistivity tensor and apparent phase tensor are:

$$\begin{aligned} \rho_{ij}^{a} &= \frac{1}{\omega\mu_0}\left|Z_{ij}\right|^2 \\ \phi_{ij} &= \tan^{-1}\left(\mathrm{Im}\left(Z_{ij}\right)/\mathrm{Re}\left(Z_{ij}\right)\right) \end{aligned} \tag{11}$$

where $i = x, y$, $j = x, y$. In the following text, the axial anisotropy response of MT is calculated by Equations 9–11.

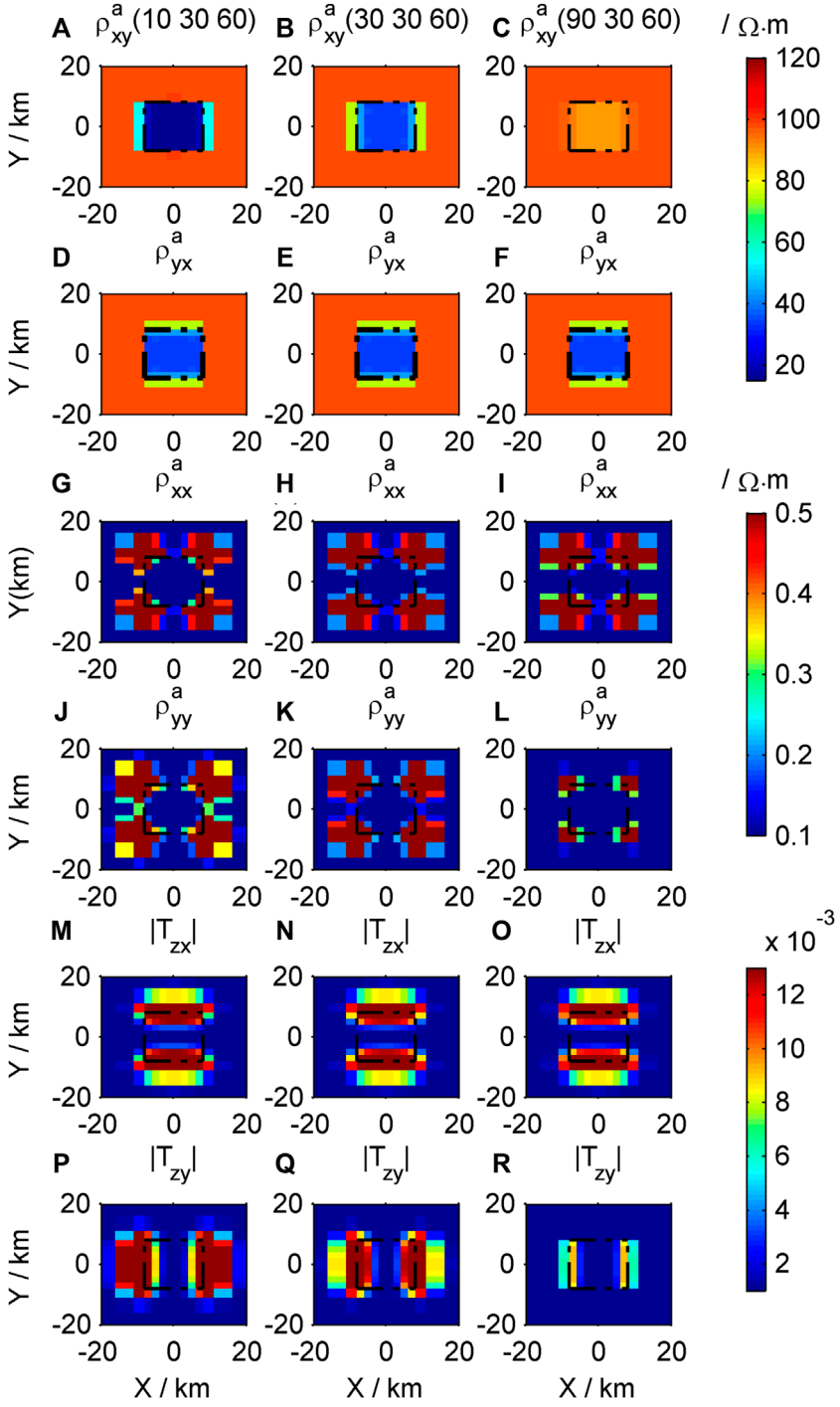

FIGURE 4
Contour maps of the response of the different low-resistivity models in the X direction: **(A–C)** ρ^a_{xy}; **(D–F)** ρ^a_{yx}; **(G–I)** ρ^a_{xx}; **(J–L)** ρ^a_{yy}; **(M–O)** $|T_{zx}|$; **(P–R)** $|T_{zy}|$.

2.3 Algorithm validation

To verify the correctness of the algorithm, we compared it with the quasi-analytic solution of Qin et al. (2013), who established a 2D axis anisotropic upright fault model (Figure 1). The left side of the fault is an axis anisotropic block, with resistivity values of 10, 100, and 10 $\Omega \cdot m$ in the X, Y, and Z directions, respectively. The right side of the fault is an isotropic block, with resistivity values of 1,000 $\Omega \cdot m$. A frequency of 0.1 Hz is used.

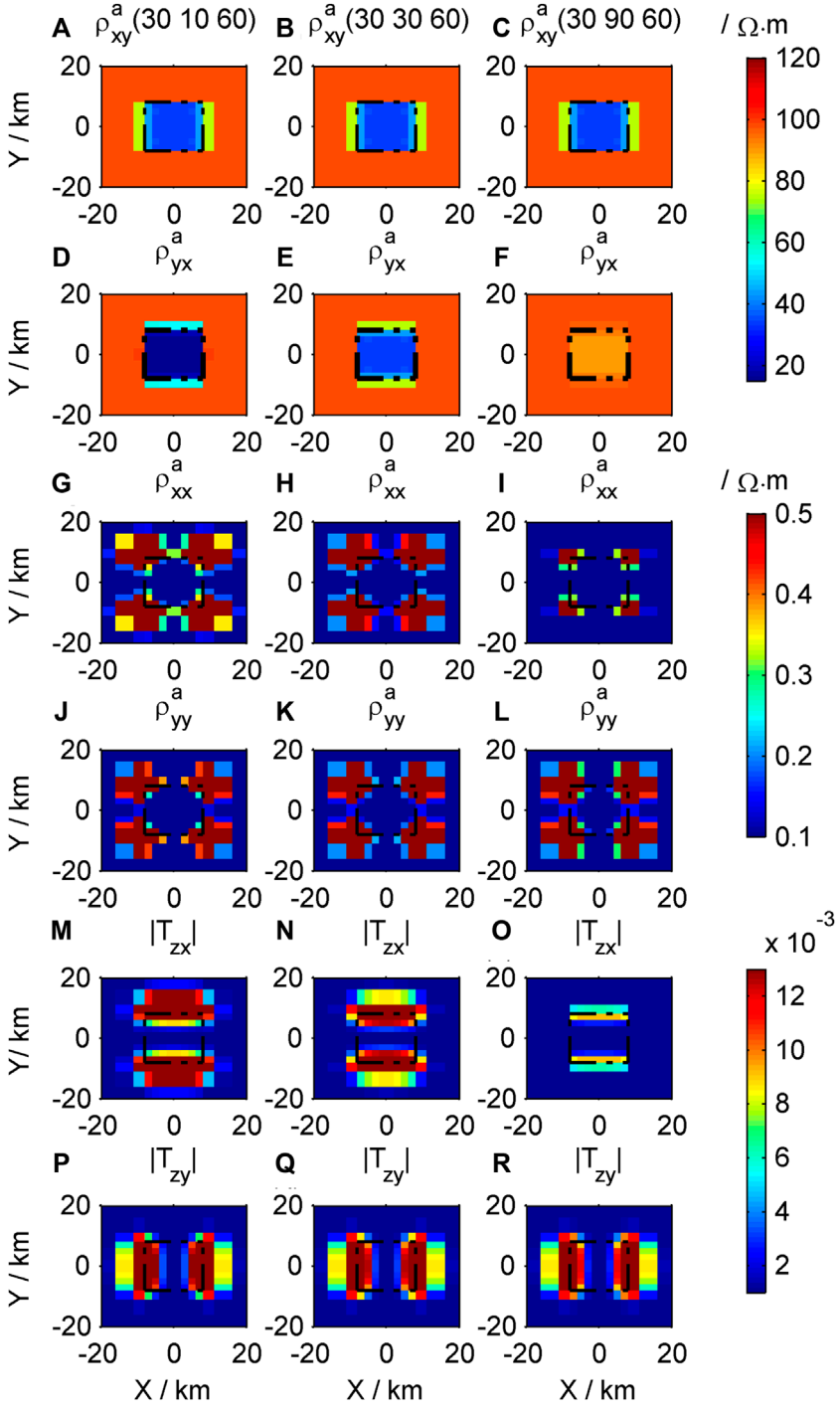

FIGURE 5
Contour maps of the response of the different low-resistivity models in the Y direction: **(A–C)** ρ^a_{xy}; **(D–F)** ρ^a_{yx}; **(G–I)** ρ^a_{xx}; **(J–L)** ρ^a_{yy}; **(M–O)** $|T_{zx}|$; **(P–R)** $|T_{zy}|$.

In TM mode, the comparison results of apparent resistivity and apparent phase and curve of relative residual error of the QMR iteration are shown in Figure 2. The 3D finite difference results and 2D quasi-analytic solution fit well, with only a slight error at the fault interface (Figures 2A–D), indicating that the calculation results of the forward program are correct. The QMR iteration converges stably to the given tolerance (Figure 2E).

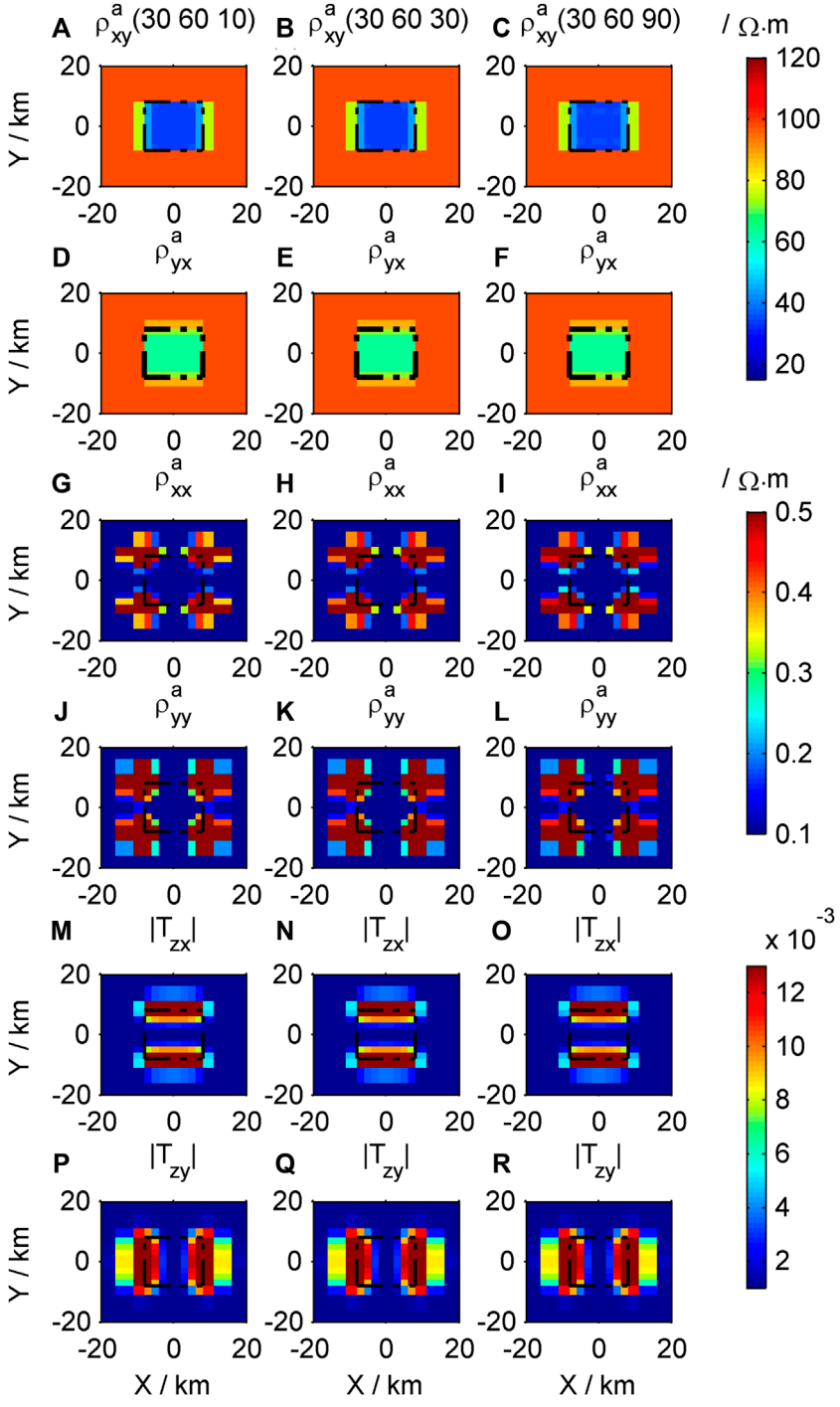

FIGURE 6
Contour maps of the response of the different low-resistivity models in the Z direction: **(A–C)** ρ^a_{xy}; **(D–F)** ρ^a_{yx}; **(G–I)** ρ^a_{xx}; **(J–L)** ρ^a_{yy}; **(M–O)** $|T_{zx}|$; **(P–R)** $|T_{zy}|$.

3 3D axis anisotropic forward modeling case of MT

3.1 Response of 3D axis anisotropic low-resistance prism

The 3D prism model is shown in Figure 3. The top surface of the prism is buried at a depth of 100 m, and the prism has a size of 8 km × 8 km × 5 km. The background resistivity is 100 Ω · *m*, and the mesh size is 28 × 28 × 28, which includes 7 air layers. The frequency of the MT used is 10 Hz.

To study the impact of the axis anisotropy of low-resistance bodies on MT forward modeling, we designed several sets of examples. We first fix the resistivity of the low-resistance body in the *Y* and *Z* directions ($\rho_y = 30\Omega \cdot m$ and $\rho_z = 60\Omega \cdot m$), with resistivity in the X-direction of 10, 30, and 90 Ω · *m*, respectively, and apply

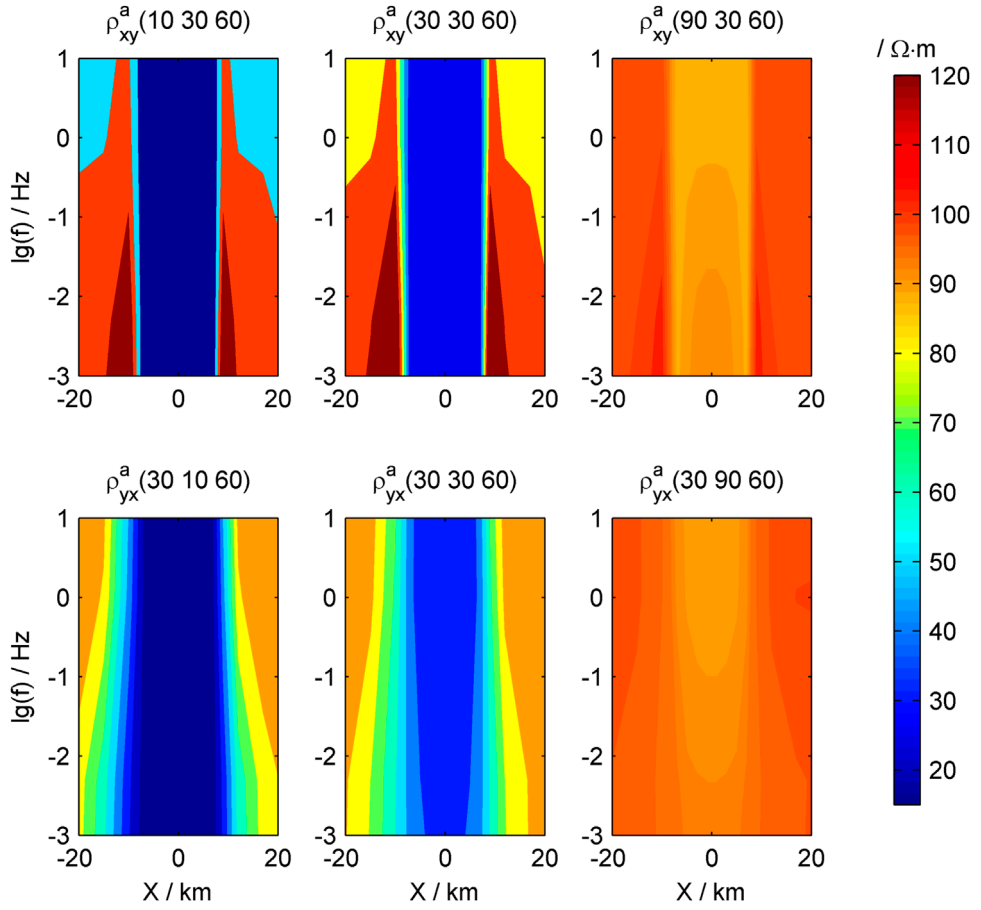

FIGURE 7
Pseudo-contour maps of the apparent resistivity of the low-resistivity body.

the algorithm proposed in this study for forward modeling. The resulting surface contour map is shown in Figure 4. Next, we fix the resistivity of the low-resistance body in the X and Z directions ($\rho_x = 30\Omega \cdot m$ and $\rho_z = 60\Omega \cdot m$), with resistivity in the Y-direction of 10, 30, and 90 $\Omega \cdot m$, respectively. These forward results are shown in Figure 5. Finally, we fix the resistivity of the low-resistance body in the X and Y directions ($\rho_x = 30\Omega \cdot m$ and $\rho_y = 60\Omega \cdot m$), with the resistivity in the Z-direction of 10, 30, and 90 $\Omega \cdot m$, respectively. The forward results for this example are shown in Figure 6.

The apparent resistivity ρ^a_{xy} and ρ^a_{yx} reflects the horizontal position of the low-resistance body, and the apparent resistivity ρ^a_{xx}, ρ^a_{yy}, and the tipper T_{zx}, T_{zy} clearly reflect the horizontal boundary of the low-resistance body (Figure 4). The amplitudes of ρ^a_{yy} and ρ^a_{yx} are much greater than those of ρ^a_{xx} and ρ^a_{yy} (Figures 4A–L). ρ^a_{xy}, ρ^a_{yy}, and T_{zy} are sensitive to changes in resistivity in the X direction (ρ_x) of the low-resistance body. When the resistivity of the low-resistance body is lower, the anomalies it produces are more obvious (Figures 4A–C, J–L, P–R). ρ^a_{yx}, ρ^a_{xx}, and T_{zx} are insensitive to changes in resistivity in the X direction of the low-resistance body (Figures 4D–I, M–O), and are less affected by the resistivity in the X-direction.

ρ^a_{xy}, ρ^a_{yy}, and T_{zy} are insensitive to changes in resistivity in the Y direction (ρ_y) of the low-resistance body, and are less affected by the resistivity in the Y direction (Figures 5A–C, J–L, P–R). ρ^a_{yx}, ρ^a_{xx}, and T_{zx} are sensitive to changes in resistivity in the Y-direction of the low-resistance body. As the resistivity of the low-resistance body becomes lower, the anomalies it produces become more obvious (Figures 5D–I, M–O).

The impacts of resistivity changes in the X and Y directions of the low-resistance body on response results are different.

The apparent resistivity tensor and tipper are not sensitive to changes in resistivity in the Z direction of the low resistivity body (Figures 6A–R), indicating that ρ_z has a weak contribution to the surface response. For MT, in TE mode, the polarization direction of the electric field is mainly in the X direction, therefore it is sensitive to changes in resistivity in the X direction; in TM mode, the polarization direction of the electric field is mainly in the Y direction, therefore it is sensitive to changes in resistivity in the Y direction (Wang et al., 2017).

A contour map of apparent resistivity based on the relationship between apparent resistivity and frequency is shown in Figure 7. The low-value anomaly areas of apparent resistivity ρ^a_{xy} and ρ^a_{yx} are not closed. As the detection depth of MT increases with decreasing frequency, the relatively low-value anomaly areas are equivalent to extending deeper underground (Figure 7).

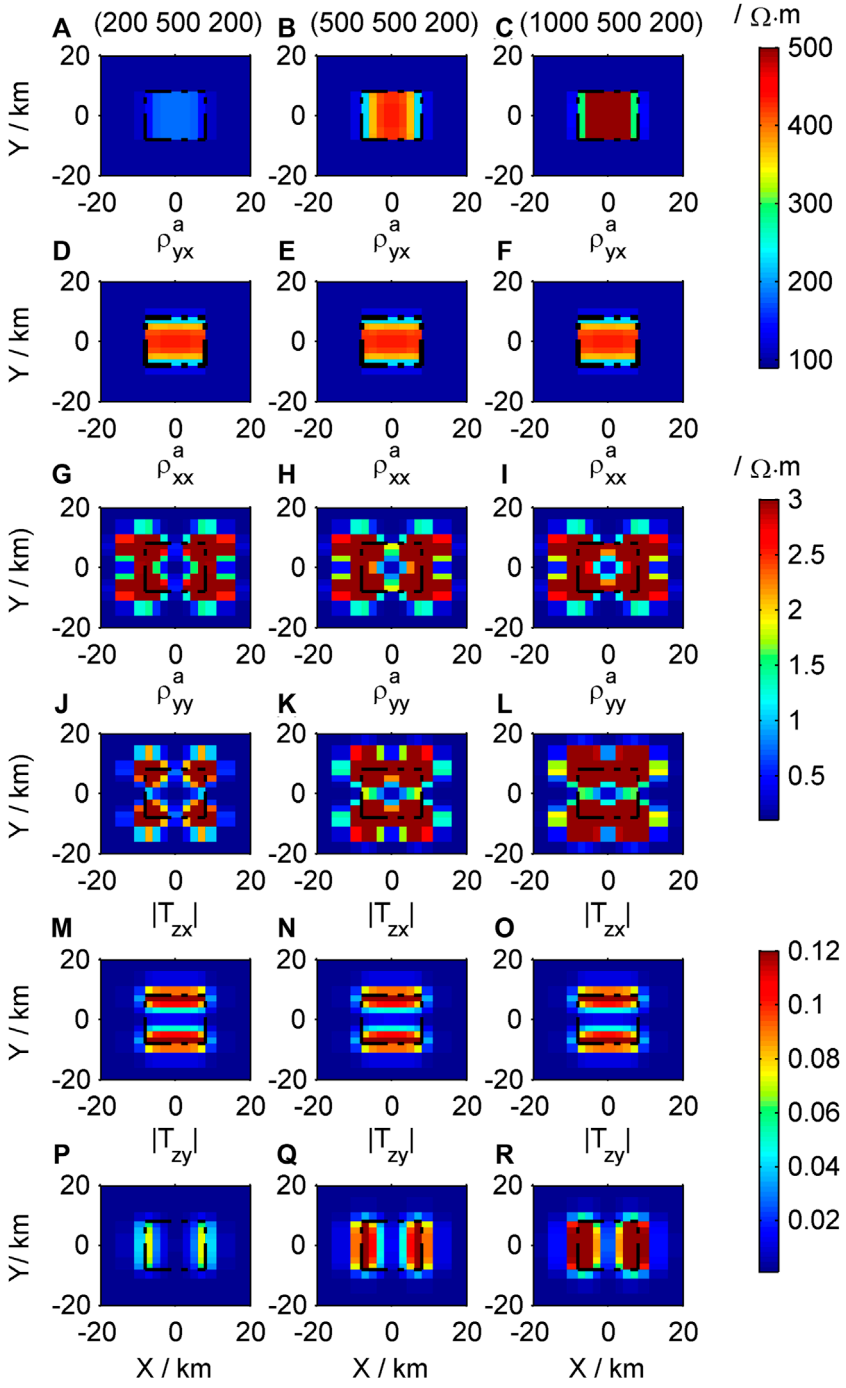

FIGURE 8
Contour maps of response of the different high-resistivity models in the X direction: **(A–C)** ρ^a_{xy}; **(D–F)** ρ^a_{yx}; **(G–I)** ρ^a_{xx}; **(J–L)** ρ^a_{yy}; **(M–O)** $|T_{zx}|$; **(P–R)** $|T_{zy}|$.

3.2 Response of 3D axis anisotropic high-resistance prism

The 3D prism model is the same as 3.1, except that the resistivity is set to high-resistance. The frequency of the MT used is 10 Hz.

We first fix $\rho_y = 500\Omega \cdot m$, $\rho_z = 200\Omega \cdot m$, with ρ_x of 200, 500, and 1,000 $\Omega \cdot m$, respectively. The forward results are shown in Figure 8. Next, we fix $\rho_x = 200\Omega \cdot m$, $\rho_z = 500\Omega \cdot m$, with ρ_y of 200, 500, and 1,000 $\Omega \cdot m$, respectively. The forward results are shown in Figure 9.

The apparent resistivity ρ^a_{xy} and ρ^a_{yx} reflects the horizontal position of the high-resistance body, and the apparent resistivity ρ^a_{xx}, ρ^a_{yy}, and the tipper T_{zx}, T_{zy} reflect the

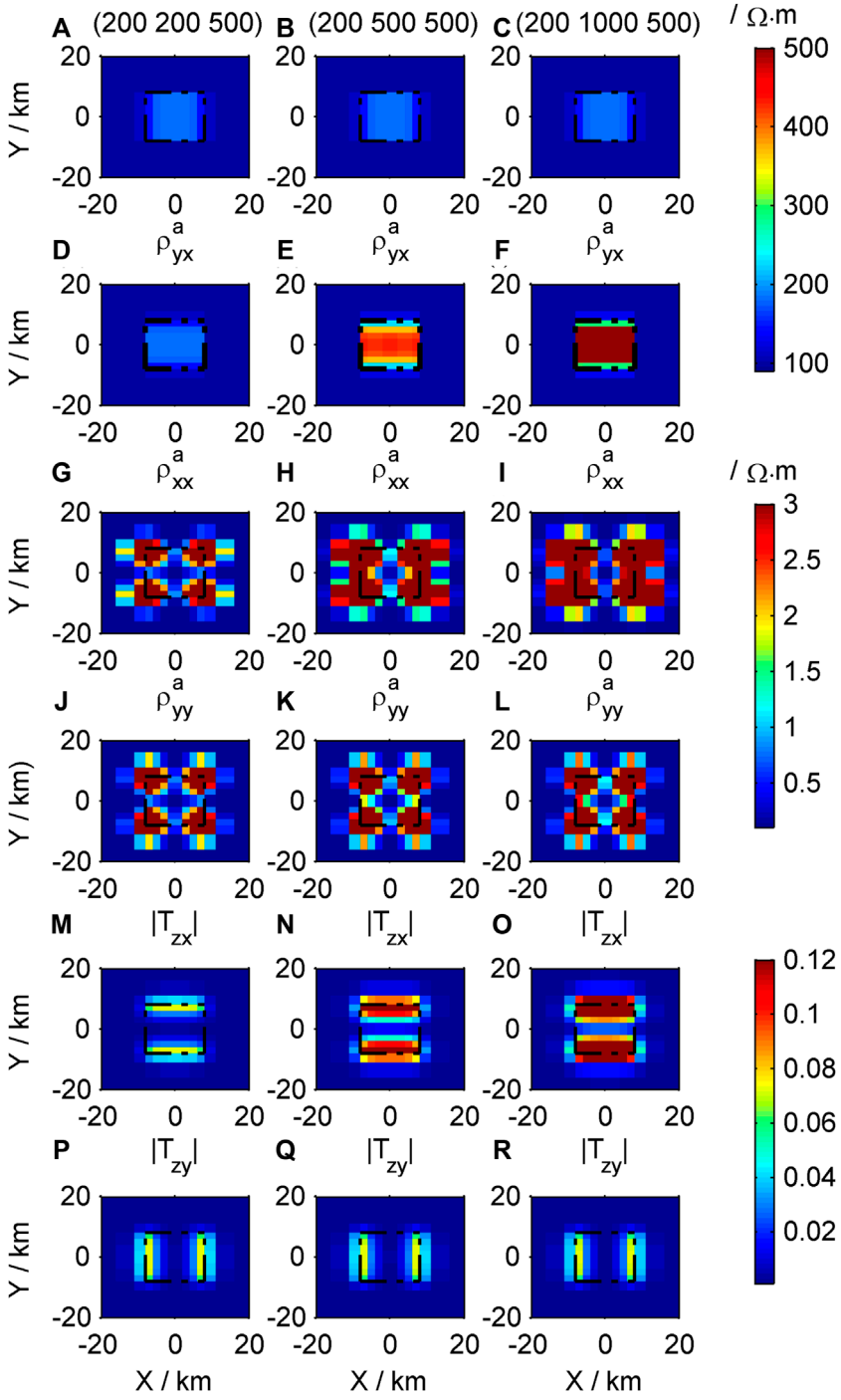

FIGURE 9
Contour maps of the response of different high-resistivity models in the Y direction: **(A–C)** ρ^a_{xy}; **(D–F)** ρ^a_{yx}; **(G–I)** ρ^a_{xx}; **(J–L)** ρ^a_{yy}; **(M–O)** $|T_{zx}|$; **(P–R)** $|T_{zy}|$.

horizontal boundary of the high-resistance body (Figure 8). ρ^a_{xy}, ρ^a_{yy}, and T_{zy} are sensitive to changes of ρ_x of high-resistance body. When the resistivity of the high-resistance body is higher, the anomalies it produces are more obvious (Figures 8A–C, J–L, P–R). ρ^a_{yx}, ρ^a_{xx}, and T_{zx} are less affected by the ρ_x (Figures 8D–I, M–O).

The apparent resistivity ρ^a_{xy}, ρ^a_{yy}, and the tipper T_{zy} are less affected by the ρ_y of high-resistance body (Figures 9A–C, J–L, P–R). ρ^a_{yx}, ρ^a_{xx}, and T_{zx} are sensitive to changes of ρ_y of the high-resistance body and are greatly affected by it (Figures 9D–I, M–O). The apparent resistivity tensor and tipper are not sensitive to changes of ρ_z of the high-resistivity body.

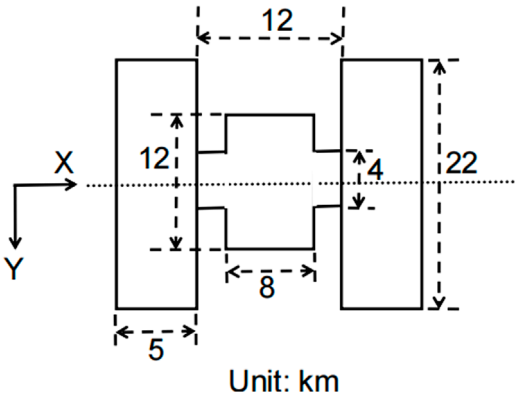

FIGURE 10
Plan view of the 3D complex model.

3.3 Response of 3D complex axis anisotropic prism

The plan view of the 3D complex prism model is shown in Figure 10. The top surface of the model is buried at a depth of 100 m, the size of the prisms on both sides is 5 km × 22 km × 5 km, and the main axis resistivity in the X, Y, and Z direction is 10, 1,000, and 100 $\Omega \cdot m$, respectively. The total length and width of the middle prism are both 12 km, and the height is 5 km. The main axis resistivity in the X, Y, and Z direction is 30, 500, and 100 $\Omega \cdot m$, respectively. The background resistivity is 100 $\Omega \cdot m$, and the frequency of MT is 10 Hz. The forward modeling results are shown in Figure 11.

Based on the previous analysis, according to Figure 11, the low-resistivity body in the X direction of the complex model caused the low value apparent resistivity anomaly zone of ρ^a_{xy}, and this anomaly zone reflects the boundary of the Y direction of the combination (Figure 11A). The high-resistivity anomaly zone of ρ^a_{yx} is caused by the high resistivity body in the Y direction of the composite, and this anomaly zone clearly reflects the boundary of the composite in the X direction (Figure 11B). The anomalous regions of T_{zx} and T_{zy} respectively reflect the boundaries of the combination in the X and Y directions, respectively (Figures 11C, D).

4 Conclusion

This study applies the finite difference method to achieve 3D MT forward modeling in axis anisotropic media and verifies the correctness of the algorithm by comparing it with 2D quasi-analytic solution. The examples show that ρ^a_{xy}, ρ^a_{yy}, and T_{zy} are sensitive to changes of ρ_x of the anomalous body and are greatly affected by it, but insensitive to changes of ρ_y. ρ^a_{yx}, ρ^a_{xx}, and T_{zx} are sensitive to changes of ρ_y of the anomalous body and are greatly affected by it, but insensitive to changes of ρ_x. The apparent resistivity tensor and tipper are not sensitive to changes of ρ_z of the anomalous body. ρ_z has a weak contribution to the surface response of MT. For the exploration of anisotropic media, the apparent resistivity tensor and tipper can identify the changes in resistivity in two horizontal axes directions and the boundaries of the anomalous body, which has the

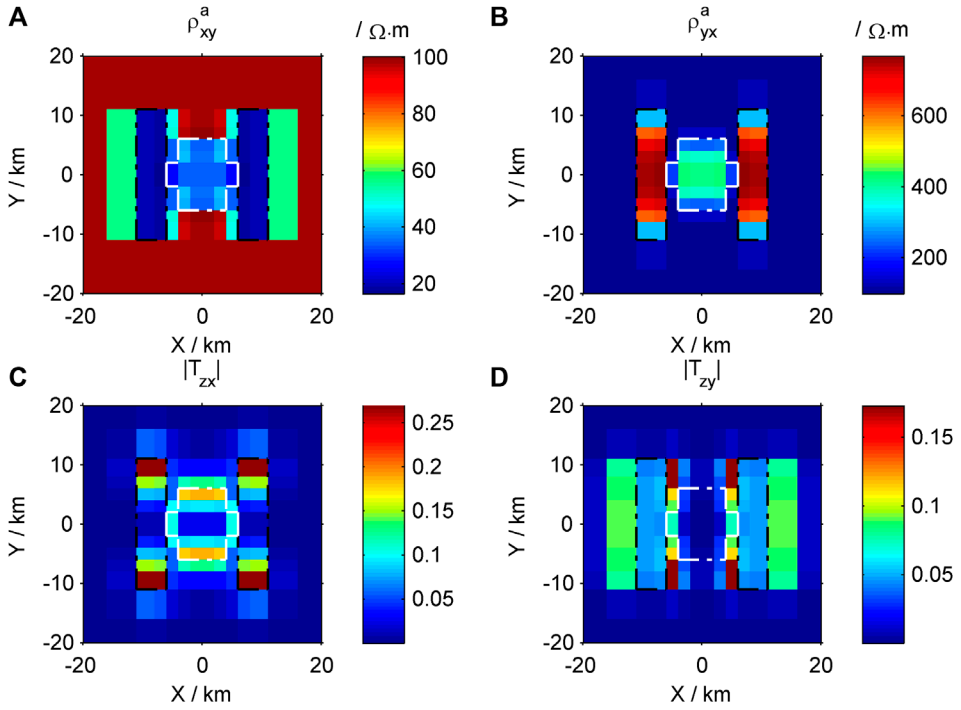

FIGURE 11
Contour maps of response of the 3D complex model.

advantage for exploration. The study provides a basis for conducting the forward modeling and inversion research of MT with arbitrary anisotropy.

Data availability statement

The original contributions presented in the study are included in the article/supplementary material, further inquiries can be directed to the corresponding author.

Author contributions

XL: Conceptualization, Data curation, Formal Analysis, Funding acquisition, Investigation, Methodology, Project administration, Resources, Software, Supervision, Validation, Visualization, Writing–original draft, Writing–review and editing. Q-JS: Methodology, Validation, Writing–review and editing.

Funding

The author(s) declare that financial support was received for the research, authorship, and/or publication of this article. This work is funded financially by Heilongjiang Province Basic Research Business Expenses for Universities Heilongjiang University Special Fund Project (Grant No. 2023-KYYWF-1494) and the Natural Science Foundation of Jiangxi Province (Grant No. 20212BAB213023).

Acknowledgments

Thank you to the reviewers for their valuable feedback on this article, Professor Siripunvaraporn, and others for their previous research work, and the editor for their enthusiastic assistance. Thank you to Wenxin Kong for his enthusiastic help. We would like to thank Editage (www.editage.cn) for English language editing.

Conflict of interest

The authors declare that the research was conducted in the absence of any commercial or financial relationships that could be construed as a potential conflict of interest.

Publisher's note

References

Cao, X. Y., Yin, C. C., Zhang, B., Huang, X., Liu, Y. H., and Cai, J. (2018). A goal-oriented adaptive finite-element method for 3D MT anisotropic modeling with topography. *Chin. J. Geophys.* 61 (6), 2618–2628. doi:10.6038/cjg2018L0068

Guo, Z. Q., Egbert, G., Dong, H., and Wei, W. (2020). Modular finite volume approach for 3D magnetotelluric modeling of the Earth medium with general anisotropy. *Phys. Earth Planet. Interiors* 309, 106585. doi:10.1016/j.pepi.2020.106585

Han, B., Li, Y. G., and Li, G. (2018). 3D forward modeling of magnetotelluric fields in general anisotropic media and its numerical implementation in Julia. *Geophysics* 83 (4), F29–F40. doi:10.1190/GEO2017-0515.1

Kong, W. X. (2021). *Research on the three-dimensional anisot ropic inversion of magnetotelluric data*. Ph. D. thesis. Beijing: China University of Geosciences.

Li, Y. G. (2002). A finite-element algorithm for electromagnetic induction in two-dimensional anisotropic conductivity structures. *Geophys. J. Int.* 148 (3), 389–401. doi:10.1046/j.1365-246x.2002.01570.x

Liu, X., and Zheng, F. W. (2024). Axis anisotropic Occam's 3D inversion of tensor CSAMT in data space. *Appl. Geophys.* doi:10.1007/s11770-024-1076-9

Liu, Y., Xu, Z. H., and Li, Y. G. (2018). Adaptive finite element modelling of three-dimensional magnetotelluric fields in general anisotropic media. *J. Appl. Geophys.* 151, 113–124. doi:10.1016/j.jappgeo.2018.01.012

Liu, Y. H., Yin, C. C., Cai, J., Huang, W., Ben, F., Zhang, B., et al. (2018). Review on research of electrical anisotropy in electromagnetic prospecting. *Chin. J. Geophys.* 61 (8), 3468–3487. doi:10.6038/cjg2018L0004

Pek, J., and Verner, T. (1997). Finite -difference modelling of magnetotelluric fields in two dimensional anisotropic media. *Geophys. J. Int.* 128 (3), 505–521. doi:10.1111/j.1365-246X.1997.tb05314.x

Postma, G. W. (1955). Wave propagation in a stratified medium. *Geophysics* 20 (4), 780–806. doi:10.1190/1.1438187

Qin, L. J., Ding, W. F., and Yang, C. F. (2022). Magnetotelluric responses of an anisotropic 1-D earth with a layer of exponentially varying conductivity. *Minerals* 12 (7), 915. doi:10.3390/min12070915

Qin, L. J., Yang, C. F., and Chen, K. (2013). Quasi analytic solution of 2-D magnetotelluric fields on an axially anisotropic infinite fault. *Geophys. J. Int.* 192 (1), 67–74. doi:10.1093/gji/ggs018

Siripunvaraporna, W., Egbertb, G., and Lenbury, Y. (2002). Numerical accuracy of magnetotelluric modeling: a comparison of finite difference approximations. *Earth Planets Space* 54, 721–725. doi:10.1186/BF03351724

Siripunvaraporna, W., Egbertb, G., Lenbury, Y., and Uyeshima, M. (2005). Three-dimensional magnetotelluric inversion: data-space method. *Phys. Earth Planet. Interiors* 150 (1–3), 3–14. doi:10.1016/j.pepi.2004.08.023

Smith, J. T. (1996). Conservative modeling of 3D electromagnetic fields. Part II. Biconjugate gradient solution and an accelerator. *Geophysics* 61 (5), 1319–1324. doi:10.1190/1.1444055

Wang, T., Wang, K. P., and Tan, H. D. (2017). Forward modeling and inversion of tensor CSAMT in 3D anisotropic media. *Appl. Geophys.* 14 (04), 590–605. doi:10.1007/s11770-017-0644-7

Wannamaker, P. E. (2005). Anisotropy versus heterogeneity in continental solid earth electromagnetic studies: fundamental response characteristics and implications for physicochemical state. *Surv. Geophys.* 26 (6), 733–765. doi:10.1007/s10712-005-1832-1

Xiao, T. J., Huang, X. Y., and Wang, Y. (2018). 3D MT modeling using the T-Ω method in general anisotropic media. *J. Appl. Geophys.* 160, 171–182. doi:10.1016/j.jappgeo.2018.11.012

Ye, Y. X., Du, J. M., Liu, Y., Ai, A. M., and Jiang, F. Y. (2021). Three-dimensional magnetotelluric modeling in general anisotropic media using nodal-based unstructured finite element method. *Comput and Geosciences* 148, 104686. doi:10.1016/j.cageo.2021.104686

Yin, C. C., and Weidelt, P. (1999). Geoelectrical fields in a layered earth with arbitrary anisotropy. *Geophysics* 64 (2), 426–434. doi:10.1190/1.1444547

Yu, G., Xiao, Q. B., Zhao, G. Z., and Li, M. (2018). Three-dimensional magnetotelluric responses for arbitrary electrically anisotropic media and a practical application. *Geophys. Prospect.* 66 (9), 1764–1783. doi:10.1111/1365-2478.12690

Zhou, J. J., Hu, X. Y., and Cai, H. Z. (2021). Three -dimensional finite-element analysis of magnetotelluric data using coulomb -gauged potentials in general anisotropic media. *Pure Appl. Geophys.* 178 (11), 4561–4581. doi:10.1007/s00024-021-02882-0

frontiers | Frontiers in Earth Science

TYPE Original Research
PUBLISHED 03 December 2024
DOI 10.3389/feart.2024.1506399

OPEN ACCESS

EDITED BY
Bo Yang,
Zhejiang University, China

REVIEWED BY
Guo Yu,
Yangtze University, China
Zhanjie Shi,
Zhejiang University, China

*CORRESPONDENCE
Peng Yu,
yupeng@tongji.edu.cn

RECEIVED 05 October 2024
ACCEPTED 11 November 2024
PUBLISHED 03 December 2024

CITATION
Huang Z, Yu P, Zhao C, Zhang L and Song H (2024) Enhancing electrical structure in magnetotelluric inversion by the constraint of minimum cross-gradient support coupling. *Front. Earth Sci.* 12:1506399. doi: 10.3389/feart.2024.1506399

Enhancing electrical structure in magnetotelluric inversion by the constraint of minimum cross-gradient support coupling

Zuwei Huang, Peng Yu*, Chongjin Zhao, Luolei Zhang and Han Song

State Key Laboratory of Marine Geology, Tongji University, Shanghai, China

The geophysical inversion problem is inherently underdetermined. Constrained inversion, by incorporating prior information, can effectively reduce the ambiguity in inversion results. A key research challenge lies in establishing a reasonable coupling mechanism between the prior information and the inversion model. Traditional cross-gradient coupling methods often exhibit weak coupling effects in regions with small model gradients. In this paper, we introduce a new coupling method called "minimum cross-gradient support" (MCGS), which enhances the balance between model gradient magnitude and the influence of gradient direction by applying a minimum support function to the cross-gradient. We evaluated the coupling effects of MCGS in comparison with two others coupling methods: normalized cross-gradient (NCG) and joint minimum gradient support (JMGS), the latter of which also employs the minimum support function. Theoretical models demonstrate that MCGS retains the advantage of reduced dependence on strictly accurate prior information, enhances constraint effectiveness in weak gradient regions, and the strength of constraints can be flexibly adjusted through focusing factors. To verify the effectiveness of MCGS, we conducted two synthetic experiments: a double-blocks model and a nappe structure model, applied to magnetotelluric (MT) constrained inversion. The results showed that MCGS constrained inversion achieved better performance than both non-constrained inversion and cross-gradient constrained inversion, with lower residual cross-gradient values and higher model recovery accuracy compared to the true model. Finally, we applied the proposed MCGS coupling to real data sets from the Junggar Basin. The inversion results revealed the resistivity structure of the sedimentary layer and imaged possible residual Carboniferous sediments beneath the Permian, as well as the distribution of the Paleozoic basement. These results provide valuable evidence supporting the subduction tectonic evolution model of the region.

KEYWORDS

constrained inversion, minimum cross-gradient support, magnetotelluric, Junggar basin, nappe structure

1 Introduction

The inherent non-uniqueness of inversion is a fundamental issue in geophysical research. Joint inversion stands out as a crucial approach to mitigate this non-uniqueness. The complexity of Earth's internal structures and the diversity of geological targets

make geophysics more intricate and challenging. Thus, relying solely on the results of a single geophysical method for subsurface interpretation inevitably leads to limitations and must be supplemented by other methods for cross-validation. Combining seismic and non-seismic methods to integrated interpret the subsurface structures from different perspectives can supply more accurate explanation of geological targets. (Gallardo et al., 2012; Takougang Takam et al., 2015; Moorkamp et al., 2016).

Different geophysical methods have different sensitivities, and there might be complementarity among them. Seismic tomography provides high-resolution velocity structures of the subsurface, but it faces challenges such as uneven ray coverage. For instance, first-arrival seismic rays provide limited information beneath high-velocity targets, and constructing velocity-depth models can be subjective. (Rawlinson et al., 2010). The MT method is less affected by a high resistivity shield layer (Huang et al., 2023) but shows lower resolution. By combining these different geophysical methods properly, it is possible to obtain a more reliable subsurface structure, thereby overcoming the limitations and non uniqueness of single methods to some extent.

Joint inversion is the process of combining multiple geophysical observed data and establishing the appropriate coupling relationships on the petrophysical relationships or geometric parameters of geological targets which are reflected by different geophysical methods. It aims to invert and obtain models that are fitting with various observed geophysical data. The mainstream coupling approaches in joint inversion can be categorized into two types: coupling based on petrophysical relationships and structural geometric similarities of geological targets (Lelièvre et al., 2012).

Joint inversion approaches based on petrophysical relationships utilizes theoretical or empirical relationships between different physical properties, such as velocity, density, resistivity, etc., which can be established based on compositional structure, porosity, saturation, and other physical properties (Heincke et al., 2006; Colombo and De Stefano, 2007; Heincke et al., 2017). For example, the Gardner relationship between density and velocity (Savino et al., 1980) is commonly used. By leveraging these intrinsic empirical relationships, one geophysical model can be converted into geophysical model in other physical properties, enabling the joint inversion of different methods. However, due to the effects of various parameters such as temperature and pressure on the rock properties of geological targets, it is challenging to accurately describe the physical property relationships of subsurface medium using empirical relationships. As a result, joint inversion based on petrophysical relationships tends to have significant uncertainties. There are also related studies that realize the physical property relations converge to the given priori physical property distribution centers by fuzzy c-mean clustering methods (Lelièvre et al., 2012; Carter-McAuslan et al., 2015; Sun and Li, 2016). However, such constraints often require *a priori* determination of the number of clusters and cluster centers, limiting their general applicability.

The coupling mechanism based on structural geometric similarities has been a hot topic in joint inversion research (Zhang and Morgan, 1997; Haber and Oldenburg, 1997; Gallardo and Meju, 2003; Molodtsov et al., 2011; Haber and Holtzman, 2013). Molodtsov et al. (2013) presented a 2-D joint inversion method based on parameters' gradient dot product constraints with seismic traveltimes and MT data, this method needs *a priori* information of the two physical properties related to the specified inversed region, which limits its widespread application, Shi et al. (2018) improved the gradient dot product constraint and developed square cosine similarity coupling, which avoids the need for prior property directions. However, its mathematical properties are poor and can easily break down the inversion process. Joint total variation (JTV) (Haber and Holtzman, 2013) can be defined as $L_{1,2}$ norm of the gradient of the model, JTV coupling can make the gradient direction between two models tend to be consistent, but its practicality diminishes in cases with complex background gradient variations. Cross-gradient constraints (Gallardo and Meju, 2003) have been widely used due to their ability to avoid priori assumptions about relationships on physical properties (Gallardo, 2007; Hu et al., 2009; Fregoso and Gallardo, 2009; Doetsch et al., 2010; Gallardo and Meju, 2011; Peng et al., 2013; Moorkamp et al., 2016; Gao and Zhang, 2018; Gross, 2019; Tavakoli et al., 2021; Franz et al., 2021).

Constraint inversion is a common manifestation of joint inversion, which is based on one method can provide the high accuracy of prior constraint information for other methods. The most common constraint inversion is to use the layer information determined by seismic migration profiles to constrain MT inversion. As seismic migration results mainly focus on characterizing underground physical property interfaces, it is more reasonable to use structural geometric similarities constraints rather than petrophysical relationships when introducing seismic migration results to constrain MT inversion. Therefore, the cross-gradient constraint has become an important way to couple seismic migration results with MT inversion as the cross- gradient constraint does not affect the free inversion of MT in areas without interface constraint information.

However, traditional cross-gradient coupling has the disadvantage of weak constraint effects. When the variations in physical properties between two models are in the same or opposite direction, or one or both of the models remains unchanged, the cross-gradient function disappears. In these cases, the magnitude of the variations has no effect on the value of the cross-gradient. Only when both properties change but in different directions, the cross-gradient value is nonzero. If one of the models undergoes small changes, which means the small value of its gradient. The cross-gradient values between the two models become small, resulting cross-gradient constraint a relatively weak structural coupling (Moorkamp et al., 2011).

The core issue causing weak cross-gradient constraint capability is its lack of adaptability in regions with weak data response and gradient change. To overcome the disadvantages of the traditional cross-gradient coupling, in this paper we develop an enhanced cross-gradient coupling that balances the gradient values and direction of property variations in the cross-gradient more effectively. It achieves this by employing the minimum support function (Portniaguine and Zhdanov, 1999) on the cross-gradient coupling. The mathematical properties of the minimum support functional can highlight the cross-gradient values when they are small. For some excessively large cross gradient values, the minimum support functional can be used to suppress them to a certain extent. Therefore, it can better balance the strength changes of the cross-gradient values. Finally, by minimizing the objective function, the cross-gradient distribution in the model space tends to be minimized, achieving similar inversion model construction.

In the second section, we first illustrate the principle of MCGS coupling through numerical experiment and compare it with other coupling methods in similar mathematical forms, In the fourth section, we conducted two block and nappe structure model experiments through the developed constrained inversion algorithm. In the fifth section, we applied MCGS constrained inversion to MT data in the Junggar Basin.

2 Theory

2.1 Basic theory

Cross-gradient constraint (Gallardo and Meju, 2003) is the most widely used coupling form in joint inversion (Equation 1).

$$\tau_{CG}(\mathbf{m}_1,\mathbf{m}_2)=\int_V|\nabla\mathbf{m}_1\times\nabla\mathbf{m}_2|^2\,dv=\int_V||\nabla\mathbf{m}_1|\cdot|\nabla\mathbf{m}_2|\cdot sin\,\theta|^2\,dv \tag{1}$$

The cross-gradient constraint term $\tau(\mathbf{m}_1,\mathbf{m}_2)$ becomes zero when the gradient directions of the two models are either the same or opposite, or when one or both of the model gradients are zero. By minimizing the cross-gradient constraint term, the structural similarity between the two models can be enhanced. The value of the cross-gradient constraint term is related to both the angle between the gradients of the two models and the magnitude of the gradients. When the gradient values change very little, even if the angle θ between them is large, the cross-gradient constraint remains weak.

When the geological targets exhibit strong structural similarity between different physical properties but face weak changes in the model (i.e., in regions where the gradients are small), a stronger constraint is needed to achieve results with higher structural similarity. To address some of the potential weaknesses of the cross-gradient term, the normalized cross-gradient (NCG) was designed to enhance constraint strength (Equation 2) (Haber and Modersitzki, 2006).

$$\tau_{NCG}(\mathbf{m}_1,\mathbf{m}_2)=\int_V 1-\left(\frac{\nabla\mathbf{m}_1\cdot\nabla\mathbf{m}_2}{\sqrt{|\nabla\mathbf{m}_1|^2+\varepsilon}\sqrt{|\nabla\mathbf{m}_2|^2+\varepsilon}}\right)^2 dv \tag{2}$$

However, compared to the cross-gradient term, the derivatives of the normalized cross-gradient (NCG) term provide less obvious insight into its regularization behavior, and the NCG term often behaves as a concave operator numerically. This behavior may pose challenges in solving the joint inversion problem numerically (Crestel et al., 2018). The NCG coupling entirely removes the effect of the gradient value on the cross-gradient term; even if one of the gradients remains very small, it will still incur a penalty. Increasing the cross-gradient magnitudes without considering the gradient values may disrupt the coupling in joint inversion.

Finding an appropriate mathematical form to strengthen the cross-gradient operator in regions where the gradients are weak is crucial. Last and Kubik (1983) applied the minimum support function to regularization in geophysical inversion to obtain focused inverted results. This function can transform the values of the independent variable to a range between 0 and 1, thereby increasing the values of small variables after being supported. This process results in a more compact distribution of the independent variable, balancing it between 0 and 1. Molodtsov and Troyan (2017) and Zhdanov et al. (2021) proposed a joint minimum gradient support (JMGS) based on the minimum gradient support (Equation 3).

$$\tau_{JMGS}(\mathbf{m}_1,\mathbf{m}_2)=\int_V\frac{|\nabla\mathbf{m}_1|^2+|\nabla\mathbf{m}_2|^2}{|\nabla\mathbf{m}_1|^2+|\nabla\mathbf{m}_2|^2+\varepsilon^2}dv \tag{3}$$

The effect of JMGS is to highlight the sharp boundaries of gradient changes in homogeneous targets. However, its application to problems in complex subsurface environments can be challenging. By combining the properties of the minimum support function and the cross-gradient, we propose a MCGS constraint (Equation 4).

$$\tau_{MCGS}(\mathbf{m}_1,\mathbf{m}_2)=\int_V\frac{|\nabla\mathbf{m}_1\times\nabla\mathbf{m}_2|^2}{|\nabla\mathbf{m}_1\times\nabla\mathbf{m}_2|^2+\varepsilon^2}dv \tag{4}$$

We introduce the support of $\nabla\mathbf{m}_1\times\nabla\mathbf{m}_2$ (denoted $spt\ \nabla\mathbf{m}_1\times\nabla\mathbf{m}_2$) as the combined closed subdomains of V where $\nabla\mathbf{m}_1\times\nabla\mathbf{m}_2\neq 0$. The Equation 4 can be modified as:

$$\begin{aligned}&\tau_{MCGS}(\mathbf{m}_1,\mathbf{m}_2)\\&=\int_V\frac{(\nabla\mathbf{m}_1\times\nabla\mathbf{m}_2)^2+\varepsilon^2-\varepsilon^2}{(\nabla\mathbf{m}_1\times\nabla\mathbf{m}_2)^2+\varepsilon^2}dv\\&=\int_{spt\nabla\mathbf{m}_1\times\nabla\mathbf{m}_2}\left(1-\frac{\varepsilon^2}{(\nabla\mathbf{m}_1\times\nabla\mathbf{m}_2)^2+\varepsilon^2}\right)dv\\&=spt\nabla\mathbf{m}_1\times\nabla\mathbf{m}_2-\varepsilon^2\int_{spt\nabla\mathbf{m}_1\times\nabla\mathbf{m}_2}\frac{1}{(\nabla\mathbf{m}_1\times\nabla\mathbf{m}_2)^2+\varepsilon^2}dv\end{aligned} \tag{5}$$

Through Equation 5, it is obvious that

$$\tau_{MCGS}(\mathbf{m}_1,\mathbf{m}_2)\to spt\nabla\mathbf{m}_1\times\nabla\mathbf{m}_2,\text{if }\varepsilon\to 0. \tag{6}$$

Thus, the integral $\tau_{MCGS}(\mathbf{m}_1,\mathbf{m}_2)$ can be treated as a functional, proportional (for a small ε) to the cross-gradient support based on Equation 6. When ε is chosen to have a sufficiently small value, it can be considered a focusing parameter. A smaller ε allows the cross-gradient to be quickly focused, while different focusing parameters lead to varying degrees of focus in the minimum support function. When the focusing parameter is large, the minimum support function is smooth, resulting in a weak focusing effect. As the focusing parameter decreases, the focusing effect gradually strengthens, allowing very small cross-gradient values to be quickly enlarged. The minimum support function can enhance the values of the cross-gradient when those values are very small.

MCGS coupling minimizes the total area with nonzero departures from the cross-gradient. Consequently, a dispersed and smoothed distribution of the cross-gradient, where all values are not equal to zero, results in a large penalty function. In contrast, a well-focused distribution with a small departure yields a smaller penalty function. This approach also prevents MCGS from imposing excessive penalties on all regions with inconsistent gradient directions across the entire space, similar to the NCG coupling.

2.2 Theoretical model test

To better illustrate the mathematical mechanisms, we designed a set of theoretical models and compared them with various

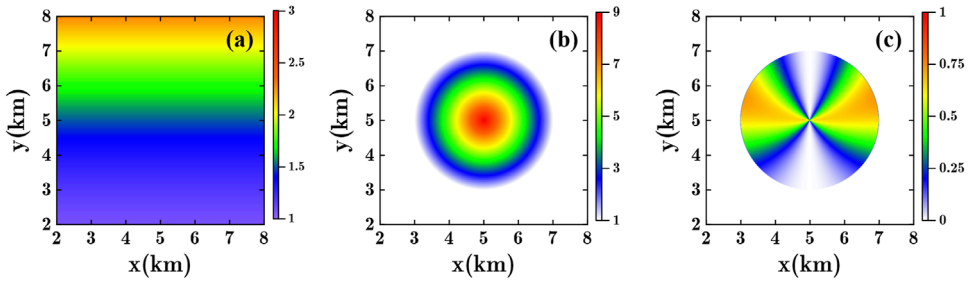

FIGURE 1
Theoretical model test. **(A)** Longitudinal variation gradient model. **(B)** Radial variation gradient model. **(C)** Cross-gradient value of **(A, B)**.

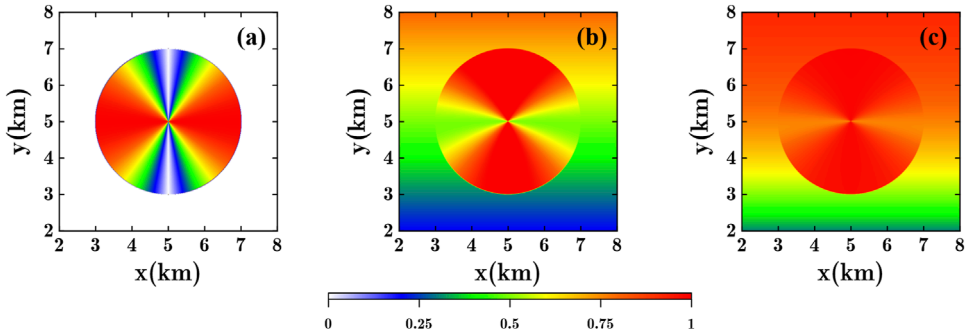

FIGURE 2
Theoretical model test. **(A)** NCG coupling result **(B)** JMGS coupling result (ε^2 = 0.1) **(C)** JMGS result (ε^2 = 0.01).

joint inversion coupling methods. Model 1 (Figure 1A) represents a gradient background that varies along the *y*-axis, with values decreasing from 3 to 1 following a quadratic function, simulating a gradually decreasing gradient with depth. Model 2 (Figure 1B) represents a radially varying circular target, where values change uniformly from 9 at the center to 1 at the outer boundary, simulating gradient variations in different directions. We then calculated the cross-gradient values for these two models (Figure 1C).

It is evident that as the depth increases, the gradient value gradually decreases. When the gradient direction of the two models remains significant, the cross-gradient value is very small, indicating that the constraint effect of the cross-gradient on regions with weak gradient values is limited. We calculated the NCG and JMGS coupling results between Model 1 and Model 2. The NCG result (Figure 2A) shows that the penalized region exhibits a lack of influence from the gradient value, leading to a uniform distribution in space. This approach partially addresses the issue of weak constraint capabilities of the cross-gradient in regions with low gradients; however, it may disrupt the joint inversion process. The JMGS method also demonstrates effectiveness in weak gradient regions (Figures 2B, C), but it penalizes areas outside the target in Model 2. This additional penalty for non-homologous regions is undesirable.

We also calculated the MCGS results for these two models with focusing parameters ε^2 of 0.1 (Figure 3A) and 0.01 (Figure 3B), respectively. It can be observed that MCGS effectively enhances the distribution in regions with weak gradients and balances the differences between strong and weak gradients. When the focusing parameter is relatively small (ε^2 = 0.01), it achieves a higher degree of focusing and exhibits a stronger effect on weak gradient regions compared to the result with a higher focusing parameter (ε^2 = 0.1). Figure 3C intuitively reflects the change in the degree of focus of the MCGS coupling. The vertical axis represents the transformed cross-gradient value, while the horizontal axis shows the cross-gradient values increasing from small to large. Both the ε^2 = 0.01 curve (blue solid line) and the ε^2 = 0.1 curve (red solid line) show significant improvement compared to the cross-gradient (black solid line). When ε^2 = 0.01, smaller cross-gradient values can be focused more quickly. In practical applications, we can select the focusing parameter based on the distribution of the cross-gradient values.

By comparing the results of the various coupling methods mentioned above, it is evident that the MCGS coupling mechanism possesses significant characteristics and advantages in balancing the effects of gradient values in the cross-gradient. MCGS demonstrates a similar ability to NCG coupling in enhancing the cross-gradient constraint in regions with weak physical property changes. Unlike the non-convex operator NCG, the operator MCGS can better ensure the stability of the inversion process.

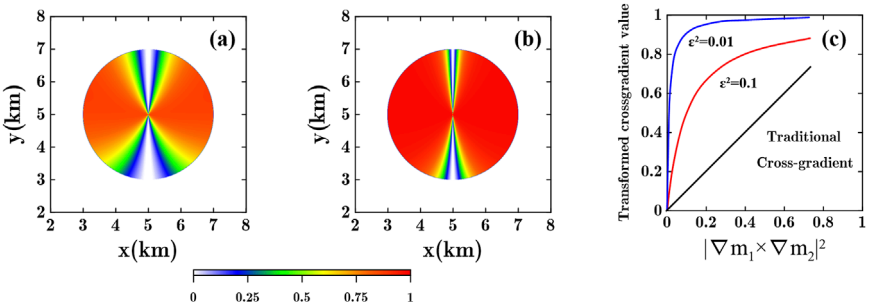

FIGURE 3
Theoretical model test. **(A)** MCGS coupling result (ε^2 = 0.1) **(B)** MCGS coupling result (ε^2 = 0.01) **(C)** MCGS coupling transforming curves.

3 Inversion algorithm

The MT forward modeling is based on finite-element method (FEM) (Wannamaker, 1987), and uses reciprocity to calculate the Jacobian matrix (De Lugao and Wannamaker 1996), the inversion code we use is OCCAM2DMT (Constable et al., 1987; deGroot-Hedlin and Constable, 1990).

deGroot-Hedlin and Constable (1990) established an inversion objective function based on smooth model constraints within the OCCAM method (Equation 7)

$$P(\mathbf{m},\mathbf{d})^{\alpha} = \alpha\left\{\| \partial_y \mathbf{m} \|^2 + \|\partial_z \mathbf{m} \|^2\right\} + \left\{\|\mathrm{W}\mathrm{d} - \mathbf{W}F[\mathbf{m}]\|^2\right\} \quad (7)$$

α is the regularization factor, and $\| \partial_y \mathbf{m} \|^2 + \|\partial_z \mathbf{m} \|^2$ is the model roughness R, $\mathbf{W}$ is a data weighting matrix related to observation data errors, d is the observation data, and $F[\mathbf{m}]$ is the expression of nonlinear MT forward operator. We construct an MT inversion objective function based on MCGS constraint inversion using OCCAM inversion framework (Equation 8).

$$P(\mathbf{m},\mathbf{d})^{\alpha} = \alpha\left\{\| \partial_y \mathbf{m} \|^2 + \|\partial_z \mathbf{m} \|^2 + \lambda\tau_{\mathrm{MCGS}}(\mathbf{m})\right\} + \left\{\|\mathrm{W}\mathrm{d} - \mathbf{W}F[\mathbf{m}]\|^2\right\} \quad (8)$$

$\tau_{\mathrm{MCGS}}(\mathbf{m})$ represents the MCGS coupling constraint, and λ determines the weight of the inversion constraint term.

4 Synthetic model tests

To provide a more intuitive demonstration of the mechanism and effectiveness of MCGS coupling, we designed two synthetic experiments in this section. The double-block model is used to illustrate the rationale behind the construction of MCGS coupling, by comparing the constrained inversion results from different constraint models with those from traditional cross-gradient coupling. The single anomaly model is employed to demonstrate the effectiveness of this method in joint inversion, again in comparison to traditional cross-gradient constraints. Additionally, we designed a complex nappe structure model, where a high-resistivity layer located at 7 km serves as the imaging target. The purpose of this model is to show that MCGS provides a stronger constraint effect than traditional cross-gradients in regions with weak MT sensitivity and low model variation values.

We set an error-fitting threshold as the iteration stopping criterion for MT inversion. The iterations will stop when the error-fitting threshold is met or when the maximum number of iterations is reached. The root mean square (RMS) error formula for MT inversion is defined as Equation 9:

$$\mathrm{MT}_{\mathrm{RMS}} = \sqrt{\frac{\sum_{i=1}^{N}\left(\frac{d_i^{cal} - d_i^{obs}}{error_i}\right)^2}{N}} \quad (9)$$

d_i^{cal} and d_i^{obs} denote the calculated and observed apparent resistivity and phase at the i^{th} observation point, and $error_i$ represents the measurement error of the i^{th} observation point, in this case, we usually stop the iteration when RMS reaches 1.0 to ensure that the observed data fit within the random noise level. We assign the maximum number of iterations to 50. If the threshold is not met even after 50 iterations, the iteration will also be terminated. To prevent excessive iterations, we have set the last iteration terminate condition: if the $\mathrm{MT}_{\mathrm{RMS}}$ is no longer decreasing or the decreasing still lower than 0.1% after 7 times of step cutting, the iteration will be terminated.

We measure the structural similarity between the inversion results and the true models using residual cross-gradients (RCG). A smaller RCG value indicates a higher structural similarity between the two models. Additionally, we use the model recovery degree (RD) (Zhang et al., 2012) to evaluate the inversion results (Equation 10).

$$RD = \sqrt{\frac{\sum(\mathbf{m}_{true} - \mathbf{m}_{inv})^2}{N_x \cdot N_z}} \quad (10)$$

$\mathbf{m}_{true}$ represents the true model, $\mathbf{m}_{inv}$ is the inversion result, and N_x and N_z denote the number of grid divisions in the horizontal and vertical directions, respectively. The RD metric helps us evaluate whether the constraint inversion results are closer to the true model, or at least not more deviated from the true model compared to the free inversion. A smaller RD value indicates that the inversion result is closer to the true model.

4.1 Double-block test

The double-block model consists of a 1,000 Ω·m high-resistivity target and a 10 Ω·m high-conductivity target within a uniform

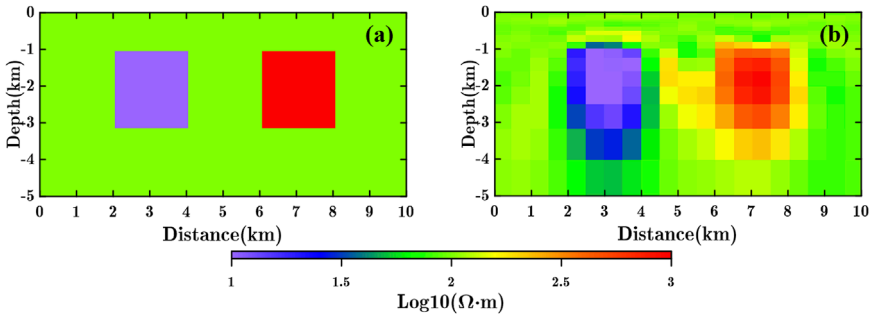

FIGURE 4
Double-block model. **(A)** True model. **(B)** Free inversion result.

background of 100 Ω·m (Figure 4A). The grid for MT inversion was discretized into 37 × 48 cells in the model region, while the cells outside the model region are extended to satisfy the boundary conditions of MT modeling (Wannamaker et al., 1987). We placed 21 observation stations on the surface, spaced equally at 0.5 km intervals. The data used for the inversions include both TE and TM modes, with 24 frequencies ranging from 1×10^{-2}~1×10^{2} Hz. The apparent resistivity and impedance phase synthetic data were both contaminated with 2% Gaussian random noise. The MT inversion started with an infinite half-space of 100 Ω·m, and the free inversion result is presented in Figure 4B.

We first used the weak gradient-contrast model (which represents weak gradient difference between the constraint information between high resistivity and low resistivity blocks) as the constraint model for inversion (Figure 6A). We performed cross-gradient and MCGS coupling constrained inversion with $\varepsilon^2 = 0.001$, 0.01, and 0.1, respectively. The weight of constrained inversion, λ, is determined by balancing data fitting and the RCG value. We selected five gradually increasing weights for each inversion process to determine the optimal λ for each focusing factor and cross-gradient constrained inversion, ensuring a balance between the RCG and RMS misfit. The final determined weights are marked in Figure 5A. A focusing factor that is too small ($\varepsilon^2 = 0.001$) can lead to excessive focusing, with small cross-gradients quickly enhanced through focusing, making it difficult to fit the data when coupling weights are large. Conversely, a large focusing factor ($\varepsilon^2 = 0.1$) weakly focuses the cross-gradient, resulting in a constrained inversion outcome that is close to traditional cross-gradient coupling.

Finally, we determined $\varepsilon^2 = 0.01$ as the focusing factor and $\lambda = 0.4$ as the coupling term weight. The inversion results are shown in Figure 6. Compared to the free inversion (Figure 4B), both the traditional cross-gradient (Figure 6C) and MCGS (Figure 6E) constrained inversions better restore the real model, with RD values of 0.25, 0.20, and 0.13, respectively. Compared to the traditional cross-gradient constrained inversion result, the MCGS constrained inversion more accurately restores the real model and achieves lower RCG values. The RCG value of the MCGS constrained inversion result is 0.63, whereas the RCG for the traditional cross-gradient constrained inversion is 0.92, indicating that the structural similarity between the MCGS constrained inversion result and the real model is higher.

One of the advantages of MCGS coupling is its ability to better balance the uneven cross-gradient values between strong and weak gradient values. To better demonstrate this advantage, we designed the strong gradient-contrast model constraint test (which represents strong gradient difference between the constraint information between high resistivity and low resistivity blocks), we adjusted the model used for constraints, setting the low resistivity block physical property value to 3 Ω·m (approximately 0.5 in base 10 logarithm resistivity), the high resistivity block physical property value to 200 Ω·m (approximately 2.3 in base 10 logarithm resistivity), while maintaining the background resistivity at 100 Ω·m (Figure 6B). Since OCCAM inversion employs base 10 logarithm resistivity values, the cross-gradient value of the low resistivity block is approximately five times that of the high resistivity block relative to the background resistivity of 100 Ω·m. This adjustment aims to simulate the numerical imbalance between the cross-gradient values caused by strong gradient-contrast prior constraint information, a situation commonly encountered in field studies.

The parameter selection method for constrained inversion aligns with the previous section (Figure 5B). The cross-gradient and MCGS constrained inversion results are presented in Figure 11, where the RD of the cross-gradient constrained inversion result is 0.18. From the cross-gradient constrained inversion results (Figure 6D), it is evident that the constraint effect of the low resistivity model has significantly improved. Compared to using a 10 Ω·m real model for constraint, the constrained inversion result utilizing a 3 Ω·m model is closer to the actual model. However, in contrast to using a 100 Ω·m real model for constraint, the high resistivity model exhibits poorer constraint effectiveness, as the adjusted constraint model results in a significant numerical difference in the cross-gradient values between high and low resistivity blocks.

The MCGS constrained inversion result (Figure 6F) demonstrates that focusing on the imbalanced cross-gradient can better address the numerical discrepancies caused by variations in physical properties. The RD of the MCGS constrained inversion is 0.13, which is comparable to the RD obtained using a real model for MCGS constrained inversion. MCGS coupling can yield results similar to those achieved with weak gradient-contrast constraint information in situations where the constraint information has strong gradient-contrast.

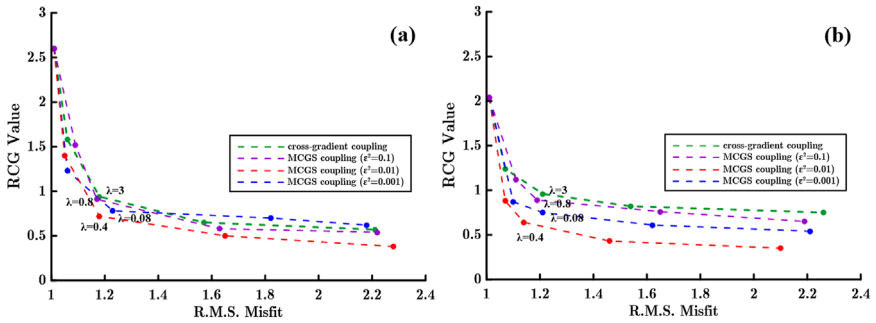

FIGURE 5
L-curves for λ determination. **(A)** L-curve in true model constrained inversion. **(B)** L-curve in adjusted model constrained inversion.

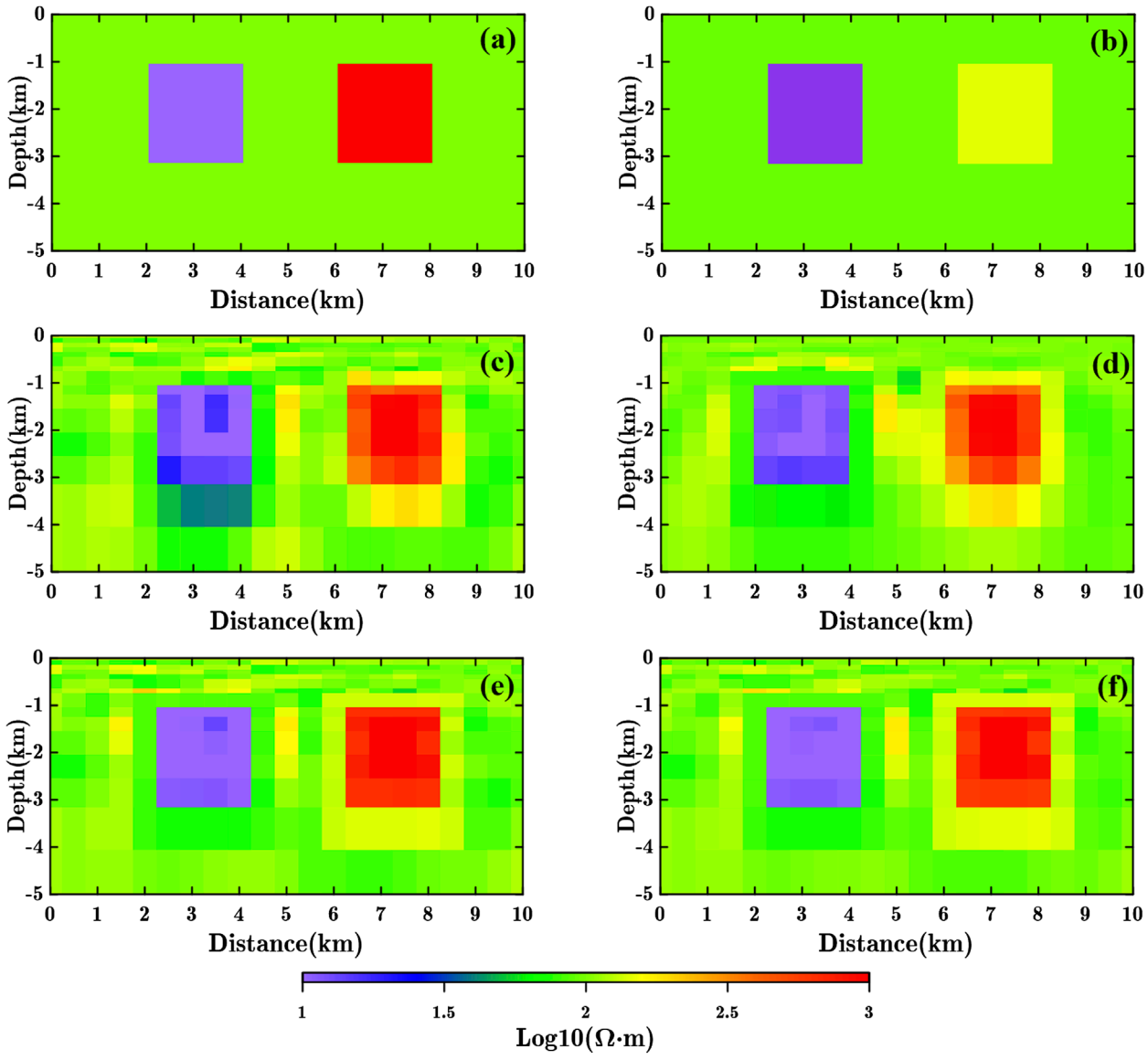

FIGURE 6
Double-block model constrained inversion results. **(A)** Constraint model (true model). **(B)** Constraint model (adjusted model). **(C)** Cross-gradient constrained inversion result using true model constraint. **(D)** Cross-gradient constrained inversion result using adjusted model constraint. **(E)** MCGS (ε^2 = 0.01) constrained inversion result using true model constraint. **(F)** MCGS (ε^2 = 0.01) constrained inversion result using adjusted model constraint.

4.2 Nappe structure model

Improving the constraint effect on regions with weak physical property variations is another significant advantage of MCGS coupling. In this section, we designed two deep nappe structure model tests to illustrate this point. The two overlay construction models we designed correspond to two target layers with different physical properties located at a depth of about 8 km. Figure 7A depicts the low resistivity target layer, while Figure 8A depicts the high resistivity target layer, resistivity values of all layers in both models are consistent except for the target layer. We placed 37 observation stations on the surface, equally spaced at 0.5 km intervals, The data used for the inversions were collected in both TE and TM modes, encompassing 40 frequencies over a range of $5.5 \times 10^{-4} \sim 3.2 \times 10^{2}$ *Hz*, the apparent resistivity and impedance phase data both contaminated with 2% gaussian random noise.

The identification of deep target bodies has always been a challenging aspect of MT inversion. Deep target bodies exhibit weak responses to data, limited model correction, and subtle variations in physical properties during the inversion process, which restricts the ability to characterize these deep targets.

The free inversion results for low the resistivity (Figure 7B) and high resistivity (Figure 8B) target layer models, after 13 and 12 iterations respectively. Neither inversion result successfully characterizes the target layer, and the resolution at the depth of the target layer is insufficient, thus, constrained inversion using prior information is necessary for accurate characterization. We utilize the region above the target layer as known prior information for the constrained inversion, while the area below the top of the target layer lacks constrained information (indicated by the grey solid lines in Figures 7, 8).

We select $\varepsilon^2 = 0.01$ as our focusing factor. The MCGS constrained inversion results (Figures 7C, 8C) and the residual cross-gradient distribution maps are presented in Figures 7E, 8E. It is evident that MCGS coupling assists MT inversion in characterizing the target layer in low-resolution regions. Both the high resistivity and low resistivity target layers are distinctly displayed under the influence of MCGS coupling, achieving lower residual cross-gradient values compared to cross-gradient coupling, with a stronger structural similarity to the real model. In comparison to the results of cross-gradient constrained inversion, MCGS coupling demonstrates significant advantages in enhancing the structural coupling effect of constrained inversion in depths with weak physical property variations, whereas cross-gradient coupling can only provide structural constraints in areas with substantial changes in physical properties.

5 Field applications

5.1 Research background

The Junggar Basin and its surrounding areas are located in northern Xinjiang, situated between the Tarim Plate, the Kazakhstan Plate, and the Siberian Plate, and belong to the ancient Asian Ocean tectonic domain. The Junggar Basin is also a significant oil-bearing region in western China, preserving important records of tectonic movement and rich oil and gas resources, making it a key area of study. Based on the structural characteristics of the Permian system within the basin and subsequent structural modifications, the Junggar Basin is divided into six primary structural units: the Western Uplift (WU), the Eastern Uplift (EU), the Luliang Uplift (LU), the North Tianshan Thrust Belt (NTTB), the Central Depression (CD), and the Wulungu Depression (WD) (Figure 9). The Junggar Basin has undergone several evolutionary stages, including the formation of its basement before the Carboniferous, the transitional development during the Carboniferous-Permian, the development of the Mesozoic-Paleogene inland lake basin, and the intense compression during the Neogene-Quaternary periods (He et al., 1994). From the late Paleozoic to the early Mesozoic, the Junggar Basin was once a marine environment where sedimentary layers were formed. With the collision of the Indian Plate and the Eurasian Plate, the sea area was gradually compressed into land. Under the influence of tectonic activity, the basin's crust was uplifted, forming mountains and plateaus. A major tectonic transformation occurred in the late Tertiary, establishing the current basement structural morphology of the Junggar Basin.

Over the past 20 years, significant progress has been made in studying the deep electrical structures of the Junggar Basin. The Xinjiang Petroleum Administration conducted MT soundings in the central part of the basin, completing three large-scale MT profiles across the entire area. In the late 1990s, the Geological Survey of the Petroleum Geophysical Exploration Bureau acquired six MT profiles. Luo et al. (2020) used MT sounding to infer the distribution characteristics of the Carboniferous in the Urumqi Depression in the northern Junggar Basin. They divided the Junggar Basin's subsurface to a depth of over 30 km into three distinct electrical layers: the sedimentary overburden, the Hercynian basement, and the Precambrian crystalline basement (also referred to as the Neoarchean to Mesoproterozoic basement).

5.2 Data processing

The data we used comes from the "xj9201"MT survey line collected by Tongji University, located in the central Junggar Basin. The survey line runs from south to north, passing through the NTTB, CD, and LU, with a length of 292 km. The red triangles in Figure 9 represent the locations of MT measurement points, with a total of 87 observation stations and 40 frequencies ranging from 5.5×10^{-4} to 3.2×10^{2} Hz.

We present the apparent resistivity and impedance phase profiles along the survey line (Figure 10). Due to limitations in data collection, data below 2×10^{-3} Hz are incomplete; therefore, we primarily used data at frequencies higher than 2×10^{-3} Hz. The apparent resistivity profile (Figures 10A, C) shows an increasing trend in resistivity values from south to north along the survey line, with values also increasing gradually with depth. The shallow sections of these profiles are predominantly conductive, while the main anomalies in the deeper sections are characterized by high resistivity. To mitigate the influence of distorted currents, we applied GB decomposition (Groom and Bailey, 1989) to the collected impedance data. The inversion results presented in this section are based on joint TM and TE mode inversion, with an error floor set at 5% and an initial model of a uniform half-space of

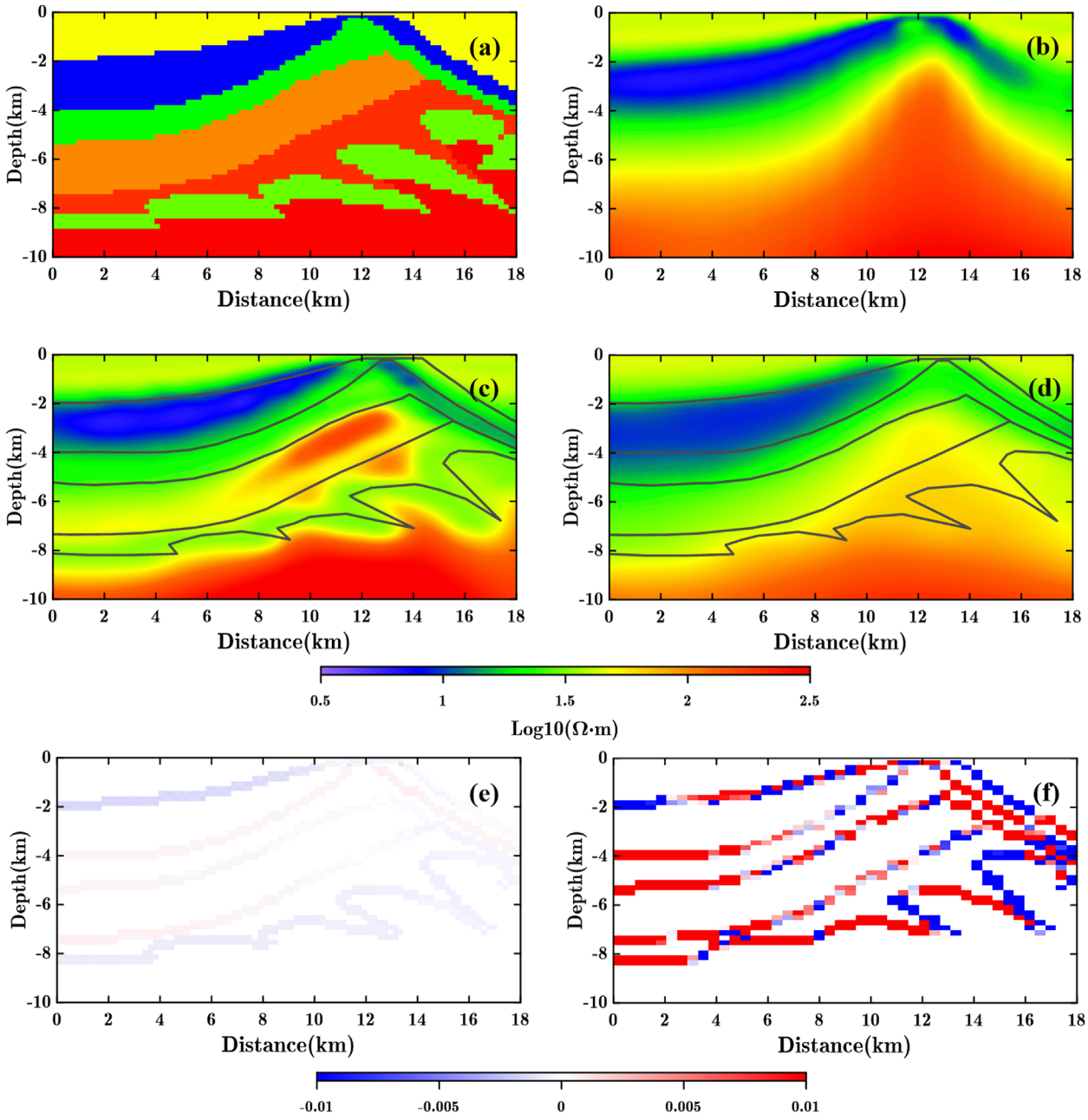

FIGURE 7
Low resistivity target layer nappe structure model test. **(A)** True model. **(B)** Free inversion result. **(C)** MCGS (ε^2 = 0.01) constrained inversion result using true model constraint (black solid lines indicate the constraint layers). **(D)** Cross-gradient constrained inversion result using true model constraint (black solid lines indicate the constraint layers). **(E)** Residual cross-gradient distribution of MCGS (ε^2 = 0.01) constrained inversion result. **(F)** Residual cross-gradient distribution of cross-gradient constrained inversion result.

10 Ω·m throughout the inversion process. The stopping criteria for the iterations are consistent with those used in the previous model tests.

The geological model used for the constrained inversion is shown in Figure 11. It includes constraints from six sedimentary strata, ranging from the Neogene to the Permian, with different colors representing different stratigraphic ages. There are no constraints below the Permian sedimentary layers, so we only present geological profiles with a depth of less than 15 km. Electrical property statistics for each stratigraphic age are also provided in Figure 11. The physical properties of the constraint model we use are derived from the statistical data of the formation velocity in the region. We assign the statistic formation velocity to each formation for constrained inversion. Although we did not use actual resistivity values for the constraints, we demonstrated in previous model tests that MCGS constraints are far less sensitive to the strength of gradient values in constraint information compared to traditional cross-gradient constraints.

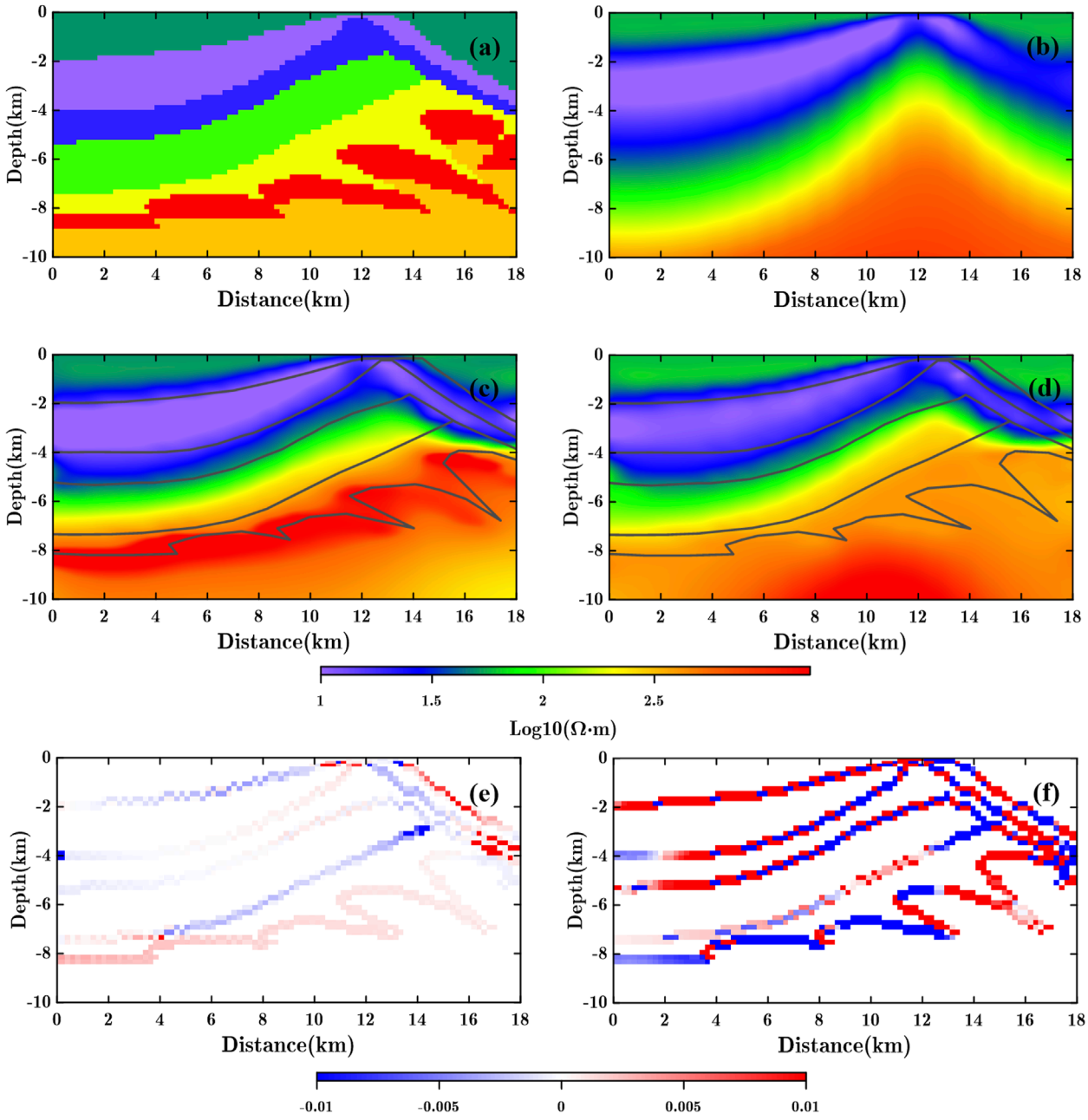

FIGURE 8
High resistivity target layer nappe structure model test. **(A)** True model. **(B)** Free inversion result. **(C)** MCGS (ε^2 = 0.01) constrained inversion result using true model constraint (black solid lines indicate the constraint layers). **(D)** Cross-gradient constrained inversion result using true model constraint (black solid lines indicate the constraint layers). **(E)** Residual cross-gradient distribution of MCGS (ε^2 = 0.01) constrained inversion result. **(F)** Residual cross-gradient distribution of cross-gradient constrained inversion result.

5.3 Inversion

The result of the free inversion (Figure 12B) show a reduction in the error from 14.81 to 2.84 after 9 iterations. We marked the Permian constraint interface with a black dashed line in the inversion results, indicating that the free inversion accurately reflects the positions of the sedimentary layers and the high-resistivity crystalline basement beneath. Additionally, the deep electrical structures exhibit distinct horizontal block-like characteristics. While the free inversion effectively portrays the geoelectric model of the area, it fails to accurately capture the resistivity differences between different layers within the sedimentary strata, and inaccuracies in the shallow resistivity structures may also influence the morphology of the deeper electrical structures. Therefore, we applied the prior sedimentary layer model shown in Figure 11 for constrained inversion. The coupling weights for MCGS and cross-gradient were set to 1 and 10, respectively, with a focusing factor of 0.01. The parameter selection was based on a trade-off between

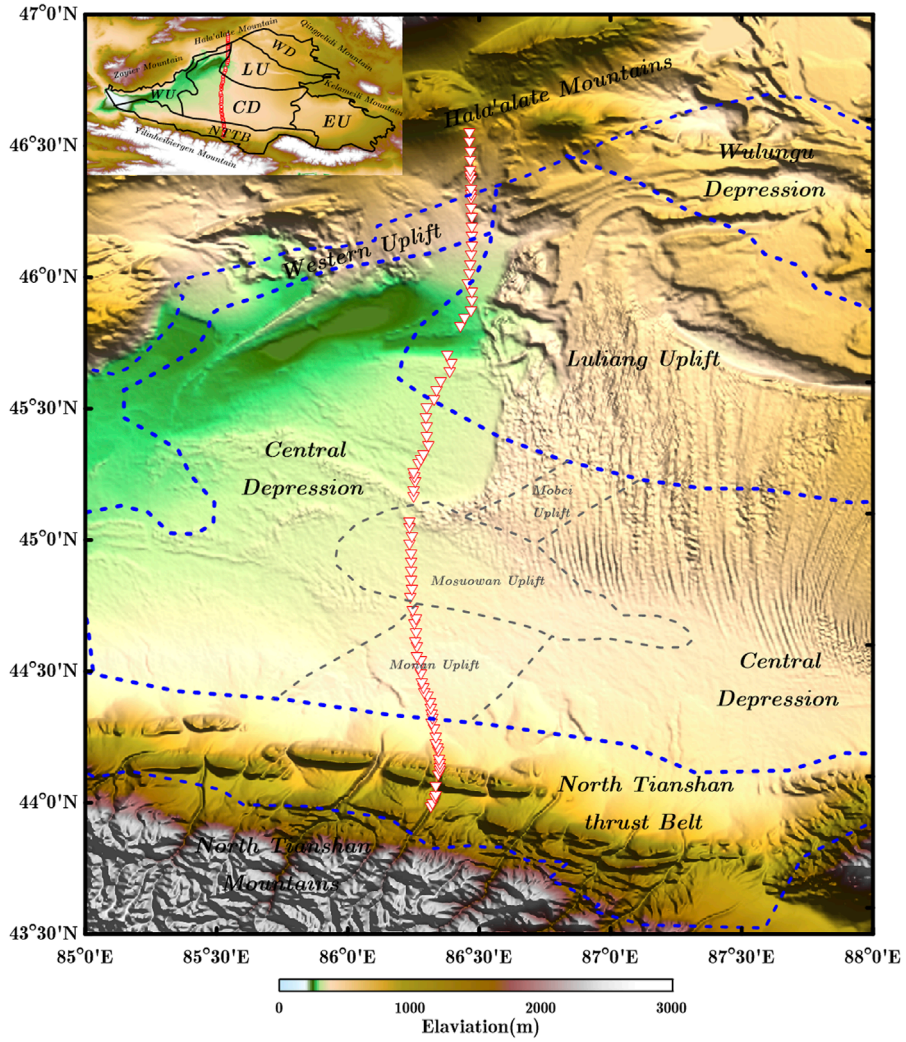

FIGURE 9
Topographic map of the Junggar basin. Red triangles indicate the location of MT observation stations, blue dash lines indicate the boundary of first-order structural unit, grey dash lines indicate the boundary of second-order structural unit.

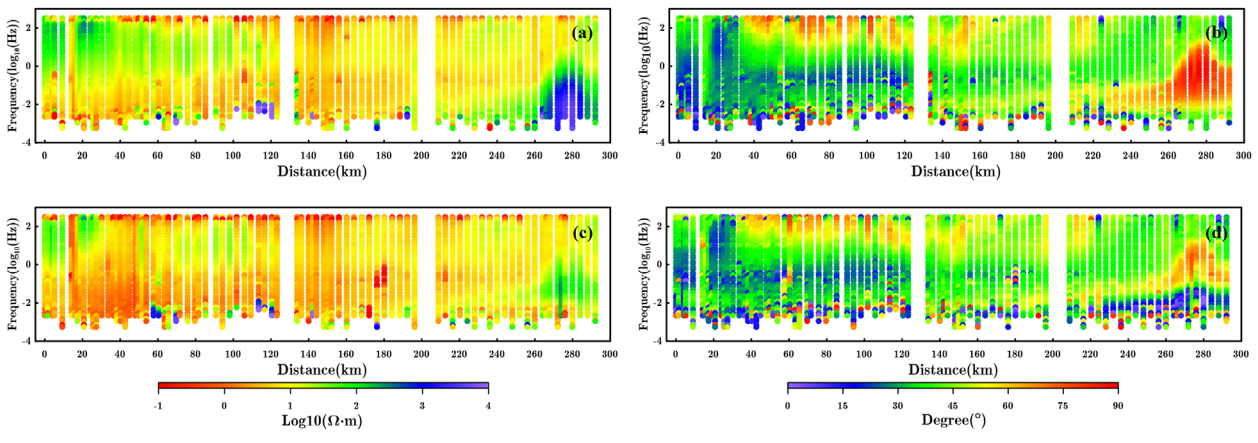

FIGURE 10
Observation data. **(A)** TE mode apparent resistivity. **(B)** TE mode impedance phase. **(C)** TM mode apparent resistivity. **(D)** TM mode impedance phase.

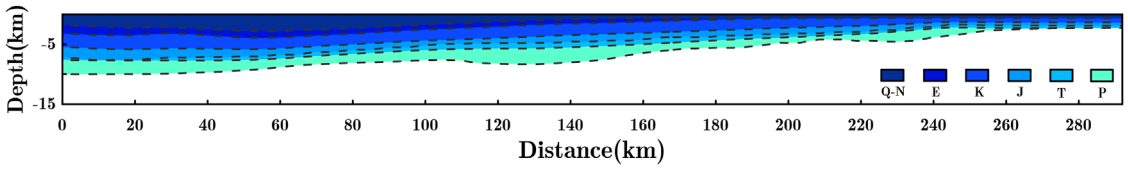

Chron	Q	N	E	K	J	T	P
Reference value(Ω·m)	40~100	5~20	5~20	1~8	10~30	10~30	10~50

FIGURE 11
Priori constraint model. Grey dash lines represent the boundary of the geological stratum, the table shows the statistical data of resistivity values in different geological stratum; Q-Quaternary; N-Neogene; E-Paleogene; K-Cretaceous; J-Jurassic; T-Triassic; P-Permian.

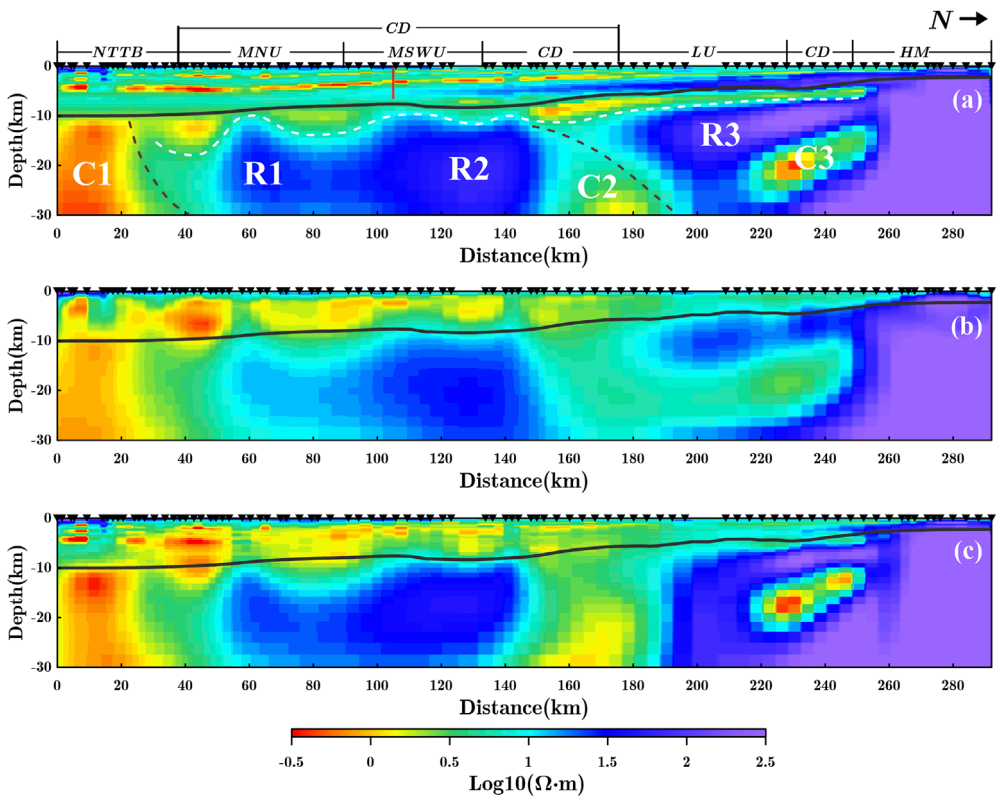

FIGURE 12
Inversion result of survey line "xj9201". **(A)** MCGS (ε^2 = 0.01) constrained inversion result. **(B)** Free inversion result. **(C)** Cross-gradient constrained inversion result. Black solid line indicates the lower bound of the stratum constraint (lower bound of the Permian strata); Red solid line on the MCGS constrained inversion result indicates the location of the nearest logging to the profile; White dash line indicates the possible Carboniferous strata; Brown dash line indicates the main faults related to subduction.

residual cross-gradient values and data fitting, consistent with the approach used in the model tests.

The results of the MCGS and cross-gradient coupling constraints are shown in Figures 12A, C. The cross-gradient constrained inversion reduced the data misfit from 14.81 to 2.79 after 14 iterations, while the MCGS constrained inversion reduced the misfit from 14.81 to 2.65 after 16 iterations. The applicability of cross-gradient coupling is limited in real-world datasets with uneven gradient distributions and complex variation directions of properties, leading to weak constraint capabilities and an inability to accurately depict the electrical structures of sedimentary layers from different ages (Figure 12C). In contrast, the MCGS constrained inversion result (Figure 12A) shows that MCGS coupling effectively incorporates constraint information into the inversion, clearly illustrating the electrical structure distribution of sedimentary layers of varying ages. Compared to free inversion and cross-gradient constraints, MCGS constrained inversion exhibits a superior ability to accurately characterize the electrical structures of sedimentary layers through stratigraphic constraint information.

Additionally, when we compared the inversion results with actual logging data (Figure 13), the MCGS constrained inversion result showed better agreement with the logging data, accurately depicting the layered electrical structure within the sedimentary layers. In contrast, the free inversion result failed to characterize these typical layered structures. Thus, the interpretations in the following chapters are all based on the MCGS constrained inversion result (Figure 12A).

5.4 Interpretation

When performing MCGS constrained inversion, there is no constraint applied between the Neogene and Quaternary sedimentary layers. However, from the inversion result profile, a distinct stratified distribution emerges, with high resistivity at the top and low resistivity at the bottom within the Neogene and overlying strata. The shallower Quaternary sediments and deeper Neogene sediments correspond to the high resistivity and high conductivity layers above the first constraint interface (Neogene), which aligns with the resistivity property statistics in Figure 11. At the southern end of the survey line, the resistivity of the Paleogene strata is higher than that of the Neogene strata. As the Paleogene and Neogene strata thin toward the north, the resistivity of the Paleogene strata decreases and becomes similar to that of the Neogene. Below the Paleogene, the Cretaceous strata present a clear set of high conductivity layers, with physical properties ranging from 0 to 10 Ω·m, as shown in Figure 11. On the inversion result profile (Figure 12C), this high conductivity characteristic of the Cretaceous strata is clearly visible, distinguishing it from the Paleogene and Jurassic strata.

The boundary between the Jurassic, Triassic, and Permian strata is less distinct in the southern part of the survey line. The resistivity values of the Jurassic and Triassic strata are slightly higher than those of the Permian, but in the northern part of the survey line, the Permian strata show an increase in resistivity, exceeding that of the Jurassic and Triassic. The MCGS constrained inversion effectively distinguishes the Permian from the strata below. Beneath the Permian and above the high-resistivity crystalline basement, there exists a discontinuous layer (marked on the Figure 12A by white dash line). This layer is neither part of the Permian nor the crystalline basement, and we speculate that it could be a remnant of the Carboniferous strata. Due to its deep burial and proximity to the high-resistivity basement, it is challenging to characterize this layer on seismic migration profiles. It is evident that the lateral depth of these strata, located above the high-resistivity basement beneath the Permian, varies significantly, and their resistivity distribution exhibits lateral block-like characteristics. This suggests that the Carboniferous strata experienced intense tectonic activity, leading to their discontinuous distribution. Furthermore, there is a notable difference in resistivity between the potential Carboniferous remnants in the LU area and the overlying Permian strata. This

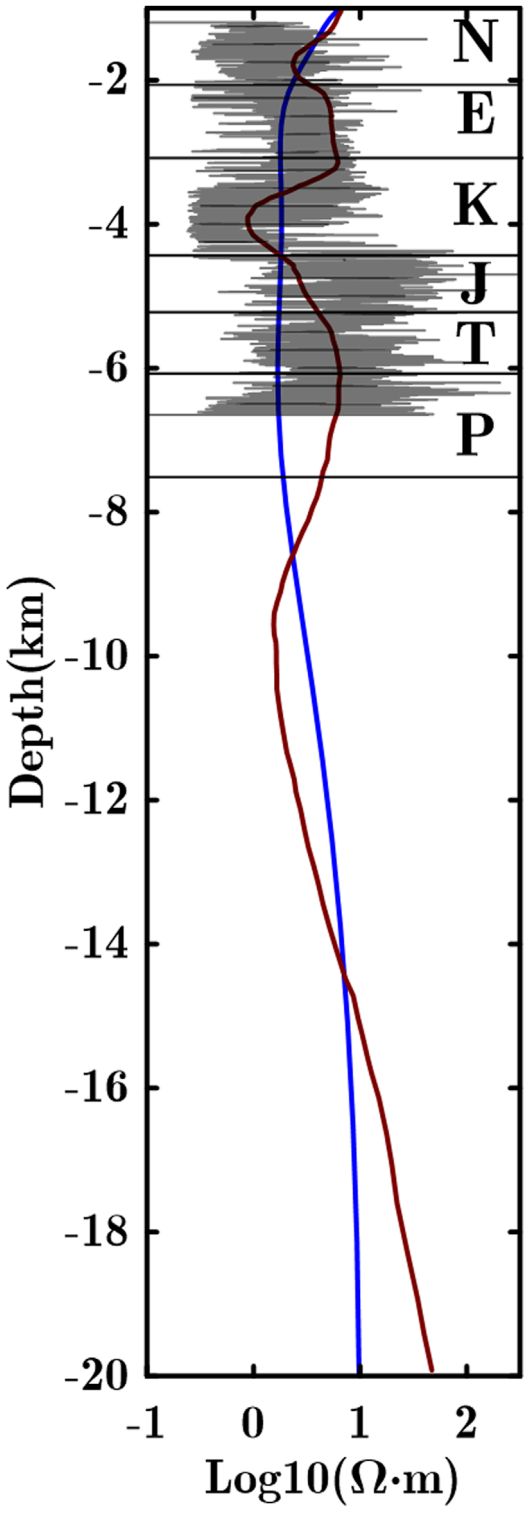

FIGURE 13
Comparison between logging curve and inversion results. Grey solid line-logging curve; Red solid line-MCGS constrained inversion result; Blue solid line-free inversion result.

difference could be attributed to the development of regional unconformities between the Carboniferous and Permian in the LU and northern regions, resulting in the strong erosion of Upper Carboniferous and some Lower Carboniferous strata, as suggested by He et al. (2013).

Through the application of MCGS coupling, we achieved a more precise characterization of the electrical structure of the sedimentary layers in this section. The improved accuracy of shallow electrical structures contributes to a better understanding of the deep electrical structures. These deep structures reflect the geological evolution of basement formation in the Junggar Basin prior to the Carboniferous period. The inversion result highlight two ocean-continent subduction zones. The three conductors, C1, C2, and C3, represent the subduction remnants of the South Junggar Ocean (SJO) and the Karamaili Ocean (KO), respectively. Due to the large amounts of fluid released during oceanic crust subduction, C1, C2, and C3 exhibit high conductivity characteristics. During the Carboniferous period, the hinterland of the Junggar Basin mainly consisted of the Mosuowan juvenile crust, which was distributed within the Paleo-Asian Ocean (He et al., 2013). The SJO subducted toward the continental crust, forming the resistor volcanic island arc R1, and the fluids released from subduction led to the formation of the C1 conductor. The resistor R2 corresponds to the Mosuowan juvenile crust. The conductors C2 and C3, located beneath the continental ridge uplift, may represent the residual oceanic crust of the KO, which closed during the Carboniferous. The resistor R3 further suggests the juvenile continental crust that was subducted northward by the KO.

6 Conclusion

In this paper, to address the issue of the weak constraint effect of cross-gradient coupling in regions with weak gradients, we developed a new constraind inversion coupling method based on MCGS coupling, which applies a minimum support function to enhance traditional cross-gradient coupling. In theoretical model tests, we compared it with NCG coupling (Haber and Modersitzki, 2006), which reduces the influence of gradient values on cross-gradient coupling but is limited by its non-convexity. We also compared JMGS coupling (Molodtsov and Troyan, 2017), which, like MCGS, uses a minimum support function. JMGS can also support weak gradients, but its applicability to constrained inversion in complex geological settings is limited, making it more suitable for cases with more comprehensive prior information and high gradient orientation consistency. In contrast, MCGS has broader applications.

To verify the effectiveness of MCGS coupling, we conducted two synthetic model experiments. First, we applied it to a double-block model, and the results demonstrated that MCGS coupling enhances structural similarity between the inversion results and the true model, partially overcoming the limitations of cross-gradient coupling as a weak structural constraint. It also proves that MCGS can maintain good constraint effects even with strong gradient contrast in prior information. Next, we designed two complex nappe models, corresponding to high resistivity and low resistivity target layers at depth, to verify the advantages of MCGS in addressing insufficient deep resolution and weak response areas in the observation data compared to traditional cross-gradient coupling. In both models, MCGS coupling allowed for the clear characterization of deep target layers, while cross-gradient constrained inversion failed to reveal the electrical structure of these layers.

Finally, we applied MCGS coupling to MT field data from the Junggar Basin, utilizing prior stratigraphic information for constrained inversion. The traditional cross-gradient inversion results exhibited a weak constraint effect, while the MCGS-constrained inversion results clearly depicted the geoelectric structure among the prior stratigraphic layers and it had good correspondence with logging data. Compared to free inversion and traditional cross-gradient coupling, MCGS coupling significantly improved the characterization of shallow electrical structures and provided more accurate depictions of deep electrical structures, offering new geophysical evidence for the development of an evolutionary model for the Junggar Basin.

Data availability statement

All the data and inversion codes used in this paper is available by contacting the corresponding author, the OCCAM2DMT code is available at https://marineemlab.ucsd.edu/Projects/Occam/2DMT/index.html.

Author contributions

ZH: Conceptualization, Formal Analysis, Investigation, Methodology, Software, Writing–original draft. PY: Conceptualization, Data curation, Formal Analysis, Funding acquisition, Investigation, Methodology, Project administration, Resources, Supervision, Validation, Visualization, Writing–review and editing. CZ: Conceptualization, Formal Analysis, Funding acquisition, Investigation, Supervision, Validation, Visualization, Writing–review and editing. LZ: Funding acquisition, Methodology, Software, Supervision, Writing–review and editing. HS: Investigation, Resources, Software, Validation, Writing–review and editing.

Funding

The author(s) declare that financial support was received for the research, authorship, and/or publication of this article. We express our sincere gratitude to General Program of National Natural Science Foundation of China (under Grant No. 42474105), the Geological Joint Fund of National Natural Science Foundation of

China (Key Fund Project, under Grant No. U2344203), General Program of National Natural Science Foundation of China (under Grant No. 42074079), Major Project of China National Petroleum Corporation (under Grant No. 2023ZZ05-05), The Jiangsu Province Carbon Peak Carbon Neutral Technology Innovation Project in China (under Grant No.BE2022034-3).

Conflict of interest

The authors declare that the research was conducted in the absence of any commercial or financial relationships that could be construed as a potential conflict of interest.

Generative AI statement

The author(s) declare that no Generative AI was used in the creation of this manuscript.

Publisher's note

References

Carter-McAuslan, A., Lelièvre, P. G., and Farquharson, C. G. (2015). A study of fuzzy c-means coupling for joint inversion, using seismic tomography and gravity data test scenarios. *Geophysics* 80 (1), W1–W15. doi:10.1190/geo2014-0056.1

Colombo, D., and De Stefano, M. (2007). Geophysical modeling via simultaneous joint inversion of seismic, gravity, and electromagnetic data: application to prestack depth imaging. *Lead. Edge* 26 (3), 326–331. doi:10.1190/1.2715057

Constable, S. C., Parker, R. L., and Constable, C. G. (1987). Occam's inversion: a practical algorithm for generating smooth models from electromagnetic sounding data. *Geophysics* 52 (3), 289–300. doi:10.1190/1.1442303

Crestel, B., Stadler, G., and Ghattas, O. (2018). A comparative study of structural similarity and regularization for joint inverse problems governed by PDEs. *Inverse Probl.* 35 (2), 024003. doi:10.1088/1361-6420/aaf129

deGroot-Hedlin, C., and Constable, S. (1990). Occam's inversion to generate smooth, two-dimensional models from magnetotelluric data. *Geophysics* 55 (12), 1613–1624. doi:10.1190/1.1442813

de Lugao, P. P., and Wannamaker, P. E. (1996). Calculating the two-dimensional magnetotelluric Jacobian in finite elements using reciprocity. *Geophys. J. Int.* 127 (3), 806–810. doi:10.1111/j.1365-246x.1996.tb04060.x

Doetsch, J., Linde, N., Coscia, I., Greenhalgh, S. A., and Green, A. G. (2010). Zonation for 3D aquifer characterization based on joint inversions of multimethod crosshole geophysical data. *Geophysics* 75 (6), G53–G64. doi:10.1190/1.3496476

Franz, G., Moorkamp, M., Jegen, M., Berndt, C., and Rabbel, W. (2021). Comparison of different coupling methods for joint inversion of geophysical data: a case study for the Namibian continental margin. *J. Geophys. Res. Solid Earth* 126 (12), e2021JB022092. doi:10.1029/2021jb022092

Fregoso, E., and Gallardo, L. A. (2009). Cross-gradients joint 3D inversion with applications to gravity and magnetic data. *Geophysics* 74 (4), L31–L42. doi:10.1190/1.3119263

Gallardo, L. A. (2007). Multiple cross-gradient joint inversion for geospectral imaging. *Geophys. Res. Lett.* 34 (19). doi:10.1029/2007gl030409

Gallardo, L. A., Fontes, S. L., Meju, M. A., Buonora, M. P., and De Lugao, P. P. (2012). Robust geophysical integration through structure-coupled joint inversion and multispectral fusion of seismic reflection, magnetotelluric, magnetic, and gravity images: example from Santos Basin, offshore Brazil. *Geophysics* 77 (5), B237–B251. doi:10.1190/geo2011-0394.1

Gallardo, L. A., and Meju, M. A. (2003). Characterization of heterogeneous near-surface materials by joint 2D inversion of dc resistivity and seismic data. *Geophys. Res. Lett.* 30 (13). doi:10.1029/2003gl017370

Gallardo, L. A., and Meju, M. A. (2011). Structure-coupled multiphysics imaging in geophysical sciences. *Rev. Geophys.* 49 (1). doi:10.1029/2010rg000330

Gao, J., and Zhang, H. (2018). An efficient sequential strategy for realizing cross-gradient joint inversion: method and its application to 2-D cross borehole seismic traveltime and DC resistivity tomography. *Geophys. J. Int.* 213 (2), 1044–1055. doi:10.1093/gji/ggy026

Groom, R. W., and Bailey, R. C. (1989). Decomposition of magnetotelluric impedance tensors in the presence of local three-dimensional galvanic distortion. *J. Geophys. Res.: Solid Earth* 94 (B2), 1913–1925.

Gross, L. (2019). Weighted cross-gradient function for joint inversion with the application to regional 3-D gravity and magnetic anomalies. *Geophys. J. Int.* 217 (3), 2035–2046. doi:10.1093/gji/ggz134

Haber, E., and Holtzman Gazit, M. (2013). Model fusion and joint inversion. *Surv. Geophys.* 34, 675–695. doi:10.1007/s10712-013-9232-4

Haber, E., and Modersitzki, J. (2006). "Intensity gradient based registration and fusion of multi-modal images," in Medical Image Computing and Computer-Assisted Intervention–MICCAI 2006: 9th International Conference, Copenhagen, Denmark, October 1-6, 2006. Proceedings, Part II (Berlin Heidelberg: Springer), 726–733.

Haber, E., and Oldenburg, D. (1997). Joint inversion: a structural approach. *Inverse probl.* 13 (1), 63–77. doi:10.1088/0266-5611/13/1/006

He, D. F., Li, D., Fan, C., and Yang, X. F. (2013). Geochronology, geochemistry and tectonostratigraphy of carboniferous strata of the deepest well moshen-1 in the Junggar Basin, northwest China: insights into the continental growth of central asia. *Gondwana Res.* 24 (2), 560–577. doi:10.1016/j.gr.2012.10.015

He, G. Q., Liu, D. C., Li, M. S., Tang, Y. L., and Zhou, R. H. (1994). *Paleozoic crustal evolutions and mineralization*. Hong Kong: Xinjiang People's Publishing House, Urumqi and Culture and Education Press of Hong Kong. 437.

Heincke, B., Jegen, M., and Hobbs, R. (2006). "Joint inversion of MT, gravity and seismic data applied to sub-basalt imaging," in *SEG technical Program expanded abstracts 2006* (Society of Exploration Geophysicists), 784–789.

Heincke, B., Jegen, M., Moorkamp, M., Hobbs, R. W., and Chen, J. (2017). An adaptive coupling strategy for joint inversions that use petrophysical information as constraints. *J. Appl. Geophys.* 136, 279–297. doi:10.1016/j.jappgeo.2016.10.028

Hu, W., Abubakar, A., and Habashy, T. M. (2009). Joint electromagnetic and seismic inversion using structural constraints. *Geophysics* 74 (6), R99–R109. doi:10.1190/1.3246586

Huang, Y., Moorkamp, M., Gao, J., and Zhang, H. (2023). Seismogenic structure of the 2014 M6.5 Ludian earthquake from three-dimensional joint inversion of magnetotelluric data and seismic arrival times. *J. Geophys. Res. Solid Earth* 128, e2022JB026151. doi:10.1029/2022jb026151

Last, B. J., and Kubik, K. (1983). Compact gravity inversion. *Geophysics* 48 (6), 713–721. doi:10.1190/1.1441501

Lelièvre, P. G., Farquharson, C. G., and Hurich, C. A. (2012). Joint inversion of seismic traveltimes and gravity data on unstructured grids with application to mineral exploration. *Geophysics* 77 (1), K1–K15. doi:10.1190/geo2011-0154.1

Luo, W., Zhifang, H. U., Guilin, L. I., Xiaopeng, YANG, Lanfang, H. E., Yang, Y., et al. (2022). Carboniferous strata and their oil and gas prospects from Wulungu depression to the north uplift in the Junggar Basin based on magnetotelluric technology. *Geol. CHINA* 49 (5), 1591–1604. doi:10.12029/gc20220515

Molodtsov, D., Kashtan, B., and Roslov, Y. (2011). "Joint inversion of seismic and magnetotelluric data with structural constraint based on dot product of image gradients," in SEG International Exposition and Annual Meeting. SEG-2011. (SEG).

Molodtsov, D., and Troyan, V. (2017). "Multiphysics joint inversion through joint sparsity regularization," in SEG International Exposition and Annual Meeting. SEG-2011. (SEG).

Molodtsov, D. M., Troyan, V. N., Roslov, Y. V., and Zerilli, A. (2013). Joint inversion of seismic traveltimes and magnetotelluric data with a directed structural constraint. *Geophys. Prospect.* 61, 1218–1228. doi:10.1111/1365-2478.12060

Moorkamp, M., Heincke, B., Jegen, M., Hobbs, R. W., and Roberts, A. W. (2016). Joint inversion in hydrocarbon exploration. *Integr. imaging earth Theory Appl.*, 167–189. doi:10.1002/9781118929063.ch9

Moorkamp, M., Heincke, B., Jegen, M., Roberts, A. W., and Hobbs, R. W. (2011). A framework for 3-D joint inversion of MT, gravity and seismic refraction data. *Geophys. J. Int.* 184 (1), 477–493. doi:10.1111/j.1365-246x.2010.04856.x

Peng, M., Tan, H.-D., Jiang, M., Qian, H., and Tan, J.-Y. (2013). Three-dimensional joint inversion of magnetotelluric and seismic travel time data with cross-gradient constraints. *Chin. J. Geophys.* 56 (8), 2728–2738. doi:10.6038/cjg20130821

Portniaguine, O., and Zhdanov, M. S. (1999). Focusing geophysical inversion images. *Geophysics* 64 (3), 874–887. doi:10.1190/1.1444596

Rawlinson, N., Pozgay, S., and Fishwick, S. (2010). Seismic tomography: a window into deep Earth. *Phys. Earth Planet. Interiors* 178 (3-4), 101–135. doi:10.1016/j.pepi.2009.10.002

Savino, J. M., Rodi, W. L., and Masso, J. F. (1980). Simultaneous inversion of multiple geophysical data sets for earth structure. *Present. A. T. 50th Ann. Internat. Mtg., Soc. Explor. Geophys.*

Shi, B., Yu, P., Zhao, C., Zhang, L., and Yang, H. (2018). Linear correlation constrained joint inversion using squared cosine similarity of regional residual model vectors. *Geophys. J. Int.* 215 (2), 1291–1307. doi:10.1093/gji/ggy336

Sun, J., and Li, Y. (2016). Joint inversion of multiple geophysical data using guided fuzzy c-means clustering. *Geophysics* 81 (3), ID37–ID57. doi:10.1190/geo2015-0457.1

Takougang Takam, E. M., Harris, B., Kepic, A., and Le, C. V. (2015). Cooperative joint inversion of 3D seismic and magnetotelluric data: with application in a mineral province. *Geophysics* 80 (4), R175–R187. doi:10.1190/geo2014-0252.1

Tavakoli, M., Kalateh, A. N., Rezaie, M., Gross, L., and Fedi, M. (2021). Sequential joint inversion of gravity and magnetic data via the cross-gradient constraint. *Geophys. Prospect.* 69 (7), 1542–1559. doi:10.1111/1365-2478.13120

Wannamaker, P. E., Stodt, J. A., and Rijo, L. (1987). A stable finite element solution for two-dimensional magnetotelluric modelling. *Geophys. J. Int.* 88 (1), 277–296. doi:10.1111/j.1365-246x.1987.tb01380.x

Zhang, J., and Morgan, F. D. (1997). "Joint seismic and electrical tomography," in *Symposium on the Application of Geophysics to Engineering and Environmental Problems Proceedings* (Environmental & Engineering Geophysical Society), 391–396. doi:10.4133/1.2922412

Zhang, L., Koyama, T., Utada, H., Yu, P., and Wang, J. (2012). A regularized three-dimensional magnetotelluric inversion with a minimum gradient support constraint. *Geophys. J. Int.* 189 (1), 296–316. doi:10.1111/j.1365-246x.2012.05379.x

Zhdanov, M. S., Jorgensen, M., and Cox, L. (2021). Advanced methods of joint inversion of multiphysics data for mineral exploration. *Geosciences* 11 (6), 262. doi:10.3390/geosciences11060262

frontiers | Frontiers in Earth Science

TYPE Original Research
PUBLISHED 16 December 2024
DOI 10.3389/feart.2024.1510962

OPEN ACCESS

EDITED BY
Maxim Smirnov,
Luleå University of Technology, Sweden

REVIEWED BY
Jinghe Li,
Guilin University of Technology, China
Rui Guo,
Tsinghua University, China

*CORRESPONDENCE
Bo Yang,
0016220@zju.edu.cn

RECEIVED 14 October 2024
ACCEPTED 28 November 2024
PUBLISHED 16 December 2024

CITATION
Liu L, Yang B and Zhang Y (2024) Inverting magnetotelluric data using a physics-guided auto-encoder with scaling laws extension. *Front. Earth Sci.* 12:1510962. doi: 10.3389/feart.2024.1510962

Inverting magnetotelluric data using a physics-guided auto-encoder with scaling laws extension

Lian Liu, Bo Yang* and Yi Zhang

School of Earth Sciences, Zhejiang University, Hangzhou, China

Artificial neural networks (ANN) have gained significant attention in magnetotelluric (MT) inversions due to their ability to generate rapid inversion results compared to traditional methods. While a well-trained ANN can deliver near-instantaneous results, offering substantial computational advantages, its practical application is often limited by difficulties in accurately fitting observed data. To address this limitation, we introduce a novel approach that customizes an auto-encoder (AE) whose decoder is replaced with the MT forward operator. This integration accounts for the governing physical laws of MT and compels the ANN to focus not only on learning the statistical relationships from data but also on producing physically consistent results. Moreover, because ANN-based inversions are sensitive to variations in observation systems, we employ scaling laws to transform real-world observation systems into formats compatible with the trained ANN. Synthetic and real-world examples show that our scheme can recover comparable results with higher computational efficiency compared to the classic Occam's inversion. This study not only perfectly fits the observed data but also enhances the adaptability and efficiency of ANN-based inversions in complex real-world environments.

KEYWORDS

inverse problem, magnetotellurics, artificial neural network, generalization, scaling laws

1 Introduction

Magnetotelluric (MT) inverse problems are inherently nonlinear and fail to produce a unique solution due to the limitations of observed data, the presence of noise, and the model's inherent null space (Backus and Gilbert, 1967; Parker, 1983). Researchers typically employ deterministic methods (Tikhonov and Arsenin, 1977; Constable et al., 1987; Newman and Alumbaugh, 2000; Rodi and Mackie, 2001; Tarantola, 2004; Kelbert et al., 2014; Key, 2016) or stochastic approaches (Jackson and Matsu'ura, 1985; Grandis et al., 1999; Ray, 2021; Peng et al., 2022) to solve the inverse problems.

With the explosive development of deep learning, artificial neural network (ANN) (Roth and Tarantola, 1994; Langer et al., 1996) has shown considerable promise in MT inversion (Guo et al., 2020; Li R. et al., 2020; Guo et al., 2021; Liu W. et al., 2023; Liu et al., 2024 W.; Xu et al., 2024). ANN is a computational model inspired by the structure and function of the human brain. It consists of interconnected neurons that work together to process complex information (Bishop, 1995; Goodfellow et al., 2014; 2016). Such inversions have primarily relied on classic supervised learning (Liao et al., 2022; Xie et al., 2023;

Liu X. et al., 2024), which is fundamentally underpinned by a mechanism akin to prior sampling-based strategies (Valentine and Sambridge, 2021). Generally, ANN learns a mapping from the feature space to the label space based on provided feature-label pairs. Then, we can apply this mapping to new features. Therefore, we need to construct a large number of geoelectric models serving as labels and estimate corresponding MT responses serving as features before training an ANN. The estimation of MT responses, typically generated through forward simulations, is straightforward. However, the construction of geoelectric models is challenging due to the complexity of Earth's structures.

Considering the difficulty of model construction, there are two primary research directions. The first is integrating prior information from sources, such as logging, near-surface geology, and geostatistical data (Wang et al., 2023; Pan et al., 2024; Rahmani Jevinani et al., 2024). Alternatively, we can build geoelectric models using simple mathematical constraints, such as the assumption that the geoelectric model should be smooth (Ling et al., 2023; Liu L. et al., 2023), which is consistent with traditional linearized inversion results. The former is beneficial in improving the inversion resolution, and the latter is more generic for different structures of the Earth. Moreover, Pan et al. (2024) developed a neural network based on deformable convolution (Dai et al., 2017), which extracts hidden relationships and allows flexible adjustments in the size and shape of the feature region. Xu et al. (2024) utilized a self-attention mechanism (Levine et al., 2022) to enhance feature extraction. The supervised ANNs promote the development of MT inversions but have limitations in physical constraints and generalization: the MT response of the model recovered from the trained ANN may not fit the observed data, and we cannot reuse the trained ANN to invert new MT data, which are collected from a different observation system.

The auto-encoder (AE) can be considered a variant of supervised learning. It comprises two key components: an encoder that transforms input features into a user-specified parameter space and a decoder that reconstructs the input features from the specified space. The AE can be trained without labels by minimizing the difference between the reconstructed predictions and the original input features. To fit MT data better, researchers replaced the decoder with the MT forward operator to create a customized AE (Liu et al., 2020; 2022; Ling et al., 2024). In this configuration, the observed MT data serves as the input to the encoder, while the encoder's output becomes the input to the MT forward operator, which generates the predicted data. Thus, the encoder's output represents the geoelectric model. Since the MT forward operator is governed by established physical laws, the system is referred to as a physics-guided AE (PGAE). The framework is utilized not only in the MT method but also in other geophysical methods, such as seismic (Calderón-Macas et al., 1998; Liu B. et al., 2023), geosteering (Jin et al., 2019; Noh et al., 2022), and transient electromagnetic methods (Colombo et al., 2021; Wu et al., 2024).

MT data typically cover a frequency range spanning more than eight orders of magnitude (10^4 Hz ~ 10^{-4} Hz). For real-world applications, varying frequency ranges may be used, which complicates the application of the trained ANN. Therefore, it is crucial to enhance the reusability of well-trained ANNs so that they can effectively handle diverse real-world data scenarios. In AVO (amplitude *versus* offset) inversion of seismic data, Meng et al. (2022) applied a transfer learning strategy (Zhuang et al., 2021) to extend ANN reusability across different systems, while in MT forward simulation, Wang et al. (2024) used transfer learning to improve training efficiency. However, such applications have yet to be reported for MT inversion.

In this study, we employ PGAE for the 1D inversion of MT data, which enables the inverted model to give better data fitting. At the same time, we incorporate scaling laws (Ward, 1967; Nabighian, 1987; Wong et al., 2009) to enhance the reusability of the trained ANN. Firstly, we introduce the fundamental theory for the MT method, PGAE, and scaling laws in Section 2. Subsequently, we demonstrate the efficacy of the proposed approach through applications to both synthetic and real-world MT data in Section 3. Finally, we provide a critical evaluation of the strengths and limitations of the proposed method.

2 Methodology

2.1 MT method

The MT method is a passive-source geophysical technique used to investigate the resistivity distribution of the Earth's subsurface by analyzing the natural electromagnetic fields at the surface (Tikhonov, 1950; Cagniard, 1953). These fields mainly originate from regional and global thunderstorm activity, as well as the interaction of solar wind with the Earth's magnetosphere. As electromagnetic waves propagate through the subsurface, their penetration depth is affected by the diffusion of waves, which varies with frequency. Specifically, waves with lower frequencies demonstrate a greater capacity for deeper penetration into geological structures. Since MT sources are sufficiently distant and the Earth possesses a higher refractive index than air, electromagnetic waves are assumed to propagate as planar waves perpendicular to the Earth's surface. However, the diffusion process through various subsurface structures can exhibit arbitrary polarization. The MT method typically measures the orthogonal components of the natural electric and magnetic fields at the Earth's surface, and a complex impedance tensor $\mathbf{Z}$ is used to describe the mathematical relationship (Equation 1) between the electric and magnetic fields (Berdichevsky, 1976):

$$\mathbf{E} = \mathbf{Z}\mathbf{H}, \tag{1}$$

where $\mathbf{E} = [E_x, E_y]^{\mathrm{T}}$ and $\mathbf{H} = [H_x, H_y]^{\mathrm{T}}$ are the electric and magnetic fields, respectively.

The apparent resistivity and phase are defined as Equations 2, 3, respectively.

$$\rho = \frac{1}{\omega\mu_0}|\mathbf{Z}|, \tag{2}$$

$$\phi = arctan\left(\frac{\mathrm{Im}(\mathbf{Z})}{\mathrm{Re}(\mathbf{Z})}\right), \tag{3}$$

where Re and Im are real and imaginary components of $\mathbf{Z}$, μ_0 is the magnetic permeability of free space, and $\omega = 2\pi f$. f is the frequency.

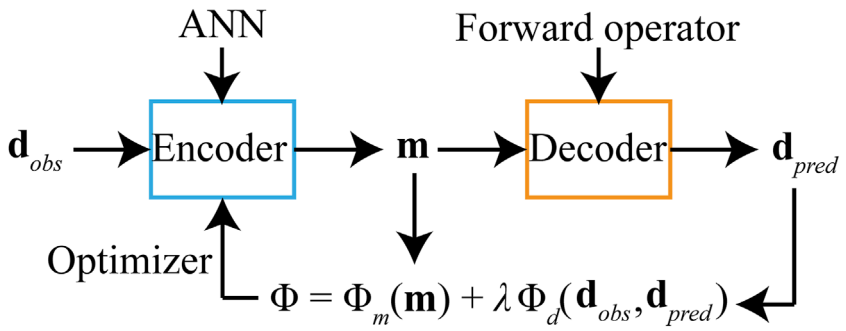

FIGURE 1
The proposed PGAE framework.

2.2 Physics-guided auto-encoder

Building on the AE framework, we replace the decoder with the MT forward operator to create a customized ANN (Figure 1). The loss function Φ_d (Equation 5) in PGAE, representing the difference between input features $\mathbf{d}^{obs}$ and output predictions $\mathbf{d}^{pre}$, corresponds to the data misfit typically employed in traditional inversions. Moreover, a regularization term Φ_m (Equation 6) is employed to ensure the smoothness of the predicted geoelectric model $\mathbf{m}$.

$$\Phi = \Phi_d + \lambda \Phi_m, \tag{4}$$

$$\Phi_d = \frac{1}{2N} \sum_{i=1}^{N} \left\| \mathbf{d}_i^{obs} - \mathbf{d}_i^{pre} \right\|_2^2, \tag{5}$$

$$\Phi_m = \frac{1}{2N} \sum_{i=1}^{N} \left\| \nabla \mathbf{m}_i \right\|_2^2, \tag{6}$$

$$\mathbf{d}_i^{pre} = \mathbf{F}\left[\mathbf{m}_i\right] = \mathbf{F}\left[\mathrm{ANN}\left(\mathbf{w}, \mathbf{d}_i^{obs}\right)\right], \tag{7}$$

where N is the batch size used in training, $\mathbf{F}$ is the forward operator, λ is the regularization parameter, and $\mathbf{w}$ is a set of network parameters.

Algorithm 1 outlines the workflow for implementing PGAE. The process begins by initializing the encoder parameters using a truncated normal distribution, which helps mitigate the exploding or vanishing gradient problems during training Li H. et al. (2020). After initialization, the training samples are shuffled randomly, and a batch of samples is selected and fed into the encoder to generate the corresponding geoelectric models. The MT forward operator is then applied to produce the predicted MT data. Subsequently, the loss function is evaluated using Equation 4. These steps constitute the forward propagation phase. Next, the gradient $\mathbf{g}$ of the loss function is computed with respect to the network parameters $\mathbf{w}$, and the parameters are updated using a suitable optimization algorithm, such as the Adam optimizer introduced by Kingma and Ba (2017). These steps constitute the back propagation phase. If the value of the loss function, Φ, falls below a predefined threshold, ε, the network is saved. Otherwise, the training loop continues until convergence.

Input: Initialize ANN weights $\mathbf{w}$, target loss ε, N_e^{max} epochs, $k = 0$;
while $k < N_e^{max}$ **do**
  Shuffle the samples randomly and divide into N_b batches;
  foreach *batch* **do**
    Compute $\mathbf{m} = \mathrm{ANN}(\mathbf{w}, \mathbf{d}^{obs})$ and $\mathbf{d}^{pre} = \mathbf{F}(\mathbf{m})$ using Equation 7;
    Compute Φ using Equation 4;
    Compute the gradient $\mathbf{g}$ of the loss Φ;
    Update $\mathbf{w} = \mathrm{Adam}(\mathbf{w}, \mathbf{g})$;
    if $\Phi \leq \varepsilon$ **then**
      save $\mathbf{w}$ and break;

Algorithm 1. The PGAE training algorithm.

2.3 Scaling laws

Scaling laws provide a crucial theoretical framework for simulating the electromagnetic response of real-world resistivity structures within a laboratory setting (Ward, 1967; Nabighian, 1987; Wong et al., 2009). Building on the foundational work of Ward (1967), we utilize the coordinates (x, y, z) to represent any point in the real-world system and the coordinates (x', y', z') to denote the corresponding point in the model-scale system. The two systems are related through a length scale factor, denoted as p, and the transformation between them is governed by Equation 8.

$$x = px', y = py', z = pz'. \tag{8}$$

Ignoring the displacement current, the MT field is described by the diffusive forms of Maxwell's equations with a time-dependent component e^{iwt}. For the real-world system, we have

$$\nabla \times \mathbf{E}(x, y, z, f) = -i\omega\mu_0 \mathbf{H}(x, y, z, f), \tag{9}$$

$$\nabla \times \mathbf{H}(x, y, z, f) = \sigma(x, y, z, f)\, \mathbf{E}(x, y, z, f), \tag{10}$$

where σ is the electrical conductivity.

For the model-scale system, we have

$$\nabla \times \mathbf{E}'(x',y',z',f') = -i\omega'\mu_0 \mathbf{H}'(x',y',z',f'), \tag{11}$$

$$\nabla \times \mathbf{H}'(x',y',z',f') = \sigma'(x',y',z',f')\mathbf{E}'(x',y',z',f'). \tag{12}$$

Generally, we want the fields from the real-world system to be linearly transformed from the model-scale system, that is

$$\mathbf{E}(x,y,z,f) = a\mathbf{E}'(x',y',z',f'), \tag{13}$$

$$\mathbf{H}(x,y,z,f) = b\mathbf{H}'(x',y',z',f'). \tag{14}$$

where a and b are scale factors for the electric and magnetic fields, respectively. Therefore,

$$\nabla \times \mathbf{E}(x,y,z,f) = \frac{a}{p}\nabla \times \mathbf{E}'(x,y,z,f), \tag{15}$$

$$\nabla \times \mathbf{H}(x,y,z,f) = \frac{b}{p}\nabla \times \mathbf{H}'(x',y',z',f'). \tag{16}$$

Putting Equations 9–16 together, we have

$$f = \frac{a}{pb}f', \tag{17}$$

$$\sigma = \frac{b}{pa}\sigma'. \tag{18}$$

According to Equations 17, 18, to simulate the MT response of real-world resistivity structures in a model-scale system, we should ensure that the model-scale system has the same induction number as the real-world system:

$$\sigma f l^2 = \sigma' f' l'^2, \tag{19}$$

where l is any characteristic dimension in the real-world system and l' is the corresponding dimension in the model-scale system.

Scaling laws enable us to model large-scale MT responses using a small-size model. While researchers generally employ these principles for physical modeling, they are also applicable to numerical modeling. When we have an ANN trained for audio-frequency MT tasks, we can leverage the trained network to invert long-period MT data by applying scaling laws, rather than training a new network from scratch. Additionally, discrepancies between the number of frequencies in the real-world data and those used in training present another challenge. A practical solution is to interpolate the frequency sampling of the real-world data to match that of the training set. The interpolation method will perform effectively since MT apparent resistivity curves are typically smooth.

3 Numerical experiments

Recent research has established the effectiveness of employing ANNs to address the 1D MT inverse problem with a fixed observation system. Nonetheless, the application of ANNs to 2D and 3D problems remains largely exploratory. Therefore, we demonstrate the integration of PGAE and scaling laws in the 1D inversion of both synthetic and real-world MT data, highlighting their potential for enhancing inversion accuracy and generalization capabilities.

3.1 Obtaining a well-trained ANN

To prepare the training dataset, we analytically compute the apparent resistivity curves for 1D layered Earth models consisting of 31 layers and 25 frequencies, ranging from 10,000 Hz–1 Hz. The thicknesses of the layers begin at 20 m and increase logarithmically, as described in Equation 20, with the final layer always being a homogeneous half-space. For the resistivity of each layer, we uniformly sample values within the range of 0.1–100,000 $\Omega \cdot m$ in the logarithmic domain and subsequently smooth the geoelectric model using a Gaussian filter (Liu L. et al., 2023). A total of 120,000 samples are generated, with 100,000 allocated for training and 20,000 for evaluation. Some random smooth geoelectric models can be found in Figure 2.

$$dz_i = 20 + 10^{0.115\times(i-1)} \qquad i = 2,3,\ldots,30, \tag{20}$$

where i represents the number of layers and dz_i denotes the thickness of the i^{th} layer.

The primary objective of this study is to enhance the generalization capabilities of the trained ANN rather than to design a high-performance ANN. Accordingly, we employ an ANN architecture that is as simple as possible. Specifically, we construct an ANN with a single hidden layer containing 500 neurons. The number of neurons in the input (output) layer corresponds to the MT data (geoelectric model) used in the training dataset. The regularization parameter λ in Equation 4 is set to 4.5, determined through trial and error. We code the whole PGAE framework using TensorFlow (an open-source Python library by Google) so that automatic differentiation (Liu L. et al., 2024) can be employed to calculate the gradient of the loss function.

We use the Adam optimizer to train the established network, as illustrated in Figure 3A, the data misfit decreases rapidly as the number of training epochs increases. A significant reduction in data misfit is observed at the end of the first epoch, indicating that the training of the network converges quickly. The gradual increase in model roughness shown in Figure 3B suggests that the well-trained PGAE possesses the capability to produce models with complex structures. After 20 epochs, the loss function, data misfit, and model roughness exhibit minimal changes, indicating the completion of the training stage. The network was trained using an NVIDIA Tesla K80 GPU with 12 GB of onboard memory, taking approximately 40 min.

3.2 Synthetic examples

To evaluate the performance of the trained PGAE, we simulate numerous synthetic 1D MT data as test samples, which share the same observation frequencies as the training samples. For comparative analysis, we also invert these synthetic data using the classical Occam's inversion (Constable et al., 1987). To further assess the noise adaptability of the trained PGAE, we introduce 5% Gaussian noise into the test samples. As illustrated in Figures 4, 5, the well-trained PGAE produces models comparable to those generated by the Occam's inversion, with both methods yielding a satisfactory data fit.

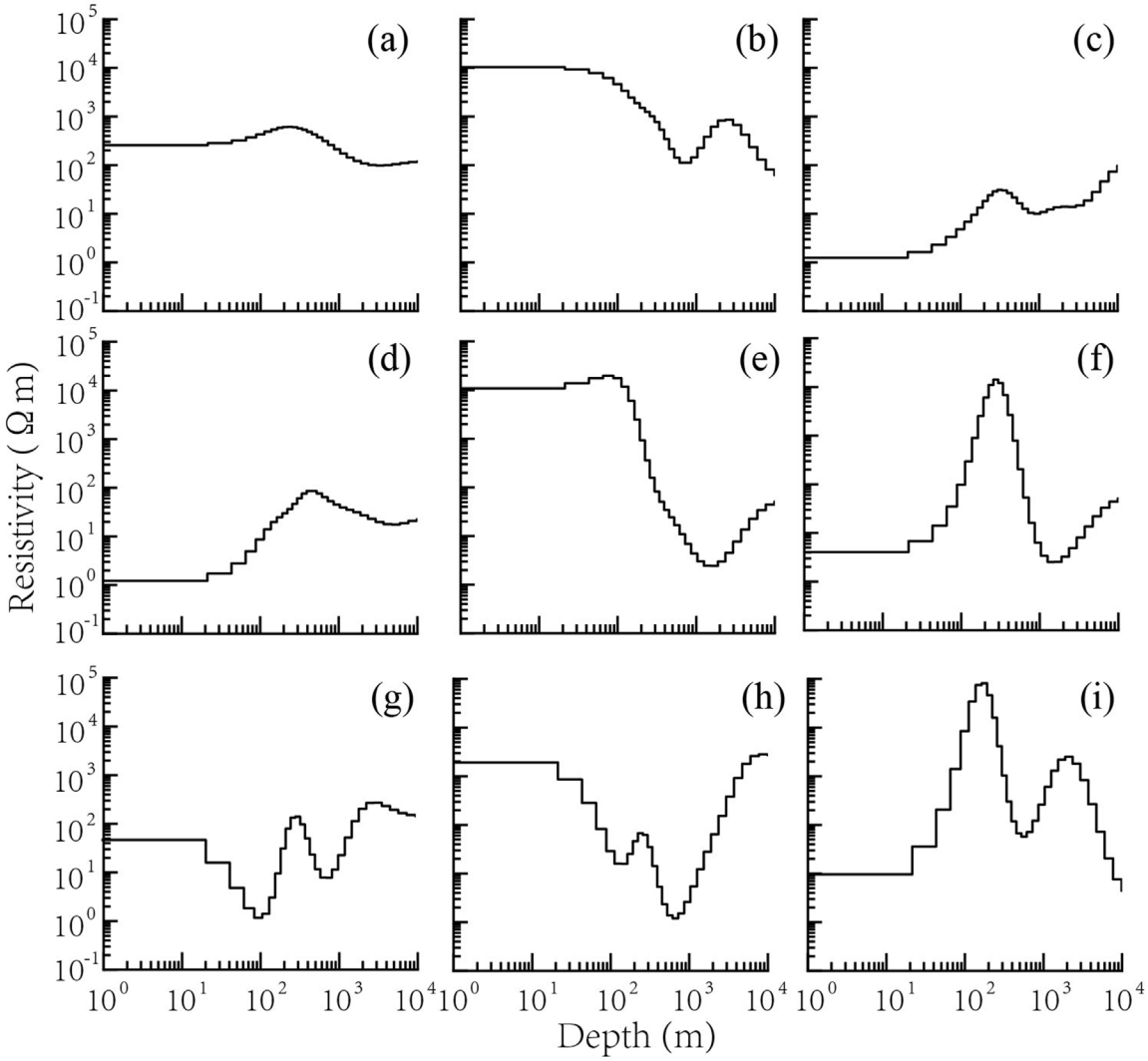

FIGURE 2
Random smooth models **(A–I)** generated according to Liu L. et al. (2023).

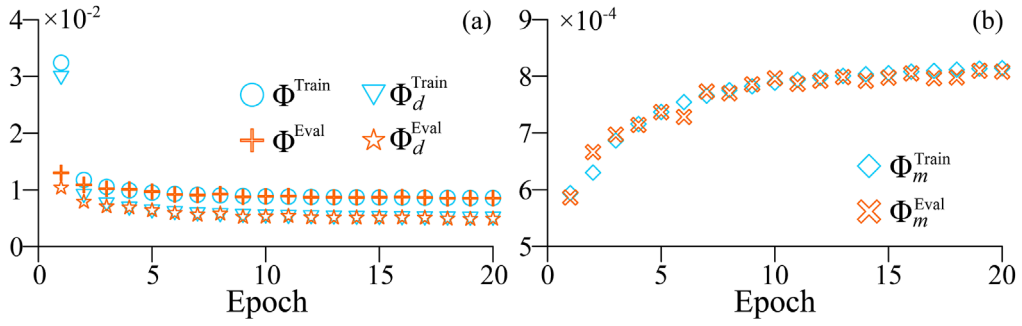

FIGURE 3
The loss function variations during training and evaluating. **(A)** the total loss function in training (sky-blue circles) and evaluating (orange crosses) and the data misfit in training (sky-blue triangles) and evaluating (orange stars). **(B)** the model roughness in training (sky-blue diamonds) and evaluating (orange crosses).

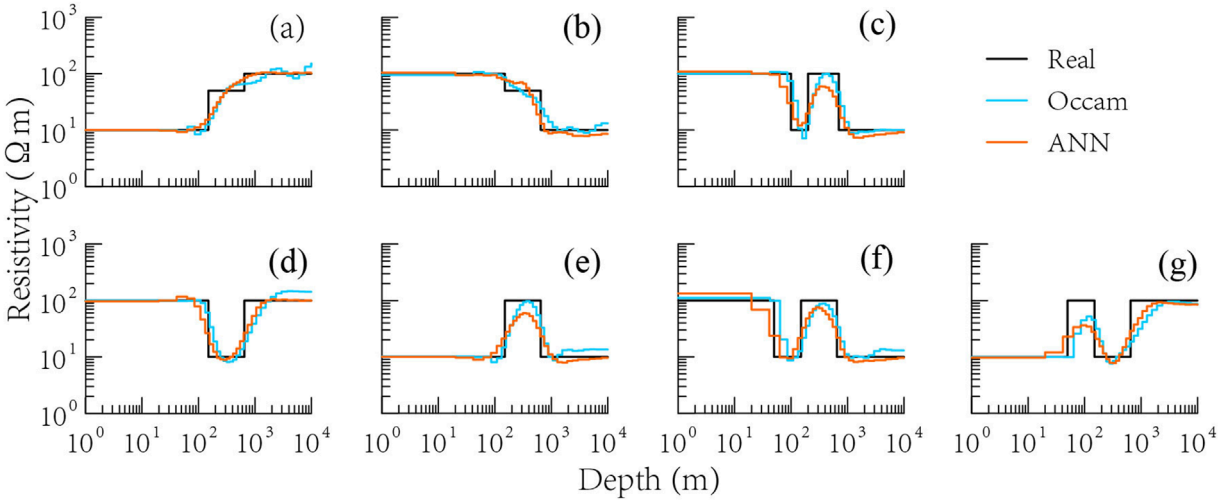

FIGURE 4
Inversion results of different synthetic data **(A–G)**. The real (black) and inverted models, obtained from PGAE (orange) and Occam's inversion (sky-blue), are shown as solid lines.

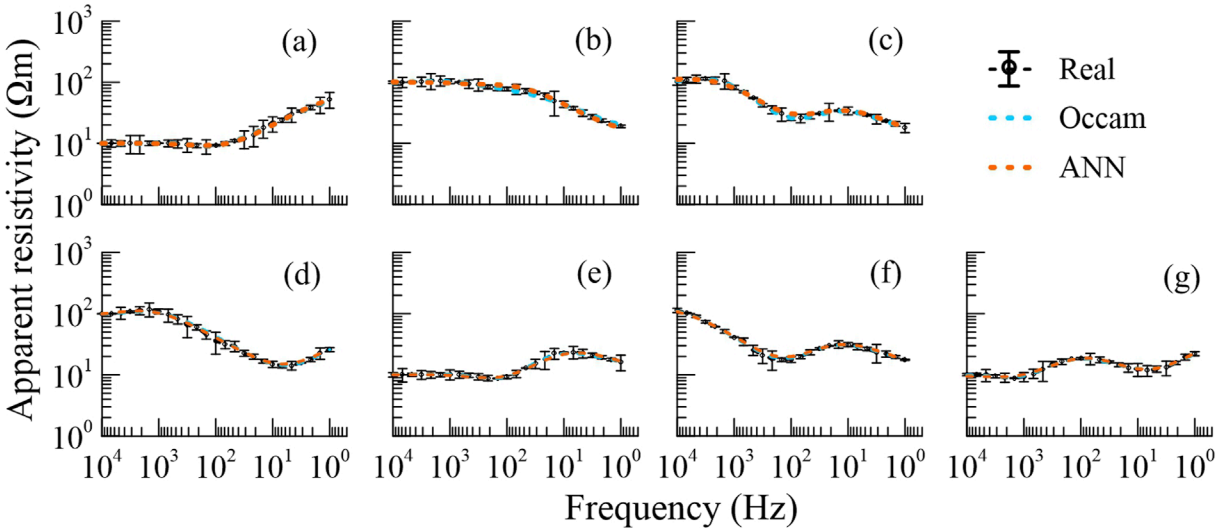

FIGURE 5
Fitting results of different synthetic data **(A–G)**. The apparent resistivity curves are shown as dashed lines in corresponding colors as Figure 4. Error bars are plotted on the observed curves.

Although no noise was intentionally added to the training samples, the network demonstrates remarkable adaptability to noise. Given that noise is unavoidable in real-world data, we further evaluate the noise tolerance of the trained PGAE by testing it against three higher levels of Gaussian noise: 10%, 20%, and 30%. As illustrated in Figures 6, 7, the models predicted by the PGAE are comparable to those derived from the Occam's inversion, indicating that the PGAE exhibits significant noise tolerance even at high levels of Gaussian noise.

3.3 Real-world examples

We select 11 MT sites recorded in the Tarim Basin for our real-world examples (Figure 8). The phase tensor analysis (Caldwell et al., 2004) shows that the resistivity distribution in the shallow area closely resembles a 1D structure (Figure 9), suitable for 1D inversion. Data from these sites were recorded using the Phoenix MTU-V5 system over approximately 22 h during the summer of 2019 and subsequently processed with the robust MT time series

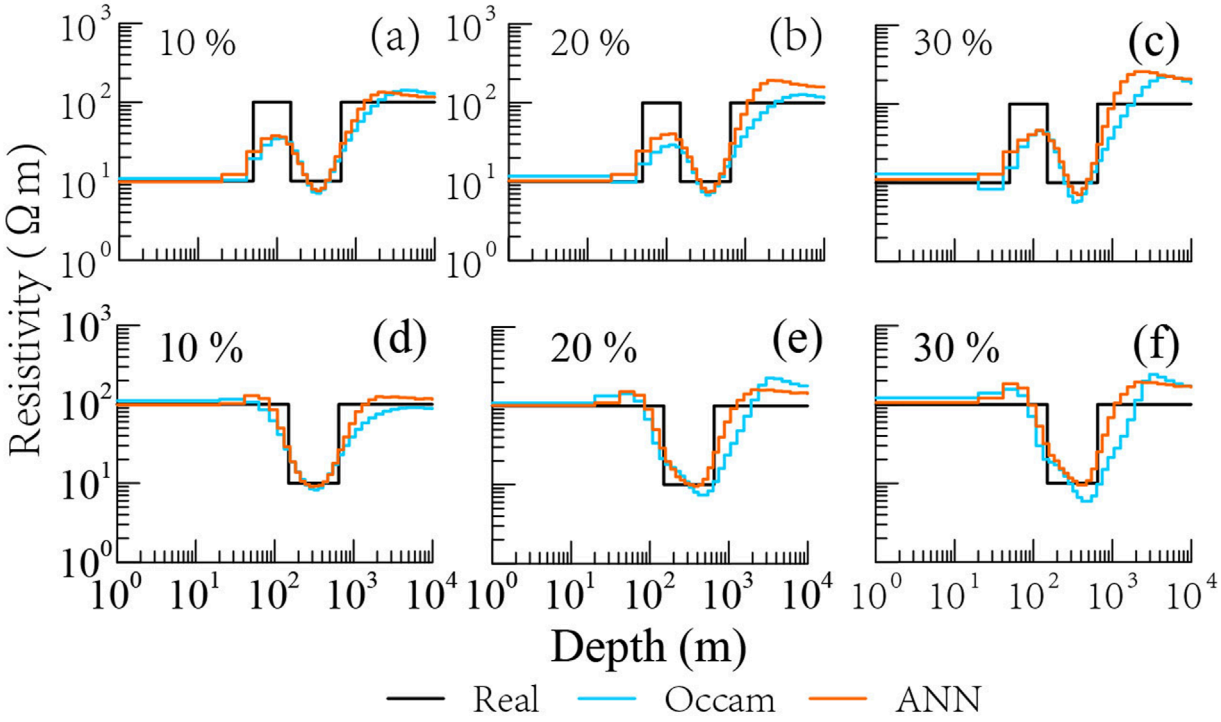

FIGURE 6
Inversion results of the noisier data. **(A–C)** have the same real model, and **(D–F)** have the same real model. Percentages denote the noise levels. The lines and colors are the same as in Figure 4.

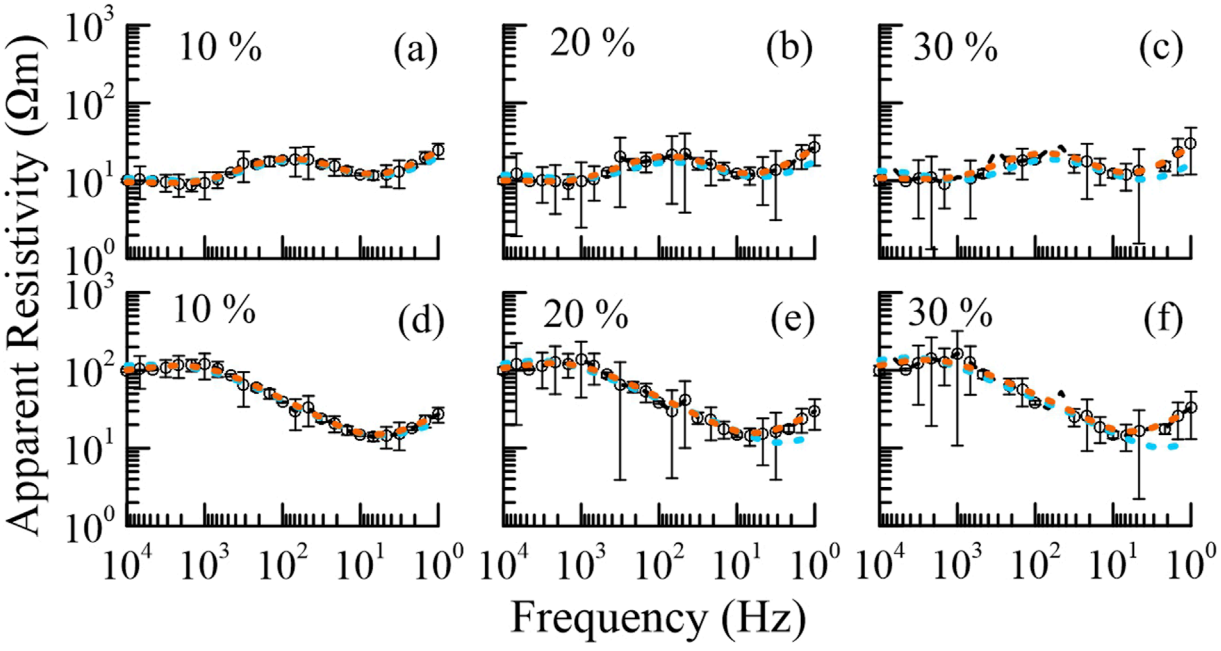

FIGURE 7
Fitting results of the noisier data. **(A–C)** have the same real model, and **(D–F)** have the same real model. Percentages denote the noise levels. The lines and colors are the same as in Figure 5.

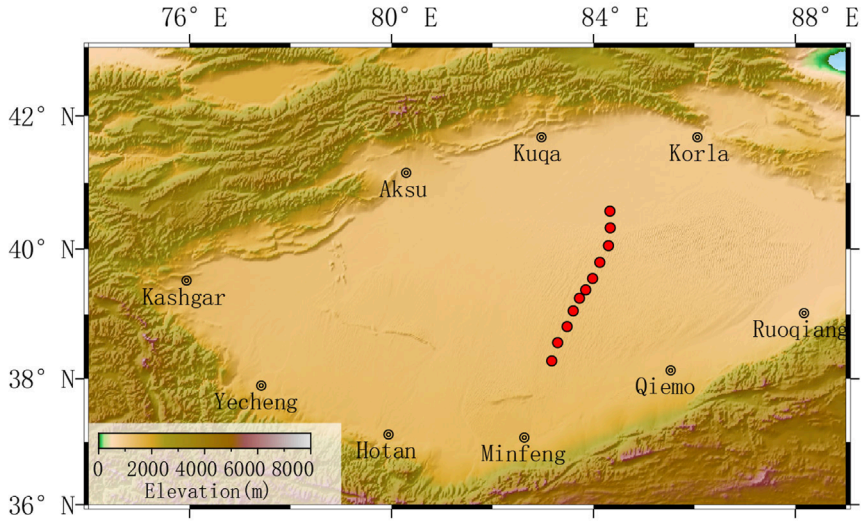

FIGURE 8
The study area of the real-world data in Tarim Basin. Red-filled circles represent the MT sites.

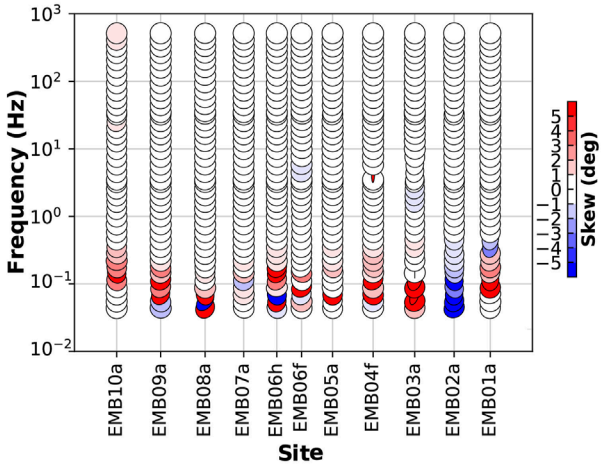

FIGURE 9
Phase tensors for all the frequencies from the survey line in Figure 8. Plotted using the MTpy library (Krieger and Peacock, 2014).

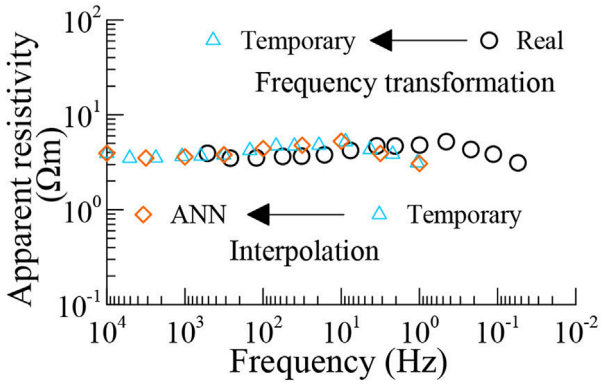

FIGURE 10
Predicting process of the well-trained ANN with scaling laws.

processing code, EMTF (Egbert and Booker, 1986), to estimate the impedance and vertical transfer functions. We utilize 41 frequencies ranging from 515 Hz to 0.0439 Hz, which share a similar bandwidth with the frequencies of the training samples but employ distinct frequency values. This enables the application of the scaling laws described in Section 2.3.

As illustrated in Figure 10, we first transform the frequencies of the real-world data to align with the frequency range of the training data. Subsequently, we employ the linear interpolation algorithm to match the number of real-world data to the neurons of the input layer of the trained ANN. Once the trained ANN generates an inverted model, the final step is transforming it back to its original scale, ensuring consistency with the real-world system. In this scenario, we scale the real-world frequencies by 10000/515, resistivity by 10, and model size by $\sqrt{515/100000}$, meeting the conditions specified in Equation 19. The models predicted by PGAE are comparable to those inverted by Occam's method (Figure 11). Both methods yield excellent data fitting (Figure 12). Additionally, we present the pseudo-sections of the 1D models derived from both methods in Figure 13, revealing consistent 2D structures. The prediction stage of PGAE requires only 0.113 s for all 11 sites, significantly faster than the Occam's inversion, which takes approximately 5 s per site.

4 Discussion and conclusion

The numerical experiments demonstrate that PGAE enhanced by scaling laws performs well, producing comparable models as the class Occam's inversion does with higher efficiency

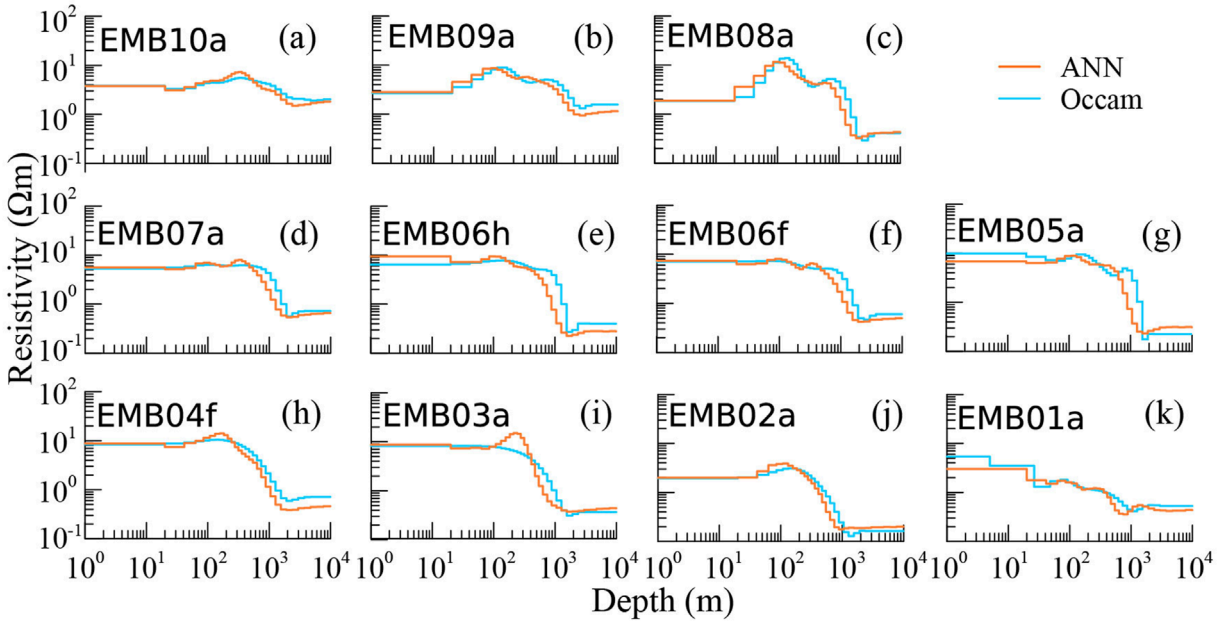

FIGURE 11
Inversion results of the real-world data. **(A–K)** indicate the sequence of MT sites along the survey line (SW-NE). The lines and colors are the same as in Figure 4.

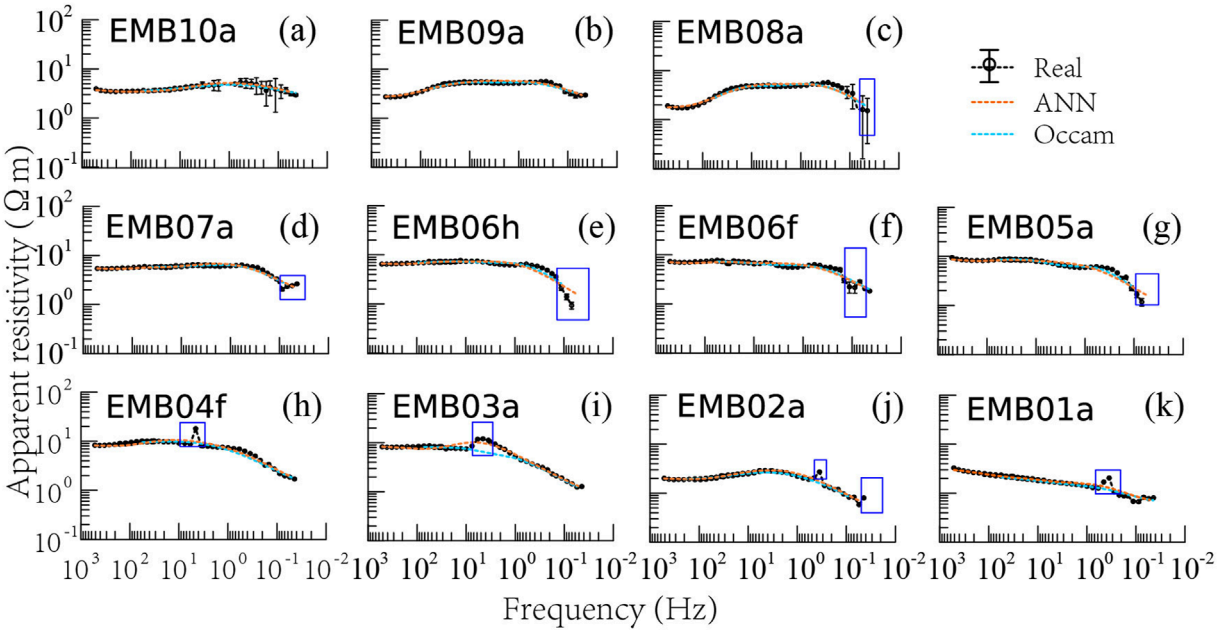

FIGURE 12
Fitting results of the real-world data. **(A–K)** indicate the sequence of MT sites along the survey line (SW-NE). Blue boxes mark the deleted outliers for 1D Occam's inversion. The lines and colors are the same as in Figure 5.

after being well-trained. Here, we discuss its advantages and flaws in three aspects: model complexity, network architecture, and reusability of the network.

Model complexity is a formidable barrier for ANN-based MT inversions, limiting both the accuracy and generalization of these methods across diverse geological settings. The real-world resistivity

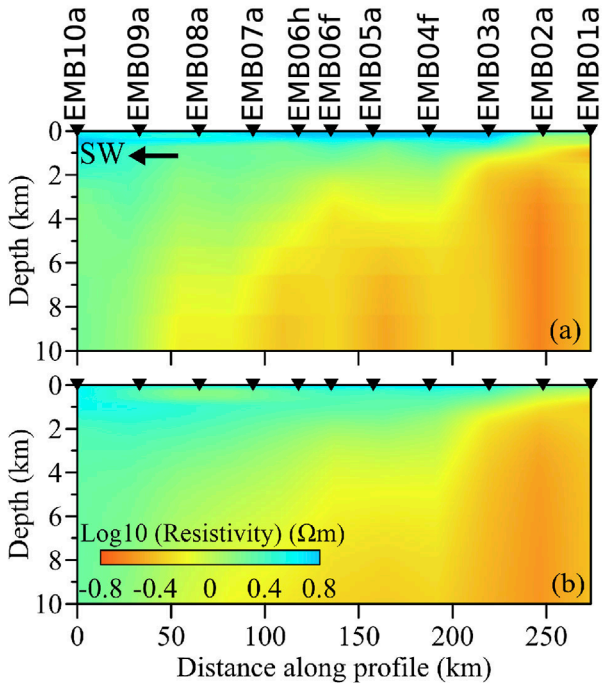

FIGURE 13
The electrical resistivity pseudo-sections of the real-world example produced by **(A)** PGAE and **(B)** Occam's inversion.

models are inherently complex due to the highly heterogeneous nature of the Earth's crust and mantle (Chave and Jones, 2012). This complexity is further compounded by varying geological features, such as fault zones, fluid-bearing formations, and volcanic structures. In traditional inversion methods (Kelbert et al., 2014; Key, 2016), model complexity can be managed through regularization techniques and by setting constraints based on prior geological information. The supervised ANNs (Liao et al., 2022; Xie et al., 2023; Liu X. et al., 2024), while powerful, are inherently data-driven and lack a physical basis. Addressing the challenge requires advances in hybrid modeling techniques and the integration of prior knowledge into the ANN framework to balance data-driven learning with geological realism. PGAE employs the forward operator as a decoder, which includes the physical laws behind the specific inverse problem. The framework can train networks without labels (models) and give a chance to add prior constraints into the training stage, which will significantly enhance the ability to reveal complex models. Moreover, future training datasets should include both synthetic and real-world data, which provide more real information related to the real tectonic and geological background.

Regarding the network architecture, it is not the primary focus of our study in the current stage. We focused on exploring the fundamental idea of PGAE, hence employing a straightforward and simple enough network with only one hidden layer. This simple design demonstrates a satisfactory ability to map the data space to the model space for 1D MT problems. However, the architecture may become crucial when addressing higher-dimensional inverse problems due to the significantly increased number of unknowns (Xu et al., 2024). A network with an insufficient degree of freedom, meaning an inadequate number of network parameters, may struggle to train effectively on the provided samples. Consequently, it would likely exhibit poor prediction performance when applied to real-world data. Conversely, while a network endowed with an excessive degree of freedom can be easily trained to fit the training and evaluation samples, this requires considerable computational time. Additionally, it may lead to overfitting, which poses challenges in maintaining the network's generalization capabilities (Bishop, 1995). This problem is particularly pronounced in MT inversions, where the resistivity structure changes significantly with depth and electromagnetic responses are frequency-dependent. Each frequency corresponds to different depths, necessitating the ANN to learn the relationships across a broad spectrum of frequencies accurately. Theoretically, no established mathematical principles definitively determine the optimal network architecture (LeCun et al., 2015; Goodfellow et al., 2016), making trial-and-error the only practical approach to designing a network.

In previous studies (e.g., Ling et al., 2023; Pan et al., 2024), trained networks cannot be reused and must be re-trained from scratch when the observation system changes. However, our study makes an important step towards improving the reusability of well-trained ANNs in different observation systems. For 1D MT inverse problems, only variations in frequency range should be considered. By applying scaling laws, the trained ANN can be used in cases with nearly identical frequency bandwidths, expanding its applicability. When the frequency range of a new application spans different orders of magnitude, the trained ANN may lose its effectiveness. Therefore, it is essential to train separate ANNs tailored to different bandwidths to ensure reliable performance across a broader range of scenarios. For 3D problems, the complexity of the observation system increases further. Differences in site locations must be considered to ensure the reusability of trained ANNs. As site locations significantly affect the data characteristics in MT inversions, data from a new group of sites cannot be directly applied to the trained network without some transformation. Thus, data reconstruction between different site groups is a critical factor that must be addressed in future ANN-based MT inversion efforts. Techniques such as compressed sensing (Donoho, 2006), which can transform data from one set of locations to another, may offer potential solutions to this issue. Developing robust methods for data reconstruction should be a significant challenge.

In summary, we utilized PGAE along with scaling laws to improve the accuracy and generalization of the well-trained ANN for MT inversion. Specifically, PGAE takes into account the data misfit, while scaling laws enable the ANN to perform effectively even when the frequency range of an MT survey differs from the range used during the network's original training. Fully enhancing the practicability, efficiency, and dependability of ANN-based inversions, particularly in the context of complex MT inverse problems, will require further research and innovation. Future research should focus on improving the adaptability of trained ANNs to both model complexity and observation systems, thereby increasing the utility of ANNs across diverse MT applications. Overcoming these challenges will be critical

before ANN-based methods can be widely adopted in industry-level MT inversion software.

Data availability statement

The datasets presented in this study can be found in online repositories. The names of the repository/repositories and accession number(s) can be found below: https://github.com/GeoLianLiu/MTPGAE.

Author contributions

LL: Conceptualization, Formal Analysis, Investigation, Methodology, Software, Validation, Writing–original draft. BY: Funding acquisition, Resources, Supervision, Validation, Writing–review and editing. YZ: Conceptualization, Investigation, Methodology, Validation, Writing–review and editing.

Funding

The author(s) declare that financial support was received for the research, authorship, and/or publication of this article. This research was financially supported by NSFC (grant 42474103).

Acknowledgments

We thank the editors and reviewers for their helpful suggestions.

Conflict of interest

The authors declare that the research was conducted in the absence of any commercial or financial relationships that could be construed as a potential conflict of interest.

Generative AI statement

The author(s) declare that no Generative AI was used in the creation of this manuscript.

Publisher's note

References

Backus, G. E., and Gilbert, J. F. (1967). Numerical applications of a formalism for geophysical inverse problems. *Geophys. J. Int.* 13, 247–276. doi:10.1111/j.1365-246X.1967.tb02159.x

Berdichevsky, M. N. (1976). "Basic principles of interpretation of magnetotelluric sounding curves," in *Geoelectric and geothermal studies (East-Central europe, soviet asia), KAPG geophysical monograph, 165–221Publisher*. Budapest: Akademiai Kiado.

Bishop, C. M. (1995). *Neural networks for pattern recognition*. Oxford, England: Clarendon Press.

Cagniard, L. (1953). Basic theory of the magneto-telluric method of geophysical prospecting. *Geophysics* 18, 605–635. doi:10.1190/1.1437915

Calderón-Macas, C., Sen, M. K., and Stoffa, P. L. (1998). Automatic NMO correction and velocity estimation by a feedforward neural network. *Geophysics* 63, 1696–1707. doi:10.1190/1.1444465

Caldwell, T. G., Bibby, H. M., and Brown, C. (2004). The magnetotelluric phase tensor. *Geophys. J. Int.* 158, 457–469. doi:10.1111/j.1365-246x.2004.02281.x02281.x

Chave, A. D., and Jones, A. G. (2012). *The magnetotelluric method: theory and practice*. Cambridge University Press.

Colombo, D., Turkoglu, E., Li, W., Sandoval-Curiel, E., and Rovetta, D. (2021). Physics-driven deep-learning inversion with application to transient electromagnetics. *Geophysics* 86, E209–E224. doi:10.1190/geo2020-0760.1

Constable, S. C., Parker, R. L., and Constable, C. G. (1987). Occam's inversion: a practical algorithm for generating smooth models from electromagnetic sounding data. *Geophysics* 52, 289–300. doi:10.1190/1.1442303

Dai, J., Qi, H., Xiong, Y., Li, Y., Zhang, G., Hu, H., et al. (2017). "Deformable convolutional networks," in *2017 IEEE international conference on computer vision (ICCV)*, 764–773. doi:10.1109/ICCV.2017.89

Donoho, D. L. (2006). Compressed sensing. *IEEE Trans. Inf. theory* 52, 1289–1306. doi:10.1109/tit.2006.871582

Egbert, G. D., and Booker, J. R. (1986). Robust estimation of geomagnetic transfer functions. *Geophys. J. R. Astronomical Soc.* 87, 173–194. doi:10.1111/j.1365-246X.1986.tb04552.x

Goodfellow, I., Bengio, Y., and Courville, A. (2016). *Deep learning*. MIT Press.

Goodfellow, I. J., Pouget-Abadie, J., Mirza, M., Xu, B., Warde-Farley, D., Ozair, S., et al. (2014). Generative adversarial networks. *arXiv:1406.2661 [cs, stat]*

Grandis, H., Menvielle, M., and Roussignol, M. (1999). Bayesian inversion with Markov chains-I. The magnetotelluric one-dimensional case. *Geophys. J. Int.* 138, 757–768. doi:10.1046/j.1365-246x.1999.00904.x

Guo, R., Li, M., Yang, F., Xu, S., and Abubakar, A. (2020). Application of supervised descent method for 2D magnetotelluric data inversion. *Geophysics* 85, WA53–WA65. doi:10.1190/geo2019-0409.1

Guo, R., Yao, H. M., Li, M., Ng, M. K. P., Jiang, L., and Abubakar, A. (2021). Joint inversion of audio-magnetotelluric and seismic travel time data with deep learning constraint. *IEEE Trans. Geoscience Remote Sens.* 59, 7982–7995. doi:10.1109/TGRS.2020.3032743

Jackson, D. D., and Matsu'ura, M. (1985). A Bayesian approach to nonlinear inversion. *J. Geophys. Res. Solid Earth* 90, 581–591. doi:10.1029/JB090iB01p00581

Jin, Y., Wu, X., Chen, J., and Huang, Y. (2019). "Using a physics-driven deep neural network to solve inverse problems for lwd azimuthal resistivity measurements," in *SPWLA annual logging symposium (SPWLA)*.D053S015R002

Kelbert, A., Meqbel, N., Egbert, G. D., and Tandon, K. (2014). ModEM: a modular system for inversion of electromagnetic geophysical data. *Comput. and Geosciences* 66, 40–53. doi:10.1016/j.cageo.2014.01.010

Key, K. (2016). MARE2DEM: a 2-D inversion code for controlled-source electromagnetic and magnetotelluric data. *Geophys. J. Int.* 207, 571–588. doi:10.1093/gji/ggw290

Kingma, D. P., and Ba, J. (2017). Adam: a method for stochastic optimization. *arXiv:1412.6980 [cs]* ArXiv: 1412.6980

Krieger, L., and Peacock, J. R. (2014). MTpy: a Python toolbox for magnetotellurics. *Comput. and Geosciences* 72, 167–175. doi:10.1016/j.cageo.2014.07.013

Langer, H., Nunnari, G., and Occhipinti, L. (1996). Estimation of seismic waveform governing parameters with neural networks. *J. Geophys. Res. Solid Earth* 101, 20109–20118. doi:10.1029/96JB00948

LeCun, Y., Bengio, Y., and Hinton, G. (2015). Deep learning. *Nature* 521, 436–444. doi:10.1038/nature14539

Levine, Y., Wies, N., Sharir, O., Cohen, N., and Shashua, A. (2022). "Tensors for deep learning theory," in *Tensors for data processing* (Elsevier), 215–248. doi:10.1016/B978-0-12-824447-0.00013-3

Li, H., Krek, M., and Perin, G. (2020a). "A comparison of weight initializers in deep learning-based side-channel analysis,". *Applied cryptography and network security workshops*. Editor J. e. a. Zhou (Cham: Springer International Publishing), 12418, 126–143. doi:10.1007/978-3-030-61638-0

Li, R., Yu, N., Wang, X., Liu, Y., Cai, Z., and Wang, E. (2020b). Model-based synthetic geoelectric sampling for magnetotelluric inversion with deep neural networks. *IEEE Trans. Geoscience Remote Sens.* 60, 1–14doi. doi:10.1109/TGRS.2020.3043661

Liao, X., Shi, Z., Zhang, Z., Yan, Q., and Liu, P. (2022). 2D inversion of magnetotelluric data using deep learning technology. *Acta Geophys.* 70, 1047–1060. doi:10.1007/s11600-022-00773-z

Ling, W., Pan, K., Ren, Z., Xiao, W., He, D., Hu, S., et al. (2023). One-dimensional magnetotelluric parallel inversion using a ResNet1D-8 residual neural network. *Comput. and Geosciences* 180, 105454. doi:10.1016/j.cageo.2023.105454

Ling, W., Pan, K., Zhang, J., He, D., Zhong, X., Ren, Z., et al. (2024). A 3-D magnetotelluric inversion method based on the joint data-driven and physics-driven deep learning technology. *IEEE Trans. Geoscience Remote Sens.* 62, 1–13. doi:10.1109/TGRS.2024.3369179

Liu, B., Jiang, P., Wang, Q., Ren, Y., Yang, S., and Cohn, A. G. (2023a). Physics-driven self-supervised learning system for seismic velocity inversion. *Geophysics* 88, R145–R161. doi:10.1190/geo2021-0302.1

Liu, L., Yang, B., and Xu, Y. (2020). "Solving geophysical inverse problems based on physics-guided artificial neural network," in *2020 annual Meeting of Chinese geoscience union abstracts (chongqing)*, 314–316. doi:10.26914/c.cnkihy.2020.059737

Liu, L., Yang, B., Xu, Y., and Yang, D. (2023b). "Magnetotelluric inversion using supervised learning trained with random smooth geoelectric models," in *Third international meeting for applied geoscience and energy expanded abstracts*, 489–492. doi:10.1190/image2023-3910431.1

Liu, L., Yang, B., Zhang, Y., Xu, Y., Peng, Z., and Yang, D. (2024a). Calculating sensitivity or gradient for geophysical inverse problems using automatic and implicit differentiation. *Comput. and Geosciences* 193, 105736. doi:10.1016/j.cageo.2024.105736

Liu, W., Wang, H., Xi, Z., Wang, L., Chen, C., Guo, T., et al. (2024b). Multitask learning-driven physics-guided deep learning magnetotelluric inversion. *IEEE Trans. Geoscience Remote Sens.* 62, 1–16. doi:10.1109/TGRS.2024.3457893

Liu, W., Wang, H., Xi, Z., and Zhang, R. (2023c). Smooth deep learning magnetotelluric inversion based on physics-informed Swin Transformer and multiwindow Savitzky–Golay filter. *IEEE Trans. Geoscience Remote Sens.* 61, 1–14. doi:10.1109/TGRS.2023.3304313

Liu, W., Wang, H., Xi, Z., Zhang, R., and Huang, X. (2022). Physics-driven deep learning inversion with application to magnetotelluric. *Remote Sens.* 14, 3218. doi:10.3390/rs14133218

Liu, X., Craven, J. A., Tschirhart, V., and Grasby, S. E. (2024c). Estimating three-dimensional resistivity distribution with magnetotelluric data and a deep learning algorithm. *Remote Sens.* 16, 3400. doi:10.3390/rs16183400

Meng, J., Wang, S., Cheng, W., Wang, Z., and Yang, L. (2022). Avo inversion based on transfer learning and low-frequency model. *IEEE Geoscience Remote Sens. Lett.* 19, 1–5. doi:10.1109/LGRS.2021.3132426

Nabighian, M. N. (1987). *Electromagnetic methods in applied geophysics: volume 1, theory*. Houston, Texas: Society of Exploration Geophysicists. doi:10.1190/1.9781560802631

Newman, G. A., and Alumbaugh, D. L. (2000). Three-dimensional magnetotelluric inversion using non-linear conjugate gradients. *Geophys. J. Int.* 140, 410–424. doi:10.1046/j.1365-246x.2000.00007.x

Noh, K., Pardo, D., and Torres-Verdín, C. (2022). 2.5-d deep learning inversion of lwd and deep-sensing em measurements across formations with dipping faults. *IEEE Geoscience Remote Sens. Lett.* 19, 1–5. doi:10.1109/LGRS.2021.3128965

Pan, K., Ling, W., Zhang, J., Zhong, X., Ren, Z., Hu, S., et al. (2024). MT2DInv-Unet: a 2D magnetotelluric inversion method based on deep-learning technology. *Geophysics* 89, G13–G27. doi:10.1190/geo2023-0004.1

Parker, R. L. (1983). The magnetotelluric inverse problem. *Geophys. Surv.* 6, 5–25. doi:10.1007/BF01453993

Peng, R., Han, B., Liu, Y., and Hu, X. (2022). A Julia software package for transdimensional Bayesian inversion of electromagnetic data over horizontally stratified media. *Geophysics* 87, F55–F66. doi:10.1190/geo2021-0534.1

Rahmani Jevinani, M., Habibian Dehkordi, B., Ferguson, I. J., and Rohban, M. H. (2024). Deep learning-based 1-D magnetotelluric inversion: performance comparison of architectures. *Earth Sci. Inf.* 17, 1663–1677. doi:10.1007/s12145-024-01233-6

Ray, A. (2021). Bayesian inversion using nested trans-dimensional Gaussian processes. *Geophys. J. Int.* 226, 302–326. doi:10.1093/gji/ggab114

Rodi, W., and Mackie, R. L. (2001). Nonlinear conjugate gradients algorithm for 2-D magnetotelluric inversion. *Geophysics* 66, 174–187. doi:10.1190/1.1444893

Roth, G., and Tarantola, A. (1994). Neural networks and inversion of seismic data. *J. Geophys. Res.* 99, 6753–6768. doi:10.1029/93JB01563

Tarantola, A. (2004). *Inverse problem theory and methods for model parameter estimation*. USA: Society for Industrial and Applied Mathematics.

Tikhonov, A. (1950). *On determining electrical characteristics of the deep layers of the Earth's crust*, 73. Leningrad: Dokl. Akad. Nauk. SSSR, 295–297.

Tikhonov, A. N., and Arsenin, V. Y. (1977). *Solutions of ill-posed problems*. Hoboken, New Jersey: John Wiley & Sons.

Valentine, A., and Sambridge, M. (2021). Emerging directions in geophysical inversion. *Phys. ArXiv 2110.06017*. doi:10.48550/arXiv.2110.06017

Wang, H., Liu, Y., Yin, C., Su, Y., Zhang, B., and Ren, X. (2023). Flexible and accurate prior model construction based on deep learning for 2-D magnetotelluric data inversion. *IEEE Trans. Geoscience Remote Sens.* 61, 1–11. doi:10.1109/TGRS.2023.3239105

Wang, X., Jiang, P., Deng, F., Wang, S., Yang, R., and Yuan, C. (2024). Three-dimensional magnetotelluric forward modeling through deep learning. *IEEE Trans. Geoscience Remote Sens.* 62, 1–13. doi:10.1109/TGRS.2024.3401587

Ward, S. H. (1967). "Part C: the electromagnetic method," in *Mining geophysics volume II, theory* (Houston, Texas: Society of Exploration Geophysicists), 224–372. doi:10.1190/1.9781560802716.ch2c

Wong, J., Hall, K. W., Gallant, E. V., Bertram, M. B., and Lawton, D. C. (2009). "enSeismic physical modeling at the University of Calgary," in *SEG technical program expanded abstracts 2009* (Houston, Texas: Society of Exploration Geophysicists), 2642–2646. doi:10.1190/1.3255395

Wu, S., Huang, Q., and Zhao, L. (2024). Physics-guided deep learning-based inversion for airborne electromagnetic data. *Geophys. J. Int.* 238, 1774–1789. doi:10.1093/gji/ggae244

Xie, L., Han, B., Hu, X., and Bai, N. (2023). 2D magnetotelluric inversion based on ResNet. *Artif. Intell. Geosciences* 4, 119–127. doi:10.1016/j.aiig.2023.08.003

Xu, K., Liang, S., Lu, Y., and Hu, Z. (2024). Magnetotelluric data inversion based on deep learning with the self-attention mechanism. *IEEE Trans. Geoscience Remote Sens.* 62, 1–10. doi:10.1109/TGRS.2024.3411062

Zhuang, F., Qi, Z., Duan, K., Xi, D., Zhu, Y., Zhu, H., et al. (2021). A comprehensive survey on transfer learning. *Proc. IEEE* 109, 43–76. doi:10.1109/JPROC.2020.3004555

frontiers | Frontiers in Earth Science

TYPE Original Research
PUBLISHED 07 January 2025
DOI 10.3389/feart.2024.1511153

OPEN ACCESS

EDITED BY
Ying Liu,
China University of Geosciences
Wuhan, China

REVIEWED BY
Nian Yu,
Chongqing University, China
Tiaojie Xiao,
National University of Defense
Technology, China

*CORRESPONDENCE
Jing Han,
han_jing_cd@163.com

RECEIVED 14 October 2024
ACCEPTED 13 December 2024
PUBLISHED 07 January 2025

CITATION
Yu G and Han J (2025) Divergence correction for three-dimensional magnetotelluric forward modelling with arbitrary electrical anisotropy.
Front. Earth Sci. 12:1511153.
doi: 10.3389/feart.2024.1511153

Divergence correction for three-dimensional magnetotelluric forward modelling with arbitrary electrical anisotropy

Guo Yu[1] and Jing Han[2]*

[1]College of Geophysics and Petroleum Resources, Yangtze University, Wuhan, China, [2]School of Geosciences, Yangtze University, Wuhan, China

This paper presents an enhanced framework for three-dimensional (3D) magnetotelluric (MT) forward modeling that incorporates a current density divergence correction procedure for arbitrary anisotropic conditions. The method accelerates the convergence of iterative solvers in solving forward equations in anisotropic media. The divergence correction is adapted from techniques initially developed for isotropic MT modeling. Through four numerical examples—a 1D anisotropic model, a 2D anisotropic model with an infinite lateral fault overlying perfect conductor, a 2D anisotropic model with upper and lower structure and a challenging 3D anisotropic model with random parameters—the validity and efficiency of the proposed approach are demonstrated. The results show that the incorporation of divergence correction significantly reduces the number of iterations required for convergence, improving computational performance and stability. The framework proves robust even in demanding scenarios involving long periods and complex anisotropic structures.

KEYWORDS

magnetotelluncs, electrical anisotrophy, three-dimentional forward, finite difference, divergence correction

1 Introduction

The magnetotelluric (MT) method is a passive geophysical exploration technique that measures natural electromagnetic (EM) fields at the Earth's surface. These measurements are employed to infer subsurface resistivity distributions, enabling the mapping of geological structures at depths ranging from tens of meters to several hundred kilometers. In recent years, MT has been widely adopted across various resource exploration areas, including mineral, hydrocarbon, and geothermal exploration (Farquharson and Craven, 2009; Smith, 2014; Patro, 2017), as well as in tectonic studies (Xiao et al., 2017; 2018). Increasing attention has been directed towards electric anisotropy, with numerous three-dimensional (3D) EM forward modeling algorithms now incorporating anisotropic conditions (e.g., Jaysaval et al., 2016; Löwer and Junge, 2017; Wang et al., 2017; Han et al., 2018; Liu et al., 2018; Yu et al., 2018; Cao et al., 2018; Kong et al., 2021; Rivera-Rios et al., 2019; Xiao et al., 2019; Guo et al., 2020; Ye et al., 2021; Bai et al., 2022).

Initially, Smith (1996) observed that in the staggered-grid finite-difference (FD) solution of the magnetotelluric (MT) method, the convergence rate of the iterative solver considerably slowed at low frequencies. Smith attributed this to the reduced significance of the conductivity term in the electric-field equation as frequency decreased, which consequently lessened the necessity for the finite-difference approximation of the electric field corresponding to a divergence-free current density. To address this, Smith introduced a divergence correction technique that significantly improved the convergence rate of the FD solution. This correction procedure was subsequently adopted in other studies (e.g., Sasaki, 2001; Siripunvaraporn et al., 2002; Uyeshima and Schultz, 2000). Farquharson and Miensopust (2011) also applied this divergence correction approach to tackle a similar convergence issue in finite-element (FE) solutions for MT modeling. Notably, these methods were developed for use in isotropic media.

For anisotropic scenarios, several approaches have been proposed to avoid the current density divergence issue mentioned earlier. One such approach involves decomposing the electric field into discrete magnetic vector potential and electric scalar potential components. This transforms the forward equation system of the electric field into the form of vector and scalar potentials, commonly referred to as the A-φ system, which inherently includes the charge conservation equation (Han et al., 2018; Ye et al., 2021; Bai et al., 2022). The A-φ system has also been employed in isotropic cases (Everett and Schultz, 1996; Badea et al., 2001; Stalnaker et al., 2006; Yoshimura and Oshiman, 2002; Mitsuhata and Uchida, 2004; Mukherjee and Everett, 2011; Long, 2024). However, the primary focus here is on the electric-field method.

Liu and Yin (2013) applied a correction scheme similar to Smith's (1996) to helicopter-borne EM finite-difference (FD) responses under arbitrary electrical anisotropy. Wang et al. (2017) employed this approach for a 3D tensor controlled-source audio-frequency magnetotelluric (CSAMT) FD solution with axial electrical anisotropy. Similarly, Cao et al. (2018) applied divergence correction to solve a 3D axial anisotropic MT forward problem, while Zhou et al. (2021) integrated a divergence correction technique in a 3D finite-element (FE) solver for axially anisotropic MT forward modeling. Xiao (2019) implemented a current density divergence correction method to enhance the convergence of the iterative solution for the 3D FE equation system in arbitrary anisotropic MT forward modeling. Building on this, Cheng et al. (2024) extended the approach by incorporating the divergence correction technique into a 3D MT algorithm that accounts for both electrical and magnetic anisotropy.

From the preceding discussion, it is evident that only a limited number of studies have addressed the issue of divergence correction in electromagnetic (EM) methods under conditions of electric anisotropy. In this paper, we focus on incorporating divergence correction into the FD solution for three-dimensional 3D MT with arbitrary anisotropy. The effectiveness and accuracy of the approach are demonstrated through three numerical examples, and its stability is validated through a highly challenging numerical computation, highlighting the robustness of the forward modeling with the divergence correction procedure. We also examine the impact of the forward iteration interval between successive divergence corrections on the overall computational time.

2 Methods

2.1 Basic theory

The frequency-domain Maxwell's equations, in the MT quasi-stationary approximation, are in the form of Equations 1, 2,

$$\nabla \times \mathbf{E} = i\omega\mu\mathbf{H}, \tag{1}$$

$$\nabla \times \mathbf{H} = \bar{\sigma}\mathbf{E} \tag{2}$$

where a time factor $e^{-i\omega\mu}$ is considered. The magnetic permeability μ is equal to the vacuum value, $4\pi \times 10^{-7}$ H/m. The ω is the angular frequency. **E** and **H** denote electric and magnetic fields. In anisotropic medium, conductivity is a tensor expressed as 3 × 3 matrix in Equation 3,

$$\bar{\sigma} = \begin{pmatrix} \sigma_{xx} & \sigma_{xy} & \sigma_{xz} \\ \sigma_{yx} & \sigma_{yy} & \sigma_{yz} \\ \sigma_{zx} & \sigma_{zy} & \sigma_{zz} \end{pmatrix} \tag{3}$$

This matrix is symmetric and positive definite and can be rewritten with Equations 4, 5,

$$\bar{\sigma} = \mathbf{R}_z(\gamma)\mathbf{R}_x(\beta)\mathbf{R}_z(\alpha)\mathbf{\Lambda}\mathbf{R}_z^T(\alpha)\mathbf{R}_x^T(\beta)\mathbf{R}_z^T(\gamma), \tag{4}$$

$$\mathbf{\Lambda} = \begin{pmatrix} \sigma_x & & \\ & \sigma_y & \\ & & \sigma_z \end{pmatrix} \tag{5}$$

where σ_x, σ_y, σ_z, α, β, γ are three principle conductivity and three rotation angles (Pek and Verner, 1997; Martí, 2014). $\mathbf{R}_x$ and $\mathbf{R}_z$ are the rotation matrix for rotation around the σ_x and σ_z axis, respectively. In the following, the anisotropic parameters are expressed as $\sigma_x/\sigma_y/\sigma_z/\alpha/\beta/\gamma$.

After some straightforward algebraic operations, we obtain an electric field governing equation,

$$\nabla \times \nabla \times \mathbf{E} = i\omega\mu\bar{\sigma}\mathbf{E} \tag{6}$$

Based on a FD approximate, this equation can be written as a large linear system,

$$\mathbf{Ax} = \mathbf{b}, \tag{7}$$

where **A**, **x** and **b** respectively denotes coefficient matrix, unknown vector and right side vector. Upon obtaining the solution to Equation 7, **H** can be obtained via Equation 1.

We have developed a MT forward algorithm for calculating **E** and **H** fields on a 3D FD grid. Detailed information on the method can be found in Yu et al. (2018). In that earlier work, Equation 7 was solved using the direct solver PARDISO (Schenk and Gärtner, 2004; Kuzmin, Luisier, and Schenk, 2013). In this study, while the forward modeling framework remains the same as in Yu et al. (2018), the final linear system in Equation 7 is now solved using the preconditioned quasi-minimal residual (QMR) iterative method. The solver terminates when the normalized residual reaches 2×10^{-8} or the maximum number of iterations is reached. Additionally, we incorporate a current density divergence correction into the forward solution, which will be demonstrated in subsequent sections.

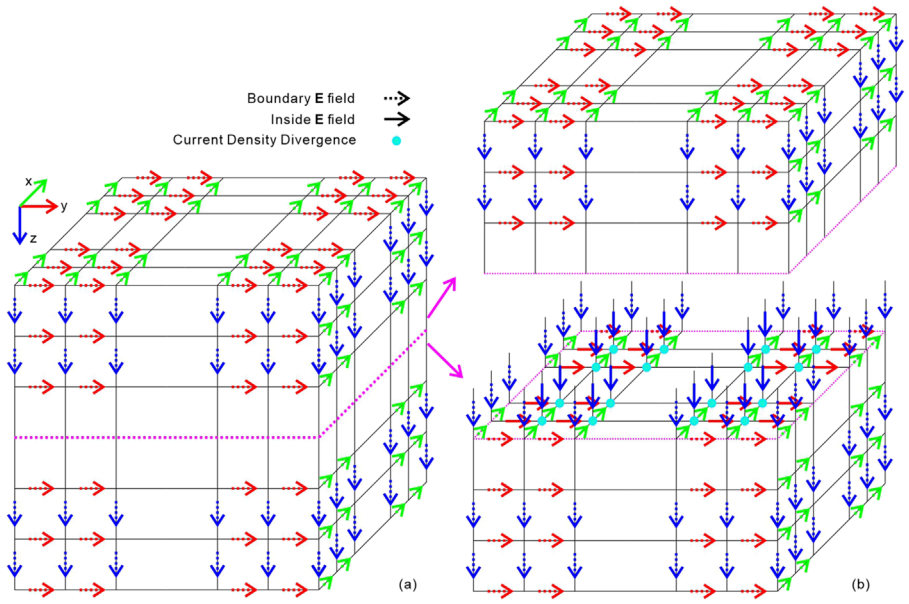

FIGURE 1
Discretization of electric fields and current density divergence points. **(A)** Boundary electric fields. **(B)** Inside electric fields and divergence points shown by separating the model from top to bottom at the plane corresponding to the dashed purple rectangular box.

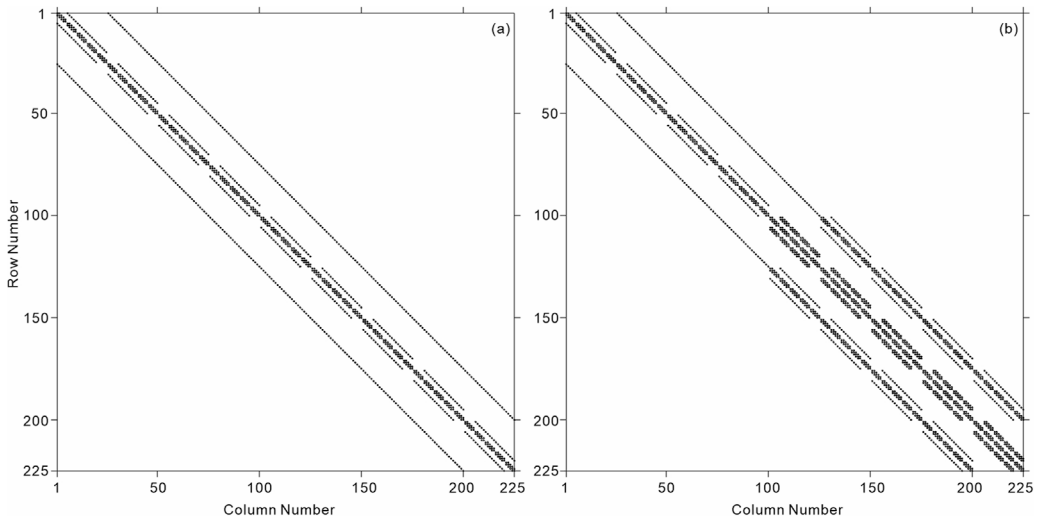

FIGURE 2
Nonzero element pattern of the coefficient matrix of the divergence correction linear equation. **(A)** Isotropy. **(B)** Anisotropy.

2.2 Current density divergence correction

As described by Smith (1996), the influence of the conductivity term in Equation 6 is weak even for what are considered high frequencies in geophysical electromagnetic methods, and becomes weaker as frequency decreases. Consider an approximate **E** solution at one certain iterative solution of Equation 7, such **E** would not satisfy the conservation of charge principle. As noted by Smith (1996), the impact of the conductivity term in Equation 6 is relatively weak, even at what are considered high frequencies in geophysical electromagnetic methods, and diminishes further as frequency decreases. In the case of an approximate **E** solution at a given iteration of Equation 7, this **E** would not fully satisfy the conservation of charge principle, which states that,

$$\nabla \cdot \mathbf{J} = 0, \tag{8}$$

where **J** is the current density corresponding to the approximate **E**,

$$\mathbf{J} = \bar{\sigma}\mathbf{E} \tag{9}$$

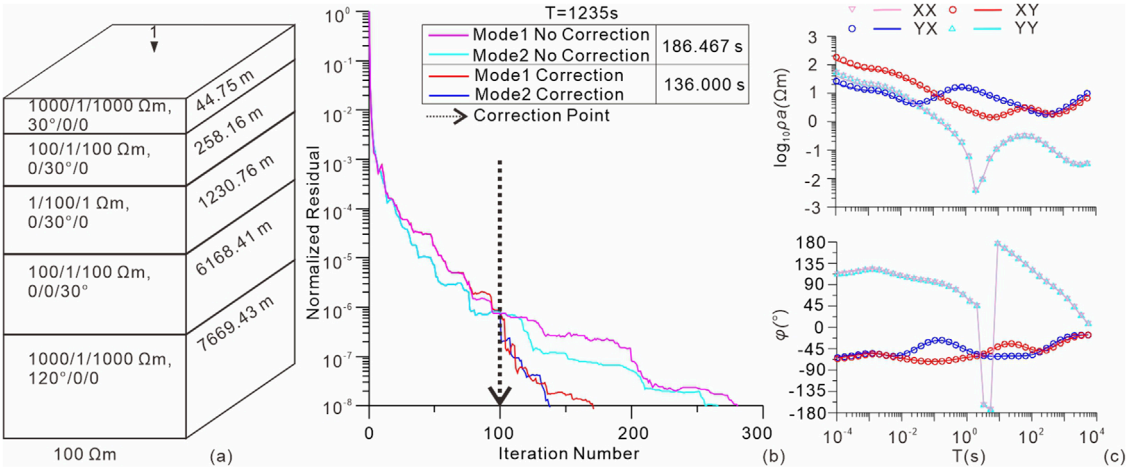

FIGURE 3
1D numerical example. **(A)** 1D anisotropic model with five layers. Six anisotropic parameters are expressed as $\sigma_x/\sigma_y/\sigma_z/\alpha/\beta/\gamma$. **(B)** Iterative information. Purple and cyan curves denote iterative information of Mode1 and Mode2 solutions, respectively, without applying divergence correction. Red and blue curves denote iterative information of Mode1 and Mode2 mode solutions, respectively, with applying divergence correction. The dashed line show the point when divergence correction is applied. The total computational time is 186.467 s without divergence correction and 136.000 s with divergence correction. **(C)** Comparison of the apparent resistivity and phase between the 3D numerical and 1D analytical solutions. The scattered points and solid lines indicate 1D analytical and 3D numerical results, respectively.

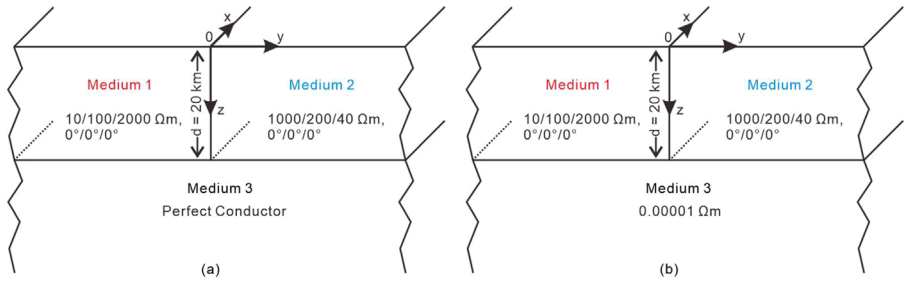

FIGURE 4
2D model. **(A)** 2D model with a lateral infinite fault overlying a perfect conductor (Qin and Yang, 2016). **(B)** 2D model with a lateral infinite fault overlying a high conductor. A very low resistivity value of 10^{-5} Ωm is assigned to approximate the perfect conductor.

The current density divergence cannot vanish. The residual divergence is computed,

$$\psi = \nabla \cdot \mathbf{J} \tag{10}$$

We solve the following divergence equation,

$$\nabla \cdot (\bar{\sigma}(\nabla\varphi)) = \nabla \cdot \mathbf{J} = \psi \tag{11}$$

where φ is the static potential used to correct **E**. It takes too much less computation than solving Equation 7 does. When the static potential φ is determined, the corrected electric field $\mathbf{E}_c$ is given by the Equation 12,

$$\mathbf{E}_c = \mathbf{E} - \nabla\varphi \tag{12}$$

Then, $\mathbf{E}_c$ is used as the starting solution for the new iterative loop of Equation 7, which significantly increase convergence of the forward iteration.

2.3 Current density divergence equation system

Figure 1 depicts the locations of the discretized electric fields and current density divergence points. The boundary and internal electric fields are represented by dashed and solid arrows, respectively, as shown in Figures 1A, B. Additionally, Figure 1B indicates that the static potential φ is defined at the grid cross nodes, denoted by cyan circles. With the discretization scheme, Equation 11 is approximated as the following linear equation system,

$$\mathbf{D}\varphi = \mathbf{t}, \tag{13}$$

where **D** denotes the coefficient matrix and **t** is the right-hand vector composing of each node's current density divergence computed by Equation 9 and Equation 10.

Figures 2A, B illustrate the distribution of nonzero elements in the coefficient matrix **D**, discretized for isotropic and anisotropic media, respectively. To clearly present the nonzero element patterns,

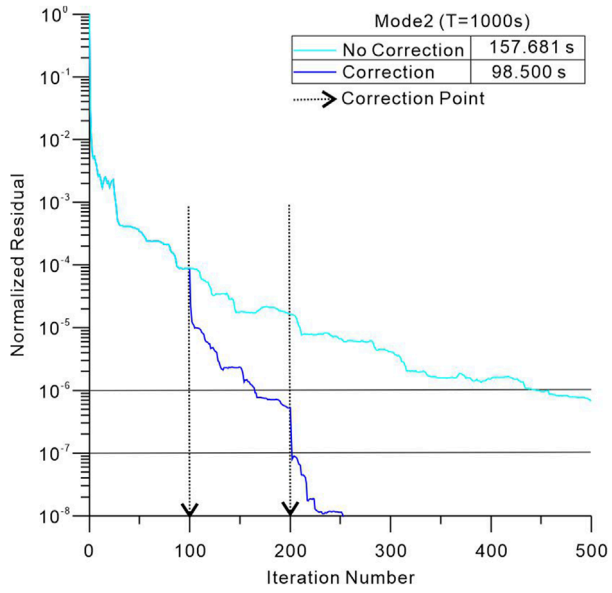

FIGURE 5
Iterative information of the Mode2 mode solution for 2D model (Figure 4) at a period of 1000 s. The blue and cyan curves denote the case with and without the application of divergence correction procedure, respectively. The total computational time is 157.681 s without divergence correction and 98.500 s with divergence correction.

a simplified model subdivided into 5 (x-axis) × 5 (y-axis) × 9 (z-axis) cells is used. Both matrices exhibit a similar banded diagonal structure of nonzero elements. Due to the presence of 4 air layers within the 9 z-axis cells, the upper-left portion of the pattern in Figure 2B is identical to that in Figure 2A. However, when anisotropy is introduced in the subsurface, the number of nonzero elements increases slightly compared to the isotropic case, as the conductivity is represented by a 3 × 3 tensor in Equation 11. Equation 13 is solved using a preconditioned QMR iterative method with an incomplete LU preconditioner. Compared to solving Equation 7 for the electric field, the iterative solution of Equation 13 is more straightforward for this method.

3 Numerical examples

In this section, three synthetic models in section 3.1, 3.2 and 3.4.1 are discretized on a 28 × 47 × 60 grid (along the x, y, and z-axis). The model discussed in Section 3.3 is discretized into a 28 × 88 × 120 grid, with the y- and z-axis dimensions matching those of the 2D model presented by Pek (as detailed in Section 3.3). The computational complexity of these models increases progressively. Both 1D and 2D anisotropic models are utilized to demonstrate the effectiveness of accelerating iterative convergence. The accuracy of the forward results is verified by comparison with analytical, quasi-analytical and numerical solutions. The last numerical example illustrates the stability of our forward framework, which incorporates the divergence correction procedure, in a highly challenging scenario involving a long-period computation and a random 3D fully anisotropic model. Furthermore, the impact of the interval between divergence corrections is analyzed in Section 3.4.2. All computations were performed on a PC equipped with 32 GB of RAM and two Intel (R) Xeon (R) Gold 5,218 CPUs (2.10 GHz).

In a 2D isotropic scenario, the polarizations in the north and east directions are commonly referred to as TE and TM modes, respectively. However, in a 3D anisotropic medium, these modes are not decoupled. In this paper, the polarizations in the north and east directions are designated as Mode1 and Mode2, corresponding to the TE and TM modes in the 2D case, respectively.

3.1 1D anisotropic model

Figure 3A illustrates a 1D model consisting of five anisotropic layers with significant variations, which was previously utilized in Yu et al. (2018). Figure 3B presents the iteration details for the forward solution at a period of 1325 s, with the divergence correction procedure applied every 100 iterations. Without divergence correction, convergence is achieved after 281 and 266 iterations for the Mode1 and Mode2 modes, respectively. In contrast, with divergence correction, the Mode1 and Mode2 residual curves reach their final levels after only 171 and 138 iterations. The iterative residuals exhibit significantly improved convergence after applying divergence correction in both Mode1 and Mode2 computations. Additionally, the total computational time is reduced from 186.467 s to 136.000 s with the incorporation of divergence correction. Figure 3C compares our results with the analytical solutions of Pek and Santos (2002), showing a high degree of agreement, consistent with the results from Yu et al. (2018).

3.2 2D anisotropic model with infinite fault overlying a perfect conductor

As shown in Figure 4A, the model represents an infinite lateral fault with axially anisotropic conductivity structures overlying a perfect conductor, for which quasi-analytical MT solutions are available (Qin and Yang, 2016). Since a resistivity value of zero cannot be used in our numerical computations, a very low resistivity value of 10^{-5} Ωm is assigned to approximate the perfect conductor. All other electrical and geometrical parameters are set according to the model of Qin and Yang, 2016.

Figure 5 shows the iterative information of Mode2 mode at period 1,000 s. The divergence correction procedure works every 100 iterations. In the absence of divergence correction, the normalized residual decreases slowly, reaching only 7×10^{-7} by the 500th iteration (the maximum iteration number). However, similar to the previous example, convergence (10^{-8}) is achieved rapidly with the application of the divergence correction procedure, requiring only 253 iterations. After the 100th and 200th iterations, the residual drops by nearly an order of magnitude following each application of divergence correction. The computation time is significantly reduced from 157.681 s to 98.500 s with the addition of divergence correction. This

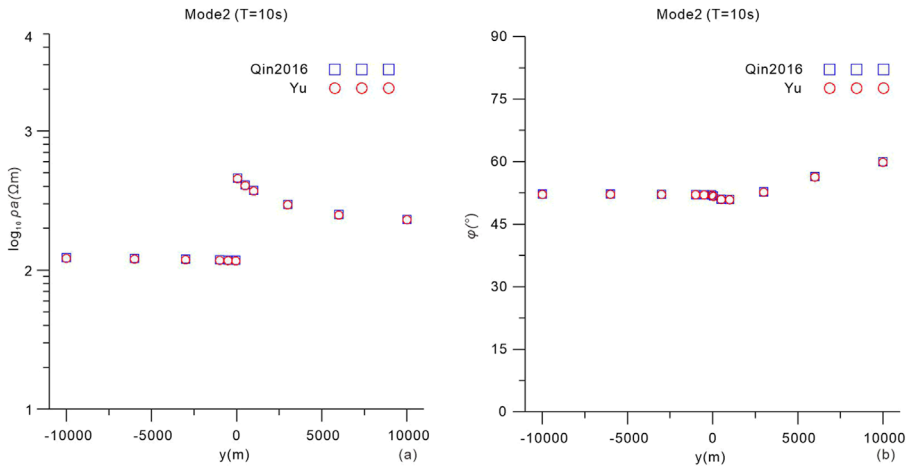

FIGURE 6
Comparison of the apparent resistivity **(A)** and phase **(B)** values perpendicularly across the fault between 3D numerical and quasi analytical (Qin and Yang, 2016) solutions at a period of 10 s.

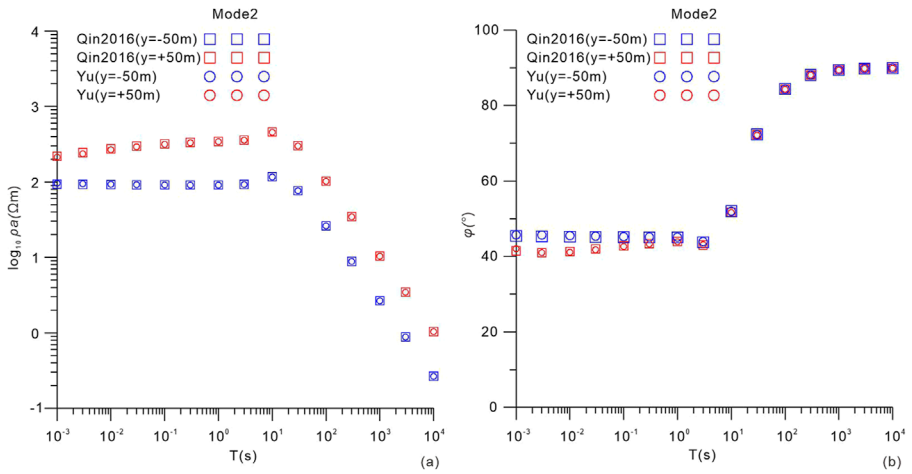

FIGURE 7
Comparison of the apparent resistivity **(A)** and phase **(B)** values of two observation points located on the opposite sides of the infinite fault at an equal distance of 50 m (y = −50 m and y = 50 m). The period varies from 10^{-3}–10^{4} s.

correction procedure notably accelerates the iterative solution of the forward problem.

Fourteen observation points are selected perpendicular to the infinite fault on both sides. As shown in Figure 6, the comparison of apparent resistivity and phase at a period of 10 s with quasi-analytical solutions (from Qin and Yang, 2016) indicates a strong agreement between our results (red circles) and the analytical solutions (blue squares). In Figure 7, two observation points, located on opposite sides of the infinite fault at an equal distance of 50 m, are selected to display the apparent resistivity and phase at different periods. The periods, ranging evenly from 10^{-3}–10^{4} s, are referenced from Qin and Yang, 2016. As demonstrated in Figure 7, our results (red and blue circles) closely match the analytical solutions (red and blue squares). The comparisons presented in Figures 6, 7 validate the accuracy of our forward computations incorporating the divergence correction procedure.

3.3 2D anisotropic model with upper and lower structure

Figure 8A illustrates a classic 2D anisotropic model featuring upper and lower structure. The background resistivity is defined as 300 Ωm. The upper anisotropic body extends from 0.300 km to 5.943 km in depth, with a width of 2.260 km. The lower layer, which is in contact with the upper body, consists of a 9.600 km thick anisotropic layer. This model, initially presented by Pek and Verner (1997), was used to investigate the Phase Rolling Out of Quadrant (PROQ) phenomenon (Heise and Pous, 2003; Yu et al., 2019). Numerical solutions at the model's center were provided by Pek's 2D program (personal communication, 2017). As shown in Figures 8B, C, the comparison between Pek's 2D results and our 3D numerical solutions further validates the accuracy of our algorithm, demonstrating high consistency.

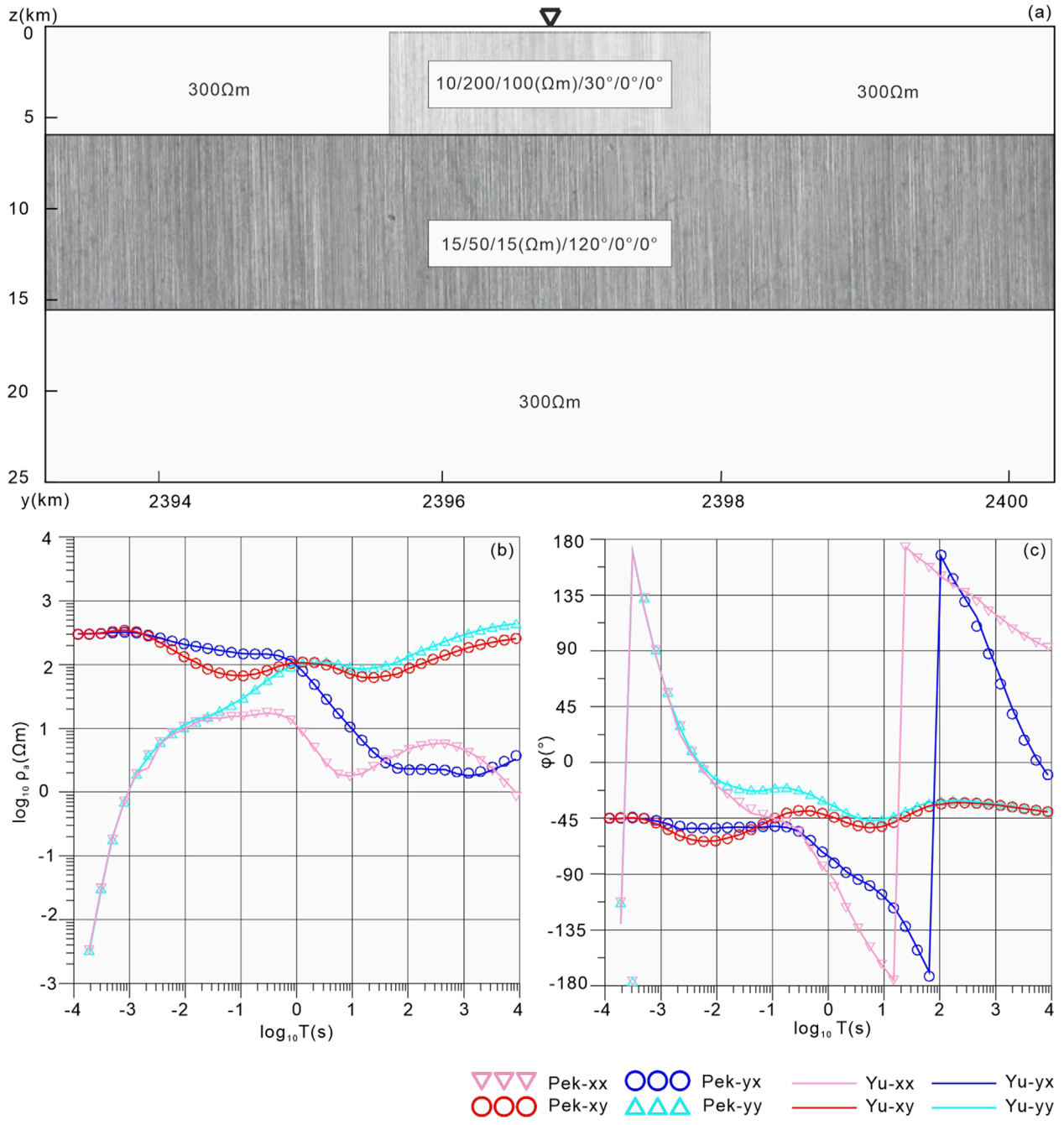

FIGURE 8
2D model. **(A)** 2D model with upper and lower structure. **(B)** and **(C)** Comparison of apparent resistivity and phase between the 2D numerical results (Pek) and the 3D numerical results (this study) at the surface central point.

3.4 3D anisotropic model with random parameters

3.4.1 Robustness

An exceptionally complex model is designed to simulate a structure that is likely more challenging than what would typically be encountered in real-world scenarios. Six anisotropic parameters of each cell is defined randomly. As illustrated in Figure 9, a horizontal (red dashed line) and a vertical (blue dashed line) profile are selected to display the parameter distributions. Figures 10, 11 show that the three principal resistivity values range from 10^{-4} to 10^{4} Ωm, while the three rotation angles vary from 0° to 180°, respectively. The long period (10,000 s) and significant variations in the principal resistivity values exacerbate the ill-condition of the coefficient matrix A in Equation 7, thereby making convergence in the computations more difficult. We assert that this challenging numerical example serves as a rigorous test of the algorithm's stability under extreme conditions. In this case, the maximum

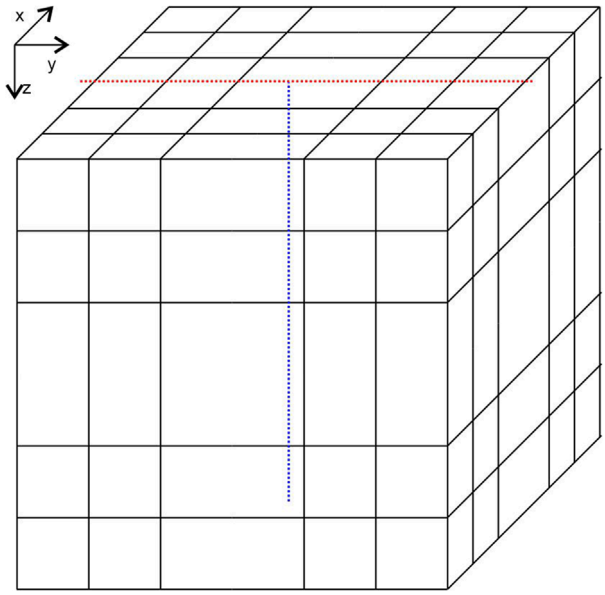

FIGURE 9
3D model assigned with random anisotropic parameters. The red and blue dashed line denotes a horizontal and a vertical profiles selected to display the distribution of anisotropic parameters.

number of iterations is set to 10,000 to ensure that the forward iteration without divergence correction achieves an acceptable level of convergence.

Figure 12A shows the iterative information. Without the application of divergence correction, the normalized residuals for the Mode1 and Mode2 modes decrease to 2.70×10^{-8} and 3.71×10^{-8}, respectively, after 10,000 iterations. Seen from Figure 12B, following the 100th iteration, 900 additional iterations only result in a reduction of about two orders of magnitude. The residuals approach the termination criterion at the maximum of 10,000 iterations, with a total computation time of 4,417.662 s. The convergence of the residuals for both the Mode1 and Mode2 modes is exceedingly slow.

In contrast, each application of divergence correction results in at least a one order of magnitude reduction (as indicated by the black dashed lines with arrows), significantly accelerating the iterative solution process with only 577.522 s. The residuals for the Mode1 and Mode2 modes finally reach 2.00×10^{-8} and 1.96×10^{-8} after 494 and 1,103 iterations, respectively, both basically satisfying the accuracy requirements around the 500th iteration. This challenging numerical example, characterized by the significant variation in anisotropic parameters and long period, demonstrates the stability of our MT forward modeling when integrated with the divergence correction procedure.

3.4.2 Interval of divergence correction

In the previous synthetic examples, the interval between successive divergence corrections, denoted as Nc, was consistently set to 100 forward iterations. These examples, particularly Figure 12A, demonstrate significant acceleration. However, while solving for divergence correction is computationally less demanding than forward computations, excessively frequent corrections can substantially increase the overall computation time in complex scenarios. Conversely, overly sparse divergence corrections may fail to effectively enhance the convergence rate of the forward iteration. Hence, an optimal interval Nc must be determined to balance the trade-off between iterative acceleration and the additional time required for divergence correction.

As illustrated in Figure 13A, a range of Nc values (50, 100, 150, 200, 300, 400) were tested. The dashed and solid lines represent the Mode1 and Mode2 iterations, respectively. Most curves achieve convergence within 1,000 iterations. Generally, more frequent divergence corrections result in fewer forward iterations needed for convergence, which is both reasonable and expected. However, as shown in Figure 13B, the minimum total computation time (444.355 s) occurs at Nc = 150, rather than at Nc = 50. This finding highlights that selecting an optimal Nc value enhances the efficiency of the forward framework with divergence correction, even though all curves in Figure 13A already demonstrate much faster convergence compared to the case without divergence correction (Figure 12A).

4 Discussion

Smith (1996) conducted pioneering work that significantly advanced iterative isotropic MT forward modeling, particularly in the context of limited computational resources at the time. This advancement proved especially valuable for MT forward computations at long periods, which are crucial for investigating deep earth's structure. Since the divergence of a curl is identically zero, applying the divergence operator to the governing Equation 6 imposes the constraint described by Equation 8, which ensures the conservation of current density. However, Smith (1996) highlighted a critical limitation: as the frequency ω approaches zero, the only term in Equation 6 that carries information about the conductive structure (the right-hand side) vanishes. Consequently, although Equation 6 can be iteratively solved to a relatively low approximate error, the divergence condition in Equation 8 is not inherently satisfied at long periods. This failure undermines the accuracy of the approximate solution, particularly in reconstructing the correct charge distribution across interfaces with conductivity contrasts, thereby impeding iterative convergence. This issue was first addressed by introducing a static divergence correction (Smith, 1996), which enforces Equation 8 and significantly accelerates the convergence of Equation 6.

With the rapid advancement of computational techniques, various numerical methods have been employed to investigate increasingly complex structures, as discussed in Section 1, "Introduction". In this study, the static divergence correction has been effectively integrated into the iterative MT forward modeling process to address fully anisotropic scenarios. Notably, we introduce, for the first time, an exceptionally complex model with randomly assigned anisotropic parameters. This novel approach is designed to closely emulate the inherent complexity of real-world scenarios, providing a rigorous test for the robustness and efficiency of our algorithm under challenging computational conditions.

While direct solvers, such as PARDISO, have become increasingly popular in recent years due to their convenience and reliability in solving forward problems, iterative methods retain

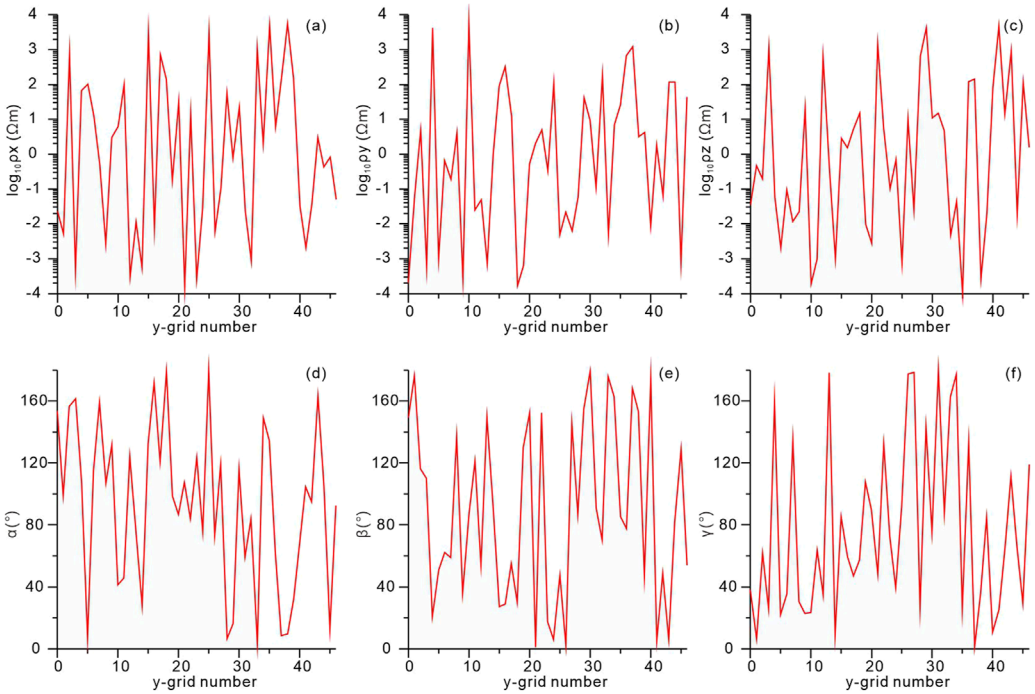

FIGURE 10
Distribution of six anisotropic parameters along the horizontal profile in 3D random model from Figure 9. **(A)** Distribution of ρ_x *versus* grid number in *y*-axis. **(B)** Distribution of ρ_y *versus* grid number in *y*-axis. **(C)** Distribution of ρ_z *versus* grid number in *y*-axis. **(D)** Distribution of α *versus* grid number in *y*-axis. **(E)** Distribution of β *versus* grid number in *y*-axis. **(F)** Distribution of γ *versus* grid number in *y*-axis.

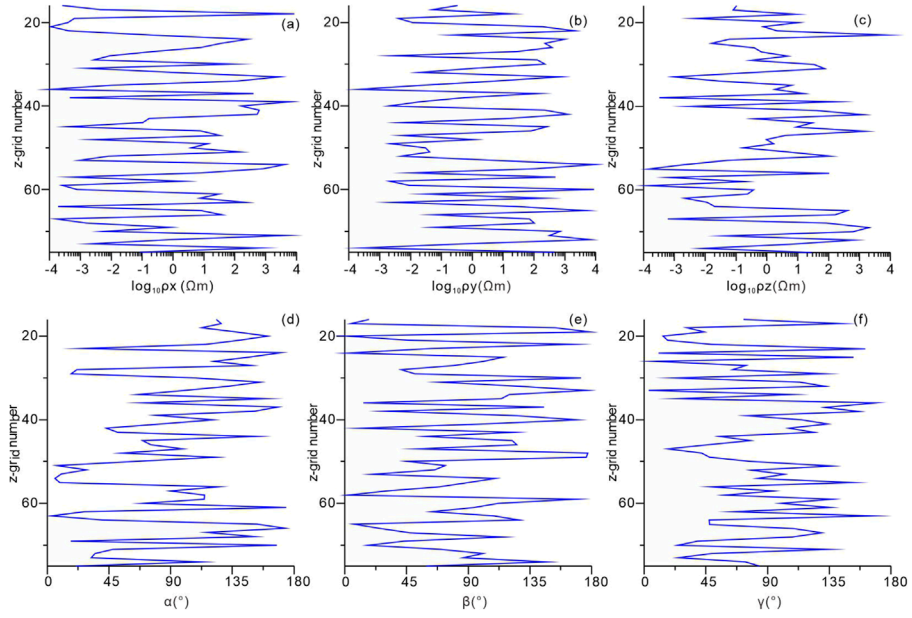

FIGURE 11
Distribution of six anisotropic parameters along the vertical profile in 3D random model from Figure 9. **(A)** Distribution of ρ_x *versus* grid number in *z*-axis. **(B)** Distribution of ρ_y *versus* grid number in *z*-axis. **(C)** Distribution of ρ_z *versus* grid number in *z*-axis. **(D)** Distribution of α *versus* grid number in *z*-axis. **(E)** Distribution of β *versus* grid number in *z*-axis. **(F)** Distribution of γ *versus* grid number in *z*-axis.

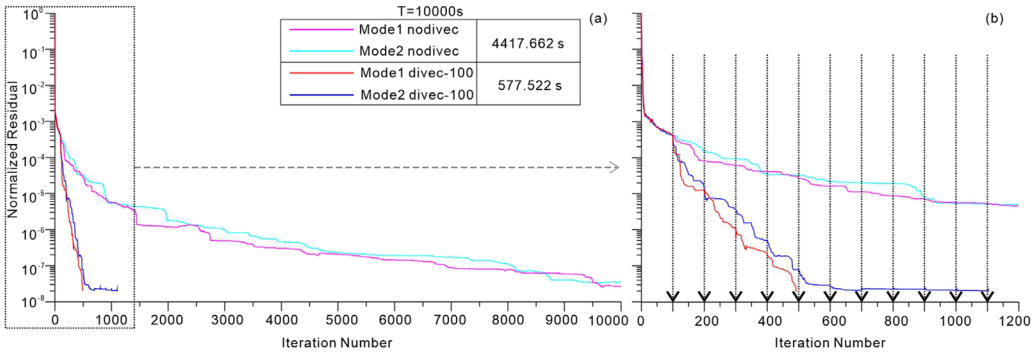

FIGURE 12
(A) Iterative information of the Mode1 and Mode2 mode solutions for 3D random model (Figure 9) at a period of 10,000 s. Purple and cyan curves denote iterative information of Mode1 and Mode2 solutions, respectively, without applying divergence correction. Red and blue curves denote iterative information of Mode1 and Mode2 mode solutions, respectively, with applying divergence correction. The dashed line shows the point when divergence correction is applied. The total computational time is 4,417.662 s without divergence correction and 577.522 s with divergence correction. **(B)** Details for the initial 1,200 iterations of **(A)**.

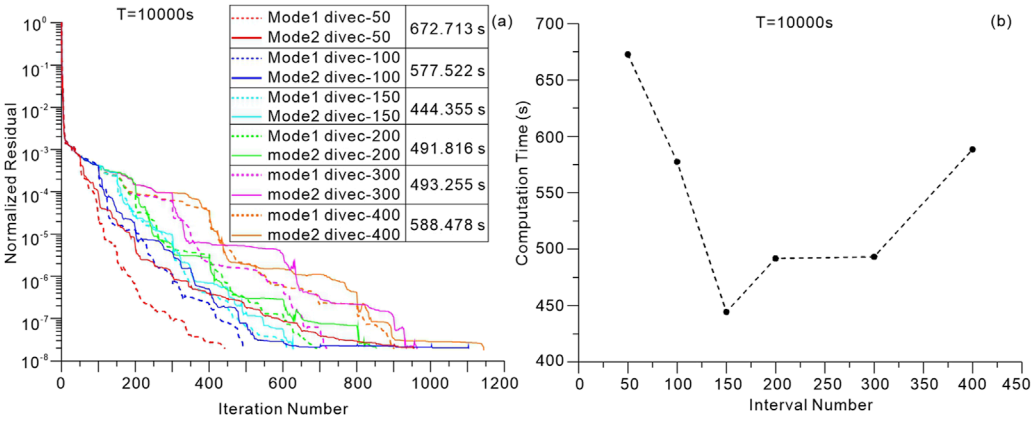

FIGURE 13
Interval Nc of forward iterations between successive divergence correction. **(A)** The total computational time is 672.713 s with Nc = 50 (red curves), 577.522 s with Nc = 100 (blue curves), 444.355 s with Nc = 150 (cyan curves), 491.816 s with Nc = 200 (green curves), 493.255 s with Nc = 300 (purple curves), 588.478 s with Nc = 400 (orange curves). **(B)** Distribution of the computational time with respect to the interval number Nc.

a distinct advantage, particularly for large-scale computations performed on standard PCs. Iterative methods require significantly less memory compared to direct solvers. However, the primary challenge of incorporating divergence correction into iterative methods lies in the complexity of the implementation. This involves carefully managing the spatial locations of electric fields and divergence points, discretizing the divergence correction equation, etc. Despite these challenges, successfully integrating divergence correction into the iterative process enables substantial reductions in computational costs, making it a highly efficient solution for large-scale forward modeling.

5 Conclusion

The fundamental theory and technical aspects of the current density divergence correction procedure are well-established, having been originally applied in isotropic MT modeling. In this paper, we extend its application to 3D MT forward modeling under arbitrary anisotropic conditions. Three numerical examples are presented to demonstrate the performance of our framework, which integrates the divergence correction procedure.

In the first example, we compute the 3D results for a 1D model comprising five anisotropic layers. In the second and third example, we calculate the 3D results for a 2D anisotropic model with an infinite lateral fault overlying a perfect conductor and with an upper and lower structure. In both cases, the 3D forward results are compared with 1D analytical, 2D quasi-analytical and 2D numerical solutions, confirming the accuracy of our algorithm. For the first case, the corrected computation requires approximately half the iterations compared to the uncorrected case. In the second example, the case utilizing divergence correction converges after 253 iterations, whereas the uncorrected case fails to converge within the maximum of 500 iterations. The third example further verifies the accuracy of our algorithm. These three examples highlight the effectiveness of the divergence correction

procedure, demonstrating a significant acceleration in iterative convergence.

In the final example, we introduce a challenging numerical problem involving a long period (10,000 s) and a fully anisotropic model with randomly assigned parameters. The effectiveness of the correction procedure is further validated in this scenario. The case with divergence correction (Nc = 100) achieves the target residual with 577.522 s, while the uncorrected case eventually reaches an accepted residual close to 10^{-8} after 10,000 iterations (the maximum allowed), with 4,417.662 s. Due to the divergence correction, the total computational time consuming significantly drops by 86.9%. This confirms that our 3D MT forward modeling framework, coupled with the divergence correction procedure, exhibits robust stability even in complex numerical computations. Furthermore, the analysis of varying Nc intervals between successive forward iterations reveals that selecting an optimal Nc value significantly enhances the efficiency of the forward framework incorporating divergence correction.

Data availability statement

The raw data supporting the conclusions of this article will be made available by the authors, without undue reservation.

Author contributions

GY: Conceptualization, Data curation, Formal Analysis, Funding acquisition, Investigation, Methodology, Project administration, Resources, Software, Supervision, Validation, Visualization, Writing–original draft, Writing–review and editing. JH: Data curation, Formal Analysis, Funding acquisition, Investigation, Methodology, Project administration, Resources, Software, Supervision, Validation, Visualization, Writing–original draft, Writing–review and editing.

Funding

The author(s) declare that financial support was received for the research, authorship, and/or publication of this article. This research is supported by National Natural Science Foundation of China (42204073).

Conflict of interest

The authors declare that the research was conducted in the absence of any commercial or financial relationships that could be construed as a potential conflict of interest.

Generative AI statement

The author(s) declare that no Generative AI was used in the creation of this manuscript.

Publisher's note

References

Badea, E. A., Everett, M. E., Newman, G. A., and Biro, O. (2001). Finite-element analysis of controlledsource electromagnetic induction using Coulomb-gauged potentials. *Geophysics* 66, 786–799. doi:10.1190/1.1444968

Bai, N., Zhou, J., Hu, X., and Han, B. (2022). 3D edge-based and nodal finite element modeling of magnetotelluric in general anisotropic media. *Comput. Geosci.* 158, 104975. doi:10.1016/j.cageo.2021.104975

Cao, H., Wang, K., Wang, T., and Hua, B. (2018). Three-dimensional magnetotelluric axial anisotropic forward modeling and inversion. *J. Appl. Geophys.* 153, 75–89. doi:10.1016/j.jappgeo.2018.04.015

Cheng, X., Gong, C. Y., Wang, G. J., Xiao, T., Yang, B., Liu, J., et al. (2024). Efficient scalable three-dimensional magnetotelluric forward modeling method considering resistive anisotropy and magnetic resistivity. *Prog. Geophys.* 39 (5), 1963–1978. doi:10.6038/pg2024HH0511

Everett, M. E., and Schultz, A. (1996). Geomagnetic induction in a heterogenous sphere: azimuthally symmetric test computations and the response of an undulating 660-km discontinuity. *J. Geophys. Res.* 101, 2765–2783. doi:10.1029/95jb03541

Farquharson, C. G., and Craven, J. A. (2009). Three-dimensional inversion of magnetotelluric data for mineral exploration: an example from the McArthur River uranium deposit, Saskatchewan, Canada. *J. Appl. Geophys.* 68 (4), 450–458. doi:10.1016/j.jappgeo.2008.02.002

Farquharson, C. G., and Miensopust, M. P. (2011). Three-dimensional finite-element modelling of magnetotelluric data with a divergence correction. *J. Appl. Geophys.* 75 (4), 699–710. doi:10.1016/j.jappgeo.2011.09.025

Guo, Z., Egbert, G., Dong, H., and Wei, W. (2020). Modular finite volume approach for 3D magnetotelluric modeling of the Earth medium with general anisotropy. *Phy. Earth. Planetary Inter.* 309, 106585. doi:10.1016/j.pepi.2020.106585

Han, B., Li, Y., and Li, G. (2018). 3D forward modeling of magnetotelluric fields in general anisotropic media and its numerical implementation in Julia. *Geophysics* 83 (4), F29–F40. doi:10.1190/geo2017-0515.1

Heise, W., and Pous, J. (2003). Anomalous phases exceeding 90° in magnetotellurics: anisotropic model studies and a field example. *Geophys. J. Int.* 155, 308–318. doi:10.1046/j.1365-246X.2003.02050.x

Jaysaval, P., Shantsev, D. V., de la Kethulle de, R. S., and Bratteland, T. (2016). Fully anisotropic 3-D EM modelling on a Lebedev grid with a multigrid pre-conditioner. *Geophys. J. Intern.* 207, 1554–1572. doi:10.1093/gji/ggw352

Kong, W., Tan, H., Lin, C., Unsworth, M., Lee, B., Peng, M., et al. (2021). Three-dimensional inversion of magnetotelluric data for a resistivity model with arbitrary anisotropy. *J. Geophys. Res. Solid Earth* 126 (8), e2020JB020562. doi:10.1029/2020JB020562

Kuzmin, A., Luisier, M., and Schenk, O. (2013). "Fast methods for computing selected elements of the Greens function in massively parallel nanoelectronic device simulations," in *Euro-par 2013 parallel processing*. Editors F. Wolf, B. Mohr, and D. Mey (Berlin: Springer), 533–544.

Liu, Y., Xu, Z., and Li, Y. (2018). Adaptive finite element modelling of three-dimensional magnetotelluric fields in general anisotropic media. *J. Appl. Geophys.* 151, 113–124. doi:10.1016/j.jappgeo.2018.01.012

Liu, Y., and Yin, C. (2013). Electromagnetic divergence correction for 3D anisotropic EM modeling. *J. Appl. Geophys.* 96, 19–27. doi:10.1016/j.jappgeo.2013.06.014

Liu, Y. H., and Yin, C. C. (2013). Electromagnetic divergence correction for 3D anisotropic EM modeling. *J. Appl. Geophys.* 96, 19–27. doi:10.1016/j.jappgeo.2013.06.014

Long, J. (2024). meshfree modelling of magnetotelluric and controlled-source electromagnetic data for conductive earth models with complex geometries. *Front. Earth Sci.* 12, 1432992. doi:10.3389/feart.2024.1432992

Löwer, A., and Junge, A. (2017). Magnetotelluric transfer functions: phase tensor and tipper vector above a simple anisotropic three-dimensional conductivity anomaly and implications for 3D isotropic inversion. *Pure. Appl. Geophys.* 174 (5), 2089–2101. doi:10.1007/s00024-016-1444-3

Martí, A. (2014). The role of electrical anisotropy in magnetotelluric responses: from modelling and dimensionality analysis to inversion and interpretation. *Surv. Geophys.* 35, 179–218. doi:10.1007/s10712-013-9233-3

Mitsuhata, Y., and Uchida, T. (2004). 3D magnetotelluric modeling using the T-Ω finite-element method. *Geophysics* 69, 108–119. doi:10.1190/1.1649380

Mukherjee, S., and Everett, M. E. (2011). 3D controlled-source electromagnetic edge-based finite element modeling of conductive and permeable heterogeneities. *Geophysics* 76, F215–F226. doi:10.1190/1.3571045

Patro, P. K. (2017). Magnetotelluric studies for Hydrocarbon and geothermal resources: examples from the Asian region. *Surv. Geophys.* 38 (5), 1005–1041. doi:10.1007/s10712-017-9439-x

Pek, J., and Santos, F. A. M. (2002). Magnetotelluric impedances and parametric sensitivities for 1-D anisotropic layered media. *Comput. Geosci.* 28 (8), 939–950. doi:10.1016/s0098-3004(02)00014-6

Pek, J., and Verner, T. (1997). Finite-difference modelling of magnetotelluric fields in two-dimensional anisotropic media. *Geophys. J. Intern.* 128, 505–521. doi:10.1111/j.1365-246x.1997.tb05314.x

Qin, L., and Yang, C. (2016). Analytic magnetotelluric responses to a two-segment model with axially anisotropic conductivity structures overlying a perfect conductor. *Geophys. J. Int.* 205, 1729–1739. doi:10.1093/gji/ggw109

Rivera-Rios, A. M., Zhou, B., Heinson, G., and Krieger, L. (2019). Multi-order vector finite element modeling of 3D magnetotelluric data including complex geometry and anisotropy. *Earth Planets. Space* 71 (1), 92. doi:10.1186/s40623-019-1071-1

Sasaki, Y. (2001). Full 3-D inversion of electromagnetic data on PC. *J. Appl. Geophys.* 46, 45–54. doi:10.1016/s0926-9851(00)00038-0

Schenk, O., and Gärtner, K. (2004). Solving unsymmetric sparse systems of linear equations with PARDISO. *J. Future Gen. Com. Sys.* 20, 475–487. doi:10.1016/j.future.2003.07.011

Siripunvaraporn, W., Egbert, G., and Lenbury, Y. (2002). Numerical accuracy of magnetotelluric modeling: a comparison of finite difference approximations. *Earth. Planets. Space* 54, 721–725. doi:10.1186/bf03351724

Smith, J. T. (1996). Conservative modeling of 3-D electromagnetic fields, Part II: Bi-conjugate gradient solution and an accelerator. *Geophysics* 61 (5), 1319–1324. doi:10.1190/1.1444055

Smith, R. (2014). Electromagnetic induction methods in mining geophysics from 2008 to 2012. *Surveys in Geophysics* 35 (1), 123–156. doi:10.1007/s10712-013-9227-1

Stalnaker, J. L., Everett, M. E., Benavides, A., and Pierce, C. J. (2006). Mutual induction and the effect of host conductivity on the EM induction response of buried plate targets using 3-D finite-element analysis. *IEEE Transactions on Geoscience and Remote Sensing* 44, 251–259. doi:10.1109/tgrs.2005.860487

Uyeshima, M., and Schultz, A. (2000). Geoelectromagnetic induction in a heterogeneous sphere: a new three-dimensional forward solver using a conservative staggered-grid finite difference method. *Geophysical Journal International* 140, 636–650. doi:10.1046/j.1365-246x.2000.00051.x

Wang, K. P., Tan, H. D., Zhang, Z. Y., Li, Z. Q., and Cao, M. (2017). Divergence correction schemes in finite difference method for 3D tensor CSAMT in axial anisotropic media. *Explor. Geophys.* 48 (4), 363–373. doi:10.1071/eg15074

Wang, T., Wang, K.-P., and Tan, H.-D. (2017). Forward modeling and inversion of tensor CSAMT in 3D anisotropic media. *Appl Geophys* 14 (4), 590–605. doi:10.1007/s11770-017-0644-7

Xiao, Q. B., Yu, G., Liu-Zeng, J., Oskin, M. E., and Shao, G. (2017). Structure and geometry of the Aksay restraining double bend along the Altyn Tagh Fault, northern Tibet, imaged using magnetotelluric method. *Geophys. Res. Lett.* 44, 4090–4097. doi:10.1002/2017GL072581

Xiao, Q. B., Yu, G., Shao, G., Li, M., and Wang, J. (2018). Lateral rheology differences in the lithosphere and dynamics as revealed by magnetotelluric imaging at the Northern Tibetan Plateau. *Journal of Geophys. Res. Solid Earth* 123, 7266–7284. doi:10.1029/2017JB015285

Xiao, T. (2019). *Three-dimensional magnetotelluric and controlled-source audio-frequency magnetotelluric modeling in anisotropic media using finite-element method*. China: Institutional Repository of University of Chinese Academy of Sciences.

Xiao, T., Huang, X., and Wang, Y. (2019). 3D MT modeling using the T-Ω method in general anisotropic media. *J. Appl. Geophys.* 160, 171–182. doi:10.1016/j.jappgeo.2018.11.012

Ye, Y., Du, J., Liu, Y., Ai, Z., and Jiang, F. (2021). Three-dimensional magnetotelluric modeling in general anisotropic media using nodal-based unstructured finite element method. *Comput. Geosci.* 148, 104686. doi:10.1016/j.cageo.2021.104686

Yoshimura, R., and Oshiman, N. (2002). Edge-based finite element approach to the simulation of geoelectromagnetic induction in a 3-D sphere. *Geophys. Res. Lett.* 29, 1039–1045. doi:10.1029/2001gl014121

Yu, G., Xiao, Q. B., and Li, M. (2019). Anisotropic model study for the phase roll out of quadrant data in magnetotelluric: with examples of upper-lower structure. *Chinese J. Geophys.* 62 (2), 763–778. doi:10.6038/cjg2019L0661

Yu, G., Xiao, Q. B., Zhao, G., and Li, M. (2018). Three-dimensional magnetotelluric responses for arbitrary electrically anisotropic media and a practical application. *Geophys. Prospecting* 66 (9), 1764–1783. doi:10.1111/1365-2478.12690

Zhou, J. J., Hu, X. Y., Xiao, T. J., Cai, H. Z., Li, J. H., Peng, R. H., et al. (2021). Three-dimensional edge-based finite element modeling of magnetotelluric data in anisotropic media with a divergence correction. *J. Appl. Geophys.* 189, 104324. doi:10.1016/j.jappgeo.2021.104324

frontiers | Frontiers in Earth Science

TYPE Review
PUBLISHED 20 January 2025
DOI 10.3389/feart.2024.1526432

OPEN ACCESS

EDITED BY
Bo Yang,
Zhejiang University, China

REVIEWED BY
Xin Li,
Chinese Academy of Sciences (CAS), China
Shiwen Li,
Jilin University, China

*CORRESPONDENCE
Letian Zhang,
letianOl@gmail.com
Sheng Jin,
jinsheng@cugb.edu.cn

RECEIVED 11 November 2024
ACCEPTED 27 December 2024
PUBLISHED 20 January 2025

CITATION
Li Y, Zhang L, Jin S, Zhou L and Zong Q (2025) A review on the magnetotelluric studies over the Central Asian Orogenic Belt—recent developments and future aspects.
Front. Earth Sci. 12:1526432.
doi: 10.3389/feart.2024.1526432

A review on the magnetotelluric studies over the Central Asian Orogenic Belt—recent developments and future aspects

Yifan Li[1], Letian Zhang[1,2,3]*, Sheng Jin[1,4]*, Lishui Zhou[1] and Qiyao Zong[1]

[1]School of Geophysics and Information Technology, China University of Geosciences (Beijing), Beijing, China, [2]State Key Laboratory of Geological Process and Mineral Resources, Beijing, China, [3]Key Laboratory of Intraplate Volcanoes and Earthquakes, Ministry of Education, Beijing, China, [4]College of Earth Sciences, Hebei GEO University, Shijiazhuang, China

The Central Asian Orogenic Belt (CAOB) was originated from the subduction, closure, convergence, and post-collisional extension of the Paleo-Asian Ocean located between the North China Craton, Tarim Craton, and the Siberian Craton during the late Permian to early Triassic. The Magnetotelluric (MT) method can detect the deep structure and properties of the orogenic belt, and further reveal the crust and mantle deformation mechanism and deep dynamic process inside the orogenic belt. In this paper, we summarize recent developments in the MT studies of the CAOB, including 2 MT studies that we recently conducted for the Beishan and Bainaimiao segments of the CAOB, which briefly describe the complex electrical structure of the crust and upper mantle, and provide valuable information for understanding its deep processes and continental dynamic mechanisms. Finally, we summarize the general characteristics of the lithospheric electrical structure and formation mechanism of low-resistivity zones, based on which we look forward to future MT studies.

KEYWORDS

magnetotellurics, Central Asian Orogenic Belt, Paleo-Asian Ocean, lithospheric electrical structure, formation mechanism of low-resistivity zones

1 Introduction

The structure and evolution of orogenic belts and their intrinsic relationship with continent growth are major issues in Earth sciences. The use of geophysical methods that detect the deep structures and properties of orogenic belts and further reveal the crust and mantle deformation mechanisms and deep dynamic processes inside orogenic belts are important frontiers in current Earth science research. The Central Asian Orogenic Belt (CAOB), located in the core region of Eurasia (Figure 1) is the largest accretion-type orogenic belt in the world. From the Neoproterozoic to the early Mesozoic, the Paleo-Asian Ocean experienced long-term, multiple subduction-accretionary orogens during its formation (Şengör et al., 1993; Xiao et al., 2003; Xiao et al., 2015). During the Hercynian tectonic period (~400–250 Ma), the scattered blocks that made up the northern part of mainland China began to drift northward, converge and accrete (Liu et al., 2021). The Paleo-Asian Ocean, between the Siberian plate, North China plate, and Tarim plate,

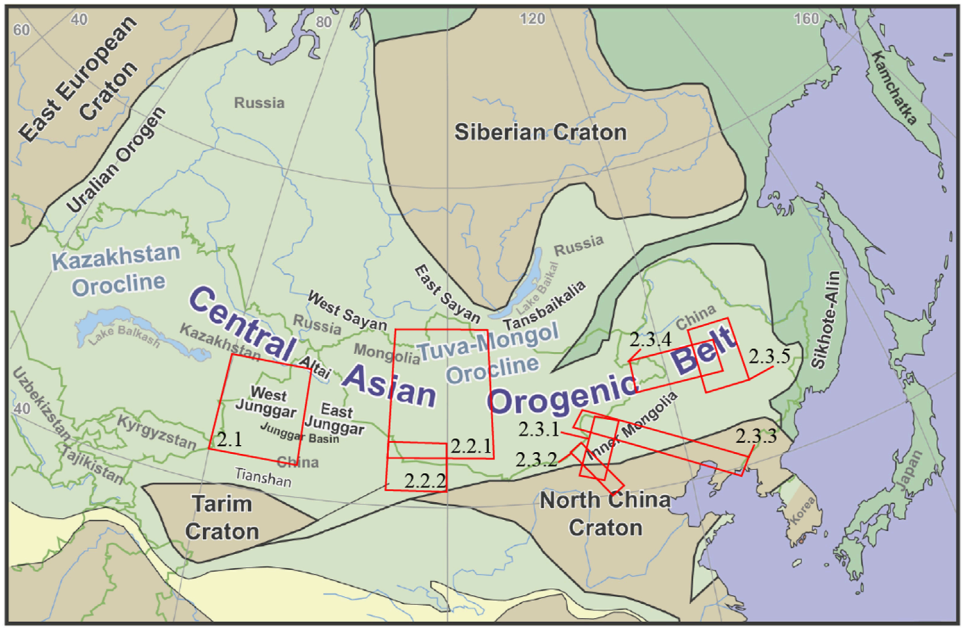

FIGURE 1
Simplified regional tectonic map of the Central Asian Orogenic Belt (CAOB) (Windley and Xiao, 2018). Red rectangles show the regions of case studies presented in this review with corresponding section numbers labeled.

gradually closed to form the CAOB (Schulmann and Paterson, 2011; Xiao et al., 2003). The North China and Tarim plates eventually aligned with the Siberia plate. Large-scale magmatic activity occurred along this orogenic belt, which combined multiple plates and produced large amounts of new crustal materials. The rocks in the CAOB are mainly composed of igneous rocks and accretionary complex rocks, and it is an area with the most intense accretion and transformation of continental crust since the Phanerozoic (Windley et al., 2007). The CAOB has experienced complex geological processes such as subduction and closure of the Paleo-Asian Ocean, convergence of the land and continent, and extension after collision, systematically preserving information on the formation and evolution of the Eurasian continent. This long tectonic evolution process makes the CAOB an ideal place for studying continental orogeny and postorogenic extension, which has attracted the attention of scholars worldwide (Cawood et al., 2009; Şengör et al., 1993; Windley and Xiao, 2018; Xiao et al., 2014; Xiao et al., 2015; Xiao et al., 2018; Xiao, 2023).

The geological evolution history of the CAOB is a complex multistage and multievent process that involves various geological processes such as continental collision, crustal accretion, postcollisional extension, and intracontinental orogeny. Together, these actions shape the tectonic characteristics of the CAOB and affect the regional and global climate and ecosystems (Xiao, 2023). Detecting the deep structure of the crust and mantle via geophysical methods can provide important clues and constraints for systematic scientific analysis. In recent years, the deep lithospheric structure of the CAOB has become a popular topic in international academia (Comeau et al., 2018; Käufl et al., 2020; Wang et al., 2022; Xu et al., 2016; Xu et al., 2020; Ye et al., 2019; Xiao et al., 2019; Zhang et al., 2014; Tan et al., 2023).

The Magnetotelluric (MT) method is an important electromagnetic geophysical sounding method in the frequency domain that uses the natural electromagnetic field of the Earth as a field source to image subsurface electrical structures at the lithospheric scale (Chave and Jones, 2012). The natural magnetotelluric field can easily penetrate high-resistivity areas and is very sensitive to the existence of low-resistivity bodies, providing important constraints on temperature, fluid and volatile distributions (Hata and Uyeshima, 2015) as well as rheological structures and deformation mechanisms (Liu and Hasterok, 2016; Xu et al., 2018) in the lithosphere. The field is useful for targeting melts, thermal fluids, saline aqueous solutions, and graphitization anomalies existing in the crust and upper mantle. Furthermore, the lithospheric structure and crust–mantle deformation mechanism of the orogenic belt can be studied, which provides an important basis for investigating the dynamic processes and dynamic mechanisms of the deep continental lithosphere.

In recent years, the MT method has been continuously improved, gradually developing from traditional 2D profile to 3D regional studies. The application results have been significantly improved, and many meaningful research results have been achieved. The MT method has been widely applied to detect the deep structures of various types of tectonic units amid the East Asian continent, from stable craton regions to tectonically active orogenic belts and subduction zones (Zhang, 2017). Among them, the CAOB of East Asia is the most complete and largest accretionary orogenic belt in the world and contains key information for cutting-edge earth science theories such as the formation of orogenic belts, the growth of continents, and the deformation of the crust and mantle (Xiao, 2023), which has attracted the attention of many scholars. In this paper, the main features of the lithospheric electrical

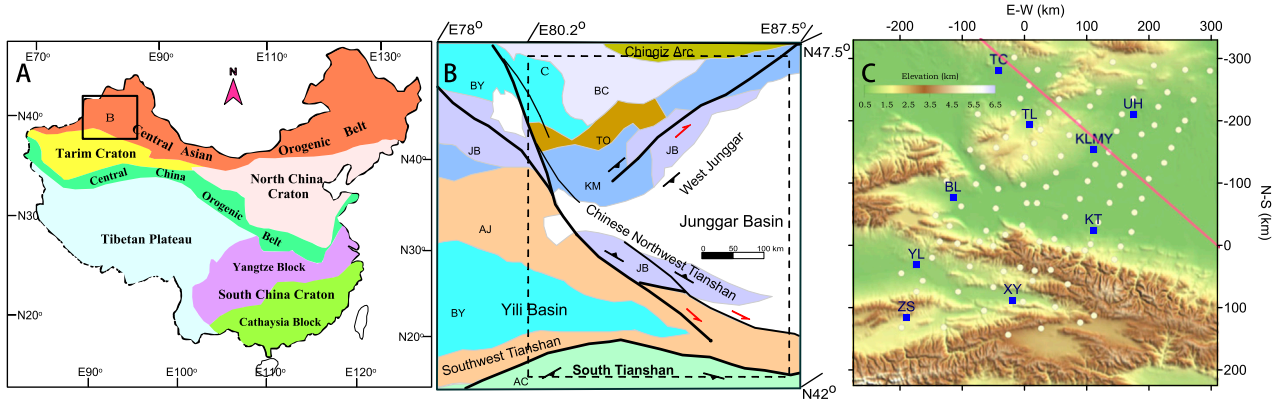

FIGURE 2
Locations of MT sites in the western Junggar area (Xu et al., 2020). **(A)** Simplified tectonic framework of China and the study area (box diagram). **(B)** Regional geological structure. AC–Late Paleozoic accretionary complex; AJ–Early Precambrian basement and Middle Precambrian to Paleozoic caprock; BC–Middle Cambrian to early Silurian island arc; BY–Late Devonian to Permian active continental margin or island arc; JB–Late Devonian to Carboniferous accretionary wedge and suture zone; KM–Ordovician to late Devonian accretionary wedge and suture zone; TO–Early-Middle Devonian active continental margin or island arc. **(C)** Locations of MT sites (white circles) and cities (squares). BL–Bole, KLMY–Karamay, KT–Kuitun, TC–Tacheng, TL–Tuoli, UH–Wuerhe, XY–Xinyuan, YL–Yili, ZS–Zhaosu. The solid line represents the location of the resistivity and Vs. cross-section in Figure 3D.

structures in these areas are introduced in the order of the western segment, the middle segment and the eastern segment of the CAOB. In addition, the preliminary results of our newly conducted MT study on the Beishan segment and the Bainaimiao segment of the CAOB are also described in this paper to provide a more complete understanding of the lithospheric electrical structure of the CAOB. Finally, we summarize the scientific understanding achieved and the remaining issues to address and provide suggestions for future research directions.

2 Progress in the MT research of the CAOB

2.1 Western segment of the CAOB

Located in the western section of the COAB, the western Junggar area is located at the intersection of three continental plates: Siberia, Kazakhstan and Tarim. It was formed by the aggregation of a multi-island ocean similar to the South China Sea in the early Paleozoic. Geologists believe that the crust is composed mainly of Paleozoic oceanic lithosphere fragments, paleo-active continental margin complexes, and intrusions of late Carboniferous to early Permian granites and dark dikes. The main tectonic strike direction in western Junggar is northeast-southwest (Figure 2). Previous studies have shown that this area retains a surviving intraoceanic subduction zone structure. Xu et al. (2020) used long-period MT array data to image possibly captured oceanic plates in the upper mantle of the western Junggar region, which elucidated the fate of the subducting oceanic plates and the evolution of the continental lithosphere.

This study deployed 101 long-period MT stations with a spacing of 25–45 km in the western Junggar region and the Tianshan region in northwestern China (Figure 2) and obtained a lithosphere-scale resistivity structure model through 3D inversion, as shown in Figure 3. The results of the 3D resistivity model for conductors with resistivities less than 25 Ω m in the depth range of 15–220 km are shown in Figure 3A. The most notable feature is that at depths between 120 and 220 km, there is a large subcontinental lithospheric mantle-scale conductor, which extends in a northeast-southwest direction, tilts northwest, and extends horizontally for more than 300 km, similar to the pattern of some remnant oceanic slabs. In the Vs. (S-wave velocity) results, the geometry of the conductor matched the mantle low-velocity zone (LVZ) (Figure 3D).

Recent studies have shown that under lithospheric mantle conditions, fluorine-containing phlogopite can greatly reduce the resistivity (Li et al., 2016; Li et al., 2017). The enrichment of volatile-bearing metasomatized minerals in the lithospheric mantle is usually related to the metasomatization process caused by the infiltration of massive fluids or melts in subduction systems. The above processes forced the subducting slab to be metasomatized by melts and/or fluids from the top and bottom. This finding matches well with the results shown in Figure 3. Therefore, in this study, metasomatic minerals containing volatiles tend to form an interconnected conductive phase and make the captured oceanic plate a conductor.

Young oceanic plates (e.g., mid-ocean ridges) or oceanic plates with thick crusts (e.g., oceanic plateaus) can avoid sinking into the deep mantle, and owing to their neutral buoyancy, they may be captured by the shallow upper mantle after subduction (Anderson, 2006). These findings indicate that the related subduction of oceanic ridges in the late Paleozoic era in the study area ensured that the subducted oceanic plates were not recycled to the deep mantle. A weak crust-mantle transition zone with a viscosity one to two orders of magnitude lower than that of the underlying mantle exists everywhere in northwestern Xinjiang (Deng and Tesauro, 2016). This weak crust-mantle transition zone effectively separates the crust from the underlying mantle lithosphere, thus protecting the existing plate from subsequent deformation and connecting the conductive phases composed of metasomatic

10.3389/feart.2024.1526432

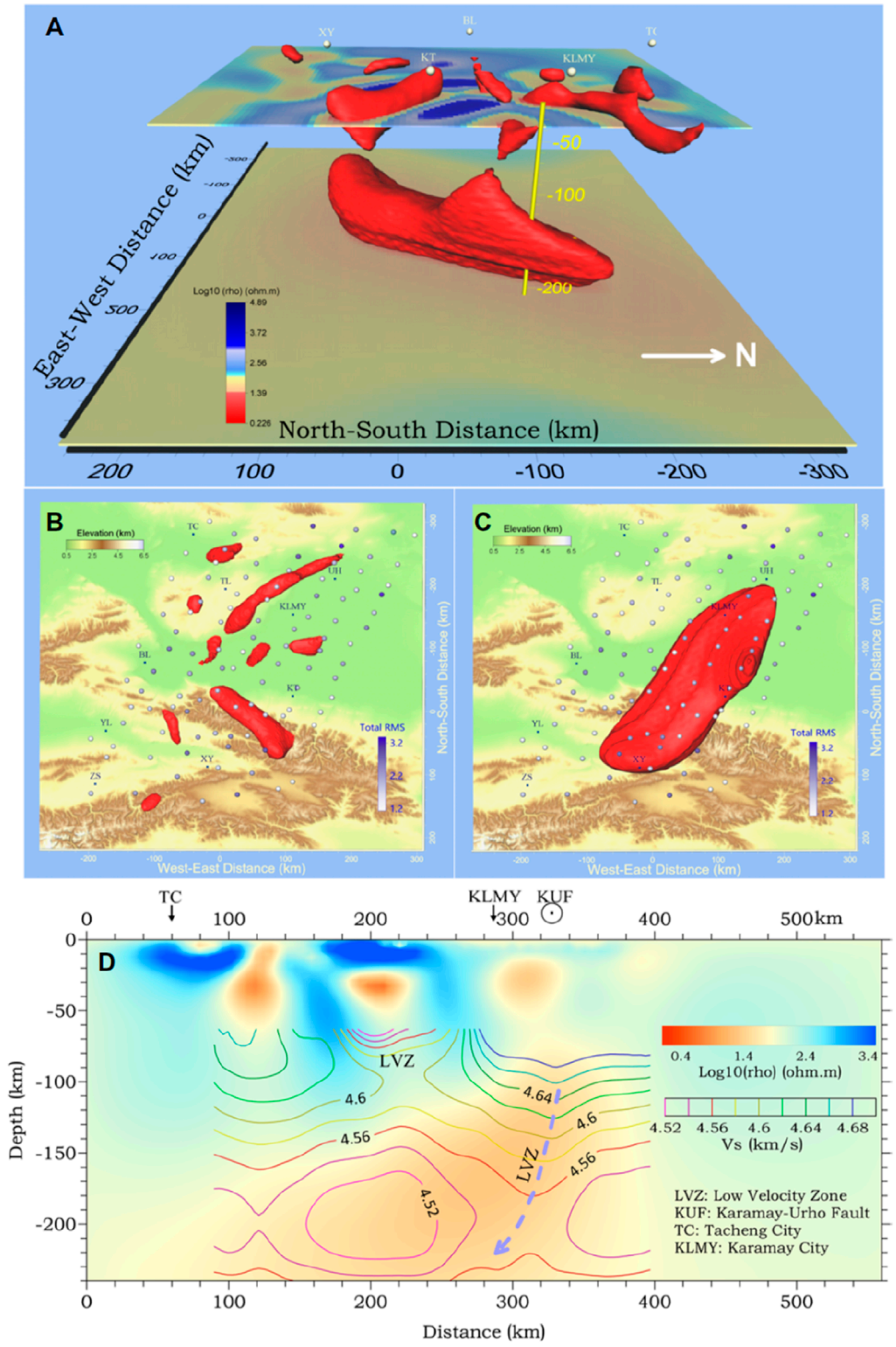

FIGURE 3
Resistivity model from western Junggar (Xu et al., 2020). **(A)** Low-resistivity anomaly at depths of 15–220 km. Two horizontal slices were made at depths of 60 km and 200 km. See the city abbreviations in Figure 2. **(B)** Conductor in the Earth's crust. **(C)** Large conductor in the lithospheric mantle. MT sites were color-filled according to their total normalized root mean square (nRMS) misfits. **(D)** Resistivity cross-section extracted from the 3D model shown in A along the line shown in Figure 2C. The superposed contours are the shear wave velocity. The blue dotted line and arrow highlight the low-velocity zone (LVZ) in the mantle.

minerals containing volatiles. This study revealed that oceanic plates can be trapped in the continental lithosphere, highlighting the importance of oceanic plate subduction for continental accretion and providing new insight into the formation and evolution of continents.

2.2 Central segment of the CAOB

2.2.1 Hangai Dome

The Hangai Dome is an inland uplift area with volcanic activity in the central segment of the CAOB. It is located in the central part of the Asian continent, far from the plate boundary. Currently, the understanding of its formation mechanism and geodynamic background is insufficient. This may be related to the interaction between the crust and the upper mantle. To study this issue, Käufl et al. (2020) collected 3D MT array data from the Hangai Dome and Gobi–Altai Mountain regions of Mongolia (Figure 4A) and, via multiscale 3D inversion, obtained an electrical structure model of the crust and upper mantle of the region (Figure 4B). Using these results, the genetic mechanisms of inland deformation and intraplate volcanic activity in this area are further assessed.

This study deployed an MT array covering a region of 650 × 400 km^2 in the Hangai and the Gobi–Altai Mountains in central Mongolia, including 97 array stations and 175 densely arranged stations along four profiles (Figure 4A). The traditional MT observation method and a geoelectric station that only measures the electric field were used. The latter can improve the spatial resolution and reduce the cost of data acquisition. With the use of finite element forward and inversion codes, multiscale model parameterization and terrain fitting were realized on the basis of an unstructured hexahedral mesh. The inversion process was divided into four stages, and more elaborate model parameterization and more data were used in each stage. A multiscale 3D resistivity structure model of the lithosphere was obtained, as shown in Figure 4B.

The model reveals that the conductivity structure of the Hangai Dome has the following main characteristics. In the high-resistivity upper crust, several low-resistivity anomalies are observed, which may be related to the late Cenozoic volcanic belts and modern geothermal regions, which are closely related to the deep mantle structure. In addition, some major fault systems, such as the boundaries that divide different geological units and ore-forming areas, also present low resistivity. In the lower crust, some nonuniform low-resistivity anomalies are found, and they may be composed of fluid-rich regions. These fluids may have originated from the dynamic processes of the mantle or deep crust. The upper mantle contains a large-scale low-resistivity area, indicating that the lithosphere–asthenosphere boundary is not uniform. There are some areas of local upwelling, which cause the asthenosphere to rise to a depth of 70 km. This low-resistivity area may be related to deep melt or fluid activity, and it may also be one of the reasons for the uplift of the Hangai Dome and volcanic activity.

This study is the first to reveal the crust-mantle resistivity structure of the Mongolian Plateau region through 3D MT inversion, which provides new constraints and clues for further understanding the geological and geodynamic processes of this region.

2.2.2 Beishan orogenic belt

The Beishan Orogenic Belt (BOB) at the southern end of the central segment of the CAOB is bordered by the Outer Mongolia accretion tectonic system in the north and the Kunlun-Qaidam-Qilian Basin system in the Tethys tectonic domain in the south. This belt is an ideal place for joint studies of the two tectonic systems. In the BOB, geophysical work is still very limited. At present, the understanding of the deep crust and mantle structure of the BOB is limited to some local areas, and the electrical structure model of the overall tectonic unit of the BOB has not been studied. We used a MT profile arranged in a northeast-southwest direction from Ejin Banner in the Inner Mongolia Autonomous Region to Jiuquan city in Gansu Province (Figure 5) to conduct profile surveying across each tectonic unit in the entire Beishan area. A total of 52 broadband MT stations were recorded at a spacing of approximately 5 km.

The ModEM code (Egbert and Kelbert, 2012; Kelbert et al., 2014) was used to perform 3D inversion of MT data via the finite memory quasi-Newton algorithm (L-BFGS). The MT data used in the 3D inversion had a frequency range of 0.01–5000 s, with a total of 35 frequency points. The full impedance tensor and vertical magnetic transfer functions (tippers) were used in the inversion, where the error floor of the four elements of the impedance tensor was 5% × $\sqrt{|Z_{xy} \times Z_{yx}|}$ and the error floor of the two components of the tipper data were both 0.05. The initial model and prior model were set to 100 Ωm uniform half-spaces, and the number of meshes for model subdivision was 85(NS) × 160(EW) × 51(Z). The initial regularization parameter is λ = 1000. During the inversion process, whenever the data fitting difference no longer decreases, λ is reduced to one-tenth of the original value. The smoothing factor in each direction was set to 0.2. The 3D inversion converged after 166 iterations, and the root-mean-square (RMS) misfit of the data was 2.187.

The preliminary resistivity model (Figure 6) shows that the southwestern part of the Beishan block is relatively stable tectonically, appearing as a high-resistivity rigid block. The central and northeastern parts are relatively active, and conductors are widely distributed from the lower crust to the upper mantle. The low-resistivity characteristics across the crust below the northeastern part of the BOB may be related to the closure of the back arc basin or ocean, indicating the locations of the paleo suture zones formed via subduction–accretion processes during the closure of the Paleo-Asian Ocean. The resistivity model of the study area revealed that the high-resistivity bodies was intersected by low-resistivity stripes.

2.3 Eastern segment of the CAOB

2.3.1 Bainaimiao arc

We used MT data collected in the central area of Inner Mongolia to study the electrical structure of the Bainaimiao segment of the CAOB. The MT data used in this study are shown in Figure 7 and are divided into two profiles. The sounding profiles all showed NNE-SSW strikes and were nearly parallel. 38 MT stations were laid out along profile Line 1, and 25 MT stations were laid out for Line 2, resulting in a total of 63 MT stations. The two profiles spanned six tectonic units, including the Hegenshan Complex Belt, the Baolidao Arc, the Solonker–Linxi suture zone, the Ondor Sum Complex Belt,

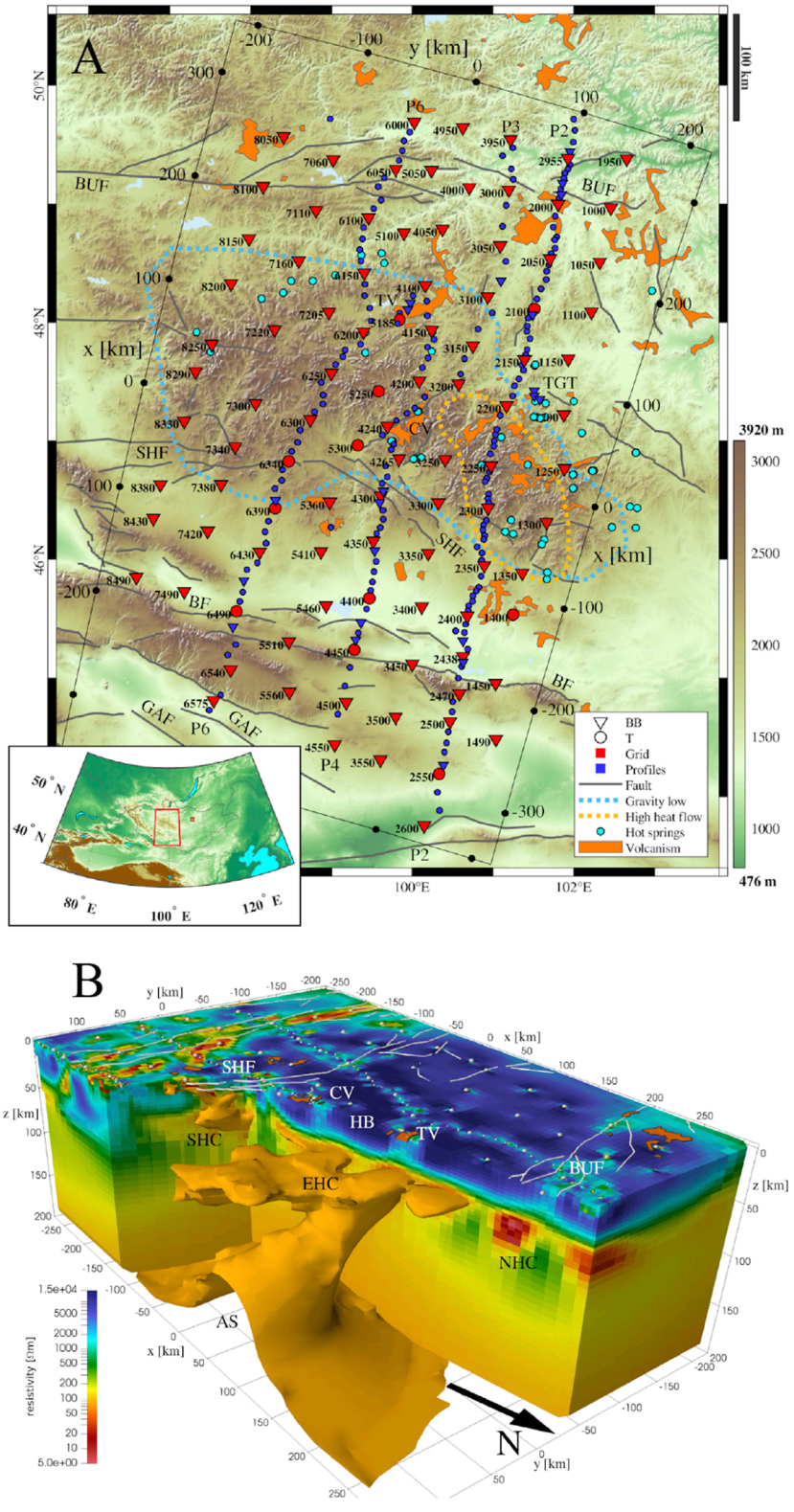

FIGURE 4
(A) Distribution of 3D MT array in the Hangai Dome area (Käufl et al., 2020). **(B)** 3D resistivity structure model of the lithosphere of the Hangai Dome (Käufl et al., 2020). AS - Asthenosphere; BF - Bogd fault; BUF - Bulnay fault; CV - Chuluut volcanic zone; EHC - East Hangai conductor; GAC - Gobi-Altai conductor; GAF–Gobi-Altai fault; HB–Hangai block; LAB–Lithosphere-asthenosphere boundary; NHC–North Hangai conductor; SHC–South Hangai conductor; SHF–South Hangai fault; TV–Tariat volcanic zone; TGT–Tsenkher geothermal area; VL–Valley of Lakes; VLR–Valley of Lakes resistor; WHC–West Hangai conductor.

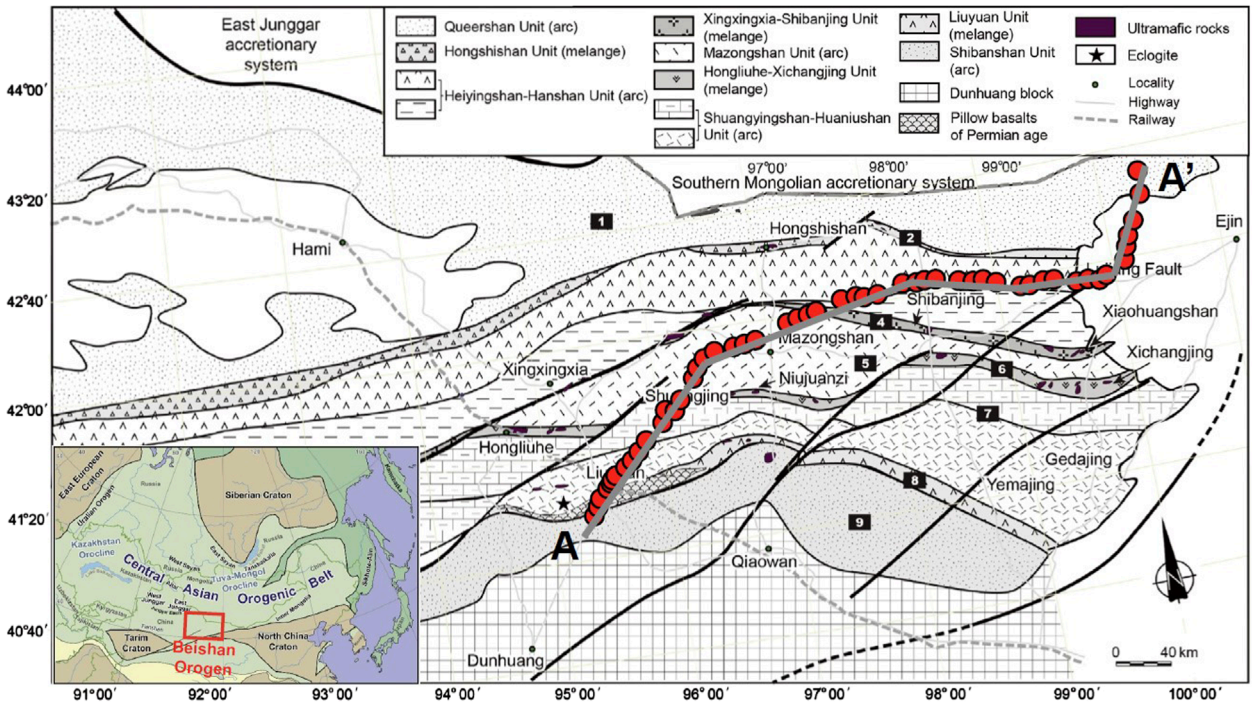

FIGURE 5
Distribution of MT sites in the Beishan area. (The red dots represent the locations of the MT surveying points; the AA' line represents the location of the vertical slice of the resistivity model in Figure 6. The base map is from Song et al., 2015).

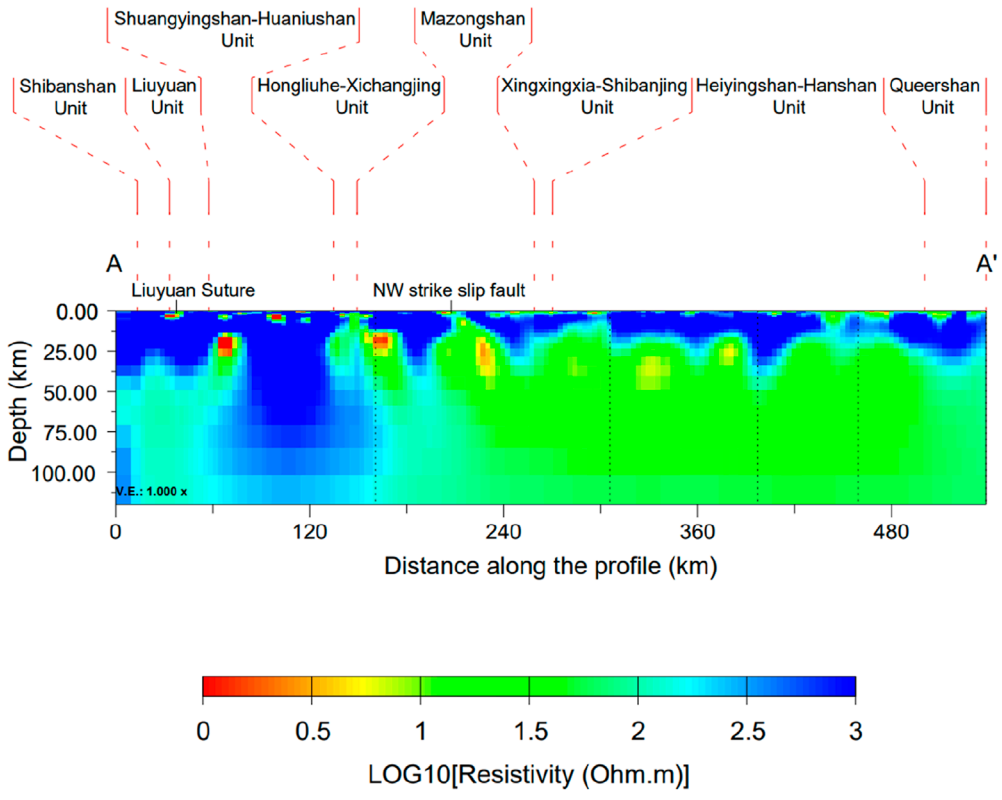

FIGURE 6
Vertical slice along the MT profile extracted from the 3D resistivity structure model of the Beishan area (The position of the cross-section is shown by the broken line AA' in Figure 5).

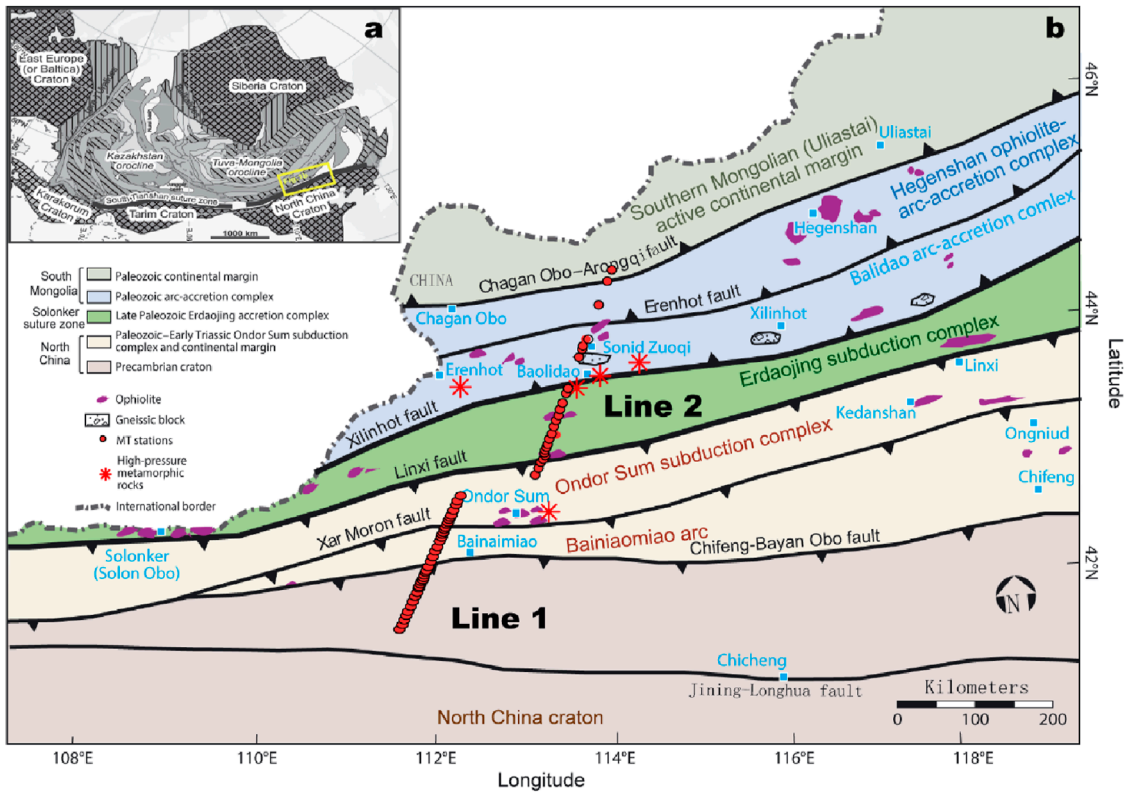

FIGURE 7
(A) Simplified tectonic map of the CAOB. **(B)** Simplified tectonic map and MT sites distribution in the study area (Base map modified from Xiao et al., 2015).

the Bainaimiao Arc and the Inner Mongolia axis, in the northeastern CAOB. The large fault zones traversed include the Erenhot fault, the Xilinhot fault, the Linxi fault, the Xar Moron fault, and the Chifeng–Bayan Obo fault.

Using the dimensionality and tectonic strike analysis of the MT data, it is found that most of the data in the study area are two-dimensional. It can be determined that the strike direction of Line one is roughly along NE 95° and the strike direction of Line two is roughly along NE 60°. On this basis, a 2D lithospheric electrical structure model was obtained through 2D inversion via the nonlinear conjugate gradient (NLCG) algorithm (Rodi and Mackie, 2001) (see Figures 8, 9, upper panels). The two profiles were inverted using both the TE and TM mode data. Considering that the TE mode data are more susceptible to 3D distortion effect (Becken et al., 2008; Jones, 1983; Wannamaker et al., 1984), the inversion parameters were set to 100% of the apparent resistivity error floor and 10% of the impedance phase error floor for the TE mode, and 10% of the apparent resistivity error floor and 5% of the impedance phase error floor for the TM mode. Different values of the regularization factor were used for inversion, and after comparison, the value $\tau = 1$ was determined as the best trade-off between model roughness and data misfits. The initial model was a 100 Ω m uniform half-space, and the initial RMS misfit of the data is 13.04 for Line 1 and 12.67 for Line 2. After 200 iterations, the RMS misfit of the data is 1.76 for Line 1 and 1.52 for Line 2. Furthermore, a 3D electrical structure model at the crust and upper mantle scales in the study area was obtained via 3D inversion using the finite memory quasi-Newton algorithm (L-BFGS) (Figures 8, 9, lower panels). The ModEM code (Egbert and Kelbert, 2012; Kelbert et al., 2014) was used for 3D inversion. The frequency range of the MT data is 0.01–10000 s, with a total of 36 frequency points. The full impedance tensor data were used in 3D inversion, and the error floors of the four elements of the impedance tensor were set as $5\% \times \sqrt{|Z_{xy} \times Z_{yx}|}$. The initial model and prior model were set to 100 Ωm uniform half-space, and the mesh size of the model was 128(NS) × 76(EW) × 50(Z). The initial regularization factor is $\lambda = 1000$. During the inversion process, whenever the data fitting difference no longer decreases, λ is reduced to one-10th of the original level. The smoothing factor in each direction was set to 0.2. The initial RMS misfit is 15.77, after 124 iterations the RMS misfit is 3.17.

A comparison revealed that the 3D model and the 2D model have relatively good consistency (Figures 8, 9). According to both the 2D and 3D models, the upper mantle of the North China Craton has a low-resistivity anomaly, and the interior of the crust is dominated by high-resistivity anomaly, with some distributed nearly vertical low-resistivity strips. The low-resistivity strips were connected with the conductor in the upper mantle, indicating that the northern margin of the North China Craton may have experienced reactivation. Under the Bainaimiao Arc, two low-resistivity zones run through the crust in opposite directions. This feature is consistent with the tectonic paleogeography model proposed by Chen et al. (2020). It is speculated that this was the

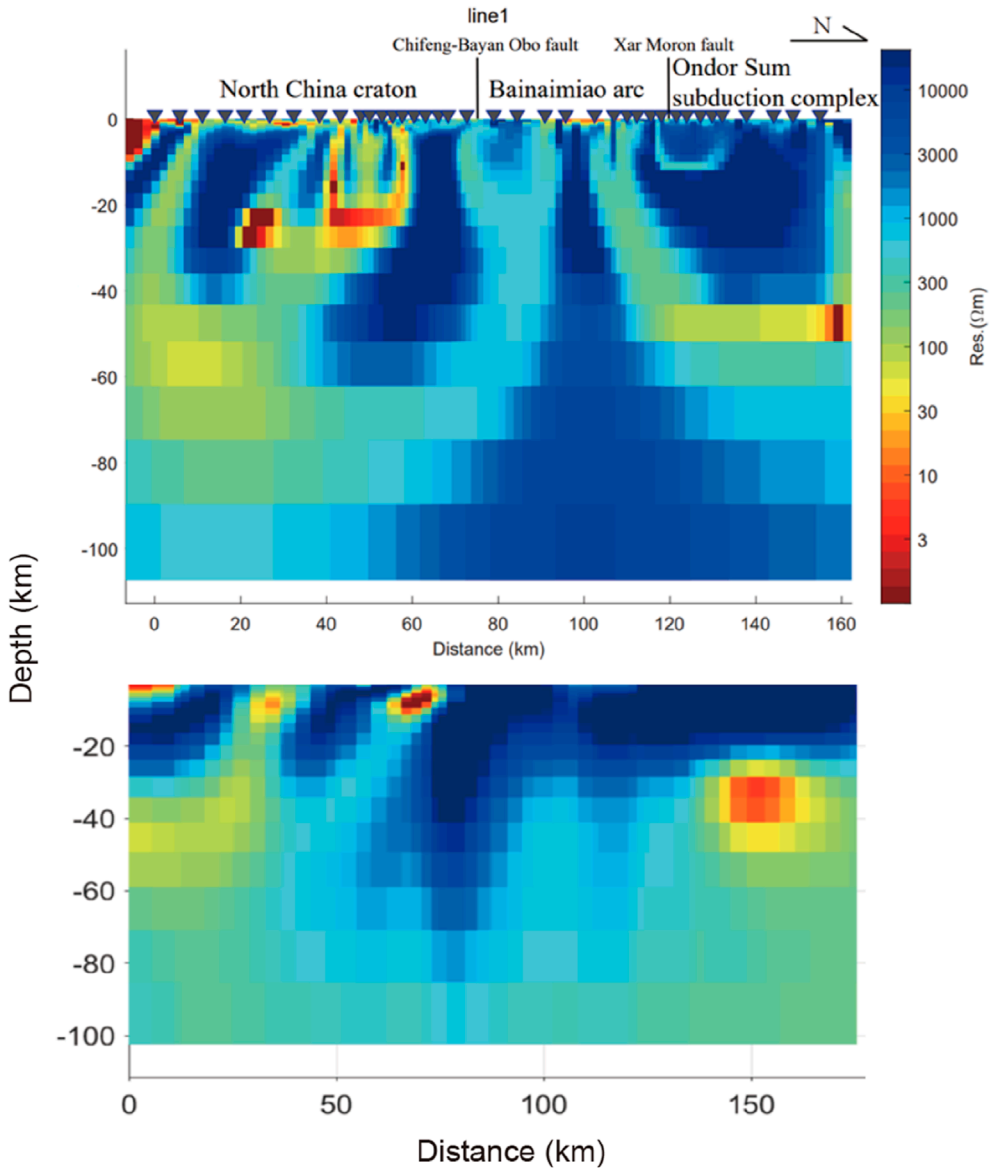

FIGURE 8
Comparison of the 2D resistivity model (upper panel) and the vertical section extracted from the 3D resistivity model (lower panel) of Line 1.

result of the closure of a paleo-ocean, with a high-resistivity zone captured in between. The high-resistivity zone runs from the crust to the upper mantle, forming an isolated lithospheric high-resistivity body. This electrical characteristic indicates that the Bainaimiao Arc may be more in line with the characteristics of an isolated arc terrane during its evolution. The crust under the Ondor Sum subduction complex, the Baolidao arc-accretion complex and the Hegenshan ophiolite arc-accretion complex all have high-resistivity anomalies. Under the Linxi fault and the Erdaojing subduction complex, which is generally recognized as the Solonker suture, there are two large-scale low-resistivity bodies with opposite dips that run through the crust in a northeast–southwest direction, which is in good agreement with the bidirectional subduction model of the Paleo-Asian Ocean (Xiao et al., 2015). The Solonker suture is speculated to be the remnant of the bidirectional subduction closure of the Paleo-Asian Ocean, and the low-resistivity anomaly is caused by sulfur- and carbon-bearing sediments (Ye et al., 2019). Graphite is the most likely carbon-bearing conductive material in this case, suggesting that the specific location of the Solonker suture may be nearly 10 km north of the Linxi fault. There are also low-resistivity zones below the Chagan Obo-Arongqi fault. This finding is consistent with the closure model of the Hegenshan back-arc basin proposed by Zhang et al. (2020), and it is speculated that the low resistivity is related to the closure of the back-arc basin. In comparison, the distribution scale of this low-resistivity body is much smaller than that of the lithospheric low-resistivity body near the Solonker suture zone. The purple patches on the geological map in Figure 10 show the distribution of ophiolites, which have a good relationship with the low-resistivity anomalies in the upper crust and are closely related to the locations of the paleo-suture zones.

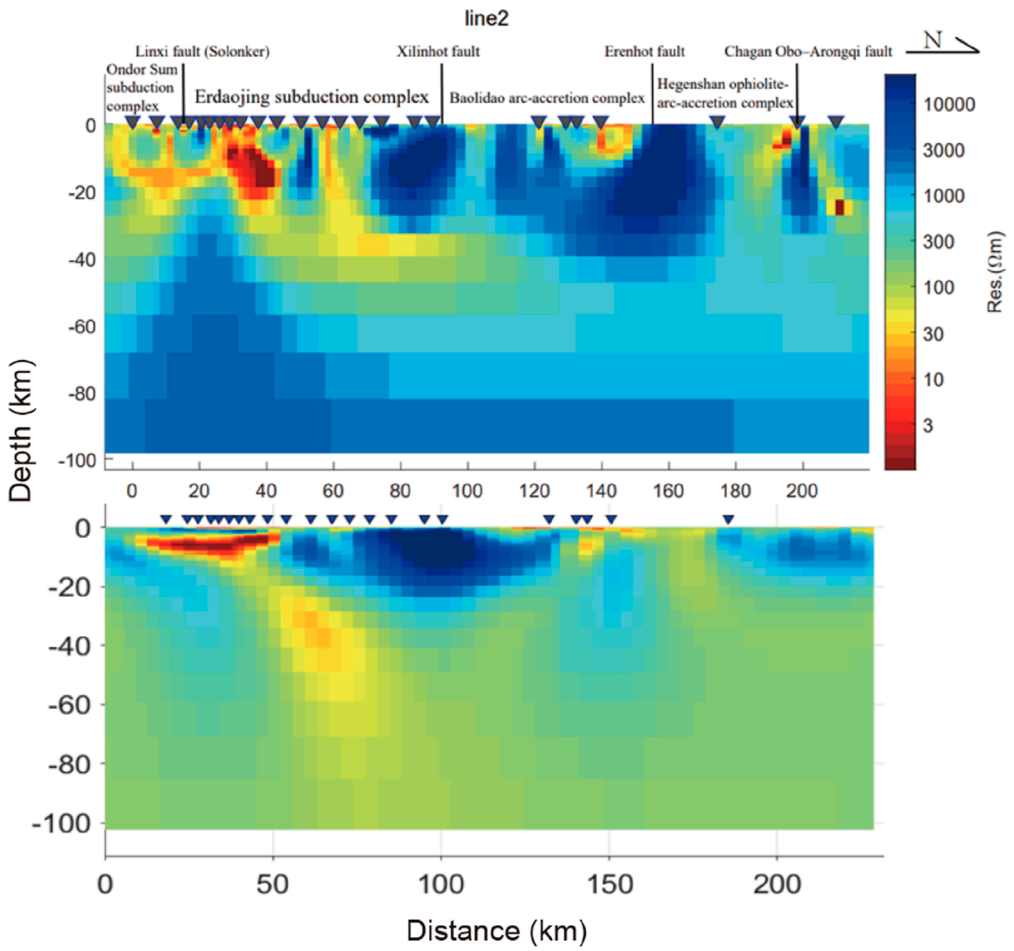

FIGURE 9
Comparison of the 2D resistivity model (upper panel) and the vertical section extracted from the 3D resistivity model (lower panel) of Line 2.

2.3.2 Solonker suture

Ye et al. (2019) conducted MT data analysis, 2D inversion, and model interpretation on the basis of a broadband to long-period, high-resolution MT profile that is approximately 400 km long and crosses the Solonker suture zone in a northwest–southeast direction (Figure 11). Using 2D anisotropy inversion and model validation, a 2D resistivity model of the study area was obtained (Figure 12). On the basis of previous study results, the model was interpreted to study the evidence and geometric characteristics of the final subduction closure of the Paleo-Asian Ocean. In the high-resistivity lithosphere, a south-dipping low-resistivity zone (Ds) with a dip angle of ~45° was found, which cuts through the entire crust and reaches the mantle. The low-resistivity anomaly is inferred to be related to sulfur- and carbon-bearing sediments originating from the southward subduction of the Paleo-Asian Ocean, with a subduction depth of up to 80 km. The low-resistivity zones caused by the subduction of oceanic crust have obvious anisotropy. On the basis of the anisotropy characteristics, it is inferred that the high strain rate caused the fold axis to rotate in the dip direction. According to the position of this low-resistivity anomaly, the Paleo-Asian Ocean was inferred to have closed along the Solonker suture zone. The high-resistivity body (R2) found under the northern margin of the North China Craton was interpreted as a thickened lithosphere caused by the southward subduction of the Paleo-Asian Ocean, whereas the north-dipping low-resistivity zones (T1–T5) found in the crust of the CAOB and the North China Craton to the south of the southward subduction location were interpreted as postcollision thrust faults. The two northward-dipping low-resistivity zones (Dn1 and Dn2) may have been related to the northward subduction of the Paleo-Asian Ocean during the closure of the Paleo-Asian Ocean. These results indicate that the Paleo-Asian Ocean exhibited bidirectional subduction characteristics during the closure process, but the deep geometry could not be well traced because of the limited MT sites distribution near the national border at the northwestern end of the MT profile.

2.3.3 Northeastern boundary zone of the north China craton

In the northeastern boundary zone of the North China Craton, Dong et al. (2015) completed a MT profile with a length of approximately 900 km in the NW–SE direction. The cross-section starts from the Hegenshan Complex Belt northwest of the CAOB and passes through the Baolidao Arc, the Solonker–Linxi suture zone, the Ondor Sum Complex Belt, the Bainaimiao Arc, the Inner

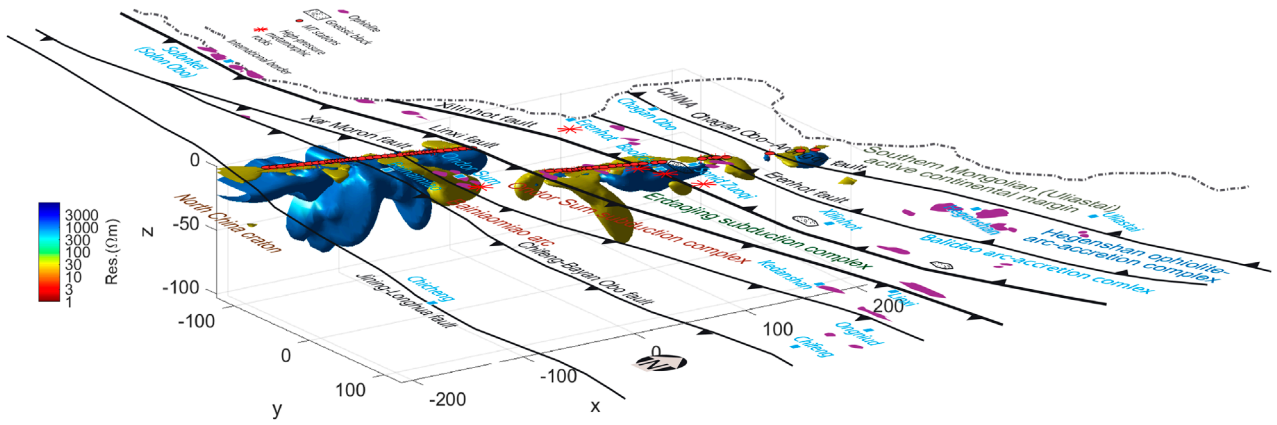

FIGURE 10
Distributions of the 1000 Ω m and 30 Ω m isosurfaces of the 3D resistivity model for the Bainaimiao arc area (surface tectonic and geological information according to Xiao et al., 2015)

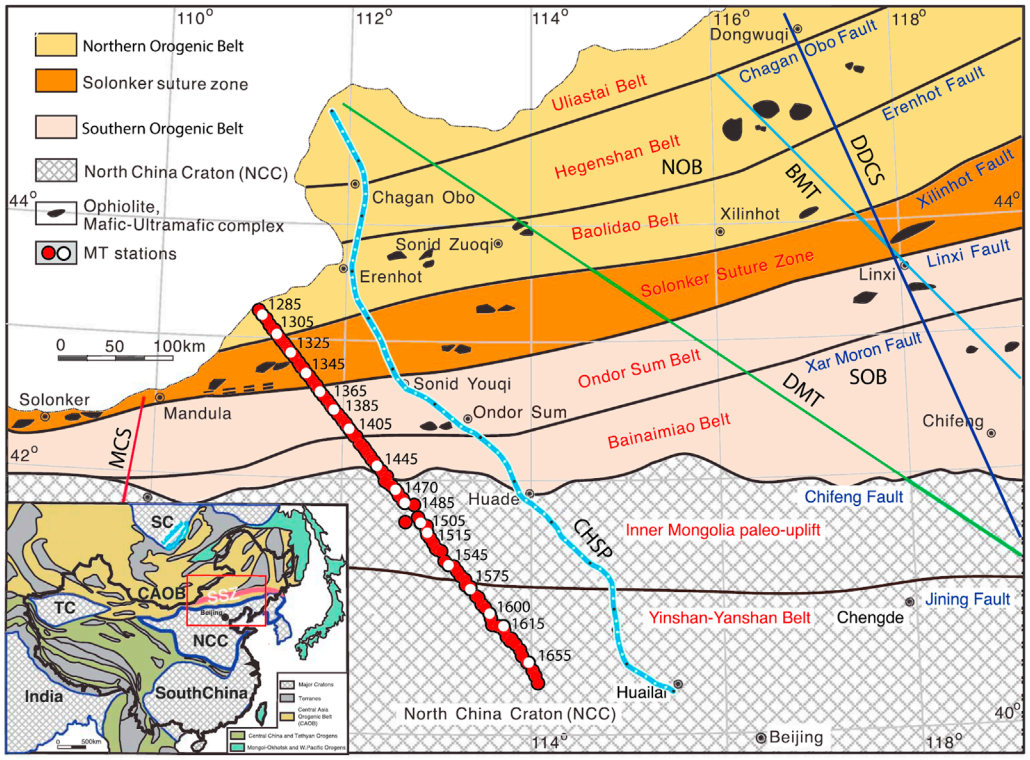

FIGURE 11
Location map of the MT profile across the Solonker suture zone (Ye et al., 2019). NOB, Northern Orogenic Belt; SOB, Southern Orogenic Belt; BMT/DMT, Previous MT profiles; CHSP, Chagan Obo - Huailai seismic profile; DDCS, Dongwu Qi - Donggou geological cross-section; MCS, Mandula geological cross-section; SC, Siberia Craton; TC, Tarim Craton; SSZ, Solonker Suture Zone.

Mongolia axis, the Yanshan Orogenic Belt, and finally terminates at the Liaohe depression inside the North China Craton (Figure 13). The MT impedance tensor decomposition technique was used to analyze the dimensionality of the MT data and determine the regional geoelectric strike directions. The MT data along the profile generally exhibit good two-dimensional traits. Using the 2D NLCG inversion method, the subsurface 2D resistivity structure along the cross-section was obtained (lower panel of Figure 13). The resistivity structure along the cross-section can be roughly divided into three main electrical zones, which vary from high-resistivity to low-resistivity to high-resistivity. Generally, the resistivity characteristics within the CAOB and North China Craton are quite different, with the former changing violently and the latter changing relatively gently. Large-scale low-resistivity bodies are found in the

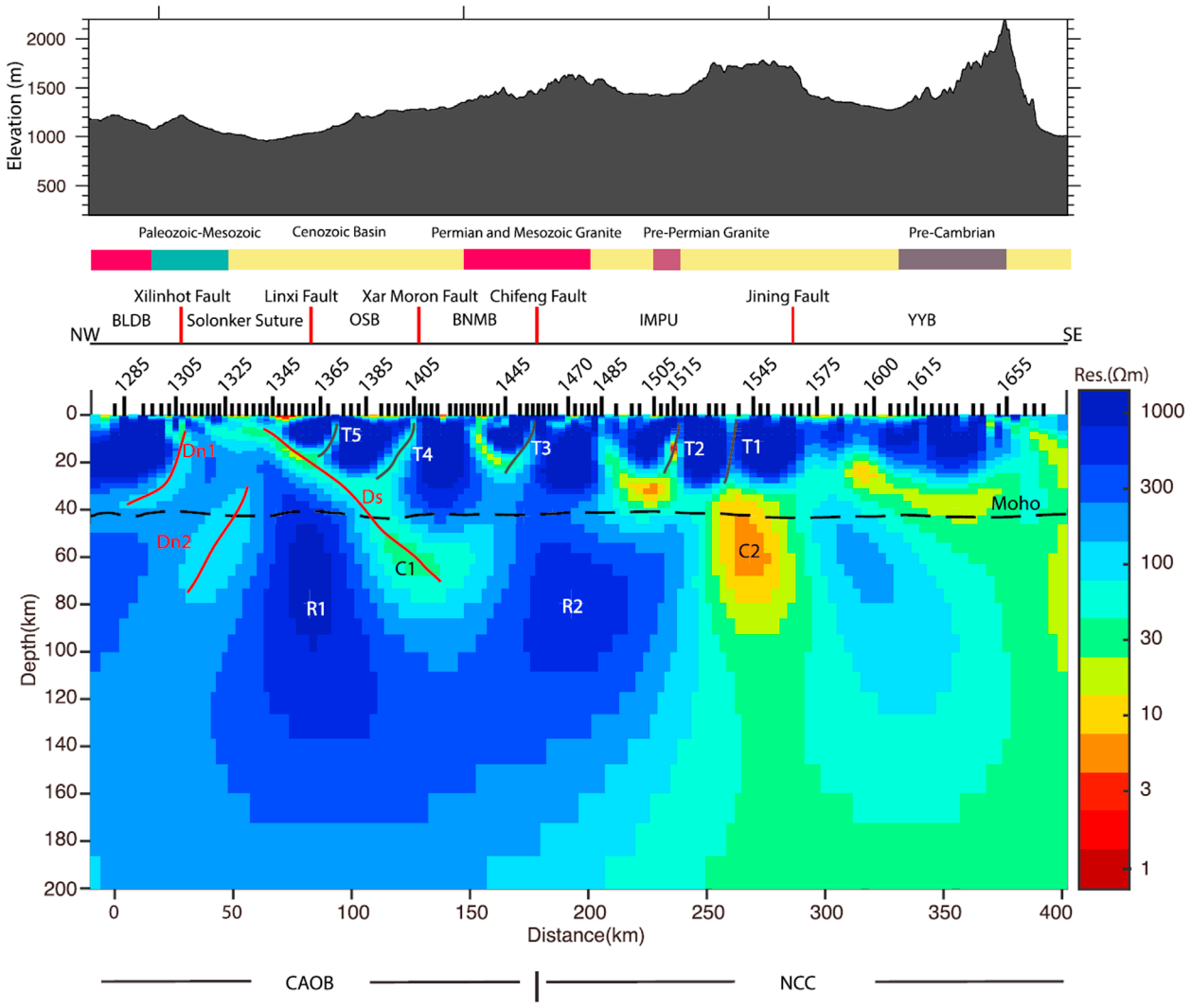

FIGURE 12
Interpretation diagram of the 2D resistivity model of the lithosphere across the Solonker suture zone (Ye et al., 2019). BLDB, Baolidao Belt; OSB, Ondor Sum Belt; BNMB, Bainaimiao Belt; IMPU, Inner Mongolia Paleo-Uplift; YYB, Yinshan-Yanshan Belt.

middle–lower crust beneath the Solonker–Linxi suture zone and the Inner Mongolia axis, which may have been formed by deep fluids and partial melting. On the basis of the deep electrical structure and other geological and geophysical observations of the study area, the final suture location between the Siberian plate and North China plate may be in the area between the Xilinhot fault and the Xar Moron fault. In addition, the thicker high-resistivity body under the Yanshan Orogenic Belt may act as a tectonic barrier, causing the uppermost mantles inside and outside the North China Craton to have different convective modes, thus weakening the influence of the tectonic evolution of the CAOB on the destruction of the eastern North China Craton.

2.3.4 Great Khingan range

Liang et al. (2015) used MT profile data across the Great Khingan range from the eastern segment of the CAOB to study the lithospheric electrical structure (Figure 14). The purpose of this study is to reveal the lithospheric structure of the CAOB from an electrical perspective and to provide new evidence and constraints for the exploration of its tectonic evolution process as well as a new basis for deep resource surveys in the study area. After standardized data processing, analysis and inversion, a reliable deep electrical structure model was finally obtained (lower panel of Figure 14). The results reveal a large area of low-resistivity anomaly in the middle and lower crust of the study area, which reflects the weak nature of the crust and may have formed in a late extensional environment. The low-resistivity anomaly of the lower crust and the formation of regional mineral resources may be related to the upwelling of hot mantle material. The uplift of mantle material may also be an important driving force for the late tectonic extension of the study area.

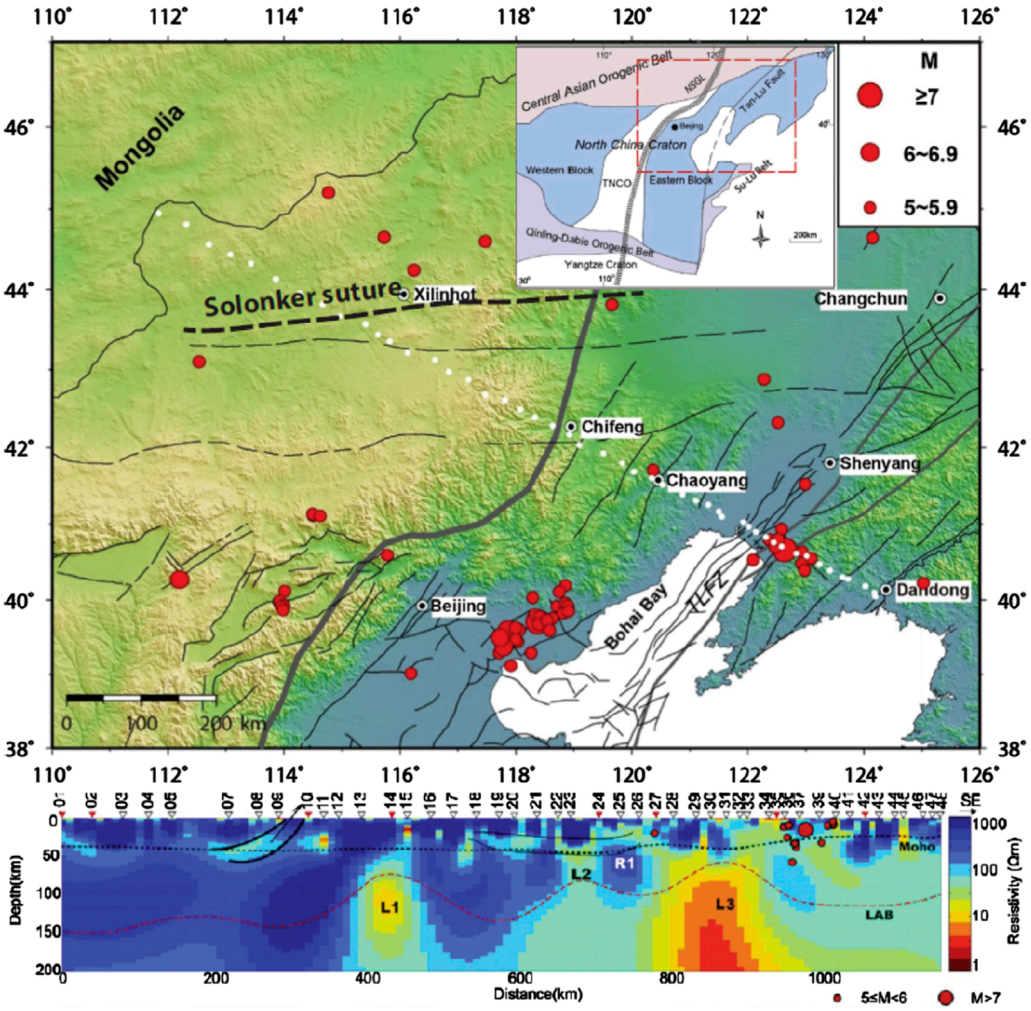

FIGURE 13
Distribution of the MT profile and 2D resistivity model in the northeastern boundary zone of the North China Craton (Dong et al., 2015)

2.3.5 Songliao block

The Songliao block in northeastern China is located in the superposition of multiple tectonic regimes. Its formation and evolution were affected by the closure of the Paleo-Asian Ocean, the closure of the Mongol-Okhotsk Ocean, and the subduction of the Paleo-Pacific plate (Figure 15A). Deep seismic reflection models revealed that there was a tilting mantle reflector under the Songliao block. This was speculated to be the result of the superposition, mutual subduction and compression of different tectonic regimes in the deep part of the Songliao block, followed by strong extension in the later stage. Despite the superposition and transformation of the later tectonic domains, residual traces of the preexisting tectonic regime can still be observed in the lithospheric structure. However, the relationship between the current lithospheric structure and the tectonic regime of the Songliao block is still unclear. One of the key problems is the unclear understanding of the lithospheric structure beneath the Songliao block.

To address the above problems, Wang et al. (2022) conducted a MT study (Figure 15) by establishing a 3D lithospheric electrical structure model in the northern Songliao Basin (Figure 16). They revealed a heterogeneous lithosphere in the northern Songliao Basin. The lithosphere contains multiple low-resistivity anomalies (~10 Ω m), and the conductivities of the upper crust (<10 km), middle and lower crust (15–35 km), and upper mantle (>45 km) are discussed. Among them, the resistivity anomalies in the upper crust are mostly distributed in the NE and NW directions, and orthogonal low-resistivity anomalies appear at the intersection locations. There is good correspondence between the electrical structure and the surface geological characteristics, and the low-resistivity anomaly identified is located at the boundary of the known orthogonal network fault system and under the rift basin. The low-resistivity anomaly is the result of temperature-controlled partial melting. On the basis of petrologic and seismic shear wave velocity studies (Zhan et al., 2020) of the study area, the melt proportion is calculated to be approximately 5%. Compared with deep seismic reflection profiles (Fu et al., 2019), these features are distributed near locations where the Moho offset is present, indicating that magma and magmatic fluids ascend through the Moho. Adjacent to the junction of the central depression area and the northern plunge area, the low-resistivity anomaly in the deep upper mantle is interpreted as asthenospheric upwelling near the center of the Songliao block, which represents the thinnest lithosphere

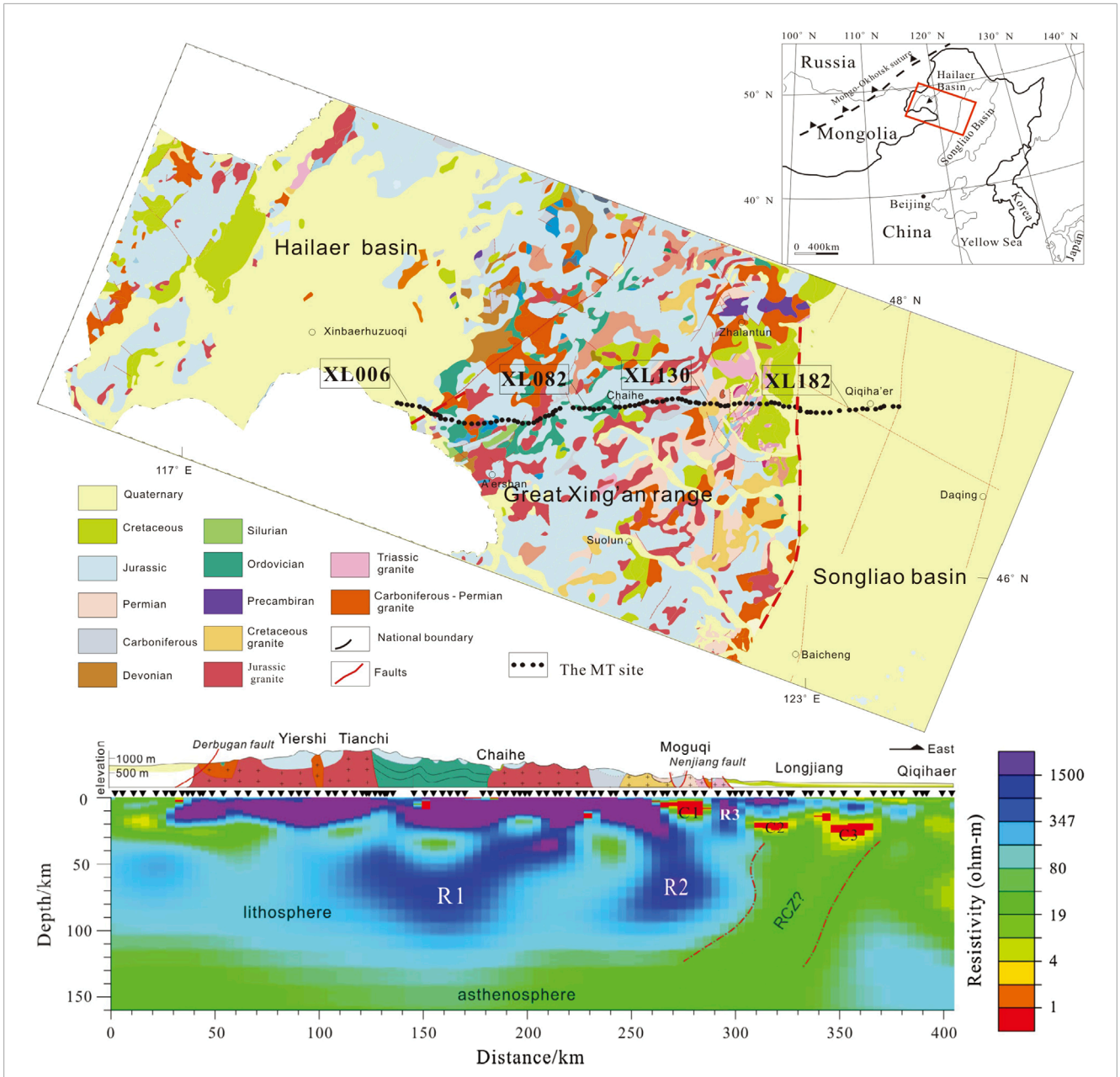

FIGURE 14
Distribution of the MT profile and 2D resistivity model across the Great Khingan range (Liang et al., 2015). RCZ, relic convergent zone; XL006-XL182 are MT station numbers.

in the Songliao Basin. On the basis of the 3D resistivity structure and comprehensive tectonic, geological and other geophysical characteristics, the following interpretations are proposed for the present tectonic mechanism of the lithosphere (Figure 17). Owing to the closure of the Pleo-Asian Ocean and the bidirectional convergence between the Mongol–Okhotsk Ocean and the Paleo-Pacific Ocean, collision, convergence and suturing of the Songliao Block and surrounding blocks occurred. These processes generated weak zones in the lithosphere at the edge of the Songliao Block, providing the structural base for the subsequent upward migration of fluids and melts. The fluids and melts were caused by water-bearing upwelling under the subduction of the Paleo-Pacific system. Therefore, even though the Paleo-Pacific tectonic system directly affects the current status of the lithospheric structure below the Songliao block, it is also closely related to the complex tectonic history and superimposed tectonic systems of the area.

3 Discussion

3.1 General characteristics of the lithospheric electrical structure

On the basis of the results of the above studies, over the vast area of the CAOB, the electrical structure of the crust and upper mantle is mostly a three-layer structure with high resistivity in the upper crust,

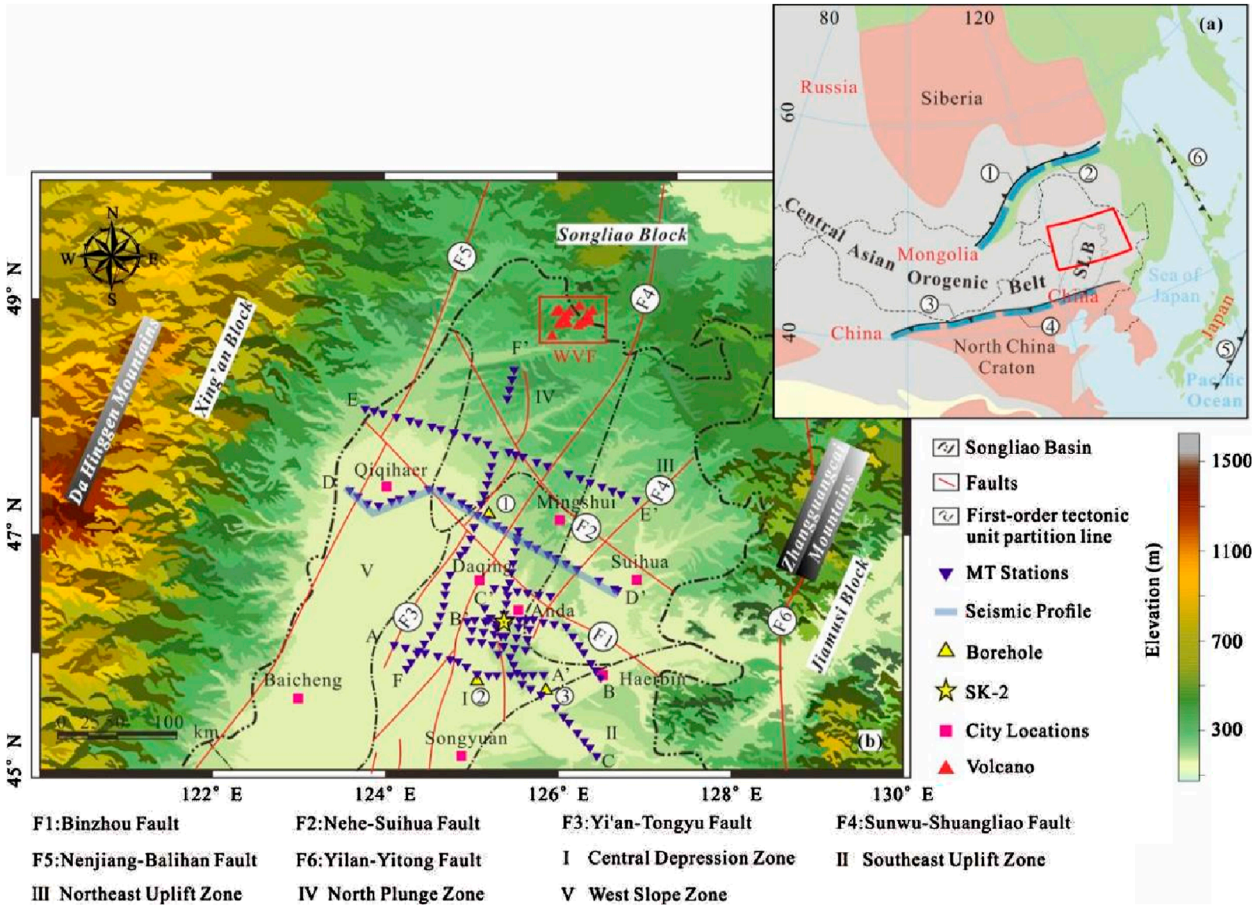

FIGURE 15
(A) Regional tectonic background of the Songliao block (SLB) and **(B)** the locations of the MT stations (Wang et al., 2022).

medium resistivity in the middle and lower crust, and low resistivity in the upper mantle (Xu et al., 2020; Käufl et al., 2020; Liang et al., 2015; Wang et al., 2022). The locations of the low-resistivity bodies in the middle and lower crust are often strongly correlated with the paleo-suture zones or paleo-subduction zones, and their spatial distribution has strong heterogeneity in the horizontal direction, as evidenced by the complex distribution pattern with horizontally alternating high and low resistivity anomalies in the middle and lower crust over the CAOB. In contrast, inside the collisional Tethys orogenic system, large-scale low-resistivity layers are widely distributed in the middle and lower crust and upper mantle (Zhang, 2017), which is generally considered due to aqueous fluids and/or partial melting, which may further weaken the lithosphere, allowing the lateral migration and flow of materials. This may reflect the significant difference in the electrical structures of the crust and upper mantle between the accretionary and collisional orogenic systems, indicating that the two essentially differ in terms of their tectonic evolution and geological processes.

Large-scale conductors were observed in the upper mantle at the northern margin of the North China Craton, which is adjacent to the southern margin of the CAOB, indicating that the lithospheric margin of the craton has been significantly modified. This phenomenon may have been common during the long process of ocean-continent transformation of the accretionary orogeny that occurred around the stable cratons. In addition, the electrical structures of the lithosphere in the eastern and western segments of the Central Asian orogenic system also differ significantly. In general, the low-resistivity anomalies in the crust and upper mantle related to the paleo-suture zones can be clearly identified in the central and eastern segments of the CAOB (Ye et al., 2019; Dong et al., 2015; Wang et al., 2022), but this feature is only reflected in the west Junggar Basin in the western segment of the CAOB (Xu et al., 2020). This may be related to the tectonic characteristics of the western segment of the CAOB, which is dominated by orocline structures (Xiao et al., 2015), despite the relatively low level of MT studies on the western segment of the CAOB.

3.2 Formation mechanism of low-resistivity zones

In recent years, MT studies conducted within the CAOB have shown that low-resistivity bodies in the crust and upper mantle are widely distributed inside the CAOB (Comeau et al., 2020; Dong et al., 2015; Xu et al., 2016; Xu et al., 2020; Ye et al., 2019).

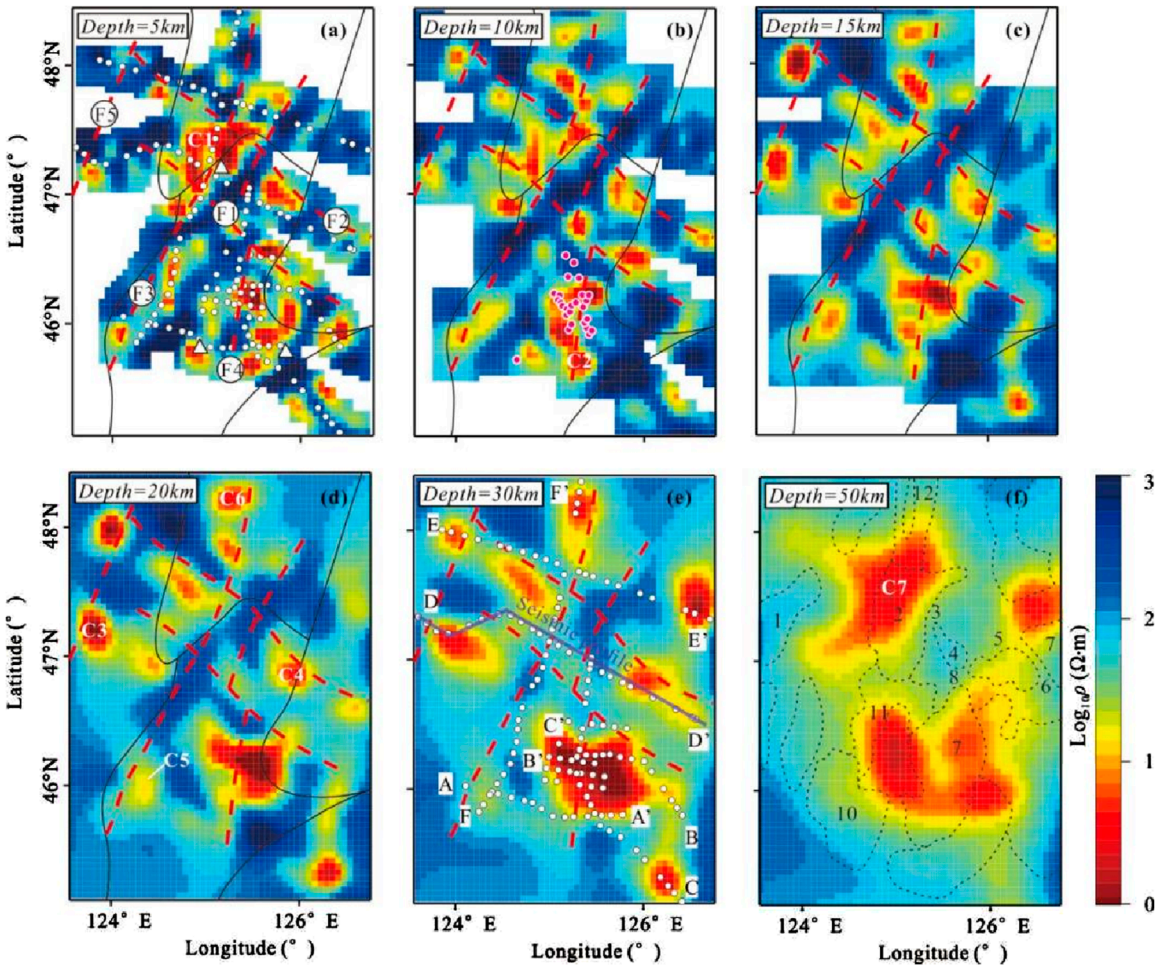

FIGURE 16
(A–F) Horizontal slices of the 3D resistivity model in the northern part of the Songliao block (Wang et al., 2022). The regions within the data coverage gaps are masked in the upper crust slices **(A–C)** due to limited constraints.

However, there is still a lack of unified understanding of the causes of low-resistivity in these accretionary orogenic belts.

For low-resistivity bodies in the crust, Comeau et al. (2020), through quantitative theoretical analysis of the length scale and viscous compaction length of crustal fluids under a convergent tectonic setting as a function of depth, proposed that in the interior of the accretionary orogenic belt, saline fluid would be confined within the lower crust, forming locally distributed and disconnected low-resistivity bodies. The inversion results of the MT profile completed in the northeastern boundary zone of the North China Craton by Dong et al. (2015) revealed that there are large areas of low-resistivity anomaly in the middle–lower crust beneath the Solonker–Linxi suture and the Inner Mongolia axis. These areas have been interpreted as deep fluids with partial melting. Ye et al. (2019) conducted a 2D inversion study on both broadband and long-period MT profile data from the eastern segment of the CAOB crossing the Solonker suture zone and reported a southward-dipping low-resistivity zone in the high-resistivity lithosphere that cuts through the entire crust and enters the mantle. The low-resistivity zone is inferred to have been caused by subducted sulfur- and carbon-bearing sediments, which originated from the southward subduction of the Paleo-Asian Ocean.

For the low-resistivity bodies of the upper mantle, the MT study conducted by Xu et al. (2016); Xu et al. (2020) in the western Junggar area of the western segment of the CAOB revealed that there was a large subcontinental lithospheric mantle conductor distributed in a depth range of 120–220 km. The conductor was considered to represent a captured fossilized oceanic slab. The subducting slab was metasomatized by a large amount of melts and/or fluids from the top and bottom, which resulted in the enrichment of volatile metasomatized minerals in the lithospheric mantle and the formation of interconnected conductive phases, thus making the captured oceanic slab behave as a conductor captured by the shallow upper mantle after subduction due to its neutral buoyancy. In contrast, Comeau et al. (2018) and Käufl et al. (2020) reported that large-scale low-resistivity bodies in the upper mantle beneath the Hangai Dome were formed by local asthenospheric upwelling caused by delamination of the lithosphere. These low-resistivity bodies occur at different locations and depths and have different geological backgrounds; thus, the main factors considered

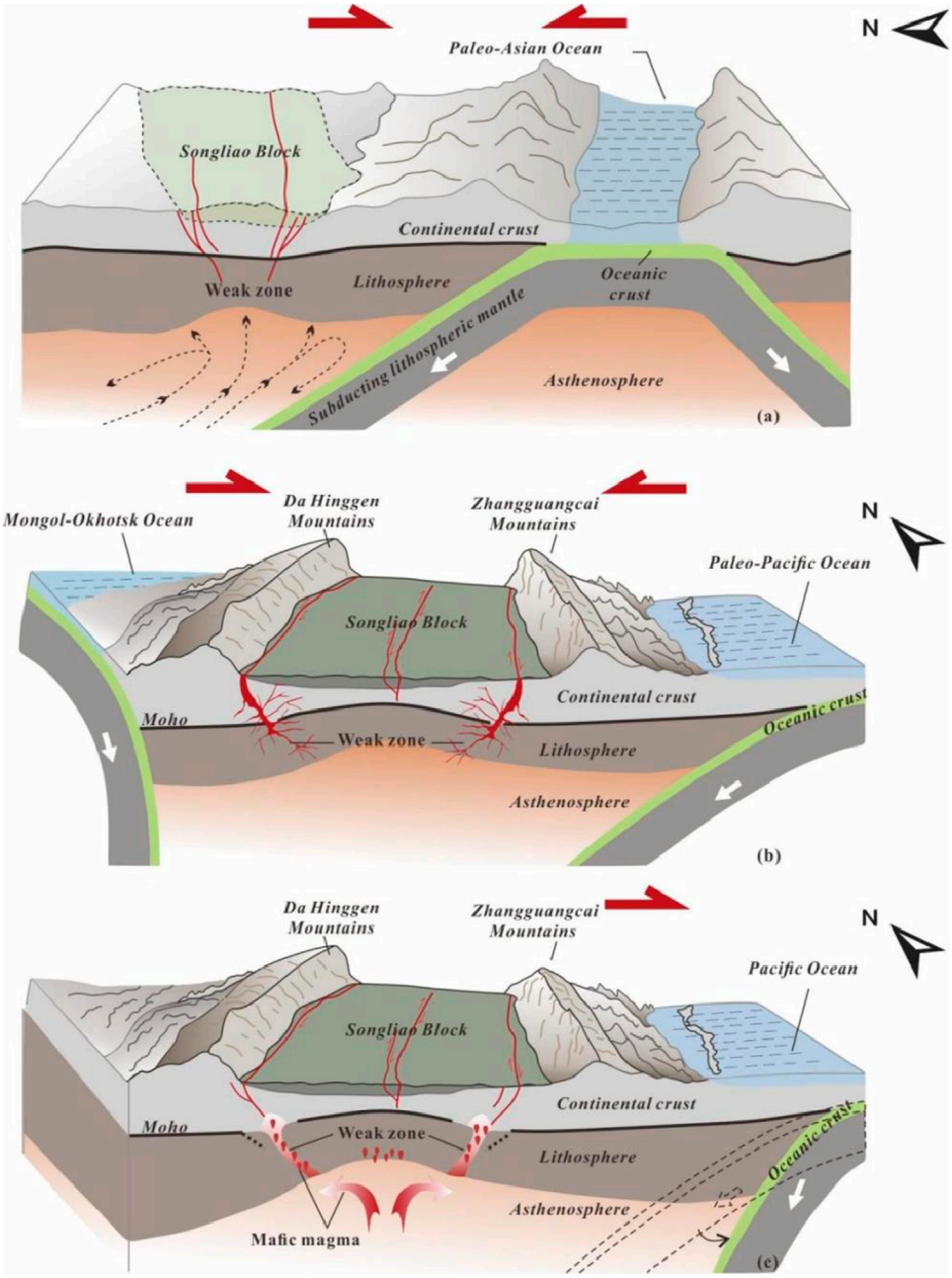

FIGURE 17
Schematic diagram of the formation and evolution of the Songliao block under the superposition of tectonic systems on the basis of the interpretation of the resistivity model (Wang et al., 2022). **(A)** Period dominated by the Paleo-Asian Ocean; **(B)** Period dominated by the Mongol–Okhotsk Ocean and the Paleo-Pacific Ocean; **(C)** present day. The red line represents fault zones; the dark green layer represents the sedimentary basin; and the red bubbles represent rising melts and fluids.

in interpretation are different. As a result, there is no unified understanding of the cause of these low-resistivity bodies to date.

In addition, owing to the uncertainty of geophysical inversion and the volume effect of the electromagnetic field, accurately determining the shape and size of low-resistivity objects in a resistivity model is often difficult. When the scale of the interpretation problem is greater than the resolution of the resistivity model, the model can provide strong constraints for interpretation. However, if the scale of the problem is smaller than the resolution of the resistivity model, it can be inaccurate and lead to misinterpretation. The difficulty in defining the boundary of a low-resistivity body is also a factor that limits the development of quantitative explanations. In addition, at present, the connection between laboratory electrical conductivity measurement (Yang, 2014) and the electrical structure model of field survey data is not close enough. On the one hand, the factors influencing subsurface electrical resistivity are much more complex than those in laboratory measurements. With the development of laboratory electrical conductivity measurement, temperature and water content are generally considered, but factors such as other volatile like carbon

dioxide, and iron ion contents are considered only in relatively few experiments. On the other hand, the composition of the crust is much more complicated than that of the mantle, and relatively simple mineral assemblage models cannot be used to simulate it. Conductivity experiments on crustal minerals require more supporting data. To better use the resistivity model to understand geological issues, interpretations should be made in combination with geological and other geophysical information based on a reliable resistivity model, and if possible, quantitative analysis should be performed in combination with laboratory electrical conductivity measurement results.

4 Conclusion and suggestions

On the basis of the review content of this paper, MT studies over the CAOB reveal the complex electrical structure of the crust and upper mantle in this region and provide valuable information for understanding its deep processes and continental dynamic mechanisms. Studies have shown that the distribution of low-resistivity bodies in the crust and upper mantle in the CAOB is closely related to paleo-suture zones or paleo-subduction zones. These features reflect the subduction, accretion and modification of the lithosphere during the long-term tectonic evolution of the CAOB. The case studies discussed in this paper verify the validity of the MT method when studying the deformation mechanism of the lithosphere in the CAOB and greatly improve our understanding of the tectonic evolution and formation mechanisms of the CAOB.

Despite significant progress, there are still different interpretations for the origins of the low-resistivity bodies in the crust and upper mantle inside the CAOB, which indicates that further studies are needed to elucidate the specific geological significance of these features. Further in-depth studies are needed to fully understand the complex geological evolution process of the CAOB. First, more comprehensive MT data collection is essentially needed, especially in the central and western segments of the CAOB, to obtain complete data coverage at the scale of the entire orogenic belt. Second, the MT method itself also needs to be improved and developed from the aspects of data processing, analysis and inversion to meet the needs of large-scale 3D MT array data acquisition, processing and inversion at the scale of the entire orogenic belt. Finally, we need to integrate MT data with other geophysical or geological data, such as through joint or constrained inversion, and compare the resistivity with other physical properties of the lithosphere (such as temperature, viscosity, water content, and melt fraction) to reduce the ambiguity of geophysical inversion, obtain a more reliable lithosphere structure model, and perform more quantitative model interpretation. A comprehensive multidisciplinary study based on geological, geochemical and other geophysical data will provide a more comprehensive perspective on the deep structure and evolution of the CAOB. This comprehensive research method helps elucidate the interactions between different geological units and how these interactions affect the accretion and evolution of continents.

In summary, these MT studies of the CAOB improves our understanding of the deep structure of the region while providing important constraints for understanding CAOB dynamics. With the advancement of technology and in-depth study, we look forward to a clearer and more complete understanding of the tectonic evolution history of the CAOB.

Author contributions

YL: Formal Analysis, Investigation, Methodology, Validation, Visualization, Writing–original draft. LeZ: Conceptualization, Data curation, Funding acquisition, Investigation, Methodology, Project administration, Resources, Writing–original draft. SJ: Funding acquisition, Project administration, Resources, Supervision, Writing–review and editing. LiZ: Investigation, Methodology, Writing–review and editing. QZ: Investigation, Methodology, Writing–review and editing.

Funding

The author(s) declare that financial support was received for the research, authorship, and/or publication of this article. This research is funded by the National Natural Science Foundation of China (42074089, 41774087, 41404060) and Deep Earth Probe and Mineral Resources Exploration - National Science and Technology Major Project (01-01-06-04). The 3D inversion is supported by the High-performance Computing Platform of China University of Geosciences (Beijing).

Acknowledgments

The authors would like to express their gratitude to the editor, BY, and the two reviewers, XL and SL, for their constructive suggestions.

Conflict of interest

The authors declare that the research was conducted in the absence of any commercial or financial relationships that could be construed as a potential conflict of interest.

Generative AI statement

The author(s) declare that no Generative AI was used in the creation of this manuscript.

Publisher's note

References

Anderson, D. L. (2006). Speculations on the nature and cause of mantle heterogeneity. *Tectonophysics* 416 (1-4), 7–22. doi:10.1016/j.tecto.2005.07.011

Becken, M., Ritter, O., and Burkhardt, H. (2008). Mode separation of magnetotelluric responses in three-dimensional environments. *Geophys. J. Int.* 172 (1), 67–86. doi:10.1111/j.1365-246x.2007.03612.x

Cawood, P. A., Kröner, A., Collins, W. J., Kusky, T. M., Mooney, W. D., and Windley, B. F. (2009). Accretionary orogens through Earth history. *Geol. Soc.* 318 (1), 1–36. doi:10.1144/sp318.1

Chave, A. D., and Jones, A. G. (2012). *The magnetotelluric method: theory and practice*. Cambridge University Press.

Chen, Y., Zhang, Z., Qian, X., Li, J., Ji, Z., and Wu, T. (2020). Early to mid-Paleozoic magmatic and sedimentary records in the Bainaimiao Arc: an advancing subduction-induced terrane accretion along the northern margin of the North China Craton. *Gondwana Res.* 79, 263–282. doi:10.1016/j.gr.2019.08.012

Comeau, M. J., Becken, M., Connolly, J. A., Grayver, A. V., and Kuvshinov, A. V. (2020). Compaction-driven fluid localization as an explanation for lower crustal electrical conductors in an intracontinental setting. *Geophys. Res. Lett.* 47 (19), e2020GL088455. doi:10.1029/2020gl088455

Comeau, M. J., Käufl, J. S., Becken, M., Kuvshinov, A., Grayver, A. V., Kamm, J., et al. (2018). Evidence for fluid and melt generation in response to an asthenospheric upwelling beneath the Hangai Dome, Mongolia. *Earth Planet. Sci. Lett.* 487, 201–209. doi:10.1016/j.epsl.2018.02.007

Deng, Y., and Tesauro, M. (2016). Lithospheric strength variations in Mainland China: tectonic implications. *Tectonics* 35 (10), 2313–2333. doi:10.1002/2016tc004272

Dong, Z., Tang, J., Unsworth, M., and Chen, X. (2015). Electrical resistivity structure of the upper mantle beneath Northeastern China: implications for rheology and the mechanism of craton destruction. *J. Asian Earth Sci.* 100, 115–131. doi:10.1016/j.jseaes.2015.01.008

Egbert, G. D., and Kelbert, A. (2012). Computational recipes for electromagnetic inverse problems. *Geophys. J. Int.* 189 (1), 251–267. doi:10.1111/j.1365-246x.2011.05347.x

Fu, W., Hou, H., Gao, R., Liu, C., Yang, J., and Guo, R. (2019). Fine structure of the lithosphere beneath the Well SK-2 and its adjacent: revealed by deep seismic reflection profile. *Chin. J. Geophys.* 62 (4), 1349–1361. doi:10.6038/cjg2019M0370

Hata, M., and Uyeshima, M. (2015). Temperature and melt fraction distributions in a mantle wedge determined from the electrical conductivity structure: application to one nonvolcanic and two volcanic regions in the Kyushu subduction zone, Japan. *Geophys. Res. Lett.* 42 (8), 2709–2717. doi:10.1002/2015gl063308

Jones, A. G. (1983). The problem of current channelling: a critical review. *Geophys. Surv.* 6 (1), 79–122. doi:10.1007/bf01453996

Käufl, J. S., Grayver, A. V., Comeau, M. J., Kuvshinov, A. V., Becken, M., Kamm, J., et al. (2020). Magnetotelluric multiscale 3-D inversion reveals crustal and upper mantle structure beneath the Hangai and Gobi-Altai region in Mongolia. *Geophys. J. Int.* 221 (2), 1002–1028. doi:10.1093/gji/ggaa039

Kelbert, A., Meqbel, N., Egbert, G. D., and Tandon, K. (2014). ModEM: a modular system for inversion of electromagnetic geophysical data. *Comput. and Geosciences* 66, 40–53. doi:10.1016/j.cageo.2014.01.010

Li, Y., Jiang, H., and Yang, X. (2017). Fluorine follows water: effect on electrical conductivity of silicate minerals by experimental constraints from phlogopite. *Geochimica Cosmochimica Acta* 217, 16–27. doi:10.1016/j.gca.2017.08.020

Li, Y., Yang, X., Yu, J.-H., and Cai, Y.-F. (2016). Unusually high electrical conductivity of phlogopite: the possible role of fluorine and geophysical implications. *Contributions Mineralogy Petrology* 171, 37–11. doi:10.1007/s00410-016-1252-x

Liang, H.-D., Gao, R., Hou, H.-S., Liu, G.-X., Han, J.-T., and Han, S. (2015). Lithospheric electrical structure of the Great xing'an range. *J. Asian Earth Sci.* 113, 501–507. doi:10.1016/j.jseaes.2015.01.026

Liu, L., and Hasterok, D. (2016). High-resolution lithosphere viscosity and dynamics revealed by magnetotelluric imaging. *Science* 353 (6307), 1515–1519. doi:10.1126/science.aaf6542

Liu, Y., Li, W., Ma, Y., Feng, Z., Guan, Q., Li, S., et al. (2021). An orocline in the eastern central Asian orogenic belt. *Earth-Science Rev.* 221, 103808. doi:10.1016/j.earscirev.2021.103808

Rodi, W., and Mackie, R. L. (2001). Nonlinear conjugate gradients algorithm for 2-D magnetotelluric inversion. *Geophysics* 66 (1), 174–187. doi:10.1190/1.1444893

Schulmann, K., and Paterson, S. (2011). Asian continental growth. *Nat. Geosci.* 4 (12), 827–829. doi:10.1038/ngeo1339

Şengör, A., Natal'In, B., and Burtman, V. (1993). Evolution of the Altaid tectonic collage and Palaeozoic crustal growth in Eurasia. *Nature* 364 (6435), 299–307. doi:10.1038/364299a0

Song, D., Xiao, W., Windley, B. F., Han, C., and Tian, Z. (2015). A paleozoic Japan-type subduction-accretion system in the beishan orogenic collage, southern central asian orogenic belt. *Lithos* 224, 195–213. doi:10.1016/j.lithos.2015.03.005

Tan, X. M., Zhou, J. B., Deng, X. F., Wang, H. Y., Hou, H. S., Li, H. L., et al. (2023). Crustal-scale seismic reflection profiling constrains how the paleo-Asian Ocean was closed. *Tectonics* 42 (9), e2023TC007921. doi:10.1029/2023tc007921

Wang, T., Ma, G., Comeau, M. J., Becken, M., Zhou, Z., Liu, W., et al. (2022). Evidence for the superposition of tectonic systems in the northern Songliao Block, NE China, revealed by a 3-D electrical resistivity model. *J. Geophys. Res. Solid Earth* 127 (4), e2021JB022827. doi:10.1029/2021jb022827

Wannamaker, P. E., Hohmann, G. W., and Ward, S. H. (1984). Magnetotelluric responses of three-dimensional bodies in layered earths. *Geophysics* 49 (9), 1517–1533. doi:10.1190/1.1441777

Windley, B. F., Alexeiev, D., Xiao, W., Kro¨ner, A., and Badarch, G. (2007). Tectonic models for accretion of the central asian orogenic belt. *J. Geol. Soc.* 164 (1), 31–47. doi:10.1144/0016-76492006-022

Windley, B. F., and Xiao, W. (2018). Ridge subduction and slab windows in the Central Asian Orogenic Belt: tectonic implications for the evolution of an accretionary orogen. *Gondwana Res.* 61, 73–87. doi:10.1016/j.gr.2018.05.003

Xiao, W. (2023). *Altaids, continental growth and metallogeny*. Oxford University Press.

Xiao, W., Han, C., Liu, W., Wan, B., Zhang, J. e., Ao, S., et al. (2014). How many sutures in the southern Central Asian orogenic belt: insights from east Xinjiang–west Gansu (NW China)? *Geosci. Front.* 5 (4), 525–536. doi:10.1016/j.gsf.2014.04.002

Xiao, W., Song, D., Windley, B. F., Li, J., Han, C., Wan, B., et al. (2019). Research progresses of the accretionary processes and metallogenesis of the central asian orogenic belt. *Sci. China Earth Sci.* 49 (10), 1512–1545. doi:10.1360/SSTe-2019-0133

Xiao, W., Windley, B. F., Han, C., Liu, W., Wan, B., Zhang, J. e., et al. (2018). Late Paleozoic to early Triassic multiple roll-back and oroclinal bending of the Mongolia collage in Central Asia. *Earth-Science Rev.* 186, 94–128. doi:10.1016/j.earscirev.2017.09.020

Xiao, W., Windley, B. F., Hao, J., and Zhai, M. (2003). Accretion leading to collision and the Permian Solonker suture, Inner Mongolia, China: termination of the central Asian orogenic belt. *Tectonics* 22 (6). doi:10.1029/2002tc001484

Xiao, W., Windley, B. F., Sun, S., Li, J., Huang, B., Han, C., et al. (2015). A tale of amalgamation of three Permo-Triassic collage systems in Central Asia: oroclines, sutures, and terminal accretion. *Annu. Rev. earth Planet. Sci.* 43 (1), 477–507. doi:10.1146/annurev-earth-060614-105254

Xu, Y., Yang, B., Zhang, A., Wu, S., Zhu, L., Yang, Y., et al. (2020). Magnetotelluric imaging of a fossil oceanic plate in northwestern Xinjiang, China. *Geology* 48 (4), 385–389. doi:10.1130/g47053.1

Xu, Y., Yang, B., Zhang, S., Liu, Y., Zhu, L., Huang, R., et al. (2016). Magnetotelluric imaging of a fossil paleozoic intraoceanic subduction zone in western Junggar, NW China. *J. Geophys. Res. Solid Earth* 121 (6), 4103–4117. doi:10.1002/2015jb012394

Xu, Y., Zhang, A., Yang, B., Bao, X., Wang, Q., Xia, J., et al. (2018). Bridging the connection between effective viscosity and electrical conductivity through water content in the upper mantle. *Sci. Rep.* 8 (1), 1771. doi:10.1038/s41598-018-20250-2

Yang, X. (2014). Electrical petrology: principles, methods and advances. *Sci. Sin. Terrae* 44, 1884–1990. doi:10.1360/zd-2014-44-9-1884

Ye, G., Unsworth, M., Wei, W., Jin, S., and Liu, Z. (2019). The lithospheric structure of the Solonker Suture Zone and adjacent areas: crustal anisotropy revealed by a high-resolution magnetotelluric study. *J. Geophys. Res. Solid Earth* 124 (2), 1142–1163. doi:10.1029/2018jb015719

Zhan, W., Pan, L., and Chen, X. (2020). A widespread mid-crustal low-velocity layer beneath Northeast China revealed by the multimodal inversion of Rayleigh waves from ambient seismic noise. *J. Asian Earth Sci.* 196, 104372. doi:10.1016/j.jseaes.2020.104372

Zhang, L. (2017). A review of recent developments in the study of regional lithospheric electrical structure of the Asian continent. *Surv. Geophys.* 38 (5), 1043–1096. doi:10.1007/s10712-017-9424-4

Zhang, S., Gao, R., Li, H., Hou, H., Wu, H., Li, Q., et al. (2014). Crustal structures revealed from a deep seismic reflection profile across the Solonker suture zone of the Central Asian Orogenic Belt, northern China: an integrated interpretation. *Tectonophysics* 612, 26–39. doi:10.1016/j.tecto.2013.11.035

Zhang, X., Pang, Z., Liu, J., Zhang, J., Teng, C., Cao, J., et al. (2020). Geochronological and geochemical features of the Xiaowulangou complex plutons, Xilinhot, Inner Mongolia, and their geological significance. *Geol. J.* 55 (3), 2269–2299. doi:10.1002/gj.3762

frontiers | Frontiers in Earth Science

TYPE Original Research
PUBLISHED 22 January 2025
DOI 10.3389/feart.2024.1527559

OPEN ACCESS

EDITED BY
Bo Yang,
Zhejiang University, China

REVIEWED BY
Nian Yu,
Chongqing University, China
Shan Xu,
China University of Geosciences
Wuhan, China

*CORRESPONDENCE
Xiaobin Chen,
cxb@pku.edu.cn

RECEIVED 13 November 2024
ACCEPTED 31 December 2024
PUBLISHED 22 January 2025

CITATION
Zhang Y, Chen X, Wang P, Cai J, Liu Z, Zhang J and Huang X (2025) Three-dimensional electrical structure in the northwestern sector of the Sichuan-Yunnan diamond block. *Front. Earth Sci.* 12:1527559. doi: 10.3389/feart.2024.1527559

Three-dimensional electrical structure in the northwestern sector of the Sichuan-Yunnan diamond block

Yunyun Zhang[1,2,3], Xiaobin Chen[1,2]*, Peijie Wang[4], Juntao Cai[1,2], Zhongyin Liu[1,2], Jiong Zhang[1,2] and Xingxing Huang[1,2]

[1]National Institute of Natural Hazards, Ministry of Emergency Management of China, Beijing, China, [2]Key Laboratory of Compound and Chained Natural Hazards Dynamics, Ministry of Emergency Management of China, Beijing, China, [3]School of Geophysics and Information Technology, China University of Geosciences, Beijing, China, [4]Department of Earth and Space Sciences, Southern University of Science and Technology, Shenzhen, China

The Sichuan-Yunnan diamond block is a significant region of material flow from the Tibetan Plateau. However, its northwest electrical boundary remains undefined. Our study conducted a magnetotelluric profile from Chazha to Luomai across the geological boundary of the Sichuan-Yunnan block in its northwest sector. Using the nonlinear conjugate gradient three-dimensional inversion method, we obtained the deep electrical structure across the northern part of the block. Our findings reveal distinct segmental characteristics in the electrical structure along the profile. Marked by a high-resistivity zone along the Dedeng-Batang-Riyu fault, two high-conductivity layers exist in the upper-middle crust of the southwestern and central sections of the profile, at depths of 5–20 km and 10–30 km, respectively. Thus, our study suggests that the northwest boundary of the Sichuan-Yunnan diamond block, contrary to previous studies that considered it a transitional boundary, is located at the Dedeng-Batang-Riyu fault. Here, the boundary is a high-resistivity barrier, electrically isolating the Qiangtang block in the southwest from the Sichuan-Yunnan block in the northeast. The two significant high-conductivity zones in the upper-middle crust appear within the block's interior, contrasting with previous assumptions of lower crustal flow.

KEYWORDS

magnetotelluric, Sichuan-Yunnan diamond block, three-dimensional inversion, electrical boundary, upper-middle crust

1 Introduction

The Sichuan-Yunnan diamond block is a crucial lateral outflow pathway for material from the present-day Tibetan Plateau. It plays a key role in, and serves as major supporting evidence for, the lower crustal flow dynamics model, which is applied in this area (Zhang et al., 2004; Shen et al., 2005; Bai et al., 2010). Due to lateral extrusion at the eastern margin of the Tibetan Plateau and strong resistance from the South China block, the Sichuan-Yunnan diamond block, located on the eastern margin of the Tibetan Plateau, has become the most complex and distinctive mobile block in

the plateau's eastward and southward expansion (Cui et al., 2006). This block has a unique geological structure, with varying fault orientations, scales, and activities. It is highly seismically active, prone to frequent earthquake disasters, and provides a critical window for studying post-collisional tectonic deformation and evolution processes of continental plates. Therefore, research on the deep structure of the Sichuan-Yunnan block holds theoretical importance. Geologically, the block is bounded by major active faults: the nearly NS Jinshajiang fault zone (western boundary), the NW-SE Ganzi-Yushu-Xianshuihe fault zone (northern boundary), the nearly NS Anninghe-Zemuhe-Xiaojiang fault zone (eastern boundary), and the NW-SE Red River fault zone (southern boundary) (Kan et al., 1977; Deng et al., 2002; Zhang et al., 2003; Shen et al., 2005; Xu et al., 2005). The Jinshajiang fault was previously an active suture structure, showing marked compressional characteristics (Xu et al., 1992). Influenced by eastward extrusion from the Tibetan Plateau, it has exhibited clear strike-slip motion, shifting from early left-lateral to right-lateral motion since the Pliocene (4.7 Ma) (Xu et al., 1992; Deng et al., 2002). Segmented by the NE-SW Batang fault and the NW-SE Zhongdian-Deqin fault, the Jinshajiang fault is divided into southern, central, and northern sections, with seismic activity gradually decreasing from south to north. The northern segment is the least active, with its main activity period in the early Quaternary; apart from local late Quaternary activity on the western branch, there is no geological evidence for significant fault activity since the late Pleistocene (Wu et al., 2019).

Typically, the material outflow from the Tibetan Plateau is explained by two main modes: middle-lower crustal flow and rigid extrusion. The first model proposes that material from the central plateau flows toward the eastern margin through a low-viscosity channel in the middle-lower crust. Extensive geophysical surveys indicate that low-velocity (Bao et al., 2015; Yang et al., 2020) and highly conductive partially molten material may be present along the southeastern margin of the plateau (Sun et al., 2003; Bai et al., 2010; Cheng et al., 2015). The second model suggests that the rigid lithosphere extrudes laterally along large strike-slip faults, with the middle-upper crust escaping outward from the plateau, driven by internal forces, while the lower crust impedes this escape process (Tapponnier et al., 1982; Tapponnier et al., 2001).

Previous studies on the diamond block boundaries have focused on crustal deformation (Lv et al., 2002), surface strain accumulation characteristics (Liu et al., 2022a; Zheng et al., 2017), and stress field features (Guo et al., 2024), primarily using geophysical methods such as seismology and geodesy. Due to the seismic activity along the Xianshuihe fault, the eastern boundary of the diamond block has long been a hot research area. However, studies on the deep electrical structure and dynamics of the Sichuan-Yunnan diamond block have mainly concentrated around and south of the Red River fault, the Anninghe-Zemuhe-Xiaojiang fault, and the Lijiang-Xiaojinhe fault (Yu et al., 2020; Li et al., 2020), with limited research on the northern area, resulting in a lack of comprehensive understanding of the region. To investigate the deep distribution range of material flow along the eastern margin of the Tibetan Plateau and delineate the electrical boundary of the Sichuan-Yunnan diamond block, we conducted a magnetotelluric survey across the geological boundary of the block in its northwest sector. This profile extends from Chazha Township, Sichuan Province, to Luomai Township, Tibet Autonomous Region.

2 Survey region

There are primarily northwest-oriented structures in Sichuan-Yunnan block. In this study, the survey profile originates in the southern part of the Bayan Har block (BHB), cuts southwest across the northwest sector of the Sichuan-Yunnan block (SYB), and reaches the western part of the Qiangtang block (QTB). The northeastern end of the line is located at Chazha Township (C) in Ganzi County, Sichuan Province, and extends to Luomai Township (M) in Gongjue County, Tibet Autonomous Region, with a total length of approximately 220 km at an angle of 30° northeast. There are 17 survey points in total. The survey line successively crosses the Ganzi-Litang fault (GL), the Dalangsonggou fault (DLSG), the Maisu fault (MS), a branch of the Jinshajiang fault zone (JSJ), the Dedeng-Batang-Riyu fault (DBR), another branch of the Jinshajiang fault zone, and the Zigasi-Deqin fault (ZD) (Figure 1).

3 Data and qualitative analysis

3.1 Field data collection and processing

Data for this study was collected in October 2020 using the MTU-5A magnetotelluric acquisition system from Phoenix Geophysical, Canada. The data acquisition involved a five-component setup (two orthogonal horizontal electric fields, two orthogonal horizontal magnetic fields, and one vertical magnetic field), with horizontal components aligned along the true north-south and east-west directions. A broad frequency band was used for MT observations: high frequency at 2,400 Hz, mid-frequency at 150 Hz, and low frequency at 15 Hz. To ensure data quality, a remote reference station was set up 1,050 km away in Otog Front Banner, Inner Mongolia Autonomous Region (107°49′40.31″N, 38°1′27.33″E), which offered an ideal electromagnetic environment with minimal human interference. Each site collected data for over 40 h and applied remote reference techniques (Gamble et al., 1979b; Gamble et al., 1979a) and non-Robust techniques (Zhang et al., 2022) for time series processing. The apparent resistivity and phase curves for each site were generally smooth, indicating high data quality, with most sites covering an effective period range of 1/320 s–2000 s, specially, CM06, CM08, and CM17 had an effective period reaching nearly 10,000 s (Figure 2).

The apparent resistivity and impedance phase curves for each site preliminarily reveal differences in the electrical structure within the three distinct tectonic units: the southern edge of the Bayan Har block, the northwest sector of the Sichuan-Yunnan diamond block, and the western margin of the Qiangtang block. As shown in Figure 2, site CM01, located within the Bayan Har block, exhibits overlapping apparent resistivity curves in both polarization directions at high frequencies, with minimal variation. From mid to low frequencies, the apparent resistivity curves diverge and cross again, indicating a simple shallow structure and a more complex deep structure. Sites CM02 to CM04, located in the contact zone between the Bayan Har block and the Sichuan-Yunnan diamond block, display out of quadrant phases phenomena at low frequencies. Specifically, CM02 and CM03 exhibit quadrant-exceeding phases in the xy polarization, while CM04 exhibits this phenomenon in the yx polarization, suggesting that the

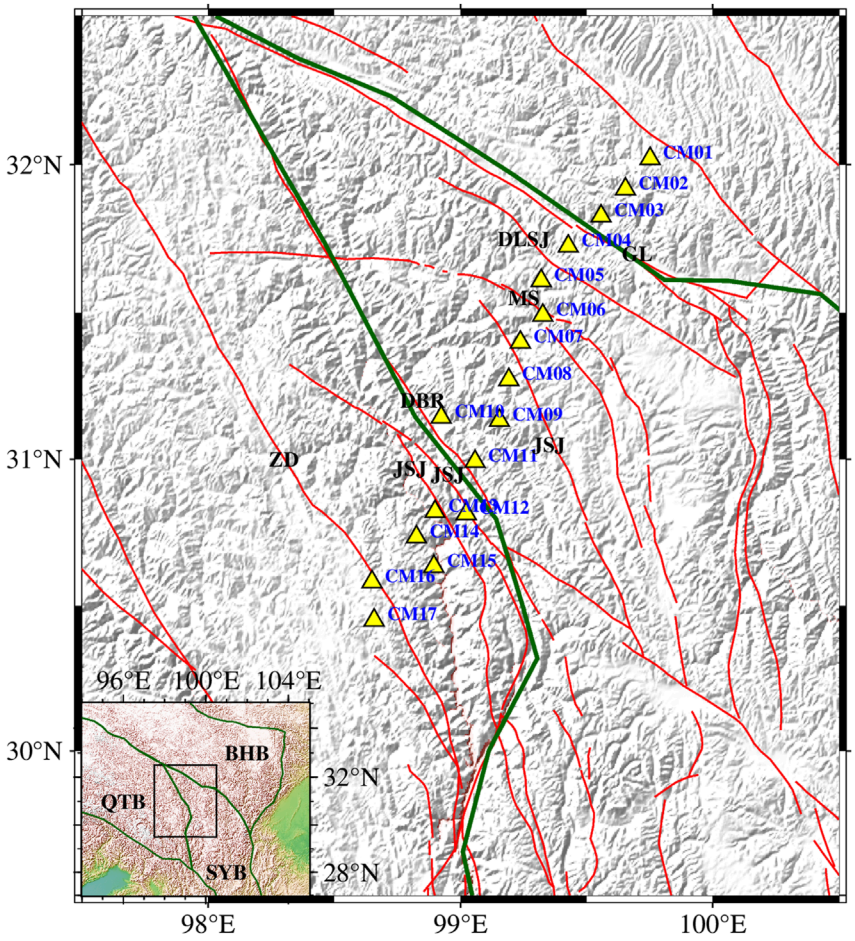

FIGURE 1
Locations of the magnetotelluric (MT)survey points. Yellow triangles represent the MT survey locations, with blue labels for point names, green lines marking block boundaries (Zhang et al., 2003), and red lines indicating active faults (Xu et al., 2016). ZD, Zigasi-Deqin Fault; JSJ, Jinshajiang Fault Zone; DBR, Dedeng-Batang-Riyu Fault; MS, Maisu Fault; DLSG, Dalangsonggou Fault; GL, Ganzi-Litang Fault Zone; BHB, Bayan Har block; QTB, Qiangtang block; SYB, Sichuan-Yunnan block.

Ganzi-Litang fault between CM03 and CM04 may serve as the boundary fault and that the deep contact relationship between these two blocks is complex. Other sites located between the Sichuan-Yunnan diamond block and the Qiangtang block exhibit high-frequency high-resistivity and low-frequency low-resistivity characteristics, though the specific curve shapes vary, indicating that the overall electrical structure of the Sichuan-Yunnan diamond block and the Qiangtang block consists of a shallow high-resistivity and a deep high-conductivity. The boundary between these blocks cannot be determined from the apparent resistivity curves alone, and details require inversion analysis.

3.2 Structural dimensionality analysis

Figure 3 illustrates the real tipper vector diagram of the CM profile, which is a new method for depicting the tipper vector orientation. The direction of the tipper's real vector aligns with the real induction vector, typically pointing from high resistivity to low resistivity. The size of the vector's tail indicates the size of the imaginary induction vector; however, the physical significance of this feature requires further investigation. The color-filled areas represent the arithmetic average of the two main phases (Pxy, Pyx), in general, a higher arithmetic average of the phase (closer to red) corresponds to low resistivity, and *vice versa* for high resistivity (closer to blue). From Figure 3, it can be seen that low resistivity is present beneath points CM17, CM14-CM12, and CM10-CM08. Most of the faults in the survey area strike NW, and the profile is oriented to the NE. The real induction vector points in different directions, and some are opposite to one another. Therefore, 2D inversion is not applicable for this profile.

The impedance tensor decomposition double rhombus diagram is a new analytical technique for constructing dimensionality analysis. In Figure 4, the rhombus is defined by the 1D deviation, 2D deviation, and the orientation of the best principal axis. The 1D deviation is represented by the long axis of the rhombus, the 2D deviation by the short axis, and the orientation of the best principal axis is the same as that of the long axis. Due to a 90° ambiguity in the orientation of the best principal axis, an orthogonal double rhombus is used to eliminate this ambiguity. A small

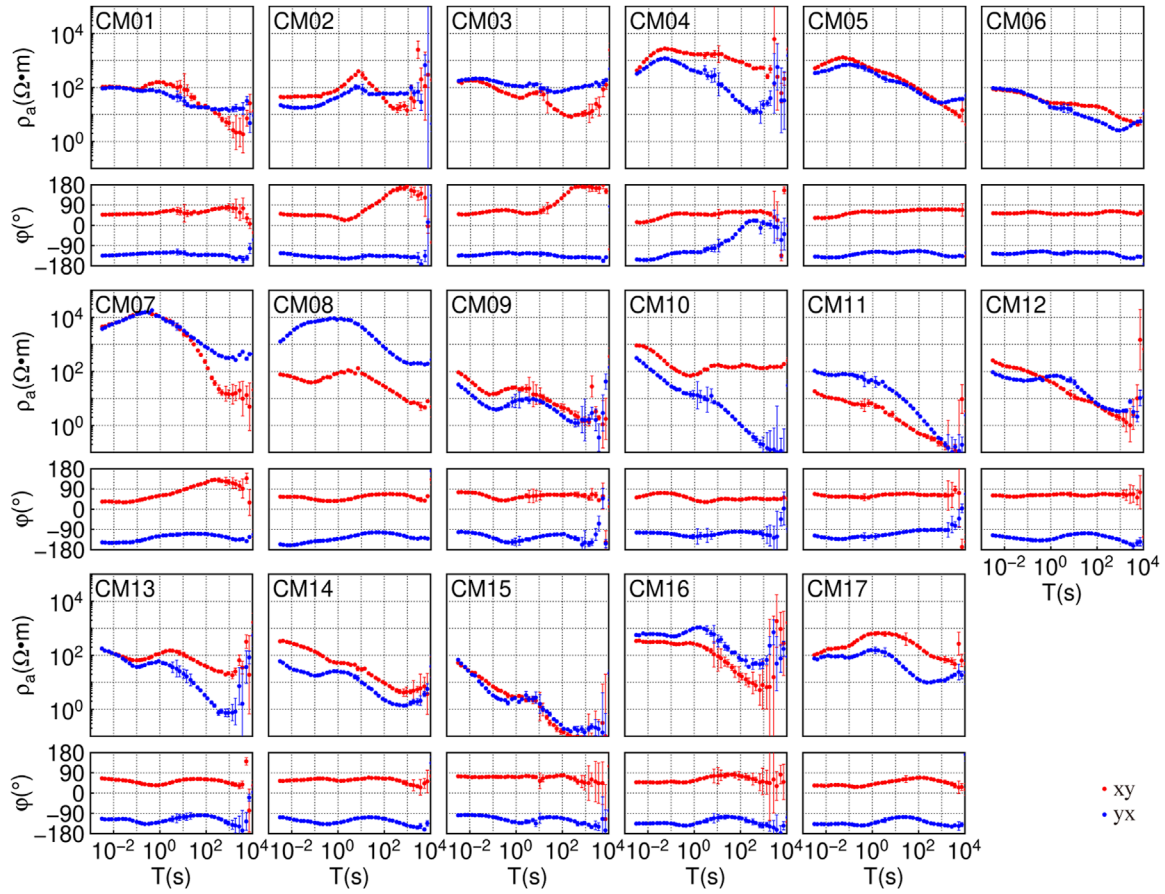

FIGURE 2
Apparent resistivity and impedance phase curves.

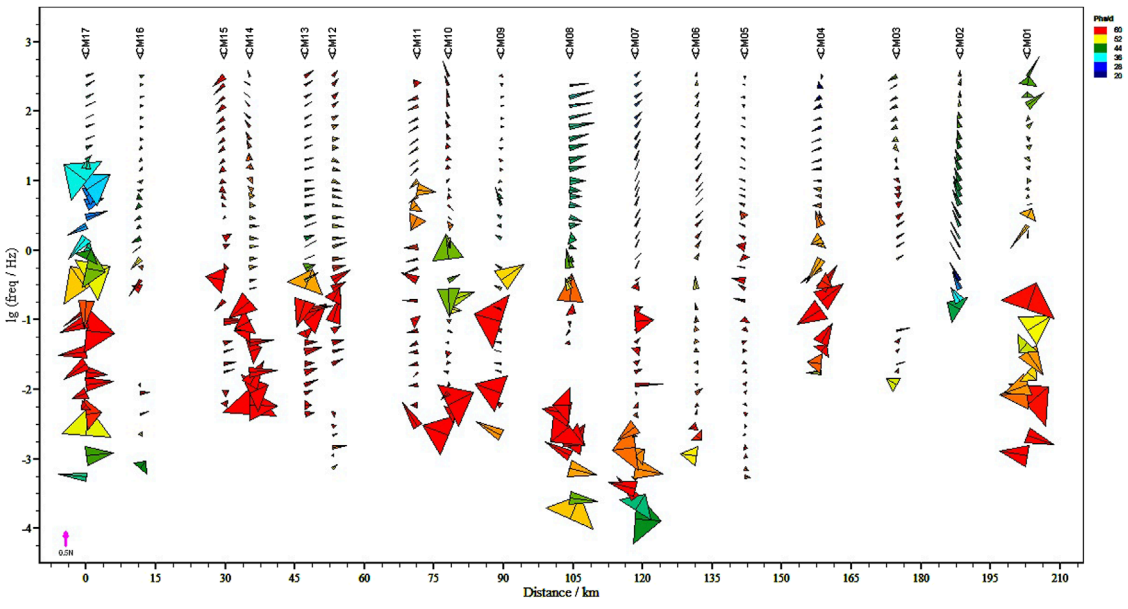

FIGURE 3
Tipper vector paper airplane diagram. The vector direction corresponds to the real induction vector, and the opening size of the tail represents the magnitude of the imaginary induction vector. The color filling indicates the arithmetic average of the main phase values.

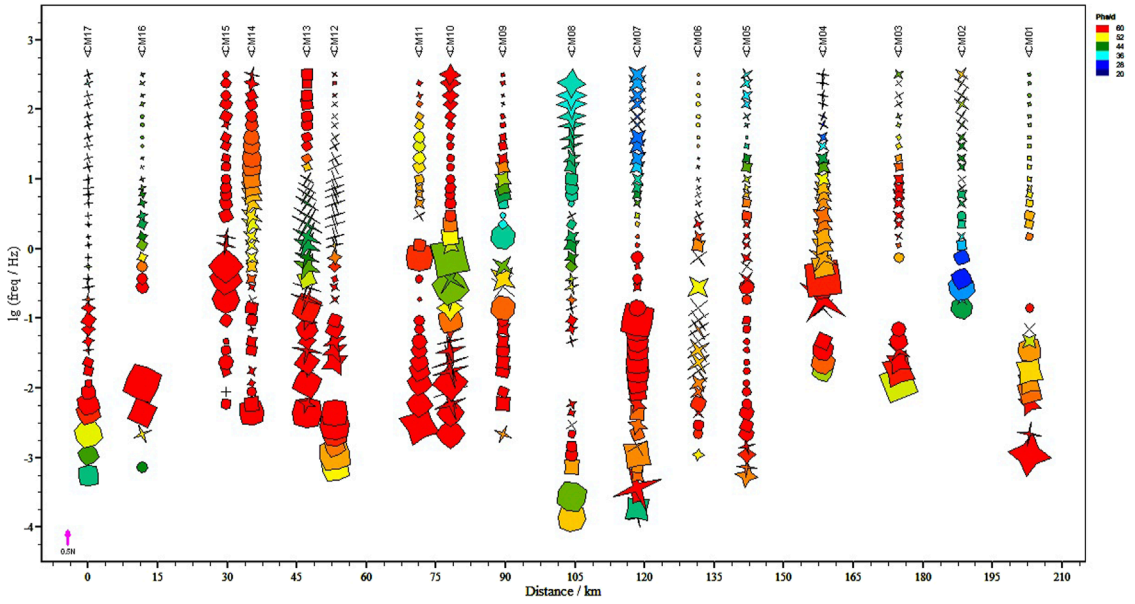

FIGURE 4
The impedance tensor decomposition double rhombus diagram. The long axis of the rhombus represents the one-dimensional deviation, the short axis represents the two-dimensional deviation, and the color filling is consistent with that in Figure 3.

double rhombus indicates strong one-dimensionality, while a large double rhombus approaching a cross shape indicates strong two-dimensionality. A large double rhombus nearing a circular shape suggests strong three-dimensionality. The color filling follows the same pattern as in Figure 3. From the diagram, it is observed that the shallow area are dominated by 1D and 2D structures, while the 3D structure is generally enhanced in the low-frequency range. In the northeastern part of the study area, specifically at the measurement points (CM01-CM06) located at the northern section of the Baren Kalla Block and the northwest sector of the Sichuan-Yunnan Diamond Block, the shallow area are mainly one-dimensional and two-dimensional, while the deep area show enhanced three-dimensionality, indicating differences between the shallow and deep area. At the measurement points CM07-CM15, the low-frequency part remains dominated by three-dimensionality, while the medium and high frequencies exhibit alternating complex features of three-dimensional and non-three-dimensional characteristics between adjacent measurement points.

By analyzing the apparent resistivity phase curves and structural dimensionality, qualitative information about the dimensionality and electrical distribution of deep structures can be obtained. More accurate quantitative information about the deep electrical structure requires inversion. The data we collected are from survey profile, where the faults and blocks intersect near-perpendicular to the survey profile. In most cases, 2D inversion would suffice; however, the data analysis above indicates that this survey profile is not suitable for 2D inversion. The main reasons are as follows: The deep structure exhibit pervasive three-dimensionality. Performing a 2D inversion with a unified principal axis orientation could introduce false structures, particularly when including the TE polarization mode, which would significantly distort the results from the true model (Cai et al., 2010). The survey profile has only 17 measurement points, and there is poor continuity in the electrical principal axes between adjacent points. Additionally, there is no consistent principal axis direction between high and low frequencies at the same point, making frequency-band or segment-based two-dimensional inversion unsuitable (Guo and Chen, 2018). CM02, CM03, CM04, and CM07 all exhibit phase over-quadrant phenomena, which typically occur in three-dimensional or anisotropic two-dimensional media. Conventional isotropic two-dimensional inversion cannot fit phase over-quadrant data (Lezaeta and Haak, 2003). Both theoretical model testing (Siripunvaraporn et al., 2005) and inversion of field data (Jiang et al., 2019) have demonstrated that 3D inversion of single-profile data can resolve local fault structures and even provide clearer deep information than 2D inversion. Therefore, this study selects 3D inversion techniques, more suited to the observed data characteristics, for subsequent inversion work.

4 Three-dimensional inversion

Traditional inversion grids generally align with the data observation direction, and there is no need to consider data rotation during the inversion process. However, for datasets like the one in this study, where the survey line direction (not oriented exactly north-south) differs from the observation direction (true north-south), conventional grid subdivision methods may result in grid cells in the two corners of missing measurement points, where the data do not constrain the model. These regions are not part of the target area and contribute to unnecessary computational resource waste. While rotating the grid or survey line to match the observation direction can avoid grid waste, it still presents the issue of misalignment between grid and observation directions. Previous

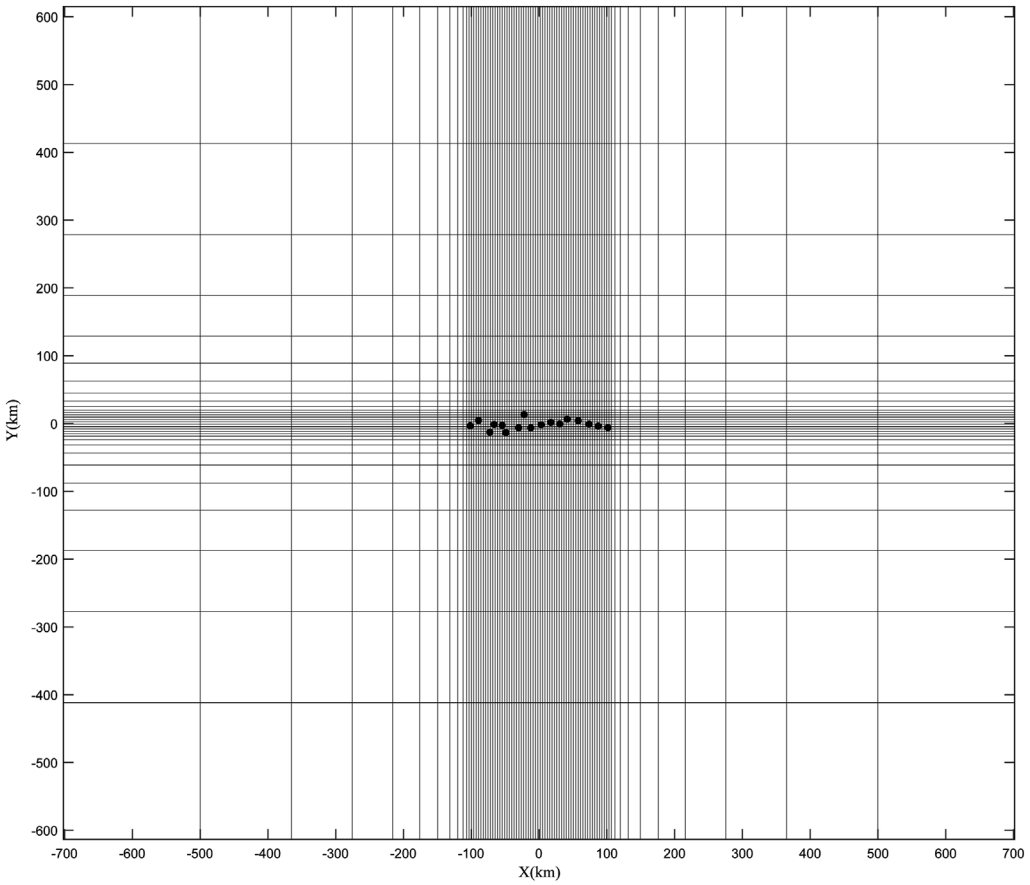

FIGURE 5
Plan view of the 3D inversion grid. From left to right are sites 17 to 1.

methods involve rotating the observed data to align with the grid direction before inversion. However, rotating the observed data carries certain risks, as the rotated data may degrade. This study adopts a new approach of rotating the model response to match the observation data (Liu et al., 2024). After each forward modeling step, the result is rotated to match the direction of the observation data, ensuring high-quality grid subdivision while also optimizing the fitting of high-quality data in the observation direction.

In the horizontal direction, the core region grid size is 3.5 km × 3.5 km, with 59 grids along the survey profile direction and 9 grids in the perpendicular direction. Outside the core region, both directions extend by a factor of 1.5 for 11 additional grids, with the maximum grid size reaching 200 km × 200 km. The terrain in the study area is highly variable, with height differences between measurement points reaching up to 0.5 km. To adequately fit the terrain, the vertical terrain grid is set at 50 m with 12 layers. The terrain grid for the core region is constructed based on actual terrain data, while the terrain for the non-core region is extended parallelly outward from the core region boundary. Below the terrain grid, the grid thickness increases gradually by a certain factor, extending downward, with a maximum grid thickness of 50 km. The final model grid size is 31 × 81 × 80 (Figure 5).

We choose apparent resistivity and phase data (RP) for inversion, rather than the full impedance data (Z4) or full impedance dipoles (ZT) commonly used in previous studies. Newman et al. found that because the xx and yy element data have lower baselines and signal-to-noise ratios, using full impedance data combinations for inversion can reduce inversion performance (Newman et al., 2008). Current understanding of the characteristics of the main diagonal elements of impedance, is still unclear, and the criteria for evaluating data quality are vague. Compared to full impedance or full impedance tipper data, apparent resistivity and phase data are more stable in quality, with clearer criteria for selecting data for inversion. Increasingly, scholars have chosen to use resistivity and phase data for inversion (Cai et al., 2017; Fan et al., 2022; Cai et al., 2023; Cui et al., 2024).

The inversion calculations are performed in the visualization-based 3D magnetotelluric inversion software system ToPeak (Liu et al., 2022b). Initially, a model with a resistivity of 100 Ω·m is constructed, incorporating topographic data, with an initial regularization factor of 1,000. During the inversion process, when the relative change in the root mean square error (RMS) of the fit falls below 0.25%, the regularization factor is reduced by a factor of 0.2. The inversion stops when the regularization factor is less than 10^{-8}. The initial inversion is exited after 78 iterations, and the RMS is 3.4. Following this, the model undergoes a "fill-hole and peak-cutting" reconstruction, limiting areas of excessively high or low resistivity within a certain range. Specifically, the contours of

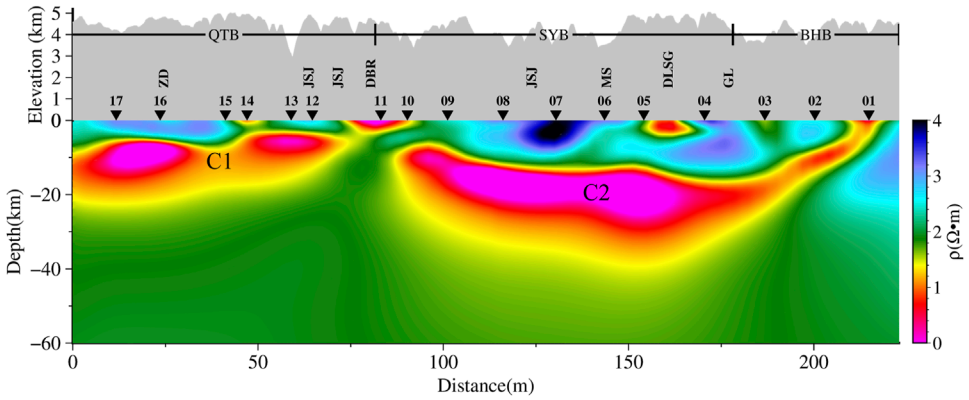

FIGURE 6
The vertical profile of the inversion results.

anomalous resistivity regions from the previous inversion results are retained. The extreme resistivity values in these anomalous regions are replaced with the surrounding resistivity values to construct a new initial model for the subsequent inversion. By doing so, the new initial model based on the existing inversion results avoids focusing excessively on local details, thereby reducing the risk of overfitting. This reconstructed model then serves as the starting model for further inversion, improving the reliability and stability of the results. After several reconstruction iterations, the final inversion consists of 212 iterations with an RMS of 0.729.

5 Result and verification

5.1 Inversion result

The vertical profile of the inversion results is shown in Figure 6. Large-scale high-conductivity bodies, C1 and C2, are present in the middle to upper crust within the Qiangtang Block and the Sichuan-Yunnan diamond block. C1 is located at depths of approximately 5 km–20 km and extends laterally for about 70 km. It has a generally eastward-low and westward-high configuration, with a weak zone beneathCM15. C2 is located at depths of approximately 10 km–30 km and extends over 100 km laterally in a "spoon" shape, with the "handle" being narrow and extending from CM01 to the surface. Above these high-conductivity bodies, there is significant electrical heterogeneity, and the regions above the high-conductivity bodies are consistent with data qualitative analysis. Below the high-conductivity bodies, there is a homogeneous half-space with a resistivity close to 100 Ω·m, consistent with the initial model's resistivity.

5.2 Verification

To assess the reliability of the inversion results and determine whether the observation data can constrain the structure beneath the high-conductivity bodies, we performed a forward modeling verification. First, we validated the high-conductivity bodies C1 and C2 by erasing the high-conductivity parts of C1 and C2 and replacing them with 20 Ω·m. The corrected model was then used for forward modeling calculations (Figures 7A, B), and the RMS was recalculated (Figure 7F). From the figure, it is clear that the RMS of the measurement points above the corrected model increases significantly, indicating that the high-conductivity bodies are constrained by the data, thus confirming the existence of the high-conductivity bodies as reliable.

Next, we verified whether the bottom boundary of the C2 structure is constrained by the data. Typically, the resolution below high-conductivity bodies is lower. We extended the C2 high-conductivity body downward by 10 km (Figure 7C) and performed forward modeling with the modified model, recalculating the RMS to obtain Figure 7F. Subsequently, we extended the high-resistivity region beneath C2 upward by 10 km (Figure 7D) and recalculated the RMS (Figure 7F). It can be observed that the RMS values above the modified model increase, which suggests that the bottom boundary of the high-conductivity body is constrained by the data, confirming the reliability of the high-conductivity layer's thickness.

Finally, we verified the connectivity between the two high-conductivity bodies, C1 and C2. Again, we filled the area between them with 10 Ω·m grids (Figure 7E), and the calculated RMS is shown in Figure 7F. It is evident that the RMS of the measurement points above and around the modified model increases significantly, proving that the high-conductivity bodies C1 and C2 are not connected.

6 Discussion

We believe that the boundary region between high-conductivity bodies C1 and C2 is the northwest electrical boundary of the Sichuan-Yunnan Diamond Block, located at the Dedeng-Batang-Riyu fault. The thickness of C1 is approximately 15 km, and C2 is about 20 km, which differs from the findings of Bai et al. (2010). Bai et al. suggested that there is a lower crustal material flow in the eastern Tibetan Plateau and provided MT evidence for plateau uplift and crustal deformation. Through theoretical calculations,

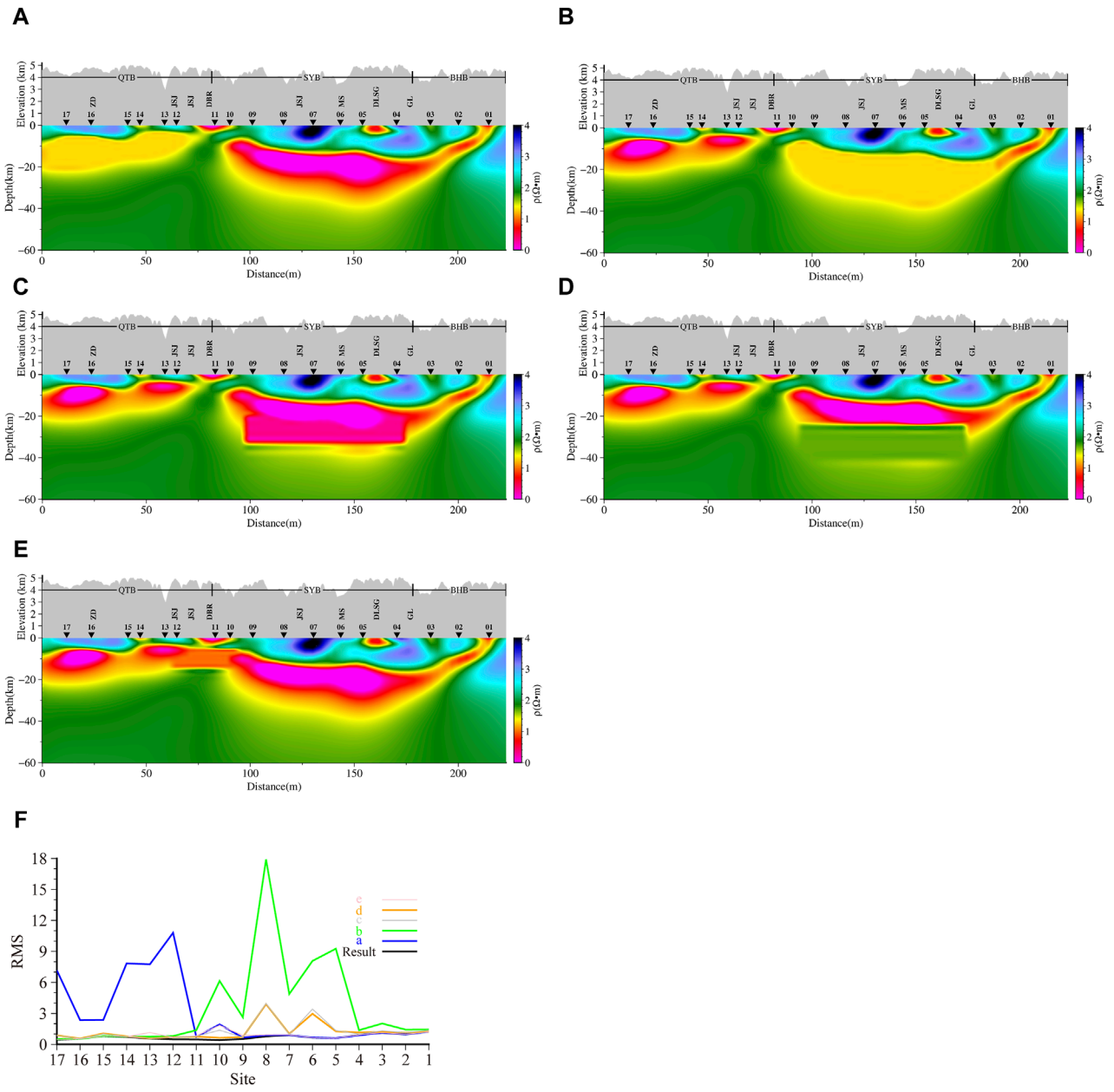

FIGURE 7
Reliability verification of inversion results. **(A)** C1, **(B)** C2, **(C)** downward extension of C2, **(D)** upward extension of high-resistivity body below C2, **(E)** C1&C2 connectivity, **(F)** abcde model RMS.

they proposed two weak material flows in the middle to lower crust: one extends eastward from the Lhasa block along the Yarlung Zangbo suture zone, turns south around the eastern Himalayas, and eventually passes through the Tengchong volcanic area; the other extends eastward from the Qiangtang block along the Jinshajiang fault Zone and the Xianshuihe fault zone, turns south at the western edge of the Sichuan Basin, and finally passes through the Sichuan-Yunnan diamond block between the Xiaojiang fault and the Honghe fault (Bai et al., 2010). Due to the limitations of MT inversion techniques at the time, previous studies only employed 2D inversion techniques, but 2D inversion has limited ability to identify the lower boundary of high-conductivity bodies. In contrast, modern 3D inversion techniques have significantly improved the vertical resolution of MT inversion. The 3D inversion results indicate that there is a high-conductivity layer within the Sichuan-Yunnan diamond block, with a thickness of only 20 km, which is insufficient to drive material outflow. This high-conductivity layer acts as a decoupling surface, a view consistent with the rigid material extrusion model (Tapponnier et al., 2001). As the upper-middle crust escapes toward the exterior of the plateau, the driving force originates from within the plateau itself, and the weak material flow is not the source of force. We speculate that the weak material layer is merely a "transition surface" where the upper and lower crust move in opposite directions.

7 Conclusion

Based on the MT profile data from the northwest sector of the Sichuan-Yunnan diamond block, a nonlinear conjugate gradient-based 3D inversion with terrain was performed. We conclude that the northwest electrical boundary of the Sichuan-Yunnan block is Dedeng-Batang-Riyu fault. There is a high-conductivity layer within Sichuan-Yunnan block, but it is shallow and does not reach the lower crust. Future studies are hoped to expand MT work in the northwest region of the Sichuan-Yunnan block.

Data availability statement

The raw data supporting the conclusions of this article will be made available by the authors, without undue reservation.

Author contributions

YZ: Data curation, Investigation, Validation, Visualization, Writing–original draft, Writing–review and editing. XC: Funding acquisition, Investigation, Methodology, Resources, Software, Supervision, Validation, Writing–review and editing. PW: Investigation, Writing–review and editing. JC: Writing–review and editing. ZL: Software, Writing–review and editing. JZ: Writing–review and editing. XH: Writing–review and editing.

Funding

The author(s) declare that financial support was received for the research, authorship, and/or publication of this article. This work is supported by the National Natural Science Foundation of China (42174093), the Fundamental Scientific Research Project of National Institute of Natural Hazards, Ministry of Emergency Management of China (ZDJ2019-26), and the Fundamental Scientific Research Project of National Institute of Natural Hazards, Ministry of Emergency Management of China (ZDJ2020-13).

Acknowledgments

We would like to thank Dr. Xingbing Xie, Dr. Yurong Mao and Dr. Lei Zhou and others who helped with the MT data acquisition in the field.

Conflict of interest

The authors declare that the research was conducted in the absence of any commercial or financial relationships that could be construed as a potential conflict of interest.

Generative AI statement

The author(s) declare that Generative AI was used in the creation of this manuscript. Optimized English expression.

Publisher's note

References

Bai, D., Unsworth, M. J., Meju, M. A., Ma, X., Teng, J., Kong, X., et al. (2010). Crustal deformation of the eastern Tibetan plateau revealed by magnetotelluric imaging. *Nat. Geosci.* 3, 358–362. doi:10.1038/ngeo830

Bao, X. W., Sun, X. X., Xu, M. J., Eaton, D. W., Song, X. D., Wang, L. S., et al. (2015). Two crustal low-velocity channels beneath SE Tibet revealed by joint inversion of Rayleigh wave dispersion and receiver functions. *Earth Planet. Sci. Lett.* 415, 16–24. doi:10.1016/j.epsl.2015.01.020

Cai, J. T., Chen, X. B., and Zhao, G. Z. (2010). Refined techniques for data processing and two-dimensional inversion in magnetotelluric I: tensor decomposition and dimensionality analysis. *Chin. J. Geophys.* 53, 2516–2526. doi:10.3969/j.issn.0001-5733.2010.10.025

Cai, J., Chen, X., Dong, Z., Zhan, Y., Liu, Z., Cui, T., et al. (2023). Three-dimensional electrical structure beneath the epicenter zone and seismogenic setting of the 1976 Ms7.8 tangshan earthquake, China. *Geophys. Res. Lett.* 50, e2022GL102291. doi:10.1029/2022gl102291

Cai, J., Chen, X., Xu, X., Tang, J., Wang, L., Guo, C., et al. (2017). Rupture mechanism and seismotectonics of the $_s$6.5 Ludian earthquake inferred from three-dimensional magnetotelluric imaging. *Geophys. Res. Lett.* 44, 1275–1285. doi:10.1002/2016gl071855

Cheng, Y., Tang, J., Chen, X., Dong, Z., Xiao, Q., and Wang, L. (2015). Electrical structure and seismogenic environment along the border region of Yunnan, Sichuan and Guizhou in the south of the North-South seismic belt. *Chin. J. Geophys.* 58, 3965–3981. doi:10.6038/cjg20151107

Cui, T. F., Chen, X. B., Fan, Y., Liu, Z. Y., and Li, W. Q. (2024). Branched crustal flow and its dynamic significance in sanjiang area, eastern Tibetan plateau–insights from 3-D magnetotelluric imaging. *J. Geophys. Research-Solid Earth* 129, 16. doi:10.1029/2024jb028678

Cui, X. F., Xie, F. R., and Zhang, H. Y. (2006). Division of modern tectonic stress fields and their dynamic significance in the Sichuan-Yunnan region. *Acta Seismol. Sin.* 28, 451–461. doi:10.3321/j.issn:0253-3782.2006.05.001

Deng, Q., Zhang, P., Ran, Y., Yang, X., Min, W., and Chu, Q. (2002). Basic characteristics of activity structure in China. *Sci. China Ser. D-Earth Sci.* 32, 1020–1031. doi:10.3969/j.issn.1674-7240.2002.12.007

Fan, Y., Chen, X. B., Tang, J., Cui, T. F., Sun, X. Y., Wang, P. J., et al. (2022). Three-dimensional modelling of magnetotelluric data from the hefei-suqian segment of the tanlu Fault Zone, eastern China. *Chin. J. Geophys.* 65, 1336–1353. doi:10.6038/cjg2022P0682

Gamble, T. D., Goubau, W. M., and Clarke, J. (1979a). Error analysis for remote reference magnetotellurics. *Geophysics* 44, 959–968. doi:10.1190/1.1440988

Gamble, T. D., Goubau, W. M., and Clarke, J. (1979b). Magnetotellurics with a remote magnetic reference. *Geophysics* 44, 53–68. doi:10.1190/1.1440923

Guo, C. L., and Chen, X. B. (2018). Refined processing and two-dimensional inversion of Magnetotelluric (MT) data(VI) Two-dimensional magnetotelluric inversion based on the staggered model. *Chin. J. Geophys.* 61, 2548–2559. doi:10.6038/cjg2018K0244

Guo, X., Fang, L., Han, L., Li, C., and Su, S. (2024). Characteristics of focal mechanism and stress field in the eastern boundary of the Sichuan-Yunnan block. *Seismol. Geol.* 46, 371–396. doi:10.3969/j.issn.0253-4967.2024.02.008

Jiang, F., Chen, X., Dong, Z., Cui, T., Liu, Z., and Wang, P. (2019). Applying 3D inversion of single-profile magnetotelluric data to identify the Shade and Yunongxi faults. *Seismol. Geol.* 41, 1444–1463. doi:10.3969/j.issn.0253-4967.2019.06.009

Kan, R., Zhang, S., Yan, F., and Yu, L. (1977). Present tectonic stress field and its relation to the characteristics of recent tectonic activity in southwestern china. *Chin. J. Geophys.* 20, 96–109.

Lezaeta, P., and Haak, V. (2003). Beyond magnetotelluric decomposition: induction, current channeling, and magnetotelluric phases over 90°. *J. Geophys. Research-Solid Earth*, 108. doi:10.1029/2001jb000990

Liu, Z. Y., Kelbert, A., and Chen, X. B. (2024). 3D magnetotelluric inversion with arbitrary data orientation angles. *Comput. and Geosciences* 188, 105596. doi:10.1016/j.cageo.2024.105596

Liu, X., Zhang, F., Ma, L., and Li, L. (2022a). Current strain accumulation characteristics and the risk of strong earthquakes on the eastern boundary of the Sichuan-Yunnan Block. *J. Geodesy Geodyn.* 42, 687–693. doi:10.14075/j.jgg.2022.07.005

Liu, Z., Chen, X., Cai, J., Cui, T., Zhao, G., Tang, J., et al. (2022b). The design and application of topeak: a threedimensional magnetotelluric inversion cloud computing system. *Seismol. Geol.* 44, 802–820.

Li, X., Ma, X. B., Chen, Y., Xue, S., Varentsov, I. M., and Bai, D. H. (2020). A plume-modified lithospheric barrier to the southeastward flow of partially molten Tibetan crust inferred from magnetotelluric data. *Earth Planet. Sci. Lett.* 548, 116493. doi:10.1016/j.epsl.2020.116493

Lv, Y., Liao, H., Su, Q., and Wang, L. (2002). The recent crustal deformation in Sichuan-Yunnan Rhombic block boundary. *Earthq. Res. China* 18, 28–37. doi:10.3969/j.issn.1001-4683.2002.01.003

Newman, G. A., Gasperikova, E., Hoversten, G. M., and Wannamaker, P. E. (2008). Three-dimensional magnetotelluric characterization of the Coso geothermal field. *Geothermics* 37, 369–399. doi:10.1016/j.geothermics.2008.02.006

Shen, Z. K., Lü, J. N., Wang, M., and BüRGMANN, R. (2005). Contemporary crustal deformation around the southeast borderland of the Tibetan Plateau -: art. no. B11409. *J. Geophys. Research-Solid Earth* 110. doi:10.1029/2004jb003421

Siripunvaraporn, W., Egbert, G., Lenbury, Y., and Uyeshima, M. (2005). Three-dimensional magnetotelluric inversion: data-space method. *Phys. Earth Planet. Interiors* 150, 3–14. doi:10.1016/j.pepi.2004.08.023

Sun, J., Jin, G., Bai, D., and Wang, L. (2003). Sounding of electrical structure of the crust and upper mantle along the eastern border of Qinghai-Tibet Plateau and its tectonic significance. *Sci. China Ser. D Earth Sci.* 46, 243–253. doi:10.1360/03dz0019

Tapponnier, P., Peltzer, G., Ledain, A. Y., Armijo, R., and Cobbold, P. (1982). Propagating extrusion tectonics in asia - new insights from simple experiments with plasticine. *Geology* 10, 611–616. doi:10.1130/0091-7613(1982)10<611:petian>2.0.co;2

Tapponnier, P., Xu, Z., Roger, F., Meyer, B., Arnaud, N., Wittlinger, G., et al. (2001). Oblique stepwise rise and growth of the Tibet plateau. *Science* 294, 1671–1677. doi:10.1126/science.105978

Wu, F., Jiang, L., Zhang, G., and Wang, D. (2019). Discussion on quaternary activity characteristics of northern section of Jinshajiang Fault Zone along sichuan-tibet railway. *High. Speed Railw. Technol.* 10, 23–28. doi:10.12098/j.issn.1674-8247.2019.04.005

Xu, X., Han, Z., Yang, X., Zhang, S., Yu, G., Zhou, B., et al. (2016). *Seismotectonic map in China and its adjacent regions*. Beijing: Seismological Press.

Xu, X., Zhang, P., Wen, X., Qin, Z., Chen, G., and Zhu, A. (2005). Features of active tectonics and recurrence behaviors of strong earthquakes in the western Sichuan province and its adjacent regions. *Seismol. Geol.* 27, 446–461. doi:10.3969/j.issn.0253-4967.2005.03.010

Xu, Z., Hou, L., Wang, Z., Fu, X., and Wang, D. (1992). *Orogenic process of the Songpan-Ganzi orogenic belt in China*. Beijing: Geology Press.

Yang, Y., Yao, H. J., Wu, H. X., Zhang, P., and Wang, M. M. (2020). A new crustal shear-velocity model in Southwest China from joint seismological inversion and its implications for regional crustal dynamics. *Geophys. J. Int.* 220, 1379–1393. doi:10.1093/gji/ggz514

Yu, N., Unsworth, M., Wang, X., Li, D., Wang, E., Li, R., et al. (2020). New insights into crustal and mantle flow beneath the Red River fault zone and adjacent areas on the southern margin of the Tibetan plateau revealed by a 3-D magnetotelluric study. *J. Geophys. Res. Solid Earth* 125. doi:10.1029/2020jb019396

Zhang, P. Z., Shen, Z., Wang, M., Gan, W. J., BüRGMANN, R., Molnar, P., et al. (2004). Continuous deformation of the Tibetan Plateau from global positioning system data. *Geology* 32, 809–812. doi:10.1130/g20554.1

Zhang, P., Deng, Q., Zhang, G., Ma, J., Gan, W., Min, W., et al. (2003). Strong seismic activity and active faults in mainland China. *Sci. China Ser. D-Earth Sci.* 33, 12–20.

Zhang, Y., Wang, P., Chen, X., Zhan, Y., Han, B., Wang, L., et al. (2022). Magnetotelluric time series processing in strong interference environment. *Seismol. Geol.* 44, 786–801. doi:10.3969/j.issn.0253-4967.2022.03.014

Zheng, G., Wang, H., Wright, T. J., Lou, Y. D., Zhang, R., Zhang, W. X., et al. (2017). Crustal deformation in the India-eurasia collision zone from 25Years of GPS measurements. *J. Geophys. Research-Solid Earth* 122, 9290–9312. doi:10.1002/2017jb014465

frontiers | Frontiers in Earth Science

TYPE Original Research
PUBLISHED 10 February 2025
DOI 10.3389/feart.2025.1527004

OPEN ACCESS

EDITED BY
Bo Yang,
Zhejiang University, China

REVIEWED BY
Angelo De Santis,
National Institute of Geophysics and Volcanology (INGV), Italy
Zeqiu Guo,
Sichuan University, China

*CORRESPONDENCE
Xiaobin Chen,
cxb@pku.edu.cn

RECEIVED 12 November 2024
ACCEPTED 13 January 2025
PUBLISHED 10 February 2025

CITATION
Zeng J, Chen X, Wang P, Liu Z and Cai J (2025) Reevaluating the necessity of static shift correction in magnetotelluric inversion. *Front. Earth Sci.* 13:1527004. doi: 10.3389/feart.2025.1527004

Reevaluating the necessity of static shift correction in magnetotelluric inversion

Jingzhong Zeng[1,2], Xiaobin Chen[1,2]*, Peijie Wang[3], Zhongyin Liu[1,2] and Juntao Cai[1,2]

[1]National Institute of Natural Hazards, Ministry of Emergency Management of China, Beijing, China, [2]Key Laboratory of Compound and Chained Natural Hazards Dynamics, Ministry of Emergency Management of China, Beijing, China, [3]Department of Earth and Space Sciences, Southern University of Science and Technology, Shenzhen, China

Magnetotelluric (MT) is a significant electromagnetic exploration method. However, due to uneven distribution of surface charges and other factors, static shift often affects observed data, reducing the accuracy of inversion and interpretation. Correcting static shift through data processing remains a challenging task. Based on the characteristic that static shift affects only apparent resistivity data without impacting phase data, this paper proposes an inversion strategy that avoids static shift correction. At sites affected by static shift, apparent resistivity data are excluded, and only phase data are used in the inversion. Synthetic and field data tests indicate that the reduced inclusion of apparent resistivity data has minimal impact on inversion results, and due to the exclusion of data influenced by static shift, the inversion accurately reflects deep anomalous structures. This demonstrates that by excluding apparent resistivity data and relying solely on phase data at static-shifted sites, accurate inversion results can be achieved without additional static shift correction.

KEYWORDS

magnetotellurics, inversion, apparent resistivity, impedance phase, static shift

1 Introduction

In the 1950s, Tikhonov and Cagniard independently developed a geophysical exploration technique that uses natural electromagnetic fields to probe subsurface electrical structures: the magnetotelluric (MT) method (Tikhonov, 1950; Cagniard, 1953). MT offers several advantages, including low cost, substantial exploration depth, and ease of field deployment. Consequently, MT has found widespread applications in earth sciences, mineral exploration, and engineering geological surveys (Cai et al., 2017; Jiang et al., 2022).

Static shift is a common source of data distortion in MT. Since MT sounding technology was first put into practical use, the static shift effect has been a persistent issue (Chave and Jones, 2012). Due to small shallow heterogeneities, surface charge accumulation generates an electric field that superimposes on the natural induction field. This frequency-independent interference results in a uniform scaling of the electric field signal across the entire frequency range. Consequently, the apparent resistivity curve shifts upward or downward on a log-log plot, while the phase curve remains unaffected (Sasaki, 2004).

Numerous methods have been developed to correct static shift, including the reference station method (Jiracek, 1990; Wang, 1992; Duan, 1994), spatial filtering methods (Bostick, 1986; Luo et al., 1991; Guo et al., 2022), and phase correction methods (Beamish and Travassos, 1992; Yang et al., 2001; Qiu et al., 2012). However, some of these approaches

fail to fully correct static shift, while others introduce new challenges, such as increased costs and procedural complexity. As a result, static shift correction remains a complex and labor-intensive process in MT, often requiring considerable time and effort with limited effectiveness.

The impact of static shift on MT data remains an unresolved challenge. To address this issue, we conducted a detailed study as presented below. After analyzing several mainstream static shift correction methods and examining the characteristics of static shift's influence on MT data, we found that static shift primarily affects the apparent resistivity curves at a limited number of measurement sites. Based on this observation, we proposed a novel inversion strategy to mitigate the effects of static shift: during the inversion process, we exclude the apparent resistivity data from affected sites and rely solely on phase data. This approach eliminates the need for explicit static shift correction. Phase data can reflect the basic morphology of the subsurface electrical structure, when combined with apparent resistivity data from undisturbed sounding sites, the internal morphology of the subsurface can be inverted. We further validated the reliability of this method using synthetic data inversion and successfully applied it to field data inversion.

2 The approaches for static shift correcting

Since the 1970s, when it was recognized that the apparent resistivity curve in MT is affected by static shift, various static shift correction methods have been developed. Commonly used methods include coincidence first branch (Wang, 1992; Duan, 1994), spatial filtering (Bostick, 1986; Luo et al., 1991; Guo et al., 2022), and joint interpretation (Sternberg et al., 1988; Spitzer, 2001; Tripaldi et al., 2010). A brief introduction to each of these methods follows.

2.1 Coincidence first branch

If there are no three-dimensional shallow heterogeneities, the shallow medium is approximately one-dimensional, the high-frequency portions of the apparent resistivity curves Rxy and Ryx should coincide. In early studies, their non-coincidence in the high-frequency range was often attributed to static shift effects. If it is determined that one of them is not affected by static displacement, then the curve of the other one, which has static displacement effects, can be shifted onto the curve of the unaffected one, so that they coincide at the high-frequency region. This approach is commonly known as coincidence first branch method.

Two-dimensional forward modeling results indicate that in a 2D situation, only the TM polarization mode is affected by static shift, while the TE mode apparent resistivity curve remains stable (Berdichevsky et al., 1998). Thus, for sites of static shift, the TM mode curve can be adjusted to align with the TE curve in the high-frequency region to correct for static shift (Jiracek, 1990). However, three-dimensional forward modeling shows that small 3D shallow heterogeneities can cause static shifts in both curves (Wang, 1997), it is difficult to determine the reasonable position of the curves. In such cases, if the local structure near the survey area is relatively simple, adjacent measurement sites may have similar curve patterns, allowing one to serve as a reference for static shift correction through the coincidence first branch (Wang, 1992; Duan, 1994; Yang et al., 2015).

This method is simple and efficient, making it the most commonly used approach for static shift correction. However, since selecting an appropriate reference curve can be challenging, the effectiveness of this method often depends on the subjective judgment of the analyst, resulting in variable correction outcomes.

2.2 Spatial filtering

The spatial filtering method assumes that along the survey line, variations in apparent resistivity reflect gradual changes in the subsurface electrical structure. Since small shallow heterogeneities affect apparent resistivity in the wavenumber domain as high-frequency components, low-pass filtering can be applied to suppress and correct static shift (Guo et al., 2022).

The spatial filtering method begins by identifying sounding sites that contain static shift. Using data from neighboring sites, static shift correction can then be performed. For this, select high-quality frequency data from each sounding sites (within a frequency range from f_m to f_n, providing n−m+1 frequency points). Next, the geometric mean ρ_{ai} of the apparent resistivity for the chosen frequency points at each sounding site is obtained using Equation 1:

$$\rho_{ai} = \sqrt[n-m+1]{\prod_{j=m}^{n} \rho_{si}(f_j)} \tag{1}$$

Where i denotes the measurement sites and j represents the frequency points, $\rho_{si}(f_j)$ is the measured apparent resistivity at the j_{th} frequency point for the i_{th} measurement site. Appropriate filter window size and coefficients need to be selected, with five-point and seven-point filtering methods commonly in use (Luo et al., 1991). The filtered resistivity $\overline{\rho_{li}}$ can be calculated using the five-point filtering method, as specified in Equation 2:

$$\overline{\rho_{li}} = 0.12\rho_{ai-2} + 0.22\rho_{ai-1} + 0.32\rho_{ai} + 0.22\rho_{ai+1} + 0.12\rho_{ai+2} \tag{2}$$

Or using the five-point filtering method, as specified in Equation 3:

$$\overline{\rho_{li}} = 0.08\rho_{ai-3} + 0.12\rho_{ai-2} + 0.175\rho_{ai-1} + 0.25\rho_{ai} + 0.175\rho_{ai+1} + 0.12\rho_{ai+2} + 0.08\rho_{ai+3} \tag{3}$$

The static shift correction coefficient can be obtained by Equation 4.

$$k_i = \frac{\overline{\rho_{li}}}{\rho_{ai}} \tag{4}$$

Finally, each site's static shift correction coefficient is multiplied by the measured apparent resistivity value at the corresponding frequency, resulting in the corrected apparent resistivity.

The EMAP method (Bostick, 1986; Luo, 1990) is a type of spatial filtering method that achieves static shift correction by increasing the density of measurement sites and directly smoothing the electric field signal through multi-electrode observations. While this approach is considered effective for static shift correction, it notably raises observation costs and diminishes lateral resolution, potentially limiting its practicality in some applications.

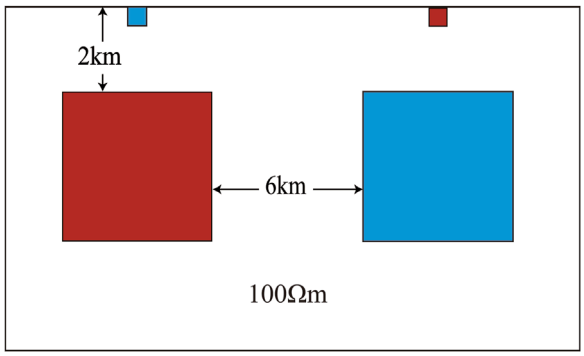

FIGURE 1
Model I Schematic. The red anomaly body has a resistivity of 10 Ω m, while the blue anomaly body has a resistivity of 1,000 Ω m. The edge length of the shallow anomaly body is 4 m, and the edge length of the deep anomaly body is 6 km.

2.3 Joint interpretation

The joint interpretation method typically uses the curve from the Transient Electromagnetic (TEM) as a correction standard, aligning the initial segment of the MT apparent resistivity curve with the TEM curve. This approach is effective because TEM only measures the magnetic field, while static shift is caused by electric field distortion; therefore, TEM data are not affected by static shift.

The skin depth of MT Z_{MT} is

$$z_{MT} = \sqrt{\frac{2}{\sigma\mu\omega}} \tag{5}$$

The skin depth of TEM Z_{TEM} is

$$z_{TEM} = 1.28\sqrt{\frac{t}{\sigma\mu}} \tag{6}$$

Combine Equation 5 with Equation 6, if $z_{MT} = z_{TEM}$, the conversion relationship between the two can be obtained.

$$f = 194/t \tag{7}$$

Where f is in Hz and t is in ms. Using Equation 7, the TEM apparent resistivity curve can be transformed into the frequency-domain. This transformation enables the MT apparent resistivity curve to be aligned with the TEM curve, facilitating a smooth connection and achieving static shift correction for the MT apparent resistivity data.

In practice, the joint interpretation method does not strictly require the use of TEM; any resistivity sounding technique with minimal sensitivity to shallow lateral heterogeneities may be applied (Wang, 1992; Spitzer, 2001; Tripaldi et al., 2010). Furthermore, this approach tends to increase observation costs substantially, and because Equation 7 is an empirical formula, it may introduce errors when applied to complex geological models, potentially impacting accuracy.

3 Considerations on the necessity of static shift correction

Static shift correction methods also include the wavelet transform (Song et al., 1995; Zhang et al., 2002; Trad and Travassos, 2012), which performs multi-scale decomposition and static shift correction of signals in the time domain. This method requires careful parameter selection, making it susceptible to subjective influence, and often results in either under-correction or over-correction. The phase shift method (Yang et al., 2001; Qiu et al., 2012) uses the Hilbert transform to derive the apparent resistivity amplitude from its phase, thus correcting the distorted apparent resistivity curve. However, because this approach relies on an indefinite integral, it introduces an undetermined constant, effectively creating an additional, unpredictable static offset. Some researchers have applied tensor decomposition in the context of static displacement correction (Gao and Zhang, 1998; Wang, 1998). However, it was explicitly stated during the development of impedance tensor techniques that impedance tensor decomposition can only address local distortions within the curve and is ineffective for correcting static offset (Groom and Bailey, 1989; Calderón-Moctezuma et al., 2022).

As previously mentioned, despite years of development and numerous proposed methods, a simple, effective, and universally applicable approach to static shift correction remains elusive. Moreover, the correction process can sometimes introduce additional errors. However, extensive practical applications suggest that even without static shift correction, most three-dimensional inversions can closely match observed curves for data from high-quality measurement sites, with only a few exceptions showing difficulties in matching apparent resistivity curves. For these outliers, if the inversion-fitted curves are similar in shape but differ by a static shift factor, the observed curves could be shifted to align with the fitted curves, effectively achieving static shift correction. However, since the apparent resistivity curve shape can be derived through the Hilbert-transform of the phase (Fischer and Schnegg, 1980), one might question the necessity of this adjustment. Does the shifted curve contribute meaningfully to the inversion? If not, is static shift correction for MT apparent resistivity truly essential?

Based on the above considerations, this paper proposes an approach that omits the apparent resistivity data from static shift affected sites and retains only their phase data for two-dimensional and three-dimensional inversions. This approach bypasses the need for static shift correction and minimizes the influence of static-shifted data on inversion results. Research indicates that while inversions based solely on phase curves cannot determine absolute resistivity values or precisely calibrate structural depths, they effectively constrain internal structural variations and offer reliable morphological details. Since most measurement sites in a survey area do not exhibit static shifts (as evidenced by successful two- and three-dimensional fits), retaining only phase data for the few static-shifted sites mitigates the impact of small heterogeneities and preserves the essential details of the internal electrical structure. The following inversion results based on theoretical model and field data validate this approach.

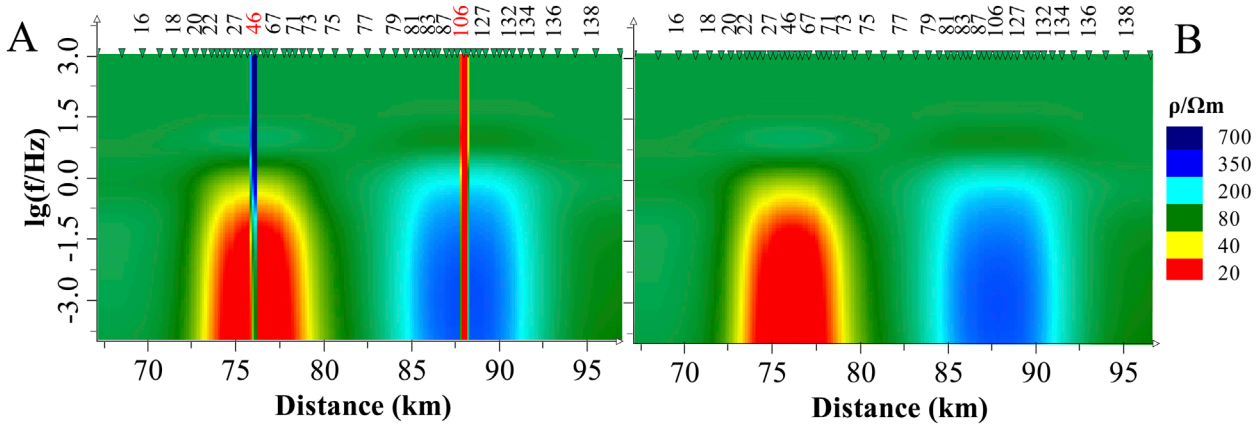

FIGURE 2
The TM apparent resistivity profile for model I **(A)** and model I without small anomalous bodies **(B)**. The numbers at the top of the image represent the measurement site names, though not all measurement site names are displayed. The red numbers indicate measurement sites with static shifts (the same applies hereafter).

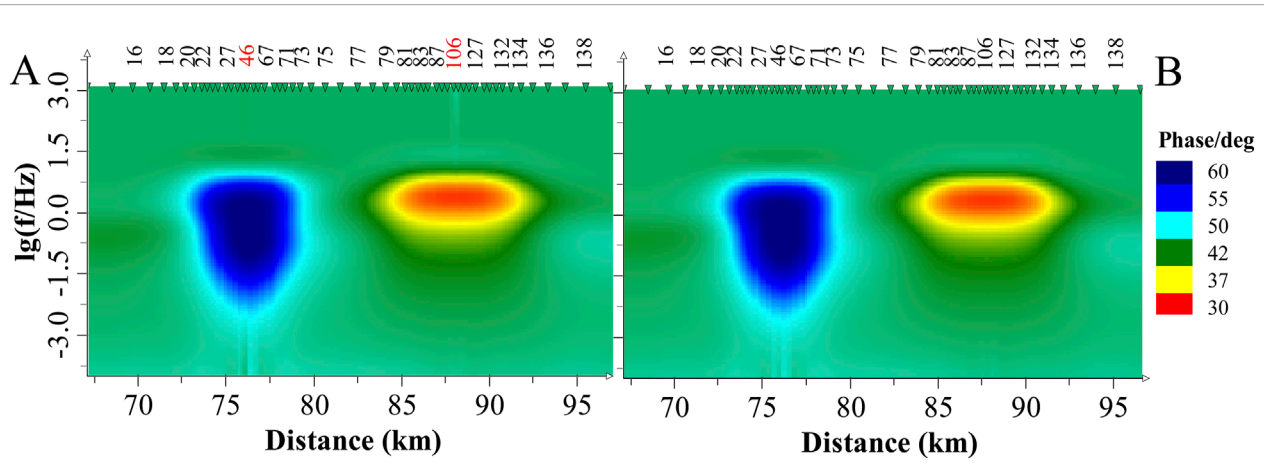

FIGURE 3
The TM phase profile for model I and model I **(A)** without small anomalous bodies **(B)**.

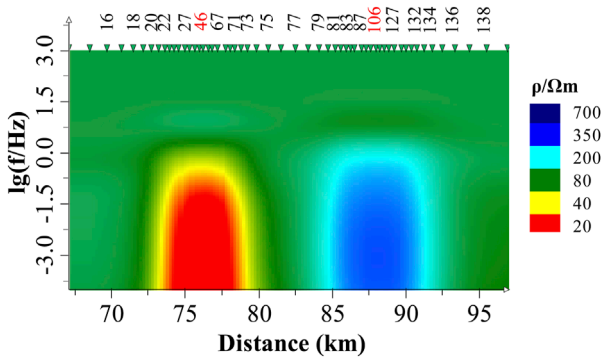

FIGURE 4
The TM apparent resistivity profile with apparent resistivity data excluded at affected sites.

4 Case study

We used synthetic data to verify the feasibility and effectiveness of the proposed new method. Two-dimensional synthetic data were generated through forward modeling with a finite element direct iteration method program (Chen and Hu, 2002). For three-dimensional synthetic data, we used the dataset developed by Cai and Chen (2010). The inversion was applied using the MT-Pioneer software (Chen et al., 2004), which Integrates the Nonlinear Conjugate Gradient (NLCG) inversion algorithm developed by Rodi and Mackie, 2001.

For two-dimensional magnetotelluric inversion, three data modes are available: TE-mode, TM-mode, and combined TE+TM mode inversion. In two-dimensional cases, small surface electrical heterogeneities typically affect TM-mode data. Previous studies (Wannamaker et al., 1984; Chen et al., 2006; Cai and Chen, 2010)

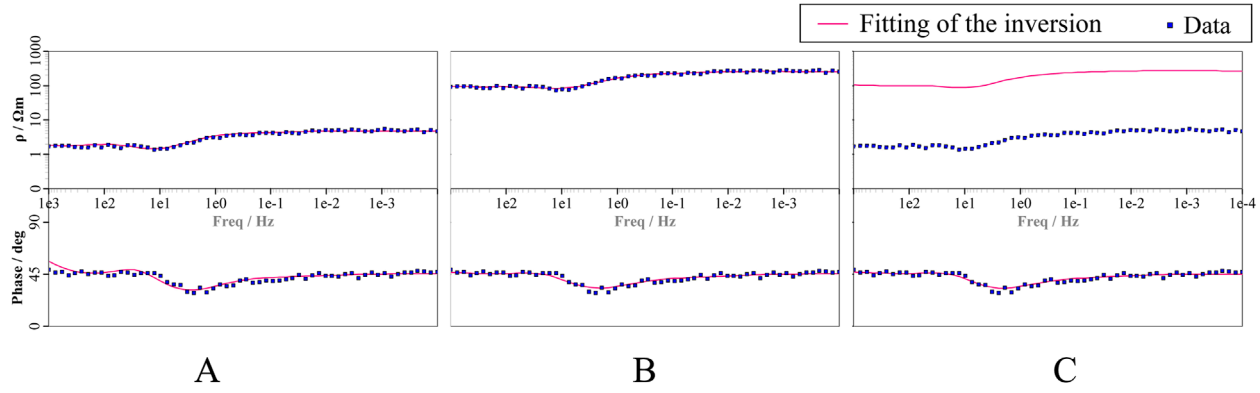

FIGURE 5
The fitting of measurement site 106 with frequency in the inversion results using different data. **(A)** Original data. **(B)** Date after static shift correction. **(C)** Original data with the apparent resistivity data from static shift sites discarded.

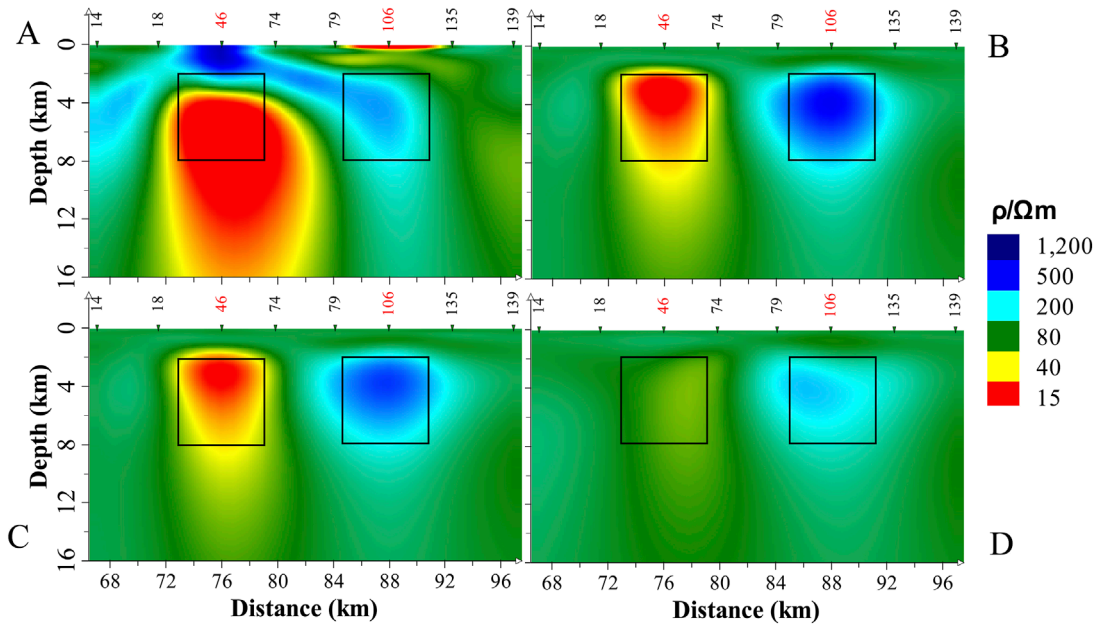

FIGURE 6
The results of inversion using different data. The black wireframe represents the location of the anomalous body. **(A)** Original data. **(B)** Date after static shift correction. **(C)** Original data with the apparent resistivity data from static shift sites discarded. **(D)** Discarding both the apparent resistivity and phase data from static shift sites.

have demonstrated that TM-mode inversion results outperform those from TE-mode or combined TE+TM inversion when applied to synthetic data derived from three-dimensional models. Therefore, this paper utilizes two-dimensional TM-mode inversion to reconstruct the subsurface electrical structure from two-dimensional synthetic data.

4.1 2D model

Model I is a two-dimensional model (Figure 1), similar to the static effect model previously designed by Zhang et al. (2016). The background resistivity of the model is 100 Ωm and contains two small anomalous bodies located on the surface. Each anomalous body has a length of 4 m, a height of 4 m, and resistivities of 1,000 Ωm and 10 Ωm, respectively, to generate static effects. Directly beneath each small anomaly is a larger anomalous body, with a top depth of 2000 m, a length of 6,000 m, and a height of 6,000 m, with resistivities of 10 Ωm and 1,000 Ωm, respectively, which are the targets to be detected. The distance between these larger anomalous body is 6,000 m, and their boundaries are sufficiently far from the forward modeling boundaries. The forward modeling frequency range is from 0.0001 Hz to 1,000 Hz, covering 60 frequency points in total.

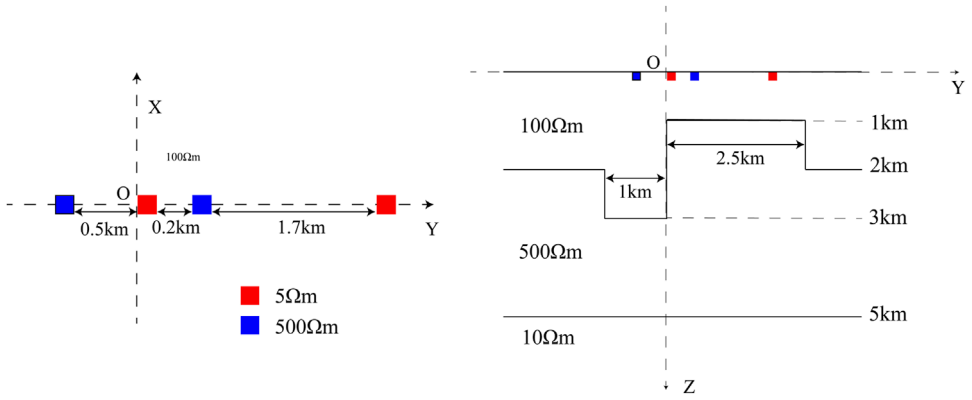

FIGURE 7
Model II Schematic. The 3D shallow heterogeneities are all cubic in shape with an edge length of 40 m (Cai, 2009).

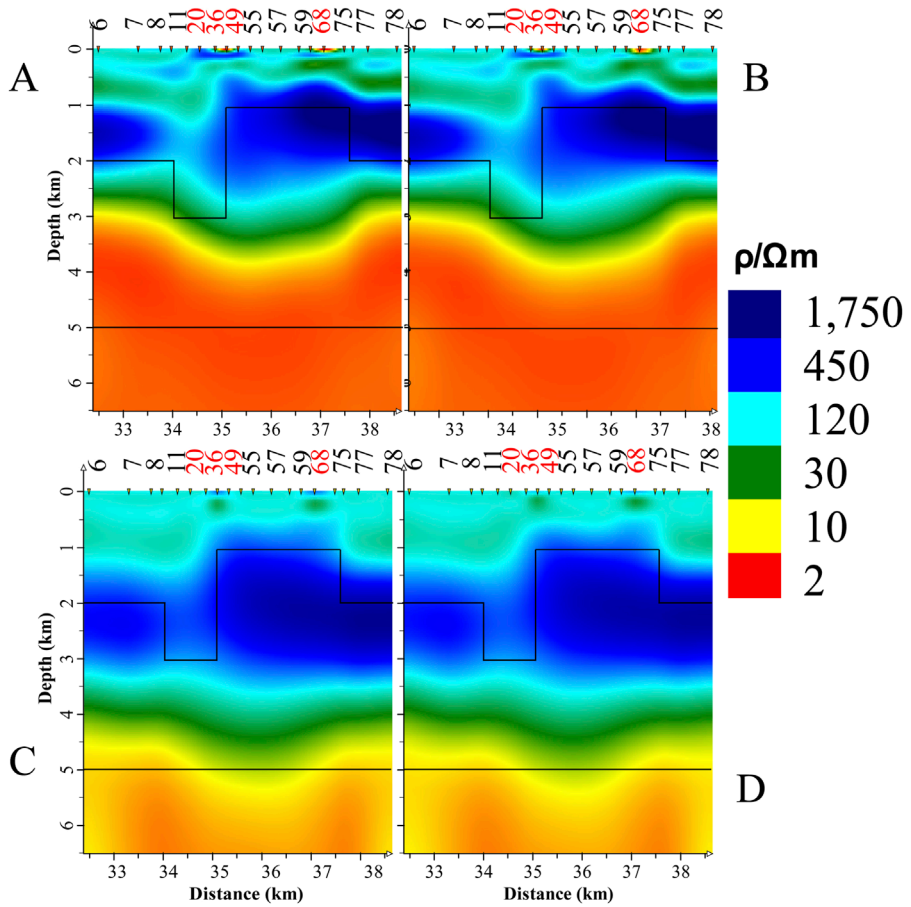

FIGURE 8
The inversion results of Model II. The black wireframe represents the layered structure. **(A)** Original data. **(B)** First time using static shift correction. **(C)** Second time using static shift correction. **(D)** Removing the apparent resistivity data from static shift site.

The apparent resistivity profile obtained from forward modeling for Model 1 is shown on the Figure 2A. After removing the small anomalous bodies from the surface while keeping other conditions unchanged, the apparent resistivity profile obtained from forward modeling is shown on Figure 2B. In Figure 2A, some sites exhibit static shift, which appear as steep stripes in the profile. Static shift obscures the original subsurface structure and complicate data interpretation. In contrast, the phase profile (Figure 3) does not

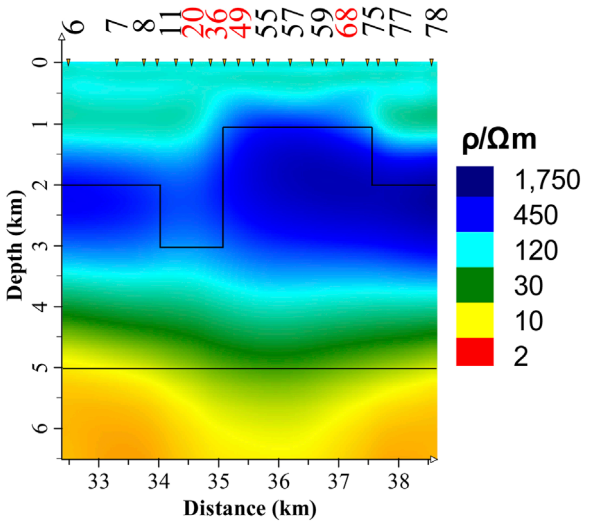

FIGURE 9
The inversion results of Model II without small anomalous bodies.

exhibit such situation. After the removal of apparent resistivity data containing static shift, the effect of static shift in the profile is significantly reduced, as shown in Figure 4. This reduction provides justification for using phase inversion without the need for static shift correction.

In the forward modeling results, a random error of 10% was added to simulate measurement errors typically found in actual data. The inversion regularization factor was set to 100, with an initial model representing a homogeneous half-space of 100 Ωm. The floor error for apparent resistivity was set at 2%, and the phase was established at 0.57°. Sparse inversion sites were employed, with neighboring sites spaced about 5 km apart. Four different inversion scenarios were conducted: (1) inversion using the original data, (2) inversion after static shift correction, (3) inversion based on the original data with the apparent resistivity data from static shift sites discarded, and (4) inversion after discarding both the apparent resistivity and phase data from static shift sites. In the static shift correction process, the TM curve was shifted to align with the high-frequency portion of the TE curve.

All four scenarios underwent multiple inversions, with the best inversion results selected for each case. The final inversion results are shown in Figure 6, where sites 46 and 106, located above the small anomalous bodies on the surface, are identified as static shift sites.

During the inversion process, the model is more inclined to closely align with the apparent resistivity curve compared to the phase curve. As demonstrated in Figure 5A with static shift site 106 as a reference, the inversion results closely replicate the displaced apparent resistivity data, yet exhibit a slightly inferior fit to the phase data, attributed to the influence of static shift. Following the application of static shift correction, as depicted in Figure 5B, the inversion results accurately align with both the apparent resistivity and phase data once the apparent resistivity curve is restored to its expected state. Figure 5C illustrates the inversion outcomes after the exclusion of the apparent resistivity data from the static shift site 106, revealing a good fit to the phase curve. Given that static shift does not impact the phase curve, the inversion results based on phase curve fitting for static shift sites are more representative of the true model than those derived from fitting the apparent resistivity curve.

The inversion results using the original data are shown in Figure 6A. Due to static shift, two large anomalous bodies appear in the shallow region, while the deep low-resistivity anomaly is exaggerated, causing notable distortions in position, shape, and size. Additionally, the high-resistivity anomaly is obscured and unrecognizable. Figure 6B demonstrates that applying curve-shifting method yields excellent results, producing a smoother near-surface region and clearly distinguishable deep anomalies. Figure 6C closely resembles Figure 6B, indicating that, for this two-dimensional model, excluding the apparent resistivity data from static shift sounding sites can achieve results comparable to static shift correction. However, when phase data from static shift sites are also excluded, the lack of phase constraints results in blurred anomaly shapes and significantly deteriorates inversion quality (Figure 6D). This outcome underscores the critical role of phase data in the inversion process.

4.2 3d/2d model

To further verify the reliability of this strategy, a 3D/2D model developed by Cai Juntao was utilized, with a schematic diagram shown in Figure 7 (Model II). This model was previously used in research by Cai and Chen (2010) on impedance tensor decomposition and structural dimensionality analysis.

The model surface contains four anomalous bodies, each measuring 40 m × 40 m × 40 m, with two high-resistivity bodies (500 Ωm) and two low-resistivity bodies (5 Ωm). The forward modeling spans a frequency range from 500 Hz to 0.0005 Hz, covering a total of 45 frequency points. Following the 3D forward modeling, data from survey lines intersecting the surface anomalies are selected for 2D inversion analysis.

Four different inversion scenarios were conducted: inversion using the original data directly, inversion after two different modes of static shift correction, and inversion after removing the apparent resistivity data from static shift measurement sites.

To implement the static shift corrections, the first correction involved shifting the TM curve to align with the TE curve using the initial branch merging method. The second correction involved globally shifting the TM curve to align its high-frequency section with the background resistivity value of 100 Ωm for the near-surface region in the forward model.

In all four scenarios, the regularization factor for inversion was set to 100. The initial model is a homogeneous half-space with a resistivity of 10 Ωm. The synthetic data used for inversion included a random error of 10%. To obtain more accurate information about the deep structures, the impressing method (Ye et al., 2013) was employed to construct the initial model during the inversion process.

Furthermore, the best inversion results for each scenario were selected, and the final inversion results are presented in Figure 8. Additionally, when the small surface anomalies in the model were removed while keeping other conditions unchanged, the inversion results obtained after forward modeling are shown in Figure 9.

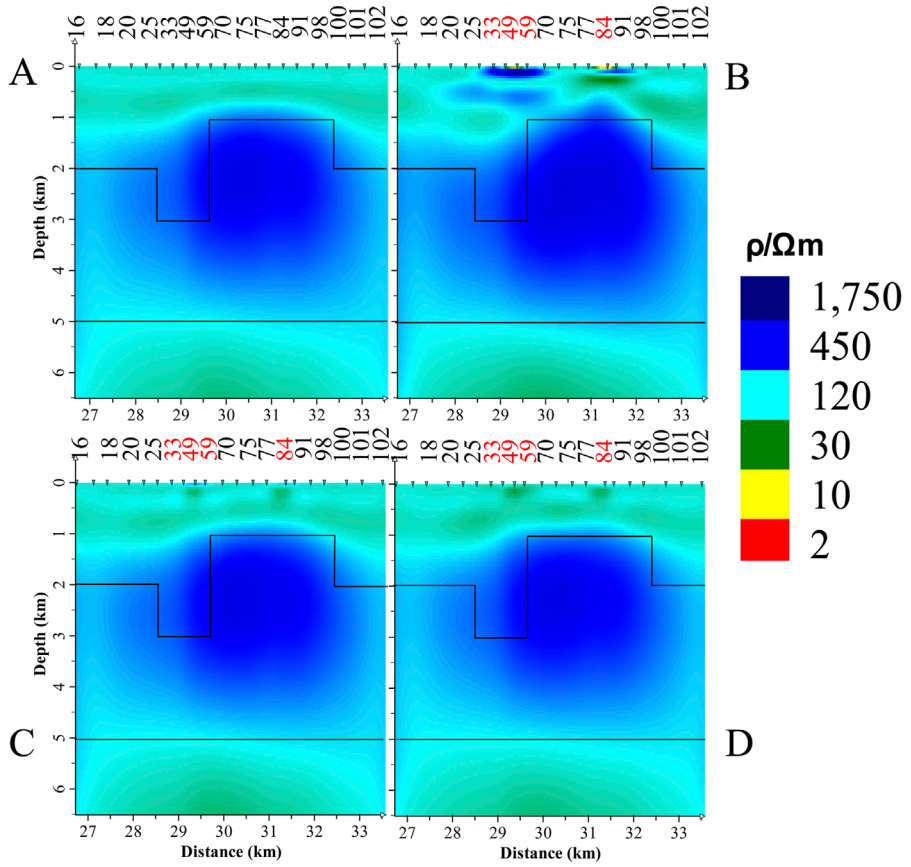

FIGURE 10
Inversion results of a 2D model similar to Model II. **(A)** Results for the 2D model without small anomalous bodies. **(B)** Inversion results for the original data. **(C)** Inversion results after static shift correction. **(D)** Inversion results excluding apparent.

By comparing Figures 8, 9, it can be observed that Figure 8A exhibits near-surface anomalies that are not actually present due to static shift, particularly around the three small anomalies. A similar situation is noted in Figure 8B, where the shallow parts of both inversion results display significant irregularities. This indicates that when the model is three-dimensional, using TE apparent resistivity curve as a reference for curve translation is ineffective. However, Figure 8C shows that with a sufficient understanding of the electrical structure of the survey area, translating the TM curve to an appropriate value can yield improved inversion results. The results from the phase inversion of static shift sites in Figure 8D is similar to those in Figure 8C and closely resemble Figure 9.

Furthermore, static shift also causes a significant discrepancy in the position of the intermediate high-resistivity layer in the inversion results compared to the forward model, which is improved in Figures 8C, D. This indicates that the effects of static shift have been effectively suppressed, demonstrating that the proposed inversion strategy works well in three-dimensional situations.

It should be noted that the inversion results shown in Figures 8, 9 do not accurately reflect the deep information of the model. This is primarily due to inadequacies in the constructed mesh model for the forward modeling, which were necessary to accommodate the mesh division of the four small anomalies, resulting in significant errors in the low-frequency part of the synthetic data. To address this, a 2D model similar to Model II was designed, both with and without small surface anomalies. The results from the two-dimensional forward modeling and inversion of the synthetic data are shown in Figure 10, which better reflects the deep information of the model.

4.3 Field test

A survey line in a specified area includes 28 sounding sites. Analysis revealed that site 51 exhibit static shift. Figure 11 displays the apparent resistivity profile along this line, where a vertical high-resistivity band appears between site 51. Removing the apparent resistivity data at this site significantly diminishes the effect of this vertical high-resistivity band. In the corresponding phase section diagram (Figure 12), no similar high-resistivity band was observed. Therefore, along this survey line, we can continue to attempt to use the inversion method proposed in this paper.

Two inversions were performed: one including the apparent resistivity data for site 51 and another excluding it. The results are shown in Figure 13. Overall, the difference between the two inversions is minor, indicating that for 2D field data, the effect of static shift on inversion results is less pronounced than in theoretical model inversions. However, some localized distortions

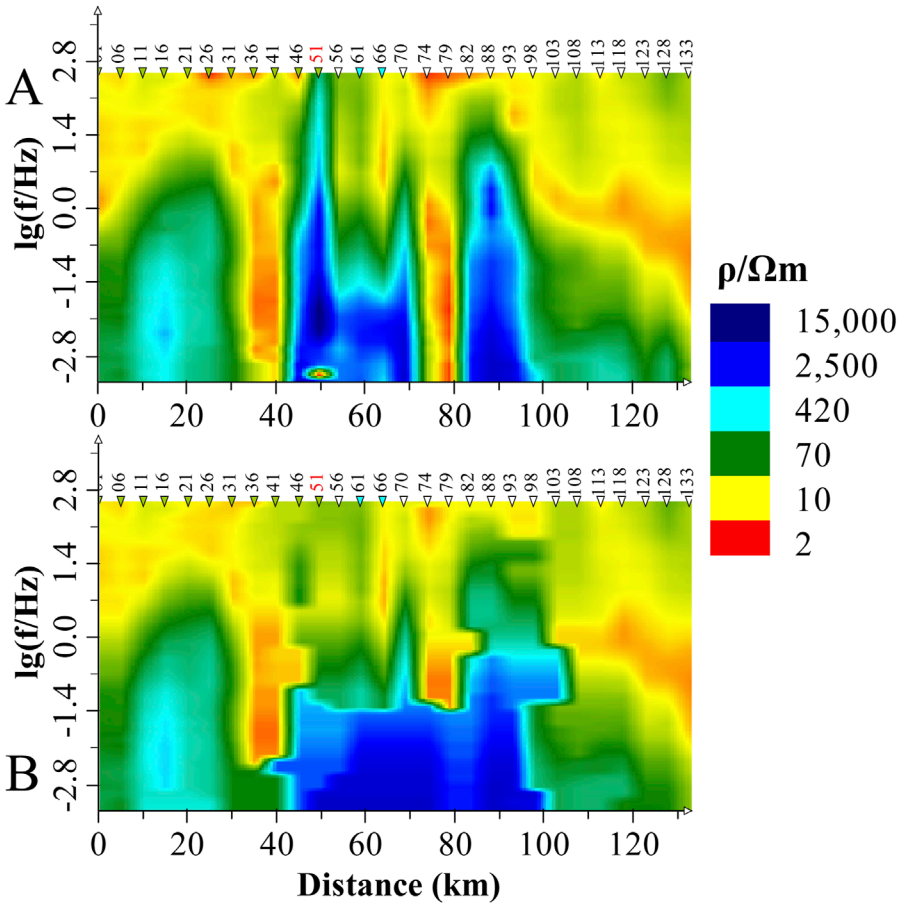

FIGURE 11
The TM apparent resistivity profile. **(A)** Original field data. **(B)** The apparent resistivity data excluded at affected site.

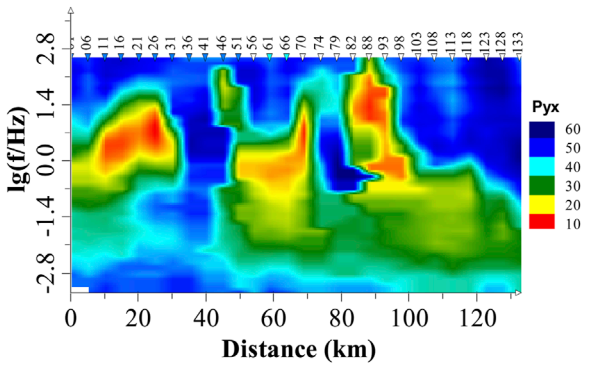

FIGURE 12
The TM phase profile for field data.

remain. At the 40 km mark along the line, a high-resistivity anomaly approximately 2 km deep and 8 km thickness distorts the shapes of adjacent low-resistivity anomalies, impacting the visibility of high-conductivity zones and potentially influencing geological interpretations (represented by black rectangles in Figure 13). After discarding the apparent resistivity data from static-shift-affected sites and conducting the inversion, the resistivity variations in this region become smoother, aligning more closely with the true resistivity values.

5 Discussion

In magnetotellurics, in addition to small surface anomalies, there are other situations, such as steep terrain, vertical fractures that cut through to the surface, and boundaries between rocks with different properties, which can also cause shifts in the apparent resistivity curve. If these factors are not properly identified, blindly applying static shift correction can easily remove data that accurately reflects the structural response. The aforementioned cases illustrate that this can have a severe impact on inversion results. Therefore, it is crucial to determine whether a measurement site is affected by static shift. Currently, static shift identification primarily relies on experience, which means there is a possibility of misidentification. When a measurement site without static shift is mistakenly identified as having static shift, which method would have a greater impact: the traditional static shift correction method or the direct discard of apparent resistivity advocated in this paper?

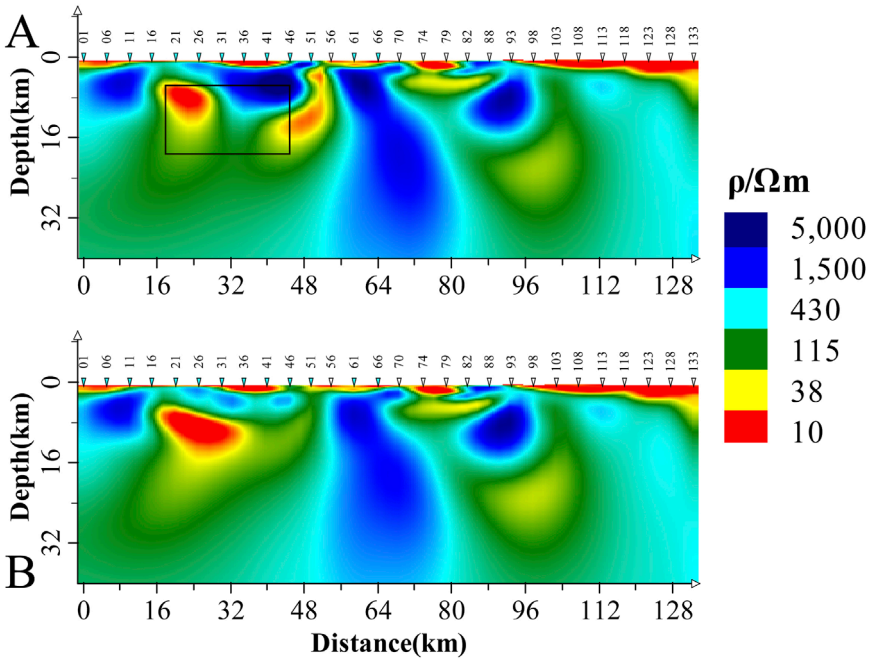

FIGURE 13
Results of Field Data Inversion. **(A)** Inversion results for the original data. **(B)** Inversion results for the original data with apparent resistivity data from static shift sites removed.

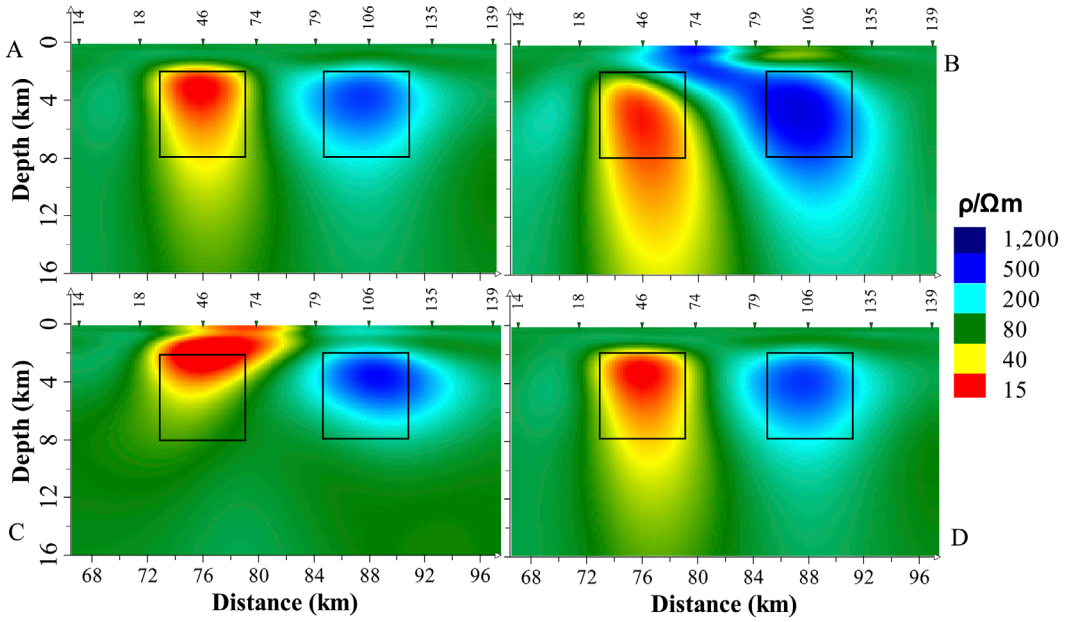

FIGURE 14
The inversion results for Model (I) **(A)** Apparent resistivity data from two measurement sites affected by static shift are discarded, consistent with Figure 6C; **(B)** Static shift correction factor for measurement site 74 is 5; **(C)** Static shift correction factor for measurement site 74 is 0.2; **(D)** The apparent resistivity data for measurement site 74 is discarded.

Figure 14 presents several inversion results based on the inversion outcome shown in Figure 6C. Assuming that measurement site 74 is misjudged as having a static shift, Figures 14B, C show the inversion results with static shift correction factors set to 5 and 0.2, respectively, while Figure 14D shows the inversion result after discarding the apparent resistivity data

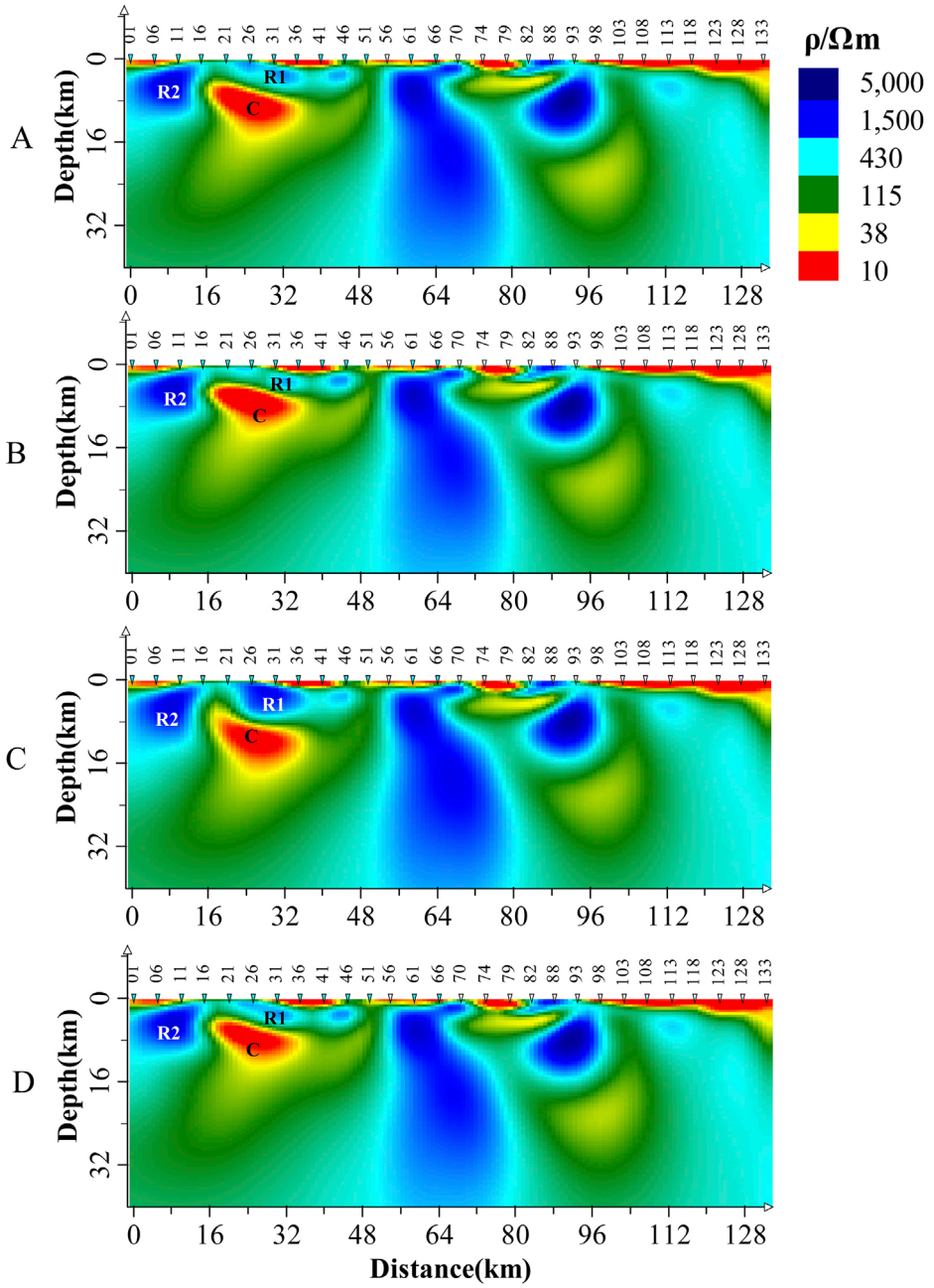

FIGURE 15
The inversion results for field data, R1, R2, and C represent the anomaly bodies. **(A)** The inversion result after excluding the apparent resistivity data of measurement site 51, consistent with Figure 13B; **(B)** Static shift correction factor of 0.2 applied to measurement site 26; **(C)** Static shift correction factor of 5 applied to measurement site 26; **(D)** The apparent resistivity data of measurement site 26 is excluded.

of measurement site 74. All other inversion parameters remain consistent with those in Figure 6.

It is clear that, after misjudgment, the traditional method of static shift correction by shifting the apparent resistivity, whether moving it upwards (Figure 14B) or downwards (Figure 14C), significantly impacts the inversion results. The upward shift (Figure 14B) causes a particularly severe distortion, likely because increasing the apparent resistivity creates high-resistivity anomalies, which in turn increases the skin depth of electromagnetic waves, resulting in a larger impact range of erroneous data. In contrast, the method proposed in this paper (Figure 14D), which involves simply excluding the apparent resistivity data of measurement site 74 from the inversion, causes negligible effects on the inversion result, with only a slight downward extension of the bottom boundary of the high-conductivity anomaly.

The same testing and processing were applied to the field data in this paper. Suppose that measurement site 26 on this profile is misjudged as a static shift site, and after applying various static shift corrections, the inversion results are compared as shown in Figure 15. From Figure 15, it can be seen that the error correction of

the misjudged static shift in this field data case is not as significant as in Figure 14, but differences are still observable. When the apparent resistivity curve of measurement site 26 is multiplied by a static shift factor of 0.2, the result, shown in Figure 15B, differs slightly from Figure 15A. However, it is still evident that R1 has become notably narrower, and the scales of R2 and C have also decreased. If the apparent resistivity curve of measurement site 26 is multiplied by a static shift factor of 5, the result, shown in Figure 15C, shows a much more obvious difference compared to Figure 15A. R1 has significantly thickened, the burial depth of the top boundary of C has increased substantially, and its shape has also changed, while R2 is less affected. However, by directly excluding the apparent resistivity data of measurement site 26 from the inversion, as done in this paper, the result, shown in Figure 15D, indicates that the difference between it and Figure 15A is mainly in the continuity between measurement sites 26 and 31 in R1, which now appears more continuous, reflecting the smallest variation among the three sites.

Both the theoretical model and the field data case demonstrate that, when a static shift site is misjudged, traditional methods have a larger impact on the inversion results compared to the method proposed in this paper. Specifically, shifting the apparent resistivity upward has a much greater impact on the inversion results than shifting it downward by the same factor. In the field data case in this paper, the correction of the misjudged static shift site has a relatively small effect on the inversion results (similar to synthetic data). This may be due to the presence of a significant high-conductivity anomaly (C) beneath the measurement site, which causes the electromagnetic wave to attenuate rapidly inside, limiting the propagation of the static shift effect to more distant areas, thus reducing the range of influence.

The above examples preliminarily suggest that if static shift measurement sites are misidentified, specifically when a measurement site without static shift effects is incorrectly determined to have a static shift, the impact of the traditional processing method is far greater than that of the method proposed in this paper. The reason for the smaller impact of the proposed method is that the information contained in the discarded apparent resistivity data can be recovered through the retained phase data and the apparent resistivity data from neighboring measurement sites. After all, both 2D and 3D inversions are collaborative processes involving multiple measurement sites to reconstruct the subsurface electrical structure. Of course, if multiple measurement sites are misjudged and too much apparent resistivity data is discarded during inversion, leading to insufficient data constraints on the electrical structure background of the survey area, the inversion results will be affected. The specific impact of this scenario requires further investigation.

6 Conclusion

This study investigates the influence of static shift on magnetotelluric data by analyzing the inversion results of both two-dimensional and three-dimensional models, as well as field data. This analysis raises a critical question: Is static shift correction necessary for every MT project? Our findings indicate that static shift correction is not an obligatory procedure in MT.

By utilizing phase data from static shift sites as the primary input for inversion, this strategy effectively reduces subjective operator bias, provided that the static shift sites are accurately identified. Additionally, this method is straightforward and does not incur additional observational costs compared to traditional static shift correction techniques. Consequently, this inversion strategy successfully mitigates the effects of static shift in the data without increasing the expenses associated with MT data acquisition or complicating data processing workflows. This approach not only addresses the challenges posed by static shift effects on inversion results but also enhances the overall reliability of these results.

This study has limitations, including the omission of topographical effects and a lack of validation through three-dimensional inversion, based on the assumption that the forward modeling results of the theoretical model are sufficiently accurate. While various two-dimensional models were designed and validated throughout the research process, producing generally satisfactory results, actual subsurface electrical structures are often far more complex. Thus, further theoretical and practical investigations are necessary to substantiate these findings in this domain.

Data availability statement

The raw data supporting the conclusions of this article will be made available by the authors, without undue reservation.

Author contributions

JZ: Investigation, Validation, Visualization, Writing - original draft, Writing - review and editing, Data curation. XC: Conceptualization, Software, Supervision, Validation, Writing - review and editing, Funding acquisition, Methodology, Resources. PW: Software, Validation, Visualization, and Writing – review and editing. ZL: Investigation, Writing - review and editing, Validation. JC: Resources, Writing - review and editing.

Funding

The author(s) declare that financial support was received for the research, authorship, and/or publication of this article. This work is supported by the National Natural Science Foundation of China (42174093) and Three-Dimensional Electrical Structure of the Central and Northern Segment of the Red River Fault Zone (ZDJ 2020-13).

Conflict of interest

The authors declare that the research was conducted in the absence of any commercial or financial relationships that could be construed as a potential conflict of interest.

Generative AI statement

The author(s) declare that Generative AI was used in the creation of this manuscript. Optimized English expression.

Publisher's note

References

Beamish, D., and Travassos, J. M. (1992). A study of static shift removal from magnetotelluric data. *J. Appl. Geophys.* 29 (2), 157–178. doi:10.1016/0926-9851(92)90006-7

Berdichevsky, M. N., Dmitriev, V. I., and Pozdnjakova, E. E. (1998). On two-dimensional interpretation of magnetotelluric soundings. *J. Geophys. Res. Solid Earth* 133, 585–606. doi:10.1046/j.1365-246X.1998.01333.x

Bostick, F. X. (1986). Electromagnetic array profiling (EMAP). *SEG Technical Program Expanded Abstracts*: 60–61. doi:10.1190/1.1892989

Cagniard, L. (1953). Basic theory of the magneto-telluric method of geophysical prospecting. *Geophysics* 18, 605–635. doi:10.1190/1.1437915

Cai, J., Chen, X., Xu, X., Tang, J., Wang, L., Guo, C., et al. (2017). Rupture mechanism and seismotectonics of the $_s$6.5 Ludian earthquake inferred from three-dimensional magnetotelluric imaging. *Geophys. Res. Lett.* 44, 1275–1285. doi:10.1002/2016GL071855

Cai, J. T. (2009). *Research on the three-dimensional distortion characteristics and correction techniques of magnetotelluric data [Doctoral dissertation]*. China Earthquake Administration: Institute of Geology.

Cai, J. T., and Chen, X. B. (2010). Refined techniques for data processing and two-dimensional inversion in magnetotelluric II: which data polarization mode should be used in 2D inversion. *Chin. J. Geophys.* 53 (11), 2703–2714. doi:10.3969/j.issn.0001-5733.2010.11.018

Calderón-Moctezuma, A., Gomez-Treviño, E., Yutsis, V., Guevara-Betancourt, R., and Gómez-Ávila, M. (2022). How close can we get to the classical magnetotelluric sounding? *J. Appl. Geophys.* 203, 104665. doi:10.1016/j.jappgeo.2022.104665

Chave, A. D., and Jones, A. G. (2012). *The magnetotelluric method: theory and practice* (Cambridge University Press CUP). doi:10.1017/CBO9781139020138

Chen, X. B., and Hu, W. B. (2002). Direct iterative finite element (DIFE) algorithm and its application to electromagnetic response modeling of line current source. *Chin. J. Geophys.* 45 (01), 119–130. doi:10.1002/cjg2.223

Chen, X. B., Zhao, G. Z., and Ma, X. (2006). Study on the 1D and 2D inversion approximation problems of magnetotelluric three-dimensional models. *Chin. J. Eng. Geophys.*, 9–15.

Chen, X. B., Zhao, G. Z., and Zhan, Y. (2004). MT data processing and interpretation Windows-based visualization integration system. *Pet. Geophys. Prospect.* 39 (S1), 11–16.

Duan, B. (1994). First branch recombination method for correcting static effects in magnetotelluric sounding. *J. Changchun Coll. Geol.*, 444–449.

Fischer, G., and Schnegg, P.-A. (1980). The dispersion relations of the magnetotelluric response and their incidence on the inversion problem. *Geophys. J. Int.* 62, 661–673. doi:10.1111/j.1365-246X.1980.tb02598.x

Gao, H., and Zhang, S. (1998). Study of correction for static shift: the decomposition of magnetotelluric impedance tensors. *Geol. Sci. Technol. Inf.* 17(1), 91–96.

Groom, R. W., and Bailey, R. C. (1989). Decomposition of magnetotelluric impedance tensors in the presence of local three-dimensional galvanic distortion. *J. Geophys. Res. Solid Earth* 94, 1913–1925. doi:10.1029/JB094iB02p01913

Guo, W., Tang, X. G., and Sheng, G. Q. (2022). Magnetotelluric static correction of two-dimensional model based on the highest frequency phase method and spatial filtering method. *Acta Seismol. Sin.* 44 (2), 302–315. doi:10.11939/jass.20210139

Jiang, F., Chen, X., Unsworth, M. J., Cai, J., Han, B., Wang, L., et al. (2022). Mechanism for the uplift of gongga Shan in the southeastern Tibetan plateau constrained by 3d magnetotelluric data. *Geophys. Res. Lett.* 49, e2021GL097394. doi:10.1029/2021GL097394

Jiracek, G. R. (1990). Near-surface and topographic distortions in electromagnetic induction. *Surv. Geophys.* 11 (2-3), 163–203. doi:10.1007/BF01901659

Jones, A. G. (2012). Static shift of magnetotelluric data and its removal in a sedimentary basin environment. *Geophysics* 53, 967–978. doi:10.1190/1.1442533

Luo, Y. Z., He, Z. X., Ma, R. W., and Guo, J. H. (1991). The correction of static effects in sonic-frequency telluric electromagnetic method of controllable source. *Geophys. Geochem. Explor.*, 196–202.

Luo, Z. Q. (1990). Study on suppressing the effect of static shift in MT by electromagnetic array profiling method. *J. China Univ. Geosciences*, 13–22.

Qiu, G., Zhong, Q., Liu, J., Bai, D., and Yuan, Y. (2012). Approximate interconversion method and program implementation between apparent resistivity and phase curves in magnetotelluric sounding. *Comput. Tech. For Geophys. And Geochem. Explor.* 34, 402–405+366.

Rodi, W., and Mackie, R. L. (2001). Nonlinear conjugate gradients algorithm for 2-D magnetotelluric inversion. *Geophysics* 66, 174–187. doi:10.1190/1.1444893

Sasaki, Y. (2004). Three-dimensional inversion of static-shifted magnetotelluric data. *Earth Planets Space* 56, 239–248. doi:10.1186/BF03353406

Song, S., Tang, J., and He, J. (1995). Wavelets analysis and the recognition, separation, and removal of the static shift in electromagnetic soundings. *Chin. J. Geophys.* 38 (1), 120–128.

Spitzer, K. (2001). Magnetotelluric static shift and direct current sensitivity. *Geophys. J. Int.* 144, 289–299. doi:10.1046/j.1365-246x.2001.00311.x

Sternberg, B. K., Washburne, J. C., and Pellerin, L. (1988). Correction for the static shift in magnetotellurics using transient electromagnetic soundings. *Geophysics* 53, 1459–1468. doi:10.1190/1.1442426

Tikhonov, A. N. (1950). On determining electric characteristics of the deep layers of the Earth's crust. *Dokl. Akad. Nauk. SSSR* 73.

Trad, D. O., and Travassos, J. M. (2012). Wavelet filtering of magnetotelluric data. *Geophysics* 65, 482–491. doi:10.1190/1.1444742

Tripaldi, S., Siniscalchi, A., and Spitzer, K. (2010). A method to determine the magnetotelluric static shift from DC resistivity measurements in practice. *Geophysics* 75, F23–F32. doi:10.1190/1.3280290

Wang, J. Y. (1990). Basic principles of the electromagnetic array profiling method. *Earth Sci. J. China Univ. Geosciences* S1, 1–11.

Wang, J. Y. (1992). On the issue of static correction in magnetotellurics. *Geol. Sci. Technol. Inf.* 11, 69–76.

Wang, J. Y. (1997). New development of magnetotelluric sounding in China. *Chin. J. Geophys.* 40 (S1), 206–216.

Wang, S. (1998). The correction of magnetotelluric curve distortion caused by surficial local three-dimension inhomogeneities: the impedance tensor decomposition technique for the correction of MT curves distortion. *Northwest. Seismol. J.* 20 (4), 1–11.

Wannamaker, P. E., Hohmann, G. W., and Ward, S. H. (1984). Magnetotelluric responses of three-dimensional bodies in layered earths. *Geophysics* 49, 1517–1533. doi:10.1190/1.1441777

Yang, J., Xiao, H. Y., Jiang, Y. D., and Yang, W. (2015). Research and application of several static shift correction methods for magnetotelluric sounding data. *Comput. Tech. Geophys. Geochem. Explor.* 37, 187–192.

Yang, S., Bao, G. S., and Zhang, S. Y. (2001). Correction of distorted apparent resistivity curves using impedance phase data in MT method. *Geol. Prospect.* 37, 42–45.

Ye, T., Chen, X., and Yan, L. (2013). Refined techniques for data processing and two-dimensional inversion in magnetotellurics (VII): electrical structure and seismogenic environment of Yingjiang-Longling seismic area. *Chin. J. Geophys.* 56 (10), 3596–3606. doi:10.6038/cjg20131034

Zhang, K., Yan, J., Cai, D., Wei, W., Qu, S., Tang, B., et al. (2016). A joint magnetotelluric field static shift 2D correction method and its application. *Earth Sci.* 41 (5), 864–872. doi:10.3799/dqkx.2016.073

Zhang, X. (1999). Identifying apparent polarized resistivity curves of TE and TM mode from magnetotelluric sounding. *J. Oil Gas Technol.* 21 (4), 72–75. doi:10.3969/j.issn.1000-9752.1999.04.026

Zhang, X., Hu, W., Yan, L., and Zhang, S. (2002). Application of wavelet transform in the static correction of magnetotelluric sounding. *J. Jianghan Petroleum Inst.* 24, 40–41.

frontiers | Frontiers in Earth Science

TYPE Original Research
PUBLISHED 21 March 2025
DOI 10.3389/feart.2025.1519524

OPEN ACCESS

EDITED BY
Yohan Guyodo,
UMR7154 Institut de Physique du Globe de Paris (IPGP), France

REVIEWED BY
Rong-wen Guo,
Central South University, China
Xiaolei Tu,
Oregon State University, United States

*CORRESPONDENCE
Yixian Xu,
xyxian@zju.edu.cn
Bo Yang,
bo.yang@zju.edu.cn

RECEIVED 30 October 2024
ACCEPTED 03 March 2025
PUBLISHED 21 March 2025

CITATION
Yang B, Meng X, Wu Y, Yang L and Xu Y (2025) Imaging Baogutu granitic intrusions in Western Junggar, NW China using an audio-frequency magnetotelluric array. *Front. Earth Sci.* 13:1519524. doi: 10.3389/feart.2025.1519524

Imaging Baogutu granitic intrusions in Western Junggar, NW China using an audio-frequency magnetotelluric array

Bo Yang[1,2]*, Xiaoling Meng[3,2], Yanjun Wu[4], Longbin Yang[5] and Yixian Xu[1]*

[1]School of Earth Sciences, Zhejiang University, Hangzhou, China, [2]Joint Laboratory of Green Geological Exploration with Zhejiang University and Inner Mongolia Geologic Survey and Research Institute, Hangzhou, China, [3]Inner Mongolia Geologic Survey and Research Institute, Hohhot, China, [4]The Surveying and Mapping Geographic Information Center of Inner Mongolia, Hohhot, China, [5]Central South Geological Survey Institute of China Metallurgical Geology Bureau, Wuhan, China

Natural-source audio-frequency magnetotelluric (AMT) data is highly sensitive to conductive anomalies associated with mineralization. To image the three-dimensional mineralized zones in the Baogutu porphyry copper belt, Western Junggar, NW China, we deployed an AMT array consisting of 176 regularly distributed sites. A parallel 3D electromagnetic data inversion scheme was employed to invert this AMT dataset. Using lab-measured electrical resistivity of rock samples, we interpret the 3D resistivity model by comparing it with borehole profiles. The most pronounced conductive anomalies in the inverted model are the east-west elongate conductive zones located at the center of the array, extending to a depth of 600 m. The inverted 3D model aligns closely with the borehole results, demonstrating that the 3D inversion of a dense AMT array can provide a high-resolution and reliable model. The electrical resistivity model shows a strong correlation with the shear wave velocity model. The positive correlation between resistivity and shear wave velocity identifies the potential mineralized areas, as supported by petrophysical and drilling data, which may assist in determining future drilling targets.

KEYWORDS

western Junggar, Baogutu, AMT, electrical resistivity structure, porphyry copper belt

1 Introduction

The audio-frequency magnetotelluric (AMT) method, along with controlled-source AMT (CSAMT), has been widely used to map shallow resistivity structures with high resolution. For example, it has been employed to trace the hydrological system of thermal fluid flow in Bakreswar hot spring, India (Sinharay et al., 2010); to image high-conductive zones at mid-crustal depths in the Otjiwarongo and Katima Mulilo regions of Namibia (Share et al., 2014); to delineate the shape of resistive granitic intrusions and their conductive surrounding metamorphic zones in West Junggar, NW China

(Yang et al., 2016); to investigate one of the major metallogenic belts in southern China, including iron and polymetallic deposits in the Longmen region (Hu et al., 2013); and to explore skarn-type ore belts in the Zhuxi polymetallic deposits (Shi et al., 2020). In the AMT procedure, we typically measure two orthogonal electrical field components (i.e., Ex and Ey) and two or three orthogonal magnetic field components (i.e., Hx, Hy, Hz) of the naturally induced electromagnetic wave in the frequency range of 20,000 Hz to approximately 1 Hz (i.e., audio-frequency). These measurements are used to estimate the impedance tensor and the vertical transfer functions, which are directly related to the electrical resistivity of the Earth. Modern 3D inversion techniques have significantly enhanced the resolution and reliability of resistivity models inverted from AMT data. However, to date, only a few 3D results have been reported. (e.g., Yang et al., 2016; Blake et al., 2016; Wang et al., 2017; Shi et al., 2021; Wan and Wang, 2023, etc.).

As the first porphyry Cu-Mo-Au deposit discovered in Western Junggar, NW China, Baogutu has garnered significant attention in recent years (e.g., Shen et al., 2010; Shen and Pan, 2013; Cao et al., 2014; Cao et al., 2015; Zheng et al., 2015; Cao et al., 2016; Cao et al., 2017, et al.). Previous studies on the metallogeny of Baogutu stocks and porphyries have predominantly relied on geological investigations. For example, Cao et al. (2014) suggested that Baogutu can be classified as a typical reduced porphyry Cu deposit. However, geophysical investigations have rarely been conducted, limiting our understanding of the deep characteristics of the deposit. This motivates us to utilize dense AMT surveying to evaluate the potential for further exploration.

Here, we present the results from imaging the 3D electrical resistivity structure of the V (5th) porphyry stock in the Baogutu area, using 176 AMT sites and 3D inversion techniques. The inverted 3D resistivity model has been interpreted in conjunction with the shear wave velocity model, as well as the electrical resistivity and shear wave velocity of rock samples, which show good agreement.

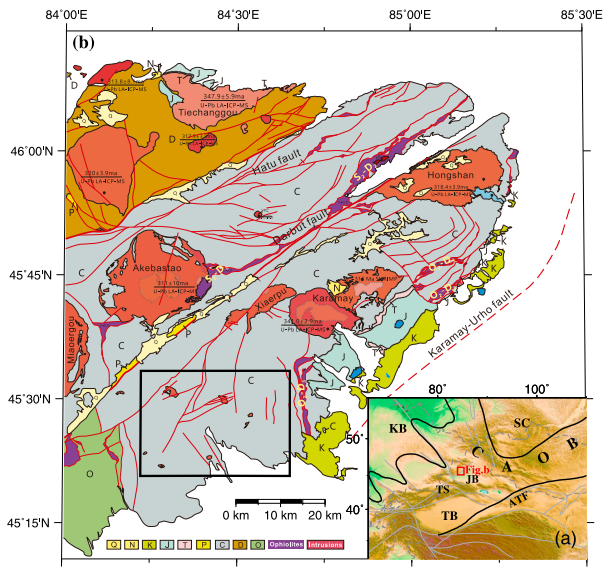

FIGURE 1
Simplified geology maps of the Western Junggar area (after Yang et al. (2016)). **(a)** Tectonic settings of NW China (after Buckman and Aitchison (2004)), illustrating that the Western Junggar area is situated in the southern part of the Central Asian Orogenic Belt (CAOB). It is surrounded by the Kazakhstan plate to the northwest, the Siberia Craton to the northeast, and the Tarim Craton to the south. The location of panel **(b)** is marked by a red box. **(b)** Simplified geology map of the Western Junggar area, showing major granitic intrusions, including Hongshan, Karamay, and Akebasitao, which are emplaced in the Carboniferous terrane. Three major faults—the Karamay-Urho Fault, the Darbut Fault, and the Hatu Fault—are indicated. The thick black rectangle outlines the range of Figure 2. Acronyms in panel **(a)**: ATF: Altyn Tagh Fault; CAOB: Central Asian Orogenic Belt; KB: Kazakhstan Block; JB: Junggar Basin; SC: Siberian Craton; TB: Tarim Block; TS: Tian Shan Mountains; Q: Quaternary; N: Neogene; K: Cretaceous; J: Jurassic; T: Triassic; P: Permian; C: Carboniferous; D: Devonian; O: Ordovician.

2 Geological settings

The Western Junggar region in NW China is situated in the southern portion of the Central Asian Orogenic Belt (CAOB, Figure 1). This area occupies a late Paleozoic convergent zone bounded by three major plates: the Tarim craton to the south, the Siberia craton to the northeast, and the Kazakhstan block to the northwest (Jahn et al., 2004; Safonova et al., 2004; Chai et al., 2009; Zhang et al., 2009; Zhao et al., 2009). The crustal growth of the CAOB, one of the most deformed areas in the Phanerozoic, has been accompanied by multi-stage and diverse crust-mantle interactions and ore-forming processes (Windley et al., 2002; Yakubchuk, 2004; Buslov et al., 2004).

The Western Junggar accretionary collage is characterized by widespread Devonian and Carboniferous island arc-related volcanic rocks, granitoids, and oceanic sediments (Buckman and Aitchison, 2004), as shown in Figure 1. The Devonian strata are mainly distributed in the northwest, while the Carboniferous strata are primarily found in the southeast (Tang et al., 2010). The most extensively distributed Lower Carboniferous layers in this area consist of three units: the Xibeikulasi Group (C1x), Baogutu Group (C1b), and Tailegula Group (C1t), from bottom to top (Zheng et al., 2009; An and Zhu, 2009; Zong et al., 2014; Zhang et al., 2015). The Late Carboniferous to Early Permian period is critical for mineral deposit formation (Yin et al., 2011). Surface exposures of ultrabasic and acidic igneous intrusions indicate that magmatism was widespread throughout the Western Junggar area during this time (Figure 1; Chen and Jahn, 2004; Chen and Arakawa, 2005; Wang and Xu, 2006).

There are two groups of intermediate-acidic intrusions in the region. The first group consists of barren granite batholiths that intruded into Devonian to Lower Carboniferous volcanic rocks and were dominant around 300 Ma (Su et al., 2006). The second group includes intermediate-acidic stocks that intruded into the Carboniferous Darbut volcanic belt, primarily between 322 and 305 Ma (Shen and Jin, 1993). Separated by the Darbut fault, alkali-feldspar granite intruded as batholiths to the north of the fault (e.g., Akebasitao and Miaoergou granitic intrusions), while the southern side of the fault is dominated by intermediate-acidic small intrusions (e.g., Baogutu and Karamay granitic intrusions) (Yin et al., 2011). Frequent and large-scale magmatism, along with simultaneous and/or late tectonic deformation and particularly multi-stage superimposed magmas, contributed to the development of the Hatu, Saertuohai, and Baogutu Cu-Au deposits in West

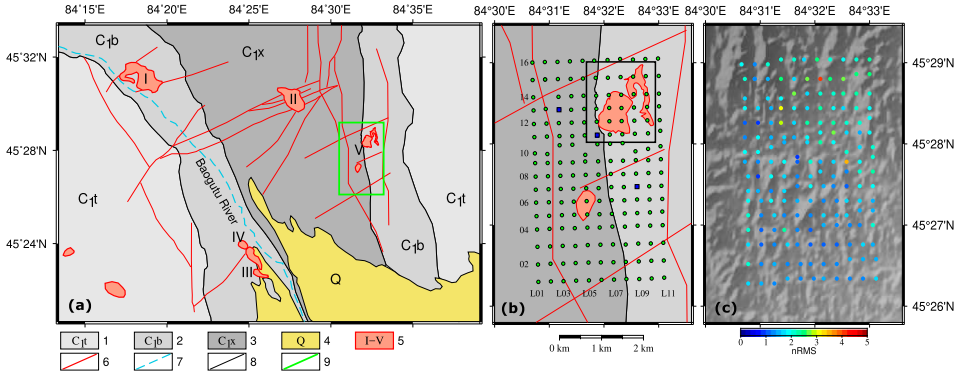

FIGURE 2
Local geology and AMT site coverage of the Baogutu area. **(a)** Simplified local geology map (after Shen et al. (2009)). Legends: 1: Tailegula Group; 2: Baogutu Group; 3: Xibeikulasi Group; 4: Quaternary; 5: Carboniferous porphyries and their corresponding numbering; 6: Faults; 7: Rivers; 8: Geological boundaries; 9: Range covered by the AMT array in panel **(b)**. **(b)** Displays the local geology of Stock V of the Baogutu granitic intrusion and AMT sites (green filled circles). Three representative sites, shown in Figure 3, are marked as dark blue squares. The black rectangular box indicates the map range for Figure 8. **(c)** The normalized root mean square errors for each AMT site of the preferred inverted model. The topography of the study area is represented in the background as a shaded relief map.

Junggar (Tang et al., 2010; Ma et al., 2012). Based on the geological structure and evolutionary history, ore deposits and mineralization have been linked to hydrothermal activity, ultrabasic rocks, and intermediate-acidic small intrusions (Cheng and Zhang, 2006). However, the nature of the granitoids and the genesis of these deposits remain subjects of debate (Cao et al., 2016).

The faults and folds are well developed in the study area (Figure 2A), with Stock V located on the eastern flank of the Baogutu anticline (Figure 2B; Yang, 2008; Zhang et al., 2010). There are three types of faults identified: NS-trending faults from the early stage, NE-trending faults from the middle stage, and sub-parallel NS-trending faults from the later stage. The early extension-shear faults are larger, extending over 10 km, and control the distribution of intermediate-acidic rocks. The middle NE-trending faults cut through the earlier NS-trending faults and intrusions, partially affecting porphyry formations. These NE-trending faults are parallel to most of the intermediate-acidic dikes and ore-bearing quartz-sulfide veins in the Baogutu Cu-Au deposits, serving as critical ore-controlling structures in the area (Wei et al., 2014). Previous studies suggest that the early NS-trending faults provide space for Cu-Au mineralization, while the NE-trending faults generally control the development of small stocks. The late-stage NS-trending faults are smaller and manifest as small cracks, which serve as the main ore-hosting structures for mineralization, often partially filled with dikes (Yang, 2008).

The Baogutu porphyry copper belt is located south of the Darbut fault in the western Junggar, approximately 40 km from Karamay city. This belt represents the eastern extension of the Tuoli Cu-Au belt in Xinjiang (Shen et al., 2009; Zhang et al., 2006). The deposits are primarily distributed in the contact zones of Hercynian intermediate-acidic intrusions and their associated dikes (Cheng and Zhang, 2006). Porphyry copper deposits develop within intermediate-acidic stocks, resulting in mineralization with thicknesses ranging from tens to hundreds of meters. While copper (Cu) is the major ore-forming element, gold (Au) and molybdenum (Mo) are also present (Cheng et al., 2009). Extensive studies have identified more than 20 ore-bearing stocks (marked with Roman numerals) (e.g., Shen et al., 2009; Shen et al., 2012; Shen and Pan, 2015; Tang et al., 2010; Zheng et al., 2015; Cao et al., 2016; Ma et al., 2012, etc.). However, limited geophysical data have been collected to delineate the deposits in Baogutu. Motivated by the successful applications of AMT data for various geological targets, we deployed a dense AMT array to image the Baogutu porphyry Cu-Au deposit within Stock V, which we present here as a case study in mineral exploration.

3 AMT data and inversion

We conducted 11 AMT profiles, with each profile consisting of 16 stations, resulting in a total of 176 sites covering a region of 3 km by 5 km (Figure 2B). The profile spacing is approximately 300 m, and the site spacing is also about 300 m in the central part of the array, increasing to around 400 m for the last 2 and 3 sites at the northern and southern ends of each profile. To minimize noise from a power line that crosses the study area from east to west, Site #10 of each profile was relocated 100 m north or south from its designated position (Figure 2B).

We used the MTU-NET system manufactured by Phoenix Geophysics to acquire the AMT data. For logistical reasons, we only recorded the horizontal electric fields (E_x, E_y) and the horizontal magnetic fields (H_x, H_y), meaning that the tipper data is not available for inversion. Two pairs of non-polarizing electrodes with 50 m arms were employed to measure the electrical field components. The study area is situated in a remote region, far from sources of cultural noise. Field tests showed that a half hour time series was sufficient to estimate the AMT transfer functions. Thus, we recorded both the electrical and magnetic field components for approximately 30 min of each site. We processed the recorded time series using the standard robust remote reference approach (open source package named EMTF, Egbert and Booker, 1986), resulting in reliable estimations of impedance from 10,000 Hz–1 Hz. The data

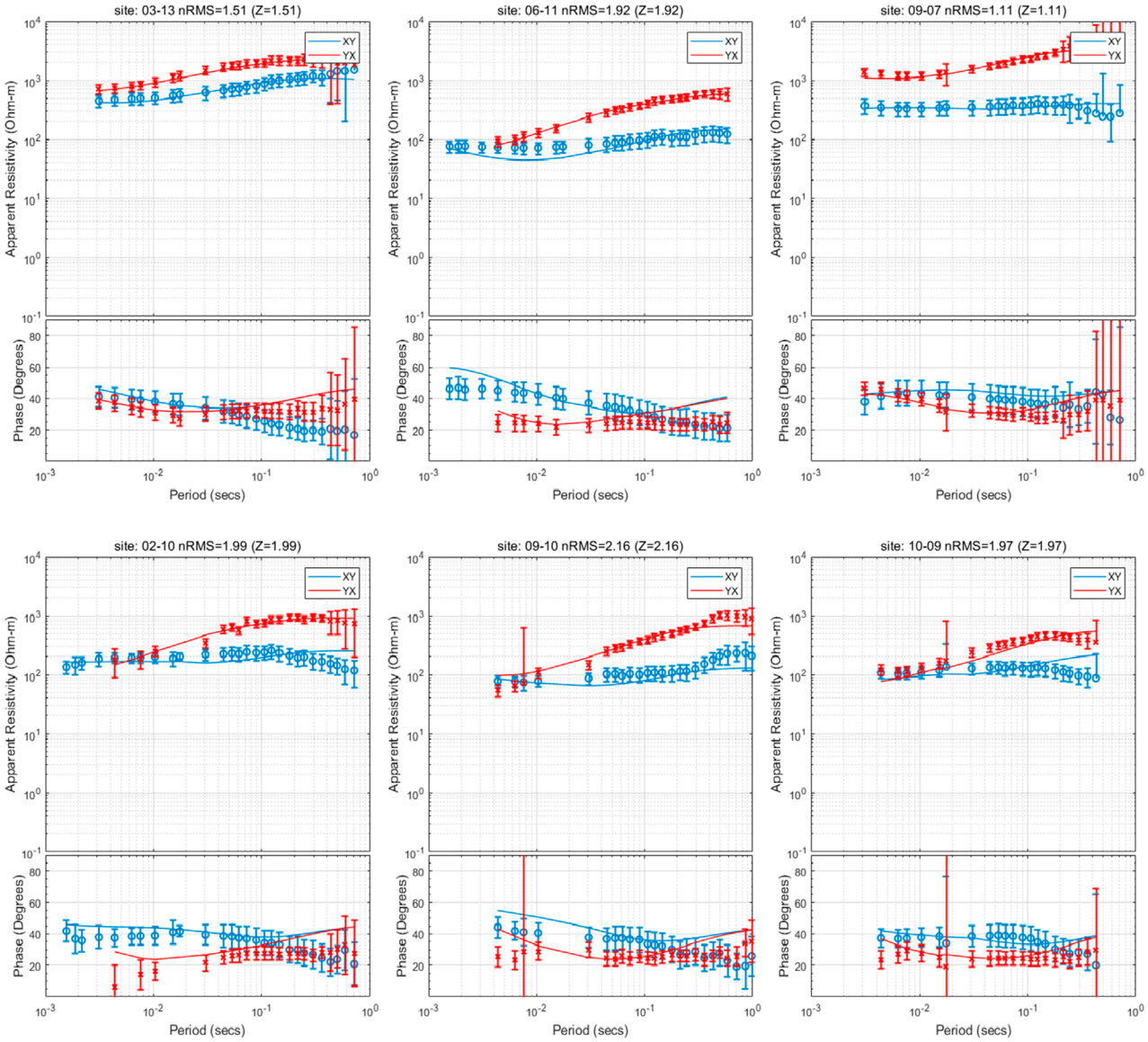

FIGURE 3
The observed (points with error bars) and predicted (solid lines) apparent resistivity and impedance phase curves of the six representative AMT sites. Site 03-13 (left panel) is situated on top of the Xibeikulasi Group; Site 06-11 is located at the boundary of the Xibeikulasi Group and Baogutu Group; Site 09-07 is situated on Baogutu Group; Site 02-10, 09-10 and 10-09 are situated on the imaged conductors C1, C3 and C4 respectively as shown in Figure 6. Note that for the error bars plotted in these apparent resistivity and phase curves, we used the ones which have applied the error floor setting, but not the original ones produced from the impedance estimation program.

quality is generally good for most sites, characterized by small error bars and low scattering. However, a few sites experienced noisy time series due to poor electrode-grounding contact and interference from the power line. For some sites, the responses in the frequency band of 10,000-1,000 Hz were discarded due to a poor signal-to-noise ratio in the magnetic field between 4,000 and 1,000 Hz, a phenomenon known as the "dead band" of AMT (Garcia and Jones, 2002). Figure 3 shows the observed apparent resistivity and phase of the off-diagonal impedance tensor for three representative stations. Sites 03-13, 06-11, and 09-07, marked by blue squares in Figure 2B, are situated atop the Xibeikulasi Group, at the boundary between the Xibeikulasi Group and the Baogutu Group, and within the Baogutu Group, respectively. These sites exhibit distinct features and good data quality.

We employed the latest parallel 3D MT data inversion scheme, the Modular system for Electromagnetic Inversion (ModEM) (Egbert and Kelbert, 2012; Kelbert et al., 2014), for 3D modeling and inversion. ModEM is widely used for interpreting MT data from continental-scale arrays (e.g., Meqbel et al., 2014; Yang et al., 2015; Bedrosian, 2016; Murphy and Egbert, 2017; Egbert et al., 2022) as well as local profiles (e.g., Xu et al., 2016b; Xu et al., 2016c), due to its power, flexibility, and availability to academic communities. The preferred 3D resistivity model presented in this paper (Figures 6, 7) was obtained by inverting the full

impedance tensor from all 176 sites across 59 periods, ranging from 10,400 Hz–0.6 Hz. The topography of the study area is relatively flat (Figure 2C), with elevation variations of less than 100 m throughout the entire region; therefore, we ignored the topographic effect in the inversion process. We tested various *a priori* models, data error floor settings, model gridding, and other inversion parameters by running the inversion multiple times to recover a reliable inverted model. For the preferred model presented here, we assigned error floors of 5% of $|Z_{xy}|$ for Z_{xx} and Z_{xy}, and 5% of $|Z_{yx}|$ for Z_{yx} and Z_{yy}. Since Z_{xx} and Z_{xy} are estimated from the same electrical-channel, they may be contaminated by similar noise sources in the electric field. Therefore, it makes sense to apply the same error floor to both components. The same rationale applies to the other row of impedance components, Z_{yx} and Z_{yy}. We believe this method of setting error floors is more reasonable, as it accounts for the inherent differences in SNR between diagonal and off-diagonal components while considering potential common noise sources.

We discretized the study area horizontally with 75 m grids in the core, padding with seven grids on all four edges, with increasing widths by a factor of 1.2 outward to the boundaries exponentially, to satisfy the boundary conditions. The model was discretized vertically with 30 layers, starting from 5 m for the first layer, and then the thickness of the layers increased logarithmically to ~20 km for the last layer. We relied upon a very fine parameterization of the uppermost layers to simulate any near-surface electrical resistivity heterogeneities, to accommodate the static shift effects caused by galvanic distortion in the observed data. Static shifts in MT data are primarily caused by static charges concentrating at the edges of shallow electrical heterogeneities. These static charges produce an electric field that does not vary with time and superposes on the varying electric field across the entire frequency band. When an MT site is located near the edge of a shallow anomaly—typically small-scale but not exclusively—the static electric field can either enhance or weaken the original time-varying E-field. This interaction results in changes to the amplitude of the MT impedance, leading to shifts in the apparent resistivity curves. Regarding the handling of static shifts, while it is theoretically possible to invert for the static shift coefficient, our practical experience suggests that parameterizing the near-surface region finely enough to model these effects directly might be a more effective approach. This method allows for a more accurate representation of the complex near-surface structures that contribute to static shifts. This discretization resulted in a $112 \times 86 \times 30$ grid, with seven additional air layers implicitly included in the modeling code.

We used the nonlinear conjugate gradient (NLCG) scheme built into ModEM to fit the data iteratively. Based on the laboratory measurements of the rock samples in the study area (Table 1), the regional background resistivity is relatively large (more than 1,000 Ω·m). Meanwhile, the median value of apparent resistivity of observed AMT sites is about 600 Ω·m. Therefore, for the preferred model we started from a 600 Ω·m half-space *a priori* model, fitting the data to a normalized root mean square (nRMS) misfit of 2.05 by 72 iterations (Figure 4). Figure 2C shows the nRMS of each site for the preferred model. Generally, the data fit is good for most of the sites, with only a few sites contaminated by noise or with poor data quality in the "dead band" showing slightly higher nRMS (orange and red dots in Figure 2C). We

TABLE 1 The electrical resistivity and shear wave velocity of rock samples in Baogutu from lab measurements.

Sample	ρ (Ω·m)	Vs. (km/s)
Quartz-rich granite-porphyry	4,508	2.76
Diorite	1909	2.43
Siltite	3,421	2.71
Granite	2,825	2.38
Gabbro	1731	2.27
Dioritic porphyrite	1,480	2.14
Altered diorite	1873	2.71

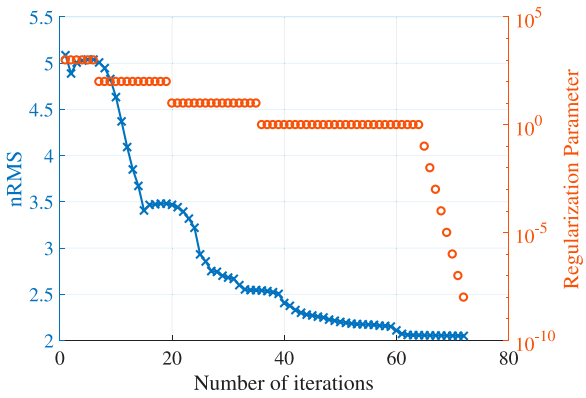

FIGURE 4
The variations of nRMS and regularization parameters as functions of number of iterations. The blue solid line and cross markers represent the variation of nRMS, while the orange circles show the regularization parameters. Note that the vertical axis for regularization parameters is on the right.

presented the apparent resistivity and phase maps of all four impedance tensor components at two representative frequencies, 320 Hz and 9.4 Hz, in Figure 5. Comparing the observed data and the predicted data (i.e., responses generated by the inverted model), almost all the main anomalies in the observed data have been reproduced in the responses of the inverted model, especially for the off-diagonal components of the impedance tensor. These three representative sites in Figure 3 also show a good fit between the predicted and observed apparent resistivities and impedance phases.

Note that the variation of nRMS with respect to the number of iterations shows fluctuations (Figure 4), particularly in the early stages. Based on our understanding, occasional small increases in nRMS are likely due to the line search scheme used in the NLCG module of ModEM. This scheme evaluates only two additional values of the objective function beyond the current nRMS value. It then uses these three points to interpolate a quadratic parabolic function. The algorithm subsequently selects the minimum of this parabola as the result of the line search. However, if the actual

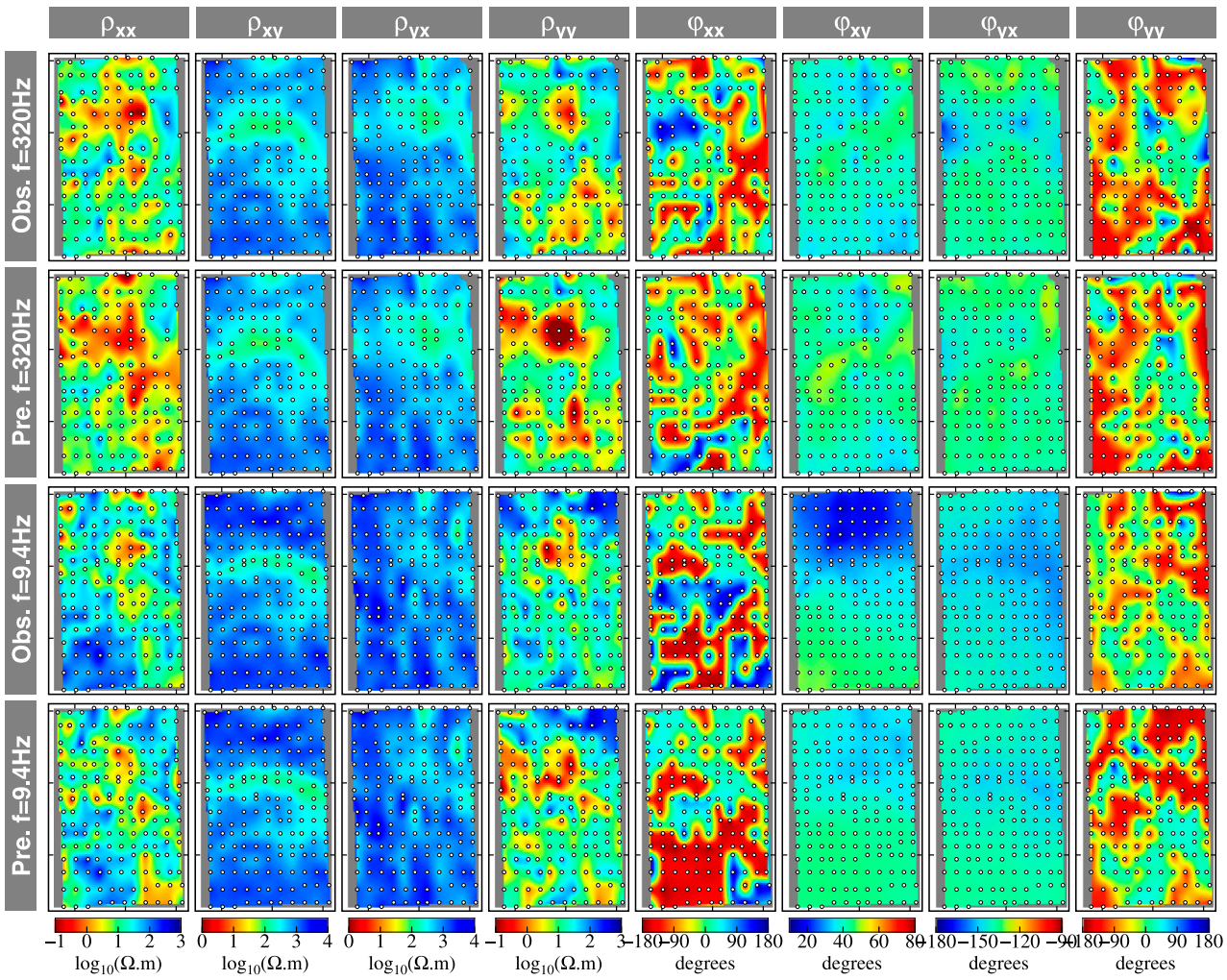

FIGURE 5
Maps of observed (1st and 3rd rows) and predicted (2nd and 4th rows) apparent resistivity (1st to 4th columns) and impedance phase (5th to 8th columns) for frequencies of 320 Hz and 9.4 Hz. The AMT sites are indicated by filled circles. All maps are interpolated from site locations using a natural neighbor interpolation algorithm. The color scales for each component are shown at the bottom of each column.

function along the search direction is not well-represented by a parabolic function, the step size determined by this method may be imprecise. This can lead to an increase in nRMS. Specifically, when the true function deviates from a parabolic shape, the chosen step size might not be optimal, resulting in temporary increases in nRMS.

4 Results and discussions

As presented in the selected depth slices (Figure 6) and the vertical cross-sections (Figure 7), the inverted 3D electrical resistivity model clearly reveals the detailed structure of the study area, ranging from dozens of meters to more than 2 km in depth. For convenience, we plotted the outlines of the outcrops V1 to V3 of Baogutu stock V from south to north in Figure 6G, along with the local faults and geological boundaries of the Xibeikulasi Group and Baogutu Group in all subplots of Figure 6. The profiles A-A' to E-E' in Figure 6H indicate the locations of the vertical cross-sections shown in Figure 7.

The most pronounced feature in the shallow depths of the model is the east-west conductive zone in the central part of the study area, which is related to the mineralized stock V. We named these conductors C1-C6 (Figure 6C). The shallow layers in the model (Figures 6A, B) indicate that C1, C3, and C4 connect to each other, while C2 does not appear until a depth of nearly 250 m (Figure 6C). In the deeper layers, as shown in the profiles A-A' and B-B' (Figure 7), C1 and C2 have merged together and connected to C3 along the east-west direction in the southern area of V2. The C4 (Figures 7D, D') and C3 (Figures 7E, E') are clearly separated from C5 by resistive intrusions beneath the outcrops V1 and V2. We have noted that two conductive spots exist in the middle and northern parts of stock V3, as shown in Figure 6D; they appear to be two independent branches. Since the current AMT array cannot constrain these two anomalies precisely, we cannot confidently describe them in detail. The conductive zone in the V1 outcrop area, which coincides with

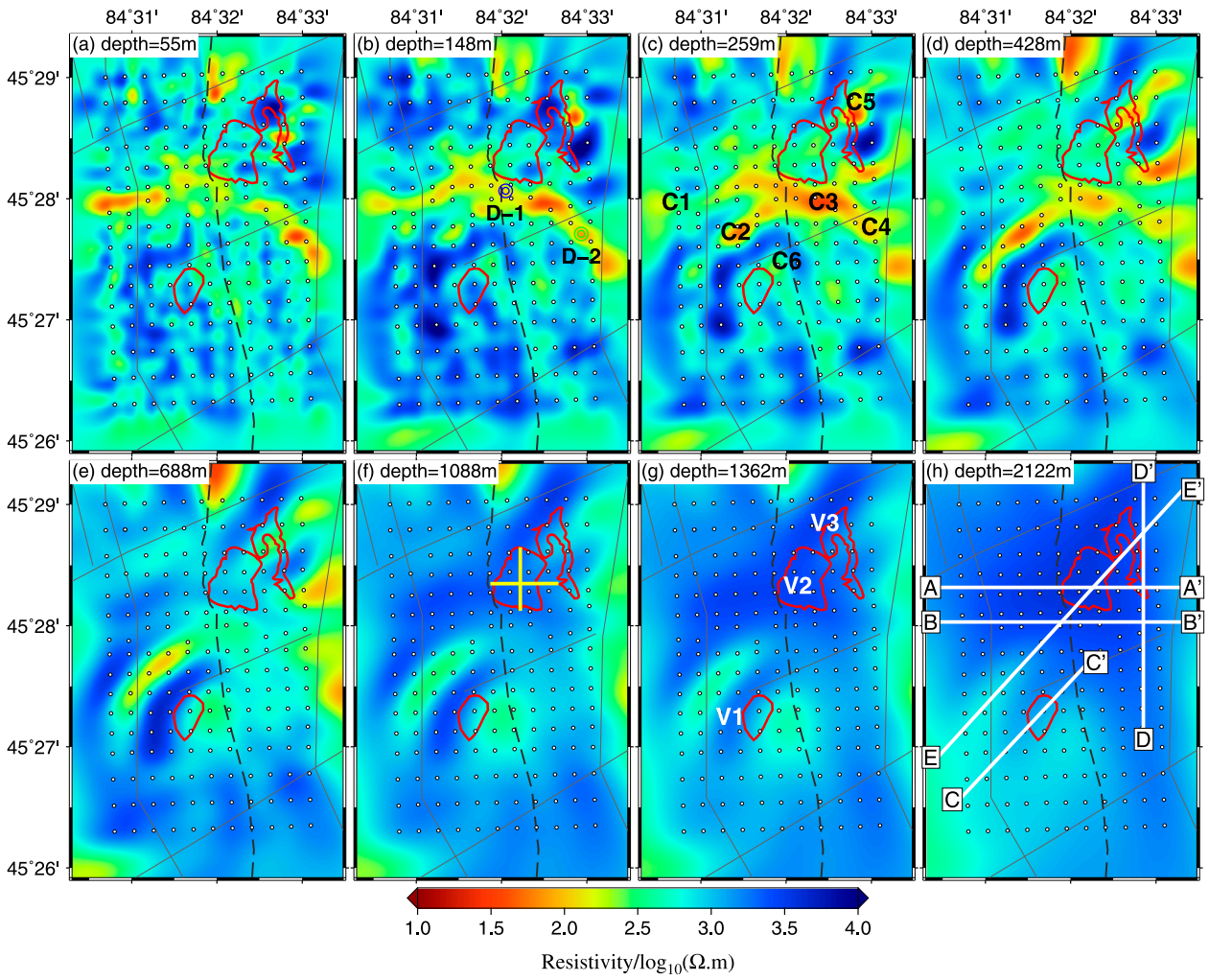

FIGURE 6
The depth slices of the preferred inverted model. **(a–h)**: Electrical resistivity at representative depths. The surficial boundaries of the V Baogutu intrusion are indicated by red solid lines. The local faults are marked by thin black lines. The boundary of the Xibeikulasi Group and Baogutu Group is outlined by black dashed line. The blue and green circles in panel **(b)** mark the prompted drilling holes: D-1 and D-2. Two thick solid yellow lines in panel **(f)** show the location of profiles in Figures 8B, C. Profiles A-A′ to E-E′ in panel **(h)** give the locations of the vertical cross-sections shown in Figure 7. C1-C6 mark the conductors discussed in the main text.

the outcrop boundary (Figures 6A–E), extends vertically from the surface to approximately 700 m in depth.

Dozens of boreholes have been drilled in stock V-2 (e.g., Shen et al., 2009; Shen et al., 2010). Two lithologic profiles have been compiled from the drilling cores of these boreholes (Shen et al., 2010). To verify the conductive anomalies in the preferred model, we plotted the vertical cross-sections alongside the lithologic and mineral profiles revealed by the borehole results (Shen et al., 2010). The lithologic outlines were adapted from Shen et al. (2010). The green polygons in Figure 8B, C indicate that the orebodies are primarily distributed in the upper 600 m of stock V-2, where a highly conductive anomaly (20-40 Ω·m) corresponds with the copper mineralization. To enhance the interpretation of the inverted model, we also collected rock samples from the Baogutu area and measured their electrical resistivity and shear wave velocity in the laboratory. As shown in Table 1, all samples, whether from volcanic rocks or sediments, are relatively resistive (1,000-4,000 Ω·m), while the copper orebodies are significantly more conductive (approximately 30 Ω·m). The two borehole profiles (Figures 8B, C) demonstrate that a dioritic intrusion extends from depth to 400 m, coinciding with the AMT imaging model.

Considering the lack of high-frequency data (10,000–1,000 Hz), which is primarily sensitive to depths of 100–300 m in a 600 Ω·m half-space, and the limited number of AMT sites (only 4-5) available to constrain the structures near the borehole profiles, the inverted model aligns surprisingly well with the borehole data. This consistency suggests that 3D inversion of AMT data from an array of regularly distributed sites can yield reliable and high-resolution imaging results.

The porphyry Cu-Au-Mo mineralization in West Junggar is associated with intermediate intrusive rocks. Typically, ore-bearing mineralization occurs in the upper stocks and in the contact zones between the stocks and their country rocks (Shen et al., 2009). In our inverted model, several high-conductivity zones can

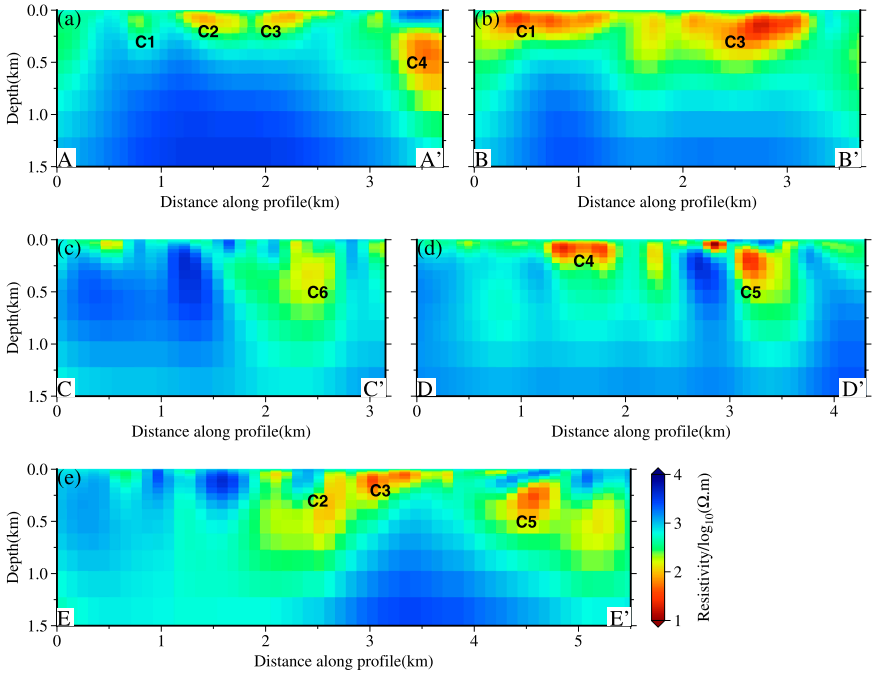

FIGURE 7
Representative vertical cross-sections passing through the intrusion and the conductors. The location of these profiles is shown in Figure 6H.

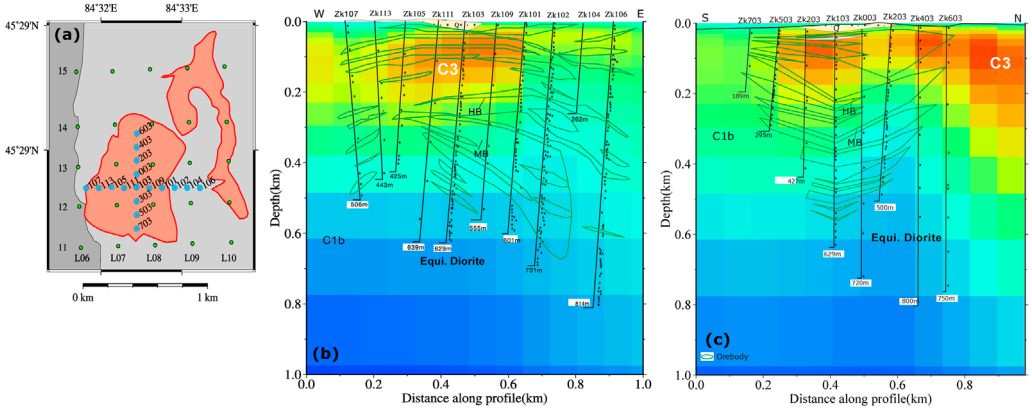

FIGURE 8
The cross sections of preferred model comparing with boreholes. **(a)** Location and numbering of boreholes from Shen et al. (2010). The boreholes are shown as skyblue circles. **(b)** The vertical cross-section of the preferred model overlies by the E-W profile interpreted from boreholes in Shen et al. (2010): Figure 7B. We only keep the outlines of the original boreholes profile for better comparison. The color bar of the resistivity is the same as in Figure 6. **(c)** The vertical cross-section of the preferred model overlies by the N-S profile. Legends are the same as in panel **(b)**.

be identified as potential mineralized zones. As noted earlier, all major conductive anomalies are located on the flanks or in the uppermost zones of the stocks.

For stock V2, the orebodies are likely distributed along the southern boundary, exhibiting a shallow east-west extension and a deeper southwest trend. Drilling results in stock V2 indicate that the ore-bearing porphyry extends to approximately 600 m in depth (Shen et al., 2009), which aligns well with our model. Furthermore, C3 connects with C2 at depth and extends more than 1 km, suggesting significant mineralization occurs at depths of 200 m to 1 km along the southern edge of stock V2. The conductor C4 may represent an orebody associated with small faults. As suggested by Richards (2003), large porphyry deposits are likely formed where magma ascents are concentrated at structural intersections. However, conductor C1 might also represent an isolated orebody developed at shallower depths within the Xibeikulasi Group. In all depth slices shallower than 1 km, we can clearly identify an independent high-conductivity area, C6, at the northeast boundary

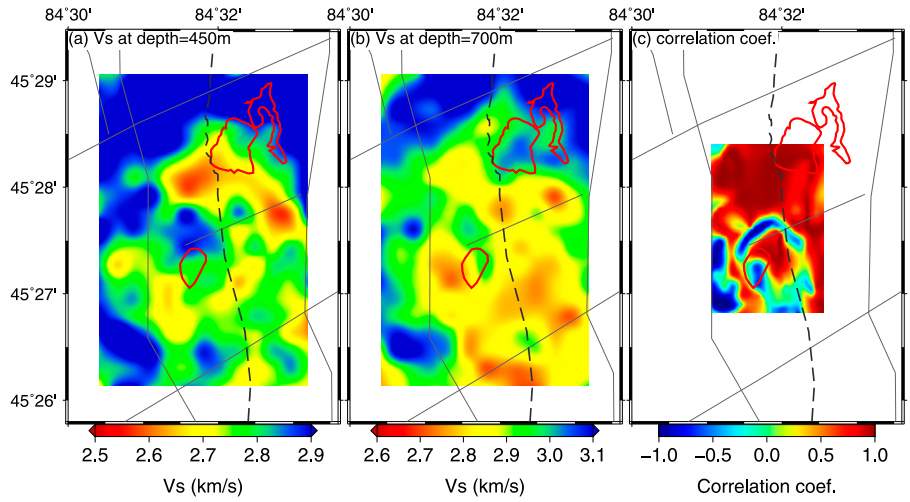

FIGURE 9
The 450 m **(a)** and 700 m **(b)** depth slices of shear wave velocity model from Xu (H) et al. (2016) and the correlation coefficients **(c)** between the electrical resistivity model and the shear wave velocity model.

of stock V1. This area is likely an ore-bearing stock extending vertically to 700 m, associated with the intermediate intrusion. For stock V3, conductor C5 likely highlights an orebody that may develop independently on the northeast flank of the stock at depths of 100 m–800 m (Figure 7D).

Shen and Pan (2015) suggested that the mineralized intrusive phases at the Baogutu porphyry belt comprise the main-stage diorite stock and minor late-stage diorite porphyry dikes. The main-stage host experienced significant hydrothermal alteration and contains the majority of the Cu-Mo-Au mineralization. This implies that the presence of high-conductivity zones near stock V is likely associated with the Cu-Au deposit.

Xu H. et al. (2016) employed the eikonal tomography method to map the shallow 3D velocity structure of the Baogutu V stock belt. They noted that the Xibeikulasi Group (C1x) in the west exhibits a higher shear wave velocity compared to the Baogutu Group (C1b) in the east. However, our model does not reveal any significant resistivity differences between these two groups, suggesting that they likely have similar conductivity. To facilitate comparison with the shear wave velocity model, we plotted two depth slices (at 450 m and 700 m) in Figures 9A, B, using the same map range as in Figure 6. In Figure 9A, the low shear wave velocity anomaly at the southern edge of stock V2 aligns closely with conductor C3. Additionally, measurements of rock samples indicate that ore-bearing intrusive rocks (e.g., gabbro, dioritic-porphyrite) possess low shear wave velocities and relatively low resistivity, especially when mineralized, suggesting that C3 could be a promising mineralized zone. To examine the overall correlation between the shear wave velocity (Vs.) model and the resistivity model, we computed their Pearson's correlation coefficient by first interpolating them onto the same grid and then calculating the correlation coefficient point by point with respect to the depth variations of the models using following Equation 1

$$R(\sigma, V) = \frac{1}{N-1}\sum_{i=1}^{N}\left(\frac{\sigma_i - \mu_\sigma}{\delta_\sigma}\right)\left(\frac{V_i - \mu_V}{\delta_V}\right) \quad (1)$$

where R is the correlation coefficient, σ_i, μ_σ and δ_σ are the electrical conductivity, its mean and standard deviation respectively, V_i, μ_V and δ_V are the shear wave velocity, its mean and standard deviation.

It is important to note that the Vs. model is best resolved only in the central part of the array (see Xu et al., 2016a, for details), so we limited our correlation analysis to this region. As shown in Figure 9C, the resistivity model strongly positively correlates with Vs. at the southern edge of stock V2, while it shows a strong negative correlation with Vs. at stock V1. This suggests that stock V1 may have different lithological properties compared to stock V2. The strong positive correlation between S-wave velocity (Vs.) and conductivity observed in Stock V1 and V2 likely indicates the presence of a fracture zone associated with a local fault. Additionally, a prominent negative correlation belt surrounding Stock V1 is one of the most notable features. This area's low conductivity and high Vs. values may suggest the formation of a fracture contact zone during the intrusion of the magmatic stock.

Regarding the metallogenesis of the Baogutu porphyry copper belt, Zhang et al. (2010) suggested that the Baogutu porphyry copper deposit may have formed in the Late Carboniferous, with its mineralization closely linked to the intrusion of intermediate-acidic porphyry bodies. They posited that the ore-forming fluid originates from deep magmatic waters. Tang et al. (2010) and Yin et al. (2010) proposed that the Baogutu Cu-Au deposits could occur above a slab window during ocean ridge subduction, where the interaction between high-oxygen fugacity slab melt and mantle peridotite leads to the decomposition of metal sulfides, subsequently promoting Cu and Au mineralization. Furthermore, Shen et al. (2009) suggested that the ore-bearing porphyry system derives from the partial melting of multiple sources, including oceanic crust and a subduction-modified mantle wedge, with significant crystal fractionation occurring during the convergence between the paleo-Junggar ocean and the Darbut arc. Given the

limitations of our AMT data, which lacks long-period information and covers only a relatively small aperture, we are unable to resolve any structures deeper than 2 km. This restriction complicates discussions surrounding the metallogenesis of the Baogutu porphyry copper deposit in our study area. However, based on the tectonic evolution inferred from the regional-scale resistivity model (Xu et al., 2016b), we support the view that the Baogutu porphyry copper belt is likely related to an intra-oceanic subduction event beneath the Darbut arc during the Late Paleozoic.

5 Conclusion

We imaged the high-resolution resistivity structure of stock V of the Baogutu intermediate-acidic intrusions using an AMT dataset consisting of 176 sites. The Baogutu porphyry copper belt is distinctly represented as conductive zones along the flanks of outcrops V1 to V3, particularly at the northeast flanks of V1 and V3, and extending in an east-west direction between V1 and V2. Our model, inverted from the AMT data, reveals that all significant high electrical conductivity zones extend from the surface to approximately 600 m in depth. When integrated with previous geological, geochemical, and geophysical studies, our model provides insights into the 3D structure of the Cu-Mo-Au mineralization zones associated with the magmatic activities of the Baogutu intrusions. Most mineralization appears to develop irregularly within the ore-bearing stocks and at the contact zones between the stocks and their country rocks, suggesting that the porphyry copper deposits may be influenced by small intermediate-acidic intrusions rather than showing significant correlations with existing faults. Comparing our results with borehole profiles, the AMT imaging aligns closely with the lithological profiles compiled from drilling cores. The resistivity model also demonstrates a strong correlation with the shear wave velocity model. We recommend that further drilling be conducted at other promising conductive anomalies. Additionally, to enhance our understanding of metallogenesis, the current array should be expanded to include broadband MT stations.

Data availability statement

The raw data supporting the conclusions of this article will be made available by the authors, with reasonable request.

Author contributions

BY: Funding acquisition, Methodology, Resources, Software, Visualization, Writing–original draft, Writing–review and editing, Data curation, Formal Analysis, Investigation, Conceptualization, Validation. XM: Formal Analysis, Investigation, Resources, Validation, Writing–review and editing. YW: Formal Analysis, Investigation, Resources, Validation, Writing–review and editing. LY: Data curation, Formal Analysis, Investigation, Resources, Validation, Writing–review and editing. YX: Conceptualization, Funding acquisition, Investigation, Project administration, Supervision, Writing–review and editing.

Funding

The author(s) declare that financial support was received for the research and/or publication of this article. This research was financially supported by China National Science and Technology Major Project: Deep Earth Probe and Mineral Resources Exploration (grant 2024ZD1000200), NSFC (grant 42474103) and China Geological Survey for the project “Deep Geological Investigation of the Karamay Back Mountain Area in Western Junggar, Xinjiang” (Grant 1212011220245).

Acknowledgments

We would like to extend our gratitude to Dr. Ying Liu from the China University of Geosciences in Wuhan, China, and Dr. Anqi Zhang from the Innovation Academy for Precision Measurement Science and Technology at the Chinese Academy of Sciences. Their extensive discussions and valuable insights were instrumental throughout this study. Additionally, we are grateful for the constructive comments and insightful suggestions provided by three reviewers, which significantly enhanced the quality of this paper.

Conflict of interest

The authors declare that the research was conducted in the absence of any commercial or financial relationships that could be construed as a potential conflict of interest.

Generative AI statement

The author(s) declare that no Generative AI was used in the creation of this manuscript.

Publisher’s note

References

An, F., and Zhu, Y. (2009). Significance of native arsenic in the Baogutu gold deposit, western Junggar, Xinjiang, NW China (in Chinese with English abstract). *Chin. Sci. Bull.* 54, 1465–1470. doi:10.1007/s11434-009-0086-6

Bedrosian, P. A. (2016). Making it and breaking it in the Midwest: continental assembly and rifting from modeling of EarthScope magnetotelluric data. *Precambrian Res.* 278, 337–361. doi:10.1016/j.precamres.2016.03.009

Blake, S., Henry, T., Muller, M. R., Jones, A. G., Moore, J. P., Murray, J., et al. (2016). Understanding hydrothermal circulation patterns at a low-enthalpy thermal spring using audio-magnetotelluric data: a case study from Ireland. *J. Appl. Geophys.* 132, 1–16. doi:10.1016/j.jappgeo.2016.06.007

Buckman, S., and Aitchison, J. C. (2004). Tectonic evolution of palaeozoic terranes in West Junggar, xinjiang, NW China. Geological Society London Special Publications 226, 101–129.

Buslov, M. M., Fujiwara, Y., Iwata, K., and Semakov, N. N. (2004). Late paleozoic-early mesozoic geodynamics of central asia. *Gondwana Res.* 7, 791–808. doi:10.1016/s1342-937x(05)71064-9

Cao, M., Qin, K., Li, G., Evans, N. J., Hollings, P., Maisch, M., et al. (2017). Mineralogical evidence for crystallization conditions and petrogenesis of ilmenite-series I-type granitoids at the Baogutu reduced porphyry Cu deposit (Western Junggar, NW China): Mössbauer spectroscopy, EPM and LA-(MC)-ICPMS analyses. *Ore Geol. Rev.* 86, 382–403. doi:10.1016/j.oregeorev.2017.02.033

Cao, M., Qin, K., Li, G., Evans, N. J., and Jin, L. (2015). *In situ* LA-(MC)-ICP-MS trace element and Nd isotopic compositions and genesis of polygenetic titanite from the Baogutu reduced porphyry Cu deposit, Western Junggar, NW China. *Ore Geol. Rev.* 65, 940–954. doi:10.1016/j.oregeorev.2014.07.014

Cao, M., Qin, K., Li, G., Jin, L., Evans, N. J., and Yang, X. (2014). Baogutu: an example of reduced porphyry Cu deposit in western Junggar. *Ore Geol. Rev.* 56, 159–180. doi:10.1016/j.oregeorev.2013.08.014

Cao, M. J., Qin, K. Z., Li, G. M., Evans, N. J., Hollings, P., and Jin, L. Y. (2016). Genesis of ilmenite-series I-type granitoids at the Baogutu reduced porphyry Cu deposit, western Junggar, NW-China. *Lithos* 246-247, 13–30. doi:10.1016/j.lithos.2015.12.019

Chai, F., Mao, J., Dong, L., Yang, F., Liu, F., Geng, X., et al. (2009). Geochronology of metarhyolites from the kangbutiebao formation in the kelang basin, altay Mountains, xinjiang: implications for the tectonic evolution and metallogeny. *Gondwana Res.* 16, 189–200. doi:10.1016/j.gr.2009.03.002

Chen, B., and Arakawa, Y. (2005). Elemental and Nd-Sr isotopic geochemistry of granitoids from the West Junggar foldbelt (NW China), with implications for Phanerozoic continental growth. *Geochimica Cosmochimica Acta* 69, 1307–1320. doi:10.1016/j.gca.2004.09.019

Chen, B., and Jahn, B. M. (2004). Genesis of post-collisional granitoids and basement nature of the Junggar Terrane, NW China: Nd-Sr isotope and trace element evidence. *J. Asian Earth Sci.* 23, 691–703. doi:10.1016/s1367-9120(03)00118-4

Cheng, Y., and Zhang, R. (2006). Mineralization regularity of Cu-Au deposits in the Baogutu area, western Junggar, Xinjiang (in Chinese with English abstract). *Geol. Prospect.* 42, 11–15.

Cheng, Y., Zhang, R., and Qi, G. (2009). "Mineralization regularity of Cu-Au deposits in the Baogutu area, western Junggar, Xinjiang,", 32. Xinjiang nonferrous metals, 29–30.

Egbert, G. D., and Booker, J. R. (1986). Robust estimation of geomagnetic transfer functions. *Geophys. J. R. Astronomical Soc.* 87, 173–194. doi:10.1111/j.1365-246X.1986.tb04552.x

Egbert, G. D., and Kelbert, A. (2012). Computational recipes for electromagnetic inverse problems. *Geophys. J. Int.* 189, 251–267. doi:10.1111/j.1365-246x.2011.05347.x

Egbert, G. D., Yang, B., Bedrosian, P. A., Key, K., Livelybrooks, D. W., Schultz, A., et al. (2022). Fluid transport and storage in the cascadia forearc influenced by overriding plate lithology. *Nat. Geosci.* 15, 677–682. doi:10.1038/s41561-022-00981-8

Garcia, X., and Jones, A. (2002). Atmospheric sources for audio-magnetotelluric (AMT) sounding. *Geophysics* 67, 448–458. doi:10.1190/1.1468604

Hu, X., Peng, R., Wu, G., Wang, W., Huo, G., and Han, B. (2013). Mineral exploration using CSAMT data: application to longmen region metallogenic belt, guangdong province, China. *GEOPHYSICS* 78, B111–B119. doi:10.1190/geo2012-0115.1

Jahn, B. M., Capdevila, R., Liu, D., Vernon, A., and Badarch, G. (2004). Sources of Phanerozoic granitoids in the transect Bayanhongor-Ulaan Baatar, Mongolia: geochemical and Nd isotopic evidence, and implications for Phanerozoic crustal growth. *J. Asian Earth Sci.* 23, 629–653. doi:10.1016/s1367-9120(03)00125-1

Kelbert, A., Meqbel, N., Egbert, G. D., and Tandon, K. (2014). ModEM: a modular system for inversion of electromagnetic geophysical data. *Comput. and Geosciences* 66, 40–53. doi:10.1016/j.cageo.2014.01.010

Ma, C., Xiao, W., Windley, B. F., Zhao, G., Han, C., Zhang, J., et al. (2012). Tracing a subducted ridge-transform system in a late Carboniferous accretionary prism of the southern Altaids: orthogonal sanukitoid dyke swarms in Western Junggar, NW China. *Lithos* 140-141, 152–165. doi:10.1016/j.lithos.2012.02.005

Meqbel, N. M., Egbert, G. D., Wannamaker, P. E., Kelbert, A., and Schultz, A. (2014). Deep electrical resistivity structure of the northwestern U.S. derived from 3-D inversion of USArray magnetotelluric data. *Earth Planet. Sci. Lett.* 402, 290–304. doi:10.1016/j.epsl.2013.12.026

Murphy, B. S., and Egbert, G. D. (2017). Electrical conductivity structure of southeastern North America: implications for lithospheric architecture and Appalachian topographic rejuvenation. *Earth Planet. Sci. Lett.* 462, 66–75. doi:10.1016/j.epsl.2017.01.009

Richards, J. P. (2003). Tectono-magmatic precursors for porphyry Cu-(Mo-Au) deposit formation. *Econ. Geol.* 98, 1515–1533. doi:10.2113/98.8.1515

Safonova, I. Y., Buslov, M. M., Iwata, K., and Kokh, D. A. (2004). Fragments of vendian-early carboniferous oceanic crust of the paleo-asian ocean in foldbelts of the altai-sayan region of central asia: geochemistry, biostratigraphy and structural setting. *Gondwana Res.* 7, 771–790. doi:10.1016/s1342-937x(05)71063-7

Share, P., Jones, A., Muller, M., Khoza, D., Miensopust, M., and Webb, S. (2014). An audio-magnetotelluric investigation of the Otjiwarongo and Katima Mulilo regions, Namibia. *Geophysics* 79, B151–B171. doi:10.1190/geo2013-0171.1

Shen, P., and Pan, H. (2013). Country-rock contamination of magmas associated with the Baogutu porphyry Cu deposit, Xinjiang, China. *Lithos* 177, 451–469. doi:10.1016/j.lithos.2013.07.019

Shen, P., and Pan, H. D. (2015). Methane origin and oxygen-fugacity evolution of the Baogutu reduced porphyry Cu deposit in the West Junggar terrain, China. *Miner. Deposita* 50, 967–986. doi:10.1007/s00126-015-0580-5

Shen, P., Shen, Y., Liu, T., Meng, L., Dai, H., and Yang, Y. (2009). Geochemical signature of porphyries in the Baogutu porphyry copper belt, Western Junggar, NW China. *Gondwana Res.* 16, 227–242. doi:10.1016/j.gr.2009.04.004

Shen, P., Shen, Y., Pan, H., Li, X. H., Dong, L., Wang, J., et al. (2012). Geochronology and isotope geochemistry of the Baogutu porphyry copper deposit in the West Junggar region, Xinjiang, China. *J. Asian Earth Sci.* 49, 99–115. doi:10.1016/j.jseaes.2011.11.025

Shen, P., Shen, Y., Pan, H., Wang, J., Zhang, R., and Zhang, Y. (2010). Baogutu porphyry Cu-Mo-Au deposit, West Junggar, northwest China: petrology, alteration, and mineralization. *Econ. Geol.* 105, 947–970. doi:10.2113/econgeo.105.5.947

Shen, Y., and Jin, C. (1993). Magmatism and gold mineralization in Western Junggar area

Shi, Y., Ouyang, Y., Xu, Y., Yang, B., and Liu, S. (2021). *Three-dimensional electrical structure of the Taqian-Zhuxi copper-tungsten polymetallic deposits, South China Denver, CO and virtual*. Society of Exploration Geophysicists, 1271–1274. doi:10.1190/segam2021-3580700.1

Shi, Y., Xu, Y., Yang, B., Peng, Z., and Liu, S. (2020). Three-dimensional audio-frequency magnetotelluric imaging of Zhuxi copper-tungsten polymetallic deposits, South China. *J. Appl. Geophys.* 172, 103910. doi:10.1016/j.jappgeo.2019.103910

Sinharay, R., Srivastava, S., and Bhattacharya, B. (2010). Audiomagnetotelluric studies to trace the hydrological system of thermal fluid flow of Bakreswar Hot Spring, Eastern India: a case history. *GEOPHYSICS* 75, B187–B195. doi:10.1190/1.3431532

Su, Y., Tang, H., Hou, G., and Liu, C. (2006). Geochemistry of aluminous A-type granites along Darabut tectonic belt in West Junggar, Xinjiang (in Chinese with English abstract). *Geochimica* 35, 55–67.

Tang, G., Wang, Q., Wyman, D. A., Li, Z. X., Zhao, Z. H., Jia, X. H., et al. (2010). Ridge subduction and crustal growth in the Central Asian Orogenic Belt: evidence from Late Carboniferous adakites and high-Mg diorites in the western Junggar region, northern Xinjiang (west China). *Chem. Geol.* 277, 281–300. doi:10.1016/j.chemgeo.2010.08.012

Wan, H., and Wang, Q. (2023). Electrical structure of gulu geothermal field in southern tibet and its implication for the high-temperature geothermal system. *Front. Earth Sci.* 11. doi:10.3389/feart.2023.1138360

Wang, J., and Xu, X. (2006). Post-collisional tectonic evolution and metallogenesis in northern Xinjiang, China (in Chinese with English abstract). *Acta Petrol. Sin.* 80, 23–31.

Wang, N., Zhao, S., Hui, J., and Qin, Q. (2017). Three-dimensional audio-magnetotelluric sounding in monitoring coalbed methane reservoirs. *J. Appl. Geophys.* 138, 198–209. doi:10.1016/j.jappgeo.2017.01.028

Wei, S., Zhu, Y., and An, F. (2014). Mineralization and elements migration characteristics of porphyry copper deposits in Baogutu area, Xinjiang (in Chinese with English abstract). *Mineral. Deposits* 33, 165–180.

Windley, B. F., Kroner, A., Guo, J., Qu, G., Li, Y., and Zhang, C. (2002). Neoproterozoic to paleozoic geology of the altai orogen, NW China: new zircon age data and tectonic evolution. *J. Geol.* 110, 719–737. doi:10.1086/342866

Xu, H., Luo, Y., Chen, C., and Xu, Y. (2016a). 3D shallow structures in the Baogutu area, Karamay, determined by eikonal tomography of short-period ambient noise surface waves. *J. Appl. Geophys.* 129, 101–110. doi:10.1016/j.jappgeo.2016.03.037

Xu, Y., Yang, B., Zhang, S., Liu, Y., Zhu, L., Huang, R., et al. (2016b). Magnetotelluric imaging of a fossil paleozoic intra-oceanic subduction zone in western junggar, NW China. *J. Geophys. Res. Solid Earth* 121, 4103–4117. doi:10.1002/2015JB012394

Xu, Y., Zhang, S., Griffin, W. L., Yang, Y., Yang, B., Luo, Y., et al. (2016c). How did the Dabie Orogen collapse? Insights from 3-D magnetotelluric imaging of profile data. *J. Geophys. Res. Solid Earth* 121, 5169–5185. doi:10.1002/2015JB012717

Yakubchuk, A. (2004). Architecture and mineral deposit settings of the Altaid orogenic collage: a revised model. *J. Asian Earth Sci.* 23, 761–779. doi:10.1016/j.jseaes.2004.01.006

Yang, B., Egbert, D. G., Kelbert, A., and Naser, M. M. (2015). Three-dimensional electrical resistivity of the north-central USA from EarthScope long period magnetotelluric data. *Earth Planet. Sci. Lett.* 422, 87–93. doi:10.1016/j.epsl.2015.04.006

Yang, B., Zhang, A., Zhang, S., Liu, Y., Zhang, S., Li, Y., et al. (2016). Three-dimensional audio-frequency magnetotelluric imaging of Akebasitao granitic intrusions in Western Junggar, NW China. *J. Appl. Geophys.* 135, 288–296. doi:10.1016/j.jappgeo.2016.10.010

Yang, Z. (2008). Geological and geochemical anomalies of porphyry Cu deposit in Baogutu area, Tuoli country, Xinjiang, China (in Chinese with English abstract). *Xinjiang nonferrous Met.* 31, 14–16.

Yin, J., Yuan, C., Sun, M., Long, X., Zhao, G., Wong, K. P., et al. (2010). Late Carboniferous high-Mg dioritic dikes in Western Junggar, NW China: geochemical features, petrogenesis and tectonic implications. *Gondwana Res.* 17, 145–152. doi:10.1016/j.gr.2009.05.011

Yin, J., Yuan, C., Wang, Y., Long, X., and Guan, Y. (2011). Magmatic records on the late paleozoic tectonic evolution of western junggar,xinjiang (in Chinese with English abstract). *Geotect. Metallogenia* 35, 278–291.

Zhang, L., Wang, G., Gao, R., Shen, T., Zong, R., and Yan, W. (2015). U-pb chronology of detrital zircons from the carboniferous sequences and its geological implications in west Junggar (in Chinese with English abstract). *Geotect. Metallogenia* 39, 704–718.

Zhang, R., Yunxiao, Z., Tong, G., Wang, J., and Li, L. (2006). Major breakthrough in copper exploration in the Baogutu porphyry copper deposit, western Junggar, Xinjiang, and its significance (in Chinese with English abstract). *Geol. China* 33, 1354–1360.

Zhang, Z., Yang, F., Yan, S., Zhang, R., Chao, F., and Geng, X. (2010). Sources of ore-forming fluids and materials of the Baogutu porphyry copper deposit in Xinjiang Constraints from sulfur-hydrogen-oxygen isotopes geochemistry (in Chinese with English abstract). *Acta Petrol. Sin.* 26, 707–716.

Zhang, Z., Zhou, G., Kusky, T. M., Yan, S., Chen, B., and Zhao, L. (2009). Late Paleozoic volcanic record of the Eastern Junggar terrane, Xinjiang, Northwestern China: major and trace element characteristics, Sr-Nd isotopic systematics and implications for tectonic evolution. *Gondwana Res.* 16, 201–215. doi:10.1016/j.gr.2009.03.004

Zhao, Z., Xiong, X., Wang, Q., Bai, Z., and Qiao, Y. (2009). Late paleozoic underplating in north xinjiang: evidence from shoshonites and adakites. *Gondwana Res.* 16, 216–226. doi:10.1016/j.gr.2009.03.001

Zheng, B., An, F., and Zhu, Y. (2009). Native bismuth found in Baogutu gold deposit and its geological significance (in Chinese with English abstract). *Acta Petrol. Sin.* 25, 1426–1436.

Zheng, B., Zhu, Y., An, F., Huang, Q. Y., and Qiu, T. (2015). As-Sb-Bi-Au mineralization in the Baogutu gold deposit, Xinjiang, NW China. *Ore Geol. Rev.* 69, 17–32. doi:10.1016/j.oregeorev.2015.01.019

Zong, R., Gong, Y., and Wang, G. (2014). Carboniferous stratal sequence and its palaeogeographical evolution in southern western Junggar, NW China (in Chinese with English abstract). *Earth Sci. Front.* 21, 216–233.

frontiers | Frontiers in Earth Science

TYPE Original Research
PUBLISHED 28 April 2025
DOI 10.3389/feart.2025.1526835

OPEN ACCESS

EDITED BY
Agata Siniscalchi,
University of Bari Aldo Moro, Italy

REVIEWED BY
Angelo De Santis,
National Institute of Geophysics and Volcanology (INGV), Italy
Tiaojie Xiao,
National University of Defense Technology, China

*CORRESPONDENCE
Ying Liu,
liuying@cug.edu.cn

RECEIVED 12 November 2024
ACCEPTED 14 April 2025
PUBLISHED 28 April 2025

CITATION
Ji X, Xu Z, Huang Z, Zhao W and Liu Y (2025) Identification and parameter estimation for electrical anisotropy in two-dimensional magnetotelluric models.
Front. Earth Sci. 13:1526835.
doi: 10.3389/feart.2025.1526835

Identification and parameter estimation for electrical anisotropy in two-dimensional magnetotelluric models

Xiaojie Ji[1], Zidong Xu[2], Zejiao Huang[2], Wei Zhao[1] and Ying Liu[1]*

[1]Hubei Subsurface Multi-scale Imaging Key Laboratory, School of Geophysics and Geomatics, China University of Geosciences, Wuhan, China, [2]Hainan Investigation Institute of Hydrogeology and Engineering Geology, Haikou, China

When the subsurface media contain electrical anisotropic structure, magnetotelluric isotropic inversion fails to recover the electrical anisotropic structure and may distort the image of isotropic structures. Besides, due to the diversity and uncertainty in inversion caused by multi-parameterization, mature and practical anisotropic inversion procedure is lacking at the case with anisotropic angle. Here, four two-dimensional models were constructed with mixed electrical anisotropic/isotropic structures including azimuthal anisotropy case. Phase tensor and real induction vector analyses, as well as two-dimensional isotropic and one-dimensional anisotropic inversions, were performed to identify and estimate the electrical anisotropic parameters. Based on the equivalence concept of electrical anisotropy, the extracted anisotropic structure was equivalent to isotropic structure with alternating high- and low-resistivity anomalies. These equivalent anomalies were then added into two-dimensional isotropic inversion as *a priori* information. Consequently, the isotropic structure of the true model is well recovered. The proposed method can identify and estimate the electrical anisotropy structure as well as the isotropic structure to a certain extent in two-dimensional magnetotelluric models. This study provides a novel approach for analyzing electrical anisotropy in magnetotelluric data.

KEYWORDS

magnetotellurics, electrical anisotropy, identification, equivalence, recovery magnetotellurics, recovery

1 Introduction

An increasing number of studies have presented the multi-scale electrical anisotropy characteristics of lithospheric composition and structure (Jones, 2012; Martí, 2014), such as the directional arrangement of specific mineral rocks or geological structures, and the spatial dominance distribution of geological fluids or volatile components (Nover, 2005; Wannamaker, 2005; Martí, 2014; Pommier, 2014). The magnetotelluric method is a passive exploration technique that utilizes a broad spectrum of naturally occurring geomagnetic variations as a power source for electromagnetic induction in the Earth. It measures natural electric and magnetic fields in orthogonal directions at the Earth's surface. Based on the theory of skin depth (i.e., the penetration depth of electromagnetic fields into the

Earth approximately expressed as $503\sqrt{\rho T}$, where ρ is the average resistivity of medium and T the period), it can determine subsurface electrical resistivities at depths ranging from a few tens of meters to several hundreds of kilometers. Lots of studies have presented the existence of electrical anisotropy within real magnetelluric data (e.g., Bhattacharya, 2005; Heinsong and White, 2005; Frederiksen et al., 2006; Padilha et al., 2006; Wannamaker et al., 2008; Brasse et al., 2009; Häuserer and Junge, 2011; Le Pape et al., 2012; Naif et al., 2013; Liu, 2016; Chave and Jones, 2018; Liu et al., 2019). Undoubtedly, studying the electrical anisotropy in the Earth's interior can provide crucial clues to reveal the lithospheric deformation history and evolution process (e.g., Tommasi et al., 1999; Hamilton et al., 2006; Jones, 2006; Jones, 2012), as well as provide fundamental information and key constraints for lithospheric composition and structure and geodynamic models (e.g., Mareschal et al., 1995; Becker et al., 2006; Heise and Ellis, 2016).

Identifying electrical anisotropy in magnetotelluric data has been a global research focus (e.g., Bahr and Duba, 2000; Bahr and Simpson, 2002; Liu et al., 2019). The over-quadrant phenomenon of impedance phase (i.e., the phase variations of Zxy or Zyx components exceeding 90°) was first observed in specific two-dimensional or three-dimensional anisotropic models with upper and lower structural relationships (Pek and Verner, 1997; Heise and Pous, 2003; Kumar and Manglik, 2012). Additionally, the real induction vectors and phase tensors can be used to indicate the presence of electrical anisotropy. Pek (2009) found that, in a two-dimensional anisotropic medium, the real induction vector deviated from the principal axes of both the regional impedance tensor and the anisotropy body, with the degree of deviation depending on the depth and horizontal extent of the anisotropic body. Based on the consistent phase differences and induction vectors, Yin et al. (2014) determined the electrical anisotropy within real magnetotelluric data. Liu et al. (2019) discriminated the electrical anisotropy from the spatially continuous directions of phase tensors and real induction vectors. Furthermore, numerous theoretical modeling studies have shown that isotropic inversion of magnetotelluric responses from a resistivity model with anisotropy will produce equivalent isotropic anomalies, i.e., alternating high- and low-resistivity anomalies (Eisel and Haak, 1999; Heise and Pous, 2003; Martí, 2014). This phenomenon facilitates the identification and parameter estimation of electrical anisotropy (Heise and Pous, 2003; Heise et al., 2006). Conversely, the occurrence of such alternating resistivity structures does not necessarily indicate the presence of electrical anisotropy. Comeau and Becken (2020) conducted two-dimensional magnetotelluric imaging in the Bulnay region of Mongolia and identified distinct low-resistivity bands in the lower crust. These features persisted even when anisotropy was incorporated into the modeling. They suggested that regional lower crustal fluid flow is primarily governed by tectonic deformation and compaction processes, rather than lithological-structural heterogeneity.

For quantitative interpretation, the three-dimensional modeling has gradually matured (e.g., Löwer and Junge, 2017; Cao et al., 2017; Cao et al., 2018; Xiao et al., 2018; Han et al., 2018; Xiao et al., 2019a; Xiao et al., 2019b; Yu, 2021; Zhou, 2022; Zhu et al., 2023). However, progress in anisotropic inversions remains slow. The main challenge is recovering the true electrical anisotropic structure without introducing artificial anomalies (Yin, 2003; Pek et al., 2011; Chen and Weckmann, 2012; Xie et al., 2022). One-dimensional anisotropic inversion accounting for azimuthal anisotropy case has become relatively mature, where the most representative and widely adopted method is the improved Occam inversion method developed by Pek and Santos (2006). Mature two-dimensional anisotropic inversion has been applied in some practical applications, but only in the case where the resistivity anisotropy direction is either parallel or perpendicular to the regional electrical principal axis (e.g., Baba et al., 2006; Key et al., 2013; Naif et al., 2013; Key, 2016; Johansen et al., 2019). Besides, for two-dimensional electrical anisotropic media, two-dimensional isotropic inversion will not only fail to recover the electrical anisotropic structure but also possibly distort the imaging of the electrical isotropic structure (Heise and Pous, 2003; Löwer and Junge, 2017; Miensopust and Jones, 2011). Therefore, considering the multiplicity and instability of inversions, it is crucial to find a way to identify and estimate anisotropic parameters, and simultaneously recover electrical anisotropic/isotropic structures.

Based on four two-dimensional theoretical models with mixed electric anisotropic/isotropic structures including azimuthal anisotropy case, we aim to identify and estimate electrical anisotropy through phase tensor and induction vector analyses, as well as two-dimensional isotropic and one-dimensional anisotropic inversions. Ultimately, the extracted electrical anisotropic parameters were equivalent to isotropic structures with alternating high- and low-resistivity anomalies, which were used as prior information for the isotropic inversion to recover the electrical isotropic structure.

2 Theoretical electrical anisotropy model

In orogenic belts and subduction zones, the crust and upper mantle are influenced by various geological processes, such as stress motion, magma intrusion, and migration of mantle fluids. These processes may include the transports of liquid-melt, graphite, and metallic sulfides, as well as the directional alignments of specific geological structures, which can result in observable electrical anisotropy (e.g., Wannamaker, 2005; Yin et al., 2014; Liu et al., 2021). For example, in Tibetan Plateau of SW China, the flow of soft materials (either molten or partially molten) under shear stress in the lower crust can lead to resistivity variations in different directions (Meyer et al., 1998; Yin et al., 2008a; Yin et al., 2008b; Zhao et al., 2011). Additionally, in Western Junggar of NW China, ancient subducted slabs modified by magmatic activity, can produce electrical anisotropy in the upper crust (Liu, 2016; Liu et al., 2019). Based on the typical characteristics of electrical anisotropy observed in Tibetan Plateau and Western Junggar, this study constructed four two-dimensional theoretical models with mixed azimuthal electrical anisotropy structures and electrical isotropy structures, as illustrated in Figure 1. Model A, referred to the electrical anisotropy in Tibetan Plateau, includes a high-resistivity (300 Ω.m) upper crust (0–20 km) embedded with an isotropic low-resistivity body of 10 Ω.m, an azimuth anisotropic mid-lower crust (20–40 km) with the principal axes resistivities of 10 Ω.m, 300 Ω.m, and 10 Ω.m, respectively, and a 10 Ω.m half-space below 40 km. When the azimuth angle α_s of anisotropic layer is 0° and 30°, the models are referred to Model A1 and Model A2, respectively. Model B,

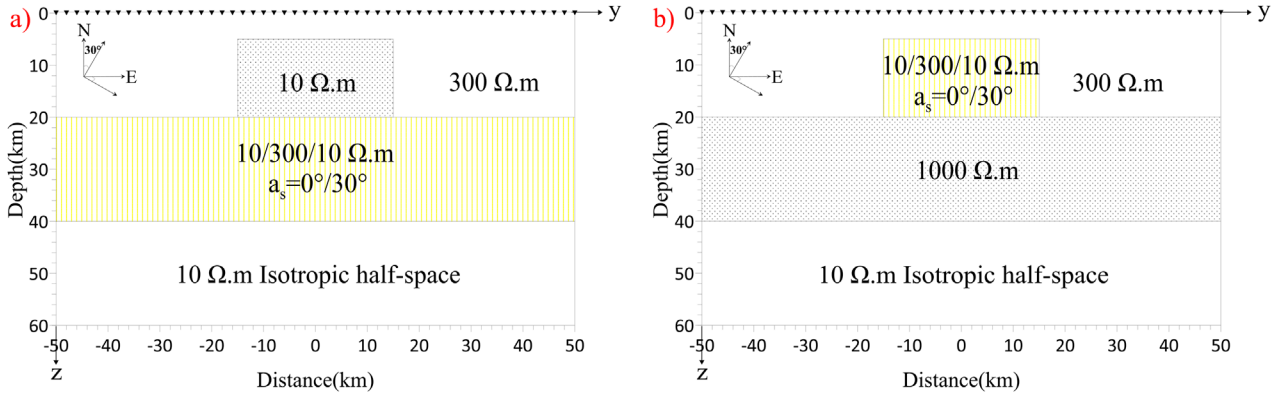

FIGURE 1
Schematic representation of two-dimensional electrical anisotropic models used in this study. **(a)** Model A represents an anisotropic layer within an isotropic structure, while **(b)** Model B features an anisotropic body within an isotropic layer. The black inverted triangles indicate the locations of magnetotelluric sites.

referred to the electric anisotropy in Western Junggar, has the consistent structure scales bodies with Model A. The differences are that the isotropic body and the anisotropic layer in Model A are changed to the anisotropic body and the isotropic layer. Similarly, the anisotropic bodies with α_s = 0° and α_s = 30° are designated as Models B1 and B2, respectively.

For the four typical models, the two-dimensional finite difference method (Pek and Verner, 1997) was utilized to calculate the response functions at 51 stations with a space of 2 km. The response periods ranged from 0.015 s to 2000 s logarithmically divided into 30 spaced periods.

3 Identification and parameter estimation for electrical anisotropy

3.1 Forward response analysis

The magnetotelluric forward responses for the four models were analyzed using phase tensor ellipses (Caldwell et al., 2004; Booker, 2014) and real induction vectors (Wiese, 1962) as illustrated in Figure 2. Phase tensor ellipses are plotted for the magnetotelluric stations with long axes (maximum phase ϕ_{max}) normalized and filled by colors representing the values of the skew angle ψ (left slide) and the minimum phase ϕ_{min} (right slide). In a two-dimensional case, ϕ_{max} and ϕ_{min} refer to the magnetotelluric phases of transverse electric (TE) and transverse magnetic (TM) modes and the skew angle ψ is 0° (Caldwell et al., 2004). The real induction vectors follow Wiese convention (Wiese, 1962), where the vectors point away from low-resistivity structures.

For the axial anisotropy Models A1 and B1 (Figures 2a,c), the phase tensor ellipses within the anisotropic regions present consistent long-axis orientation directing towards true north, with skew angle value of zero. In contrast, the one-dimensional electrical isotropic regions beneath the anisotropic body or layer exhibit distorting features with consistent long-axis orientation in certain areas. For the Model A1, the minimum phase indicates the presence of a relatively low-resistivity body within the vertical range of 5–20 km (as calculated using the skin depth formula) and the horizontal range of −15 to 15 km. In comparison, the high-resistivity layer situated beneath the anisotropic body in the Model B1 cannot be distinguished from minimum phase.

In the context of azimuthal anisotropy Models A2 and B2 (Figures 2b,d), the phase tensor ellipses within the anisotropic regions present consistent long-axis orientation directing towards 30° east of north. However, beneath these regions, the orientation of the phase tensor ellipses shifts to 30° west of north. Notably, the skew angle is no longer zero beneath the anisotropic body or layer. Especially, for the Model B2, the absolute value of skew angle exceeds 6°. Without considering anisotropy, this may mislead that three-dimensional interpretation is necessary. This suggests that azimuthal anisotropy can induce substantial changes in dimensionality analysis within the anisotropic region and its surrounding. Moreover, the minimum phase can indicate the presence of a low-resistivity body located above the azimuthal anisotropic layer in Model A2. In contrast, the high-resistivity layer beneath the anisotropic body in the Model B2 remains unclear from the minimum phase.

Furthermore, for all four models, the real induction vectors (Figure 2) are primarily oriented perpendicular to the structural strike or the direction of minimum resistivity anisotropy, indicating strong response to anomaly body. The values of the real induction vectors reach their maximum at the boundaries of these bodies.

3.2 Two-dimensional isotropic inversion

To explore the distortion patterns when inverting the responses of an anisotropic model using isotropic inversion, we performed two-dimensional isotropic Occam inversion (DeGroot-Hedlin & Constable, 1990). The impedance data from Models A2 and B2 were rotated by 30° to align with the anisotropic direction. Both apparent resistivity and phase were assigned to 5% error floor. The inversion results are presented in Figure 3.

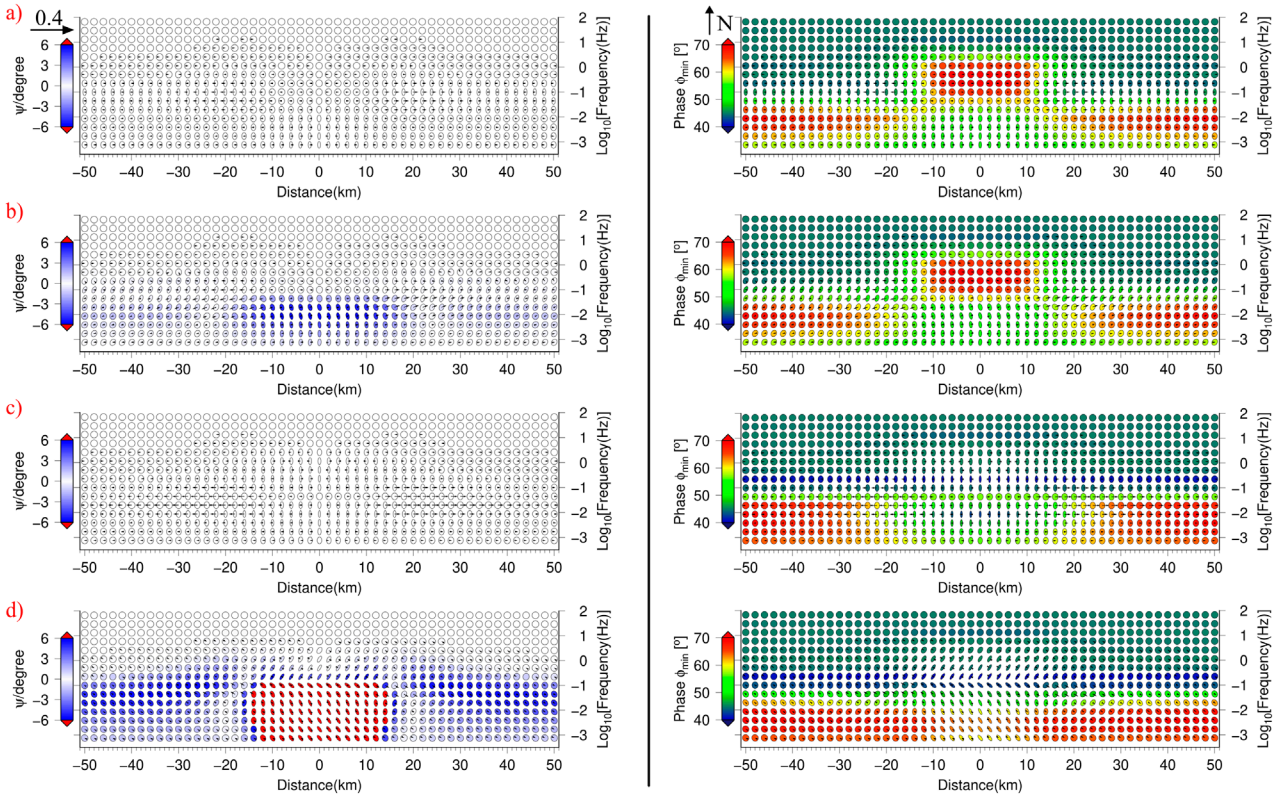

FIGURE 2
The phase tensor ellipses and real induction vectors from the anisotropic models A1 **(a)**, A2 **(b)**, B1 **(c)** and B2 **(d)**. The long axes of ellipses are normalized and the fill colors represent the skew angle ψ (left) and the minimum phase ϕ_{min} (right), respectively. The black arrow represents the Wiese real induction vector.

Within the electrically anisotropic body (Model B) and the layer (Model A), the inversion results of joint TE+TM modes manifest as vertical dyke isotropic structures characterized by alternating high- and low-resistivity anomalies. The inverted high- and low-resistivity dykes have resistivities of ~635 Ω.m and ~5 Ω.m, respectively. The average widths of the dykes are ~20 km for Model A and ~6 km for Model B. Moreover, consistent with the forward response analysis, the isotropic inversion results suggest that electrical anisotropy does not significantly affect the imaging of the overlying isotropic structure. The isotropic inversions of different polarization modes for Models A1 (Figure 3a) and A2 (Figure 3b) can effectively recover the overlying isotropic low-resistivity body. However, electrical anisotropy would distort the imaging of underlying isotropic regions. The inversion results of different polarization modes for Model B1 (Figure 3c) show that the high-resistivity layer beneath the electrical anisotropic body is disrupted and the deep isotropic half-space cannot be well recovered. Besides, in contrast to axial anisotropy (Model B1), azimuthal anisotropy can produce a more pronounced distortion in the imaging of underlying isotropic structure (Figure 3d). The inversion results of TE+TM modes reveal two low-resistivity false anomalies within the high-resistivity layer, while the inversion results of TE mode present a "T-shaped" low-resistivity anomaly within the region of the anisotropic body region.

3.3 One-dimensional anisotropic inversion

Currently, mature and practical two-dimensional anisotropic inversion is limited to cases with axial anisotropy. One-dimensional anisotropic inversion is relatively well-developed and can account for azimuthal anisotropy case. The spatial consistency of the inversion results plays a crucial role in identifying electrical anisotropy and estimating anisotropic parameters. To estimate the electrical anisotropic parameters, one-dimensional anisotropic inversion (Pek and Santos, 2006) was conducted for all stations from the four models. The pseudo two-dimensional images are shown in Figure 4, where the inversion results for the rightmost and central stations of each model are also presented. The background color represents the logarithmic difference between the maximum and minimum resistivities. The more intense red hue indicates a higher degree of anisotropy. The filling color of small square above the background represents the azimuthal angle of the minimum resistivity at various depths. The north is defined as 0° and the clockwise direction is positive.

For the Model A1 (Figure 4a), an electrical anisotropy layer can be observed at depths ranging from 20 to 40 km. The azimuth of minimum resistivity is primarily oriented at 0° or 180°, which is consistent with that of true electrical anisotropy. Moreover, the inversion results of the two typical stations (y

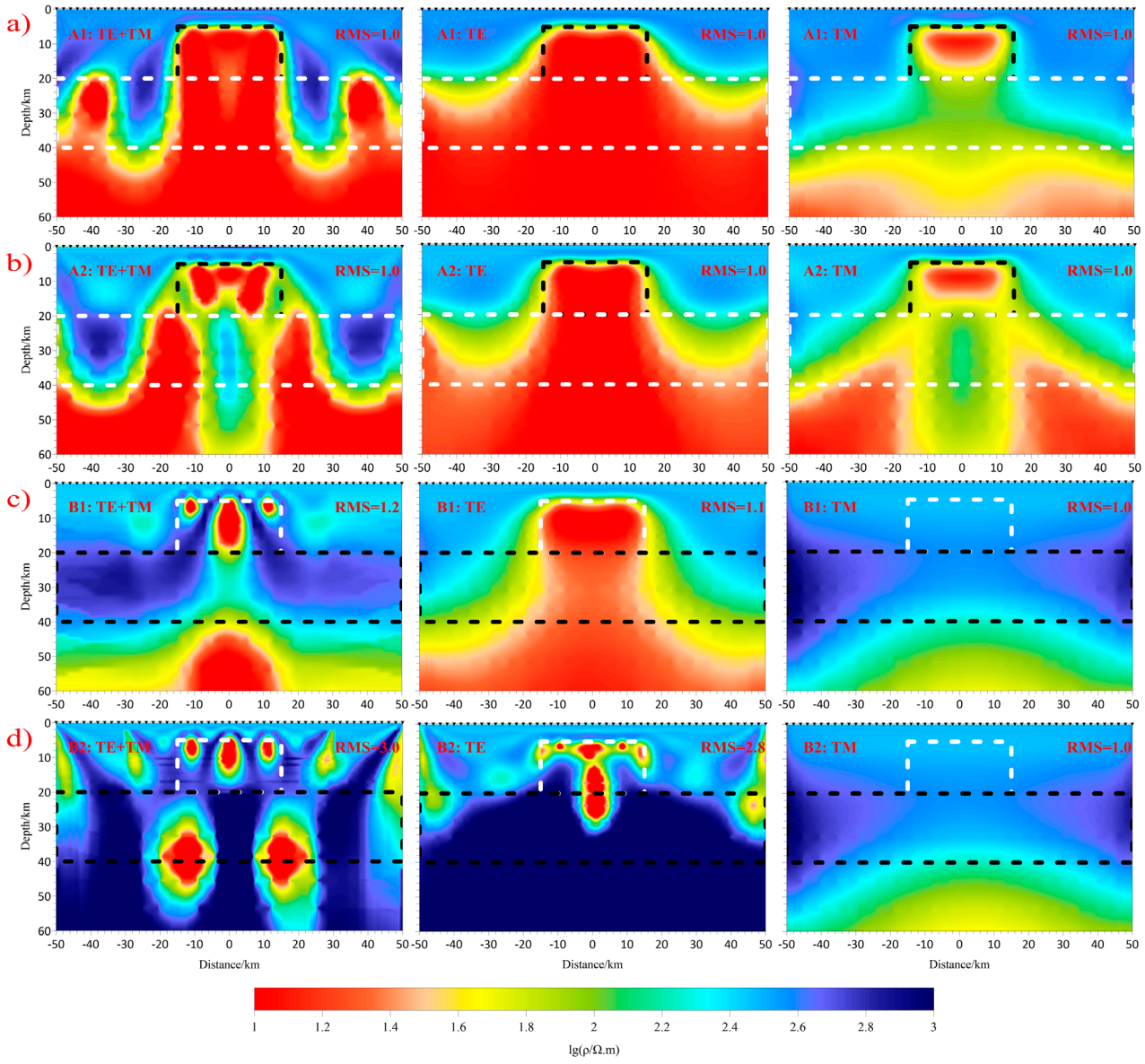

FIGURE 3
Two-dimensional isotropic inversion results of different polarization modes for Models A1 **(a)**, A2 **(b)**, B1 **(c)**, and B2 **(d)**. Black inverted triangles indicate magnetotelluric sites, white rectangles represent the true anisotropic areas, and black rectangles denote the true isotropic areas.

= 50 km and y = 0 km) show that the background resistivity at depths of 0–20 km is about 300 Ω.m, and a low-resistivity body of about 10 Ω.m is embedded at depths of 5–20 km in the middle area. The minimum and maximum resistivities at depths of 20–40 km are around 5 Ω.m and 280 Ω.m, respectively. For the Model A2 (Figure 4b), the inversion results are similar to those from Model A1. A layer with relatively high electrical anisotropy at depths of 20–40 km can also be identified with an azimuth angle of ~30°. However, large-scale false anisotropic anomalies also appear in the underlying region. The bottom boundary of the anisotropic layer can be determined through a combination of forward response analysis and two-dimensional isotropic inversion.

For the Model B1 (Figure 4c), electrical anisotropy is evident at depths greater than 5 km, with the minimum resistivity azimuth predominantly oriented at 0° or 180°. Combined with the results from both the forward response analysis and two-dimensional isotropic inversion, it can be inferred that there is an axial anisotropic body, extending horizontally from −15 km to 15 km and vertically from 5 km to 20 km. From the inversion results of the two typical stations (y = 50 km and y = 0 km), the minimum and maximum resistivities of this anisotropic body can be obtained with values of ~15 Ω.m and ~290 Ω.m, respectively. Besides, the inversion results for Model B2 are similar to those for Model B1, except that the minimum resistivity azimuth within the anisotropic region is primarily oriented at 30°.

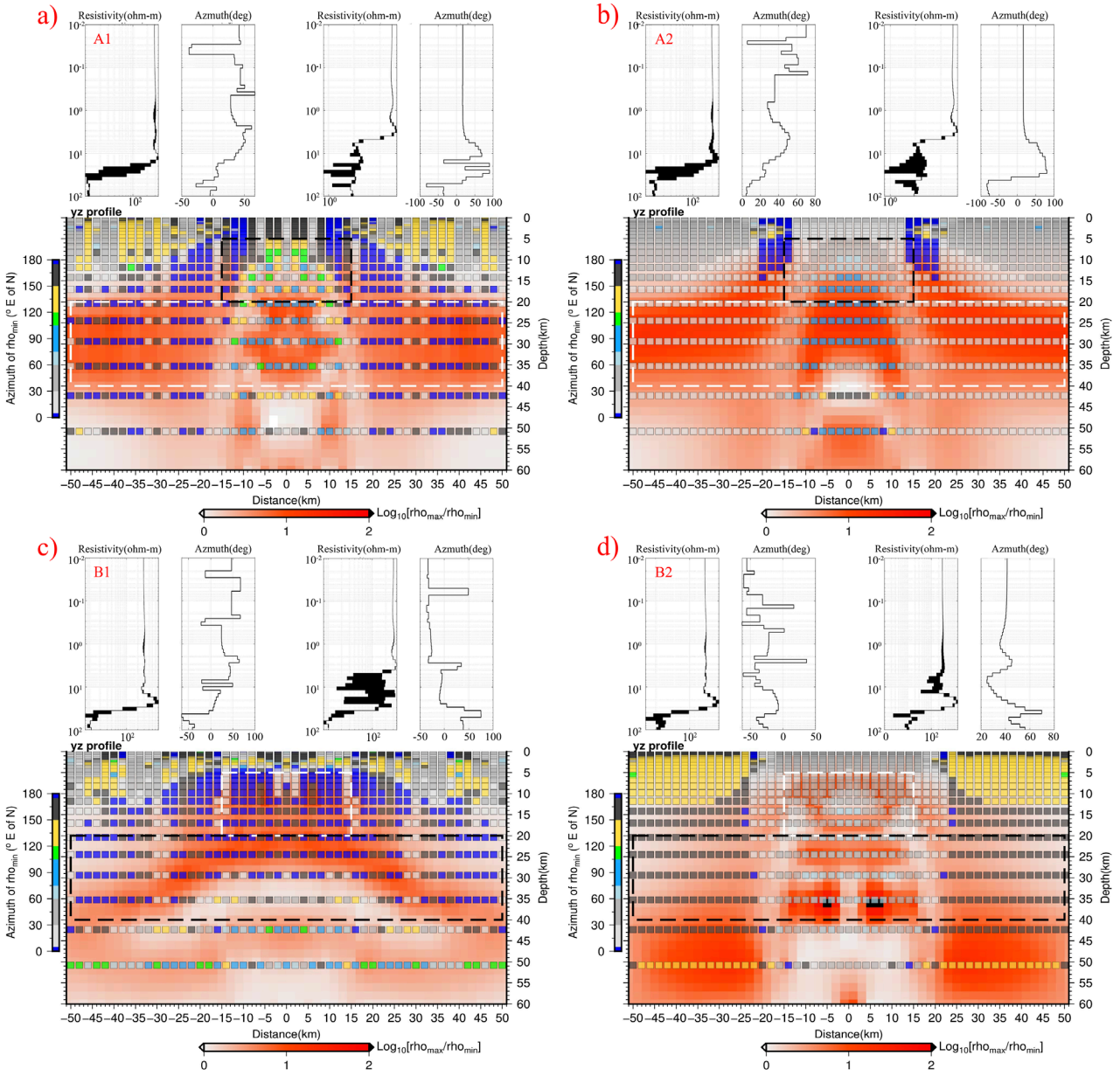

FIGURE 4
One-dimensional anisotropy inversion results for Models A1 **(a)**, A2 **(b)**, B1 **(c)** and B2 **(d)**. Profile represents the pseudo two-dimensional imaging of one-dimensional inversion results. Background color of profile shows the difference between maximum and minimum resistivities in logarithmic domain. The darker red indicates stronger electrical anisotropy. The overlaid small squares with colors indicate the azimuthal angles of minimum resistivities. The white and black dotted lines represent the locations of anisotropic and isotropic anomalies, respectively. The two plots above each profile show the one-dimensional inversion results at the y = 50 km and y = 0 km stations.

4 Isotropic constraint inversion under equivalent concept

4.1 Isotropic equivalence of electrical anisotropy

Theoretical model studies have shown that any microscopic anisotropic model can be effectively simulated using complex isotropic structures (Eisel and Haak, 1999; Weidelt, 1999; Heise and Pous, 2003; Martí, 2014). This equivalence between microscopic anisotropy and isotropy arises primarily from the limited resolution of the magnetotelluric method at the relevant detection depths (Weidelt, 1999). Eisel and Haak (1999) noted that once a macroscopic anisotropic structure, such as dyke structures with alternating high- and low-resistivities, is recovered through two-dimensional isotropic inversion, the approximate values of the microscopic anisotropic resistivities can be derived using the resistivities and average dyke widths from the

inversion. The fundamental formula for estimating axial resistivities is as follows:

$$\rho_{\max} = \frac{\rho_1 d_1 + \rho_2 d_2}{d_1 + d_2}, \rho_{\min} = \frac{\rho_1 \rho_2 (d_1 + d_2)}{\rho_1 d_1 + \rho_2 d_2} \quad (1)$$

In the above, ρ_1 and d_1 represent the resistivity and width of high-resistivity dykes from the inversion, while ρ_2 and d_2 are the resistivity and width of the low-resistivity dykes.

The two-dimensional inversions of TE+TM modes for the four models effectively fit the anisotropic response data by employing a vertical dyke structure with alternating high- and low-resistivities (Figure 3), where $\rho_1 \approx 635\,\Omega$.m, $\rho_2 \approx 5\,\Omega$.m, and $d_1 \approx d_2$. The average dyke widths are 20 km and 6 km for Model A and Model B. Utilizing Equation 1, we can obtain $\rho_{max} \approx 320\,\Omega$.m and $\rho_{min} \approx 10\,\Omega$.m. From the one-dimensional anisotropic inversions, the anisotropic layer in Model A presents $\rho_{max} \approx 280\,\Omega$.m and $\rho_{min} \approx 5\,\Omega$.m, while the anisotropic body in Model B shows $\rho_{max} \approx 290\,\Omega$.m and $\rho_{min} \approx 15\,\Omega$.m. By taking the arithmetic mean of the anisotropic resistivities obtained from two-dimensional isotropic and one-dimensional anisotropic inversions, the final optimized anisotropic resistivities for Model A and Model B are $\rho_{max} \approx 300\,\Omega$.m and $\rho_{min} \approx 7.5\,\Omega$.m, and $\rho_{max} \approx 305\,\Omega$.m and $\rho_{min} \approx 7.5\,\Omega$.m, respectively. These values are close to the true anisotropic resistivities.

4.2 Constraint inversion

From the results of two-dimensional isotropic inversion (Figure 3), it is obvious that the anisotropic layer in Model A does not influence the image of overlying isotropic structure. However, the anisotropic body in Model B distorts the imaging of the underlying isotropic medium. Therefore, this study focuses on the recovery of isotropic structures in Models B1 and B2. The basic idea is that the equivalent isotropic results of electrical anisotropy are first added into two-dimensional isotropic inversion as *a priori* information, as shown in the top two panels of Figure 5. Then, constraint isotropic inversion is conducted to suppress the influence of anisotropy and recover the isotropic structure distorted by anisotropy.

When the anisotropic body in Model B was equivalent to isotropic structures with alternating high- and low-resistivity bands of 635 Ω.m and 5 Ω.m, respectively, the constraint inversion cannot recover the underlying structure. After numbers of simulations, we found that replacing the equivalent high- and low-resistivities as approximate ρ_{max} and ρ_{min} in the constraint inversion can effectively recover the underlying isotropic structure. In this case, the prior model can produce relatively small initial misfit. Here, we adopted 305 Ω.m and 10 Ω.m as the final equivalent high- and low-resistivities for prior model (Figures 5a,b).

The constraint inversion results are shown in Figure 5. Compared with the unconstrained inversion results (Figure 3), it can be seen that the constraint inversions can well recover the resistivity values and geometrical features of the isotropic high-resistivity layer and low-resistivity half-space beneath the anisotropic body. Therefore, combined with the results of identification and parameter estimation for electrical anisotropy as previously mentioned, both electrical anisotropy and isotropic electrical structures in the models B1 and B2 have been successfully recovered to a certain content.

5 Discussion

The phase tensor analysis shows that the major axes of ellipses maintain consistent orientations within anisotropic regions. For axial anisotropy, the major axes of the ellipses align with the strike direction, while the skew angles have an absolute value of 0°. In contrast, for azimuthal anisotropy, the major axes are perpendicular to the anisotropic direction (the direction of lowest resistivity). Meanwhile, the skew angles have absolute values greater than 0° (even exceeding 6°). Without considering anisotropy, this may mislead that three-dimensional interpretation is necessary. Moreover, the real induction vectors reach maximum amplitudes at the boundaries of anomalous bodies (including anisotropic bodies), with directions always perpendicular to anisotropic direction. Significantly, the modeling reveals a new finding that electrical anisotropy anomaly can severely distort the phase tensors and real induction vectors of its underlying region but not above it.

When isotropic inversion is applied to magnetotelluric responses from an electrical anisotropy model, it fails to recover the anisotropic structure and distorts the imaging of isotropic structure below anisotropic body. However, two-dimensional isotropic inversion of TE+TM modes generally produces vertically alternating high- and low-resistivity anomalies within anisotropic region. By combining the spatial variation patterns of phase tensors and real induction vectors (particularly the spatial consistency or continuity of responses across different sites and periods) with the two-dimensional isotropic inversions, the type and boundary of electrical anisotropy can be roughly identified. Moreover, one-dimensional anisotropic inversion can reveal electrical anisotropy structure to a certain extent. The minimum and maximum resistivities and the orientation of the anisotropy anomaly can be approximately obtained from the spatial variations of one-dimensional anisotropic inversion results. However, due to fake anomalies below the anisotropic structure in the one-dimensional anisotropic inversion results, the lower boundary cannot be obtained, which can be detected from response analyses or two-dimensional isotropic inversion results. Therefore, based on the above processes, the anisotropic body and its parameters can be identified and estimated.

On the other hand, based on phase tensor and real induction vector analyses, as well as the results of two-dimensional isotropic and one-dimensional anisotropic inversions, it is obvious that the anisotropic structure can affect the isotropic structure below it. Following the principle of anisotropic equivalence (Eisel and Haak, 1999; Heise and Pous, 2003; Martí, 2014), the anisotropic structure can be equivalent to isotropic alternating high- and low-resistivity anomalies. By isotropic constraint inversion, the isotropic structure can be obtained. Thus, combined with the identification and parameter estimation for electrical anisotropy, the anisotropic and isotropic structures in the true models can be well recovered to a certain content.

This study involves multiple inversion steps, including one-dimensional anisotropic inversion and two-dimensional unconstrained and constrained isotropic inversions. The selected inversion codes are mature and widely applied with less computational costs (about 2 h for all steps on a normal desktop computer in this study). Moreover, the proposed approach is based on the assumption that electrical anisotropy can be equivalently represented by isotropic resistivity structures (Eisel and Haak, 1999;

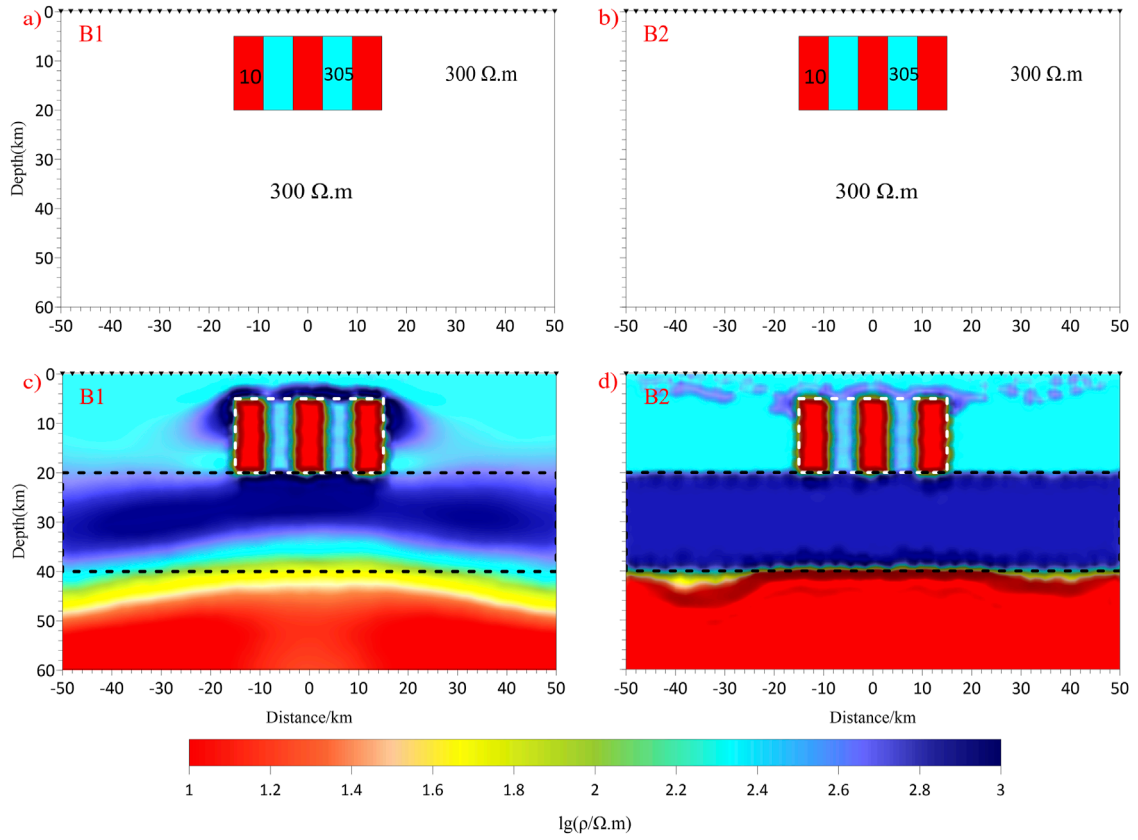

FIGURE 5
Two-dimensional isotropic constraint inversion results for Models B1 and B2. **(a, b)** show the prior models for Model B1 and Model B2, respectively, incorporating the equivalent structures proposed in this study, where the resistivity of the low-resistivity dykes is 10 Ω.m and the high-resistivity dykes is 300 Ω.m. **(c)** Constraint inversion results for Model B1; **(d)** Constrained inversion results for Model B2.

Weidelt, 1999; Heise and Pous, 2003). The theoretical modeling tests in this study indicate the validation of the assumption. Nevertheless, considering the complexity of real geological settings, the applicability of the assumption requires further studies. Furthermore, the proposed method in this study lacks the validation in real magnetotelluric data, which will be a focus in future research. Anyway, when the proposed method is used in real data, the existence of electrical anisotropy should be firstly identified and then the validation of quantitative interpretation can be studied.

6 Conclusion

It is worth noting that this study only considers the azimuthal anisotropy, which is the most common and significant case for magnetotelluric method based on plane wave theory. Following the line of evidence discussed above, several conclusions are obtained:

1. Electrical anisotropic bodies can distort the magnetotelluric responses of the underlying isotropic structure, misleadingly indicating that three-dimensional interpretation is necessary. Two-dimensional isotropic inversion of TE+TM modes can fit the anisotropic responses by introducing vertically isotropic structure with alternating high- and low-resistivity anomalies but produce fake anomalies in the underlying isotropic part.
2. Combined phase tensor and real induction vector analyses with two-dimensional isotropic and one-dimensional anisotropic inversions, the anisotropic structure and its parameters can be well identified and estimated.
3. Compared with the unconstrained isotropic inversion results, the resistivity values and geometrical features of isotropic parts beneath the anisotropic body can be reasonably recovered by constrained isotropic inversions based on the assumption that anisotropic structures can be treated as equivalent isotropic structures.

Data availability statement

The original contributions presented in the study are included in the article/supplementary material, further inquiries can be directed to the corresponding author.

Author contributions

XJ: Conceptualization, Formal Analysis, Investigation, Methodology, Validation, Visualization, Writing – original draft,

Writing – review and editing. ZX: Formal Analysis, Supervision, Writing – review and editing. ZH: Formal Analysis, Supervision, Writing – review and editing. WZ: Investigation, Validation, Writing – review and editing. YL: Conceptualization, Funding acquisition, Investigation, Project administration, Supervision, Validation, Writing – review and editing.

Funding

The author(s) declare that financial support was received for the research and/or publication of this article. This study was supported by the National Key Research and Development Program of China (No. 2024YFF0807300) and the National Natural Science Foundation of China with grants 42430307 and 41904079.

Acknowledgments

We are grateful for the constructive comments and insightful suggestions provided by the reviewers, which significantly enhanced the quality of this paper.

Conflict of interest

The authors declare that the research was conducted in the absence of any commercial or financial relationships that could be construed as a potential conflict of interest.

Generative AI statement

The author(s) declare that no Generative AI was used in the creation of this manuscript.

Publisher's note

References

Baba, K., Chave, A. D., Evans, R. L., Hirth, G., and Mackie, R. L. (2006). Mantle dynamics beneath the east pacific rise at 17°S: insights from the mantle electromagnetic and tomography (MELT) experiment. *J. Geophys. Res. Solid Earth* 111 (B2), B02101. doi:10.1029/2004jb003598

Bahr, K., and Duba, A. (2000). Is the asthenosphere electrically anisotropic? *Earth Planet. Sci. Lett.* 178, 87–95. doi:10.1016/s0012-821x(00)00070-4

Bahr, K., and Simpson, F. (2002). Electrical anisotropy below slow and fast moving plates: paleo flow in the upper mantle. *Science* 295, 1270–1272. doi:10.1126/science.1066161

Becker, T. W., Chevrot, S., Schulte-Pelkum, V., and Blackman, D. K. (2006). Statistical properties of seismic anisotropy predicted by upper mantle geodynamic models. *J. Geophys. Res. Solid Earth* 111, B08309. doi:10.1029/2005jb004095

Bhattacharya, B. B. (2005). Electrical anisotropy of asthenosphere in a region of window to mantle underneath Eastern Indian Craton. *Phys. Earth Planet. Interiors* 152 (1), 43–61. doi:10.1016/j.pepi.2005.06.001

Booker, J. R. (2014). The magnetotelluric phase tensor: a critical review. *Surv. Geophys.* 35 (1), 7–40. doi:10.1007/s10712-013-9234-2

Brasse, H., Kapinos, G., Li, Y., Mütschard, L., Soyer, W., and Eydam, D. (2009). Structural electrical anisotropy in the crust at the South-Central Chilean continental margin as inferred from geomagnetic transfer functions. *Phys. Earth Planet. Interiors* 173 (1), 7–16. doi:10.1016/j.pepi.2008.10.017

Caldwell, T. G., Bibby, H. M., and Brown, C. (2004). The magnetotelluric phase tensor. *Geophys. J. Int.* 158 (2), 457–469. doi:10.1111/j.1365-246x.2004.02281.x

Cao, H., Wang, K., Wang, T., and Hua, B. (2018). Three-dimensional magnetotelluric axial anisotropic forward modeling and inversion. *J. Appl. Geophys.* 153 (1), 75–89. doi:10.1016/j.jappgeo.2018.04.015

Cao, X., Yin, C., Zhang, B., Huang, X., Ren, X., Qiu, C., et al. (2017). "A goal-oriented adaptive finite-element algorithm for 3D anisotropic MT modelling," in 79th EAGE Conference and Exhibition, France.

Chave, A. D., and Jones, A. (2018). *The magnetotelluric method: theory and practice*. Cambridge, United Kingdom: Cambridge Univ. Press, 604.

Chen, X., and Weckmann, U. (2012). *Constriant inversion of 2D magnetotelluric data with anisotropic conductivities*. Darwin, Australia: American Geophysical Union. Extended Abstract 21 st Workshop.

Comeau, M. J., Becken, M., Connolly, J. A. D., Grayver, A. V., and Kuvshinov, A. V. (2020). Compaction-driven fluid localization as an explanation for lower crustal electrical conductors in an intracontinental setting. *Geophys. Res. Lett.* 47. doi:10.1029/2020gl088455

DeGroot-Hedlin, C., and Constable, S. (1990). Occam's inversion to generate smooth, two-dimensional models from magnetotelluric data. *Geophysics* 55 (12), 1613–1624. doi:10.1190/1.1442813

Eisel, M., and Haak, V. (1999). Macro-anisotropy of the electrical conductivity of the crust: a magnetotelluric study of the German Continental Deep Drilling site (KTB). *Geophys. J. R. Astronomical Soc.* 136 (1), 109–122. doi:10.1046/j.1365-246x.1999.00707.x

Frederiksen, A. W., Ferguson, I. J., Eaton, D., Miong, S. K., and Gowan, E. (2006). Mantle fabric at multiple scales across an archean–proterozoic boundary, grenville front, Canada. *Phys. Earth Planet. Interiors* 158 (2), 240–263. doi:10.1016/j.pepi.2006.03.025

Hamilton, M. P., Jones, A. G., Evans, R. L., Fourie, C., Garcia, X., Mountford, A., et al. (2006). Electrical anisotropy of South African lithosphere compared with seismic anisotropy from shear-wave splitting analyses. *Phys. Earth Planet. Interiors* 158 (2), 226–239. doi:10.1016/j.pepi.2006.03.027

Han, B., Li, Y., and Li, G. (2018). 3D forward modeling of magnetotelluric fields in general anisotropic media and its numerical implementation in Julia. *Geophysics* 83 (4), F29–F40. doi:10.1190/geo2017-0515.1

Häuserer, M., and Junge, A. (2011). Electrical mantle anisotropy and crustal conductor: a 3-D conductivity model of the Rwenzori Region in western Uganda. *Geophys. J. Int.* 185 (3), 1235–1242. doi:10.1111/j.1365-246x.2011.05006.x

Heinsonq, and White, A. (2005). Electrical resistivity of the Northern Australian lithosphere: crustal or mantle heterogeneity? *Earth Planet. Sci. Lett.* 232 (1), 157–170. doi:10.1016/j.epsl.2004.12.029

Heise, W., Caldwell, T. G., Bibby, H. M., and Brown, C. (2006). Anisotropy and phase splits in magnetotellurics. *Phys. Earth Planet. Interiors* 158 (2), 107–121. doi:10.1016/j.pepi.2006.03.021

Heise, W., and Ellis, S. (2016). On the coupling of geodynamic and resistivity models: a progress report and the way forward. *Surv. Geophys.* 37 (1), 81–107. doi:10.1007/s10712-015-9334-2

Heise, W., and Pous, J. (2003). Anomalous phases exceeding 90° in magnetotellurics: anisotropic model studies and a field example in magnetotellurics: anisotropic model studies and a field example. *Geophys. J. Int.* 155 (1), 308–318. doi:10.1046/j.1365-246x.2003.02050.x

Johansen, S. E., Panzner, M., Mittet, R., Amundsen, H. E. F., Lim, A., Vik, E., et al. (2019). Deep electrical imaging of the ultraslow-spreading Mohns Ridge. *Nature* 567 (7748), 379–383. doi:10.1038/s41586-019-1010-0

Jones, A. G. (2006). Electromagnetic interrogation of the anisotropic Earth: looking into the Earth with polarized spectacles. *Phys. Earth Planet. Interiors* 158 (s2–4), 281–291. doi:10.1016/j.pepi.2006.03.026

Jones, A. G. (2012). Distortion decomposition of the magnetotelluric impedance tensors from a one-dimensional anisotropic Earth. *Geophys. J. Int.* 189, 268–284. doi:10.1111/j.1365-246x.2012.05362.x

Key, K. (2016). MARE2DEM: a 2-D inversion code for controlled-source electromagnetic and magnetotelluric data. *Geophys. J. Int.* 207 (1), 571–588. doi:10.1093/gji/ggw290

Key, K., Constable, S., Liu, L., and Pommier, A. (2013). Electrical image of passive mantle upwelling beneath the northern East Pacific Rise. *Nature* 495 (7442), 499–502. doi:10.1038/nature11932

Kumar, G. P., and Manglik, A. (2012). Electrical anisotropy in the main central thrust zone of the Sikkim himalaya: inference from anomalous MT phase. *J. Asian Earth Sci.* 57 (57), 120–127. doi:10.1016/j.jseaes.2012.06.017

Le Pape, F., Jones, A. G., Vozar, J., and Wenbo, W. (2012). Penetration of crustal melt beyond the kunlun fault into northern tibet. *Nat. Geosci.* 5 (5), 330–335. doi:10.1038/ngeo1449

Liu, S. Y., Xu, Y., Yang, B., Guo, Z., Shi, Y., and Liu, Y. (2021). Deciphering fine electrical conductivity structuresin the crust from MT data using the equivalent conductivity formula. *J. Geophys. Res. Solid Earth* 126 (10). doi:10.1029/2021jb022519

Liu, Y. (2016). *Investigation of lithospheric electrical anisotropy in Western Junggar*. Ph.D. thesis (Wuhan: China University of Geosciences). (in Chinese with English abstract).

Liu, Y., Liu, J. P., Chen, C., Wang, G., Liao, Q., and Zhang, X. (2019). The application of audio magnetotelluric for 3D geological mapping in the Gobi Desert area. *Geol. J.* 55, 7335–7345. doi:10.1002/gj.3627

Löwer, A., and Junge, A. (2017). Magnetotelluric transfer functions: phase tensor and tipper vector above a simple anisotropic three-dimensional conductivity anomaly and implications for 3D isotropic inversion. *Pure Appl. Geophys.* 174 (5), 2089–2101. doi:10.1007/s00024-016-1444-3

Mareschal, M., Kellrttt, R., Kurtz, R. D., Ludden, J. N., Ji, S., and Bailey, R. C. (1995). Archaean cratonic roots, mantle shear zones and deep electrical anisotropy. *Nature* 375 (6527), 134–147. doi:10.1038/375134a0

Martí, A. (2014). The role of electrical anisotropy in magnetotelluric responses: from modelling and dimensionality analysis to inversion and interpretation. *Surv. Geophys.* 35 (1), 179–218.

Meyer, B., Tapponnier, P., Bourjot, L., Métivier, F., Gaudemer, Y., Peltzer, G., et al. (1998). Crustal thickening in Gansu-Qinghai, lithosphericmantle subduction, and oblique, strike-slip controlled growth of the Tibet plateau. *Geophys. J. Int.* 135 (1), 1–47. doi:10.1046/j.1365-246x.1998.00567.x

Miensopuѕт, M. P., and Jones, A. G. (2011). Artefacts of isotropic inversion applied to magnetotelluric data from an anisotropic Earth. *Geophys. J. Int.* 187 (2), 677–689. doi:10.1111/j.1365-246x.2011.05157.x

Naif, S., Key, K., Constable, S., and Evans, R. L. (2013). Melt-rich channel observed at the lithosphere-asthenosphere boundary. *Nature* 495 (7441), 356–359. doi:10.1038/nature11939

Nover, G. (2005). Electrical properties of crustal and mantle rocks—a review of laboratory measurements and their explanation. *Surv. Geophys.* 26 (5), 593–651. doi:10.1007/s10712-005-1759-6

Padilha, A. L., Vitorello, Í., Pádua, M. B., and Bologna, M. S. (2006). Lithospheric and sublithospheric anisotropy beneath central-southeastern Brazil constrained by long period magnetotelluric data. *Phys. Earth Planet. Interiors* 158 (2), 190–209. doi:10.1016/j.pepi.2006.05.006

Pek, J. (2009). "Effects of electrical anisotropy upon magnetotelluric data: modelling and experiments," in *Modern methods of electromagnetic data measurement, processing and interpretation*. Editor V. V. Spichak (Moscow: Librokom Publ), 110–135. (in Russian).

Pek, J., and Santos, F. A. M. (2006). Magnetotelluric inversion for anisotropic conductivities in layered media. *Phys. Earth Planet. Interiors* 158 (2), 139–158. doi:10.1016/j.pepi.2006.03.023

Pek, J., Santos, F. A. M., and Li, Y. G. (2011). "Non-linear conjugate gradient magnetotelluric inversion for 2-D anisotropic conductivities," in Schmicker-Weidelt-Kolloquium, Nustadt and der Weinstral (GFZ), NY, United States, 187–206.

Pek, J., and Verner, T. (1997). Finite-difference modelling of magnetotelluric fields in two-dimensional anisotropic media. *Geophys. J. Int.* 128 (3), 505–521. doi:10.1111/j.1365-246x.1997.tb05314.x

Pommier, A. (2014). Interpretation of magnetotelluric results using laboratory measurements. *Surv. Geophys.* 35 (1), 41–84. doi:10.1007/s10712-013-9226-2

Tommasi, A., Tikoff, B., and Vauchez, A. (1999). Upper mantle tectonics: three-dimensional deformation, olivine crystallographic fabrics and seismic properties. *Earth Planet. Sci. Lett.* 168, 173–186. doi:10.1016/s0012-821x(99)00046-1

Wannamaker, P. E. (2005). Anisotropy versus heterogeneity in continental solid Earth electromagnetic studies: fundamental response characteristics and implications for physicochemical state. *Surv. Geophys.* 26 (6), 733–765. doi:10.1007/s10712-005-1832-1

Wannamaker, P. E., Hasterok, D. P., Johnston, J. M., Stodt, J. A., Hall, D. B., Sodergren, T. L., et al. (2008). Lithospheric dismemberment and magmatic processes of the Great Basin-Colorado Plateau transition, Utah, implied from magnetotellurics. *Geochem. Geophys. Geosystems* 9 (5), 620–628. doi:10.1029/2007gc001886

Weidelt, P. (1999). "3D conductivity models: implications of electrical anisotropy," in *Three-dimensional electromagnetics*. Editors M. Oristaglio, and B. Spies (Tulsa, OK, United States: SEG), 119–137.

Wiese, H. (1962). Geomagnetiseche Tiefentellurik Teil II: Die Streichrichtung der untergrundstrukturen des elektrischen Widerstandes, erschlossen aus geomagnetischen Variationen. *Geofis. Pura E Appl.* 52 (1), 83–103. doi:10.1007/bf01996002

Xiao, T. J., Hiu, Y., Wang, Y., and Fu, L. Y. (2018). Three-dimensional magnetotelluric modeling in anisotropic media using edge-based finite element method. *J. Appl. Geophys.* 149, 1–9. doi:10.1016/j.jappgeo.2017.12.009

Xiao, T. J., Huang, X. Y., and Wang, Y. (2019a). 3D MT modeling using the T–Ω method in general anisotropic media. *J. Appl. Geophys.* 160, 171–182. doi:10.1016/j.jappgeo.2018.11.012

Xiao, T. J., Huang, X. Y., and Wang, Y. (2019b). Three-dimensional magnetotelluric modelling in anisotropic media using the A-phi method. *Explor. Geophys.* 50 (1), 31–41. doi:10.1080/08123985.2018.1564274

Xie, J., Cai, H., Hu, X., Han, S., and Liu, M. (2022). Three-dimensional magnetotelluric inversion for triaxial anisotropic medium in data space. *Minerals* 12, 734. doi:10.3390/min12060734

Yin, A., Dang, Y., Wang, L., Jiang, W. M., Zhou, S. P., Chen, X. H., et al. (2008a). Cenozoic tectonic evolution of Qaidam basin and its surrounding regions (Part 1): the southern Qilian Shan-Nan Shan thrust belt and northern Qaidam basin. *Geol. Soc. Am. Bull.* 120, 813–846. doi:10.1130/b26180.1

Yin, A., Dang, Y., Zhang, M., Chen, X. H., and McRivette, M. W. (2008b). Cenozoic tectonic evolution of the Qaidam basin and its surrounding regions (Part 3): structural geology, sedimentation, and regional tectonic reconstruction. *Geol. Soc. Am. Bull.* 120 (7–8), 847–876. doi:10.1130/b26232.1

Yin, C. C. (2003). Inherent nonuniqueness in magnetotelluric inversion for 1D anisotropic models. *Geophysics* 68 (1), 138–146. doi:10.1190/1.1543201

Yin, Y., Unsworth, M., Liddell, M., Pana, D., and Craven, J. A. (2014). Electrical resistivity structure of the Great Slave Lake shear zone, northwest Canada: implications for tectonic history. *Geophys. J. Int.* 199 (1), 178–199. doi:10.1093/gji/ggu251

Yu, G. (2021). *Two-dimensional anisotropic magnetolluric inversion and applications in northern tibet*. Ph.D. thesis (Beijing, China: Institute of Geology, China Earthquake Administration). (in Chinese with English Abstract).

Zhao, W., Kumar, P., Mechie, J., Kind, R., Meissner, R., Wu, Z., et al. (2011). Tibetan plate overriding the Asian plate in central and northern Tibet. *Nat. Gioscience* 4, 870–873. doi:10.1038/ngeo1309

Zhou, J. (2022). *Three-dimensional anisotropic finitie element modeling and inversion of magnetotelluric data*. Ph.D. thesis (Wuhan, China: China University of Geosciences). (in Chinese with English Abstract).

Zhu, Y., Shao, G., Wang, X., and Zhang, W. (2023). A rapid 3D magnetotelluric forward approach for arbitrary anisotropic conductivities in the Fourier domain. *Front. Earth Sci.* 11. doi:10.3389/feart.2023.1183191

Frontiers in Earth Science

Investigates the processes operating within the major spheres of our planet

Advances our understanding across the earth sciences, providing a theoretical background for better use of our planet's resources and equipping us to face major environmental challenges.

Discover the latest Research Topics

See more →

Frontiers

Avenue du Tribunal-Fédéral 34
1005 Lausanne, Switzerland
frontiersin.org

Contact us

+41 (0)21 510 17 00
frontiersin.org/about/contact